Towards High Spatial Resolution Vibrational Spectroscopy

in a Scanning Transmission Electron Microscope

by

Kartik Venkatraman

A Dissertation Presented in Partial Fulfillment
of the Requirements for the Degree
Doctor of Philosophy

Approved June 2020 by the
Graduate Supervisory Committee:

Peter Crozier, Chair
Peter Rez
Robert Wang
Sefaattin Tongay

ARIZONA STATE UNIVERSITY

August 2020

ABSTRACT

Vibrational spectroscopy is a ubiquitous characterization tool in elucidating atomic structure at the bulk and nanoscale. The ability to perform high spatial resolution vibrational spectroscopy in a scanning transmission electron microscope (STEM) with electron energy-loss spectroscopy (EELS) has the potential to affect a variety of materials science problems. Since 2014, instrumentation development has pushed for incremental improvements in energy resolution, with the current best being 4.2 meV. Although this is poor in comparison to what is common in photon or neutron vibrational spectroscopies, the spatial resolution offered by vibrational EELS is equal to or better than the best of these other techniques.

The major objective of this research program is to investigate the spatial resolution of the monochromated energy-loss signal in the transmission-beam mode and correlate it to the excitation mechanism of the associated vibrational mode. The spatial variation of dipole vibrational signals in SiO_2 is investigated as the electron probe is scanned across an atomically abrupt SiO_2/Si interface. The Si-O bond stretch signal has a spatial resolution of 2 – 20 nm, depending on whether the interface, bulk, or surface contribution is chosen. For typical TEM specimen thicknesses, coupled surface modes contribute strongly to the spectrum. These coupled surface modes are phonon polaritons, whose intensity and spectral positions are strongly specimen geometry dependent. In a SiO_2 thin-film patterned with a 2x2 array, dielectric theory simulations predict the simultaneous excitation of parallel and uncoupled surface polaritons and a very weak excitation of the orthogonal polariton.

It is demonstrated that atomic resolution can be achieved with impact vibrational signals from optical and acoustic phonons in a covalently bonded material like Si. Sub-nanometer resolution mapping of the Si-O symmetric bond stretch impact signal can also

be performed in an ionic material like SiO_2. The visibility of impact energy-loss signals from excitation of Brillouin zone boundary vibrational modes in hexagonal BN is seen to be a strong function of probe convergence, but not as strong a function of spectrometer collection angles. Some preliminary measurements to detect adsorbates on catalyst nanoparticle surfaces with minimum radiation damage in the aloof-beam mode are also presented.

This dissertation is dedicated to:

Dada, who set all of this in motion

ACKNOWLEDGMENTS

I would like to express my sincerest gratitude to Prof. Peter Crozier for his timeless dedication towards my professional and personal development; he has provided me with thorough guidance and constant support without which any of this would not be possible. Over the years, our relationship has blossomed into a friendship that I would cherish forever. I would also like to deeply thank Prof. Peter Rez for his guidance and direction that is always focused on the bigger picture, which one tends to overlook while being involved with the minutiae of a Ph.D. I will always remember our discussions on climate change, batteries, Pink Floyd, and the history of microscopy.

I also want to acknowledge my other committee members, Prof. Robert Wang, and Prof. Sefaattin Tongay, for their critical feedback and valuable insights. I have had many great discussions with Prof. Ray Egerton on EELS, all of which were full of warmth and wisdom. To the current and past members of the Crozier research group, thanks for all your support – I appreciate it immensely. I would like to acknowledge Dr. Qianlang Liu, Dr. Katia March, and Dr. Barnaby Levin for helping with experiments and data processing, Dr. William Bowman for innumerable discussions in the brief time we shared at ASU, Dr. Ethan Lawrence for helping me develop outside the technicality of my Ph.D., and Dr. Diane Haiber and Joshua Vincent for insightful discussions on a wide range of topics, both technical and social. I was fortunate to mentor a bright undergraduate in Sunny Situ, who was a great help in getting the COMSOL project off the ground.

While all the people mentioned above have directly affected some part of the research in this dissertation, it would not be possible to do any of it without my incredible support system of family and friends, for which I am forever grateful. Amma, Appa, Dada, and Manni have been foundational pillars for me to stand tall on in this entire period. Ritwik, Abhinav, and Bhushan – my roommates in this journey have always been available

for a chat on topics ranging from the most personal to the most technical. The lunch sessions with Shanthan and Abhinandan used to be my most sought-after time on campus to recalibrate all emotions for the rest of the day. I am also eternally grateful to all the other friends I have made along the way – Somya, Piyush, Rutvik, Sisir, Ayush, Loy to name a few – thanks for being a part of my life over the past five years.

For financial support, I would like to thank the National Science Foundation Division of Chemistry under Grant No. NSF CHE-1508667. Finally, I would like to thank the Eyring Materials Center for the use of their microscopes, the specimen preparation facility and the FIB, and Dr. Bin Mu for the use of his DRIFTS instrument.

TABLE OF CONTENTS

Page

CHAPTER Page

APPENDIX Page

LIST OF TABLES

LIST OF FIGURES

Figure Page

CHAPTER 1

INTRODUCTION

1.1 History of vibrational spectroscopy

Materials consist of atoms, particles of finite mass that are connected to each other by elastic bonds due to which they can perform translational, rotational, and vibrational motions about their equilibrium positions. The ability to perform such motion independently of others is described as a degree of freedom for the atom. Every atom has three degrees of freedom – it can move independently along any of the three Cartesian axes. Thus, a system of n atoms has 3n degrees of freedom. Three of these are translational, when the entire system moves simultaneously along either of the three Cartesian axes. Three more are rotational (two if the system of atoms is linear), when the system rotates about either of its three principal axes. Translational and rotational degrees of freedom do not change the distance between atoms. The remaining 3n – 6 (3n – 5 in a linear system) degrees of freedom do; they change the lengths of bonds and the angles between them. Due to the elastic nature of chemical bonds, the motion caused by a change of bond length or bond angle is periodic. Hence, these are referred to as vibrational degrees of freedom on the whole and as *normal vibrations* individually. The 9 degrees of freedom available to a water molecule are shown schematically in Figure 1.1. In principle, all vibrational modes of a system are superpositions of these 3n-6 normal vibrations in which all atoms vibrate with the same phase and *normal frequency*. The investigation of the response from a system due to excitation of vibrational modes by an external probe, by decomposing the response into its normal vibrations and their overtones, is called vibrational spectroscopy.

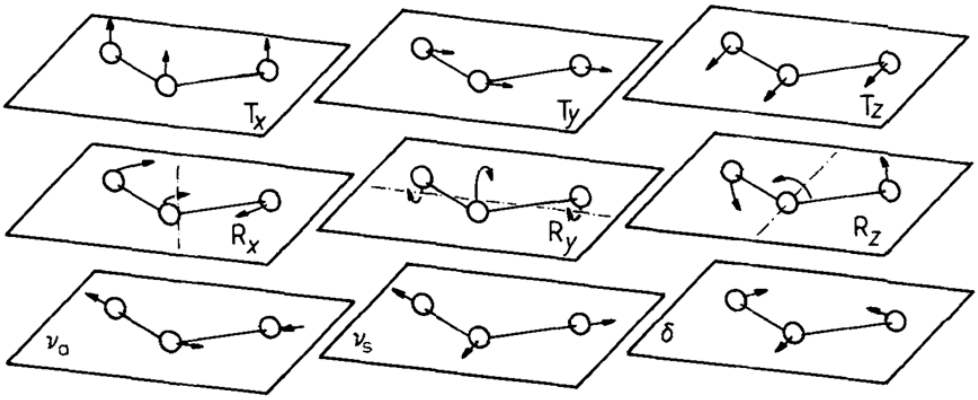

Figure 1.1. Motional degrees of freedom of the water molecule, T_x, T_y, and T_z are translations; R_x, R_y, and R_z are rotations of the whole molecule; ν_a is the antisymmetric while ν_s is the symmetric stretching vibration, and δ is the deformation vibration (Schrader, 2008).

Vibrational spectroscopy has become an important tool in elucidating atomic structure, both in the bulk and at the nanometer scale (Asmis, 2012; Bakker & Skinner, 2010; Brehm et al., 2006; Kurouski et al., 2015; Schmid et al., 2013; Weissenrieder et al., 2005). It is used to study a wide miscellany of sample types, in bulk or in microscopic amounts, over a range of temperatures and physical states, and can be carried out from a simple identification test to an in-depth, full spectrum, qualitative and quantitative analysis, thus making it a ubiquitous tool for materials characterization in recent times (Gupta, 2015; Larkin, 2017). In crystalline materials, spectroscopy of quantized lattice vibrational excitations or phonons can be used to study their transport (Balandin, 2011) and determine the integrated phonon density of states within the unit cell (Delaire et al., 2013; Dorner, 1982). Such understanding of phonon transport can be leveraged to engineer more efficient thermoelectric materials by reducing thermal conductivity while not hampering electrical conductivity (Shakouri, 2011). In the catalysis community, vibrational spectroscopy has been widely used to understand the adsorption, dissociation, diffusion, reaction and desorption of gaseous molecules on catalyst surfaces, and this understanding has helped make progress towards identifying the relevant intermediate

products during catalysis and thus, engineer better catalysts (van Santen et al., 2000). Vibrational spectroscopic methods have also been used to clarify our understanding of surface chemistry by using simple gaseous molecules like CO, H_2, O_2 etc. as probes which chemisorb to transition metal surfaces with a high binding energy, sticking probability, and surface coverage area. The vibrational frequencies of the chemisorbed molecule are analyzed to draw conclusions about the crystallographic symmetry, structure and bonding at the chemisorption surface sites (Ertl, 2008; Imelik & Vedrine, 2013; Somorjai & Li, 2010). The vibrational spectroscopies employed to study these scientifically important problems are diverse in nature and make use of photon (Stuart, 2004; McCreery, 2005; Griffiths & De Haseth, 2007), neutron (Mitchell, 2005), and electron (Stipe et al., 1998; Ibach & Mills, 2013) beams to excite vibrational modes in materials.

Before delving into the mechanisms of exciting normal vibrations in materials by making use of different external probes, a brief history of vibrational spectroscopy is presented. The first spectra of molecular vibrations were recorded in February 1880 by Abney and Festing using photographic emulsions that were sensitive in the near infrared region (Abney & Festing, 1881), ~80 years after the discovery of infrared electromagnetic radiation by Herschel in 1800 (Herschel, 1800). They recorded photographs of the absorption spectra from 48 organic liquids and observed that certain molecular groups absorbed radiation only within a band of wavelengths while other groups absorb wavelengths from a different band. An ethyl radical was always associated with absorption at 740 nm and within 907 – 942 nm, while an aromatic group definitely absorbed at 867 nm. They concluded with the claim that they could identify the spectral position of any hydrogen that was replaced in a molecule, which was very important to organic chemistry. They realized that the absorption bands were associated with hydrogen in the molecular

group, but did not realize that they were looking at overtones of normal vibrations of the C-H, N-H, and O-H bonds.

In subsequent years, infrared absorption vibrational spectra from hundreds of compounds up to wavelengths between 10 and 20 μm were reported by various researchers (Angstrom, 1889, 1890; Rubens & Aschkinass, 1898; Coblentz, 1905), including those from carbon dioxide, carbon monoxide, water vapor, methane, benzene etc. It was concluded from these endeavors that the character of infrared absorption was intricately related to intramolecular movements and thus, to the bonding between atoms in a molecule. The atom loses its chemical identity in a compound, and a knowledge of the spectra of constituent elements does not mean that one can predict the spectrum from a compound. It was also concluded that simple functional groups like CH_2, CH_3, NH_2, OH, NO_2 etc. have fingerprint vibrational frequencies. Due to instrumental limitations, vibrational spectroscopy using absorption of infrared radiation did not see major advancements until the Second World War. After the war, automatically recording infrared spectrometers became available, and further improvements in the 1960s such as grating spectrometers, large optical conductance interferometers, and computer algorithms that could compute the Fourier transforms of interferograms routinely, etc. made this vibrational spectroscopy the routine analytical laboratory technique we see widely used across physics, chemistry and materials science disciplines today.

In the 1920s, a new type of vibrational spectroscopy was discovered. In December 1921, Raman and colleagues observed that the depolarization of light transversely scattered by distilled water increased markedly when a blue-violet filter was placed between the source and the specimen (Raman, 1928). It was also observed that the increase in depolarization was less marked when the filter was placed between the specimen and the screen instead. This was originally suspected to be due to some “weak

fluorescence" from impurities in the specimen. However, it was found to be a universal effect in 1928, observed with many specimens in solid, liquid, and gaseous states, and possibly associated with molecular oscillations (Raman and Krishnan, 1928). Another interesting aspect was that when passed through a complimentary green filter after scattering, this new radiation still had a very strong polarization that made it stand out from fluorescence which is usually unpolarized after passing through a complimentary filter (Raman and Krishnan, 1928). Examination of the line spectrum of this new radiation from carbon tetrachloride and liquid benzene obtained by employing monochromated incident light showed bright lines at a shifted longer-wavelength position which were associated with molecular vibrations, in a remarkable analogy with the Compton effect in X-ray scattering (Raman and Krishnan, 1928; Raman and Krishnan, 1928).

Many researchers had predicted the Raman effect theoretically by applying quantum mechanics to molecules before its experimental observation (Smekal, 1923; Kramers & Heisenberg, 1925; Schrödinger, 1926; Dirac, 1927). Raman identified this shift in wavelength with the Kramers-Heisenberg effect, which said that a part of the incident quantum of radiation is absorbed by molecules that sets up vibrational modes in the specimen and the unabsorbed part is scattered (Raman, 1928). Other interpretations of the effect were that it is an optical modulation by the oscillating molecule (Rocard, 1928; Rocard, 1928) or an 'optical beating' (Cabannes, 1928) or due to inelastic scattering of light quanta (Landsberg & Mandelstam, 1928). A semi-classical polarizability theory approach was given (Placzek, 1934) which formed the basis of subsequent experimental and theoretical investigations as the importance of Raman spectroscopy as a tool for qualitative and quantitative analysis and structural determination was realized worldwide. It was realized that Raman spectroscopy was not an alternative to but was complimentary to infrared absorption spectroscopy. Until the Second World War, Raman spectroscopy

was more widely used amongst the two. After the war, infrared spectroscopy became more of a routine technique due to the advances stated earlier. The most significant advancement for Raman spectroscopy was the invention of the laser (Maiman, 1960) which were highly monochromatic and powerful light sources. Other instrumental improvements such as multiple monochromators, scanning grating spectrometers and charge-coupled devices and the ability to investigate resonance and non-linear phenomena with variants of the technique has contributed immensely to the routine use of Raman spectroscopy. However, due to the high cost of these instruments, the number of instruments for Raman spectroscopy is a fraction of those for infrared spectroscopy. Other techniques to study vibrational excitations like inelastic neutron scattering, inelastic electron tunneling, and electron energy-loss spectroscopies were invented much later and are not as ubiquitous in comparison with the photon based techniques discussed yet.

1.2 Mechanism of vibrational excitation with common techniques

Now that we have discussed some of the history of vibrational spectroscopy, a brief description of the mechanism of exciting vibrational modes by infrared (IR) absorption, Raman scattering and inelastic neutron scattering spectroscopy is presented. In IR absorption spectroscopy, the spectrometer scans over a frequency range (25000 to 2500 nm = 400 to 4000 cm^{-1} = 49.6 to 496 meV) and an interferometer is used to ensure that only photons of a single frequency reach the sample at a time. When this frequency matches that of the fingerprint vibrational frequency of a chemical bond in a molecular group in the sample, a resonance condition is created that involves a transition from the ground state to an excited state in the energy-level of the vibrating entity. This modulates the bond dipole moment which causes bonds to stretch and compress, as shown in Figure 1.2. The detector measures reduction in the intensity of the frequency of electromagnetic radiation absorbed by the sample which in turn leads to a peak in the absorbance

spectrum. Only those vibrational excitations which modulate the bond electric-dipole moment are IR active. If the stretching of a bond is symmetric, the change in the bond polarization on either side of the center cancels and the vibration is IR inactive. This is not the case if the bond stretching is asymmetric; the vibration then is IR active. Thus, polar bonds are always IR active while only non-polar bonds with asymmetrical stretching are IR active (Reichenbächer & Popp, 2012).

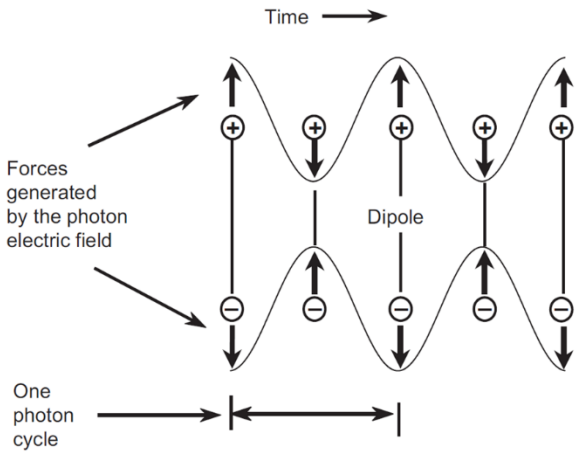

Figure 1.2. The oscillating electric field of the incident IR photon generates oscillating and oppositely directed forces on positive and negative charges of the molecular dipole. The dipole spacing oscillates with the same frequency as the incident photon. This modulates the molecular dipole moment, which makes the vibration IR active (Larkin, 2017).

In Raman spectroscopy, the incident photon has much higher energy or frequency than that of the vibration, and loses a very small amount of energy in exciting the vibration, while the remaining energy is scattered as a photon with reduced frequency (Reichenbächer & Popp, 2012). Most photons scatter elastically i.e. they begin to excite and end the excitation in the same vibrational energy-state; this is Rayleigh scattering. Other photons scatter inelastically wherein the small energy lost to excite the vibration is spent in changing the bond polarizability, which is much easier for non-polar bonds than polar bonds. Thus, only vibrational excitations that modulate the bond-polarizability are Raman active. The energy transfer to excite the vibration happens in two steps, first, an

electron that participates in the vibration absorbs energy from the photon and transitions from its ground state to an excited electronic state. The electron then falls to an excited vibrational state by simultaneously emitting a photon of reduced frequency. This type of scattering is called Stokes scattering, and the frequency difference between the incident and scattered photon gives the fingerprint frequency of vibrational modes in materials (Larkin, 2017). Another inelastic scattering mechanism is observed in Raman spectroscopy, albeit at a much lesser probability, that requires the excitation of a vibrational mode before the mechanism begins. The electron at the excited vibrational state absorbs energy from the photon to transition to an excited electronic state, after which it falls to the ground electronic state by emitting a photon of increased frequency as compared to the absorbed photon. This is called anti-Stokes scattering, and again, the frequency difference determines the fingerprint vibrational mode (Larkin, 2017). These three processes are depicted schematically in Figure 1.3. Thus, it can be seen that in terms of the type of fingerprint vibrational modes detected, IR and Raman spectroscopies are complementary to each other (Reichenbächer & Popp, 2012).

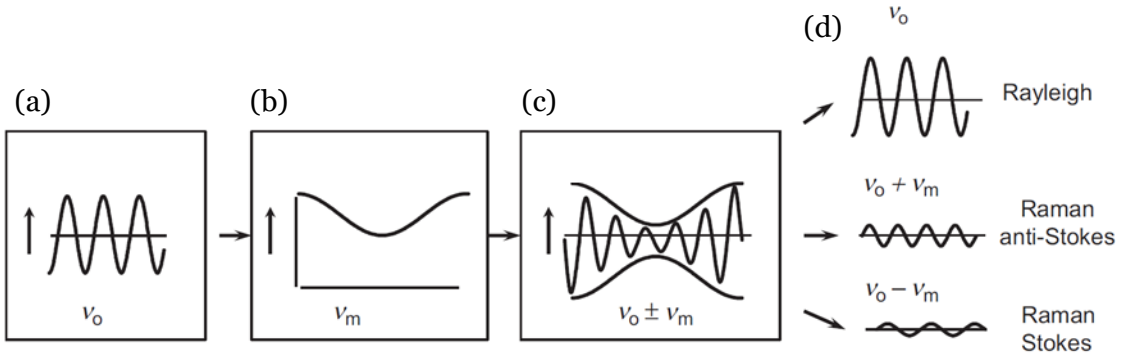

Figure 1.3. Rayleigh and Raman scattering. (a) The incident radiation makes the induced dipole moment of the molecule oscillate at the photon frequency, ν_o. (b) The molecular vibration, ν_m, can change the polarizability which changes the amplitude of the dipole moment oscillation. (c) An amplitude modulated dipole moment oscillation. (d) The components with steady amplitudes which can emit electromagnetic radiation (Larkin, 2017).

In inelastic neutron scattering vibrational spectroscopy (Squires, 2012), a high thermal-neutron flux of a finite energy and momentum is scattered by the sample and the difference in the initial and final energy and momentum of all neutrons is measured. Neutrons have no charge and are scattered inelastically only by nuclear forces. This allows them to penetrate deeper into the atom, and a scattering event happens much closer to the nucleus than optical techniques, due to which scattering angle is large that makes studying light elements easier. Moreover, as the energy of neutrons (between 0.1 and 500 meV) are of the same order as many vibrational excitations in solid-state physics, change in energy after inelastic scattering is a large fraction of the incident energy. This helps in accurate measurement of the vibrational excitation energy. Unlike IR absorption or Raman scattering spectroscopies, inelastic scattering of neutrons is not subjected to any selection rules and will activate all vibrational modes sustained in the specimen.

1.3 Spatial resolution of common vibrational spectroscopies

IR absorption and Raman scattering vibrational spectroscopies suffer from a poor spatial resolution in the far-field mode due to an inherent wavelength limitation of photons. For IR absorption, the diffraction imposed limit implies that a spatial resolution of only about half the wavelength ($\lambda/2$) of the radiation employed is possible, which comes out to about 5 μm. As Raman spectroscopy generally uses visible light radiation, its far-field spatial resolution is better than IR absorption, of the orders of 100 nm.

The spatial resolution for optical microscopy was first improved to about $\lambda/10$ for scanning near-field optical microscopy (SNOM) in the aperture mode (Lewis et al., 1984; Pohl et al., 1984). The idea was to utilize the high spatial frequency information contained in the evanescent non-propagating radiation field that is collected by an aperture (30 to 50 nm in size) near the specimen surface when a laser beam is incident on it (Figure 1.4b) and by scanning the aperture relative to the specimen, a high-resolution optical image is

formed. The aperture needs to be close to the surface (<100 nm) because the near-field collimation is maintained only up to such distances. The IR realization of the SNOM in the aperture mode had a spatial resolution of the order of 1 μm (Piednoir et al., 1996). Knoll and Keilmann reported the first apertureless design for scanning near-field infrared microscopy (SNIM) which enabled a spatial resolution of better than λ/100 or about 30 nm with IR absorption vibrational spectroscopy (Knoll & Keilmann, 1999). In this design, the aperture was replaced with a sharp metal tip which acts as a field scattering center, as shown schematically in Figure 1.4c (Wessel, 1985). An infrared laser beam is incident on the tip which generates a stationary background type of scattering from all over the tip. The scattering on the tip's sharpest point is sensitive to molecular vibrations in the sample and modulating the distance between the tip and the sample helps to isolate the high resolution content from the stationary background. This configuration also reportedly results in enhancement of infrared absorption by two to three orders of magnitude, referred to as surface enhanced infrared absorption (SEIRA), thereby enabling sub-100 nm infrared vibrational spectroscopy even from weakly absorbing nanoparticles (Knoll & Keilmann, 1999; Keilmann, 2002). Improvements in instrumentation and tip design has further pushed the achievable spatial resolution in near-field IR spectroscopy typically to better than 20 nm (Huth et al., 2012; Lu et al., 2014).

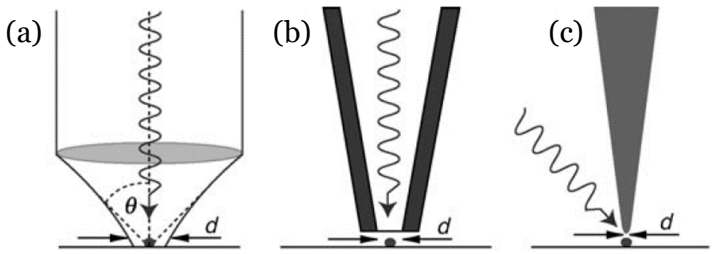

Figure 1.4. (a) Far-field focusing using a lens. The angular frequency range of propagating waves and thus the focus diameter, d, is limited by the aperture angle of the lens. (b) Aperture-type scanning near-field optical/IR microscopy. (c) Aperture-less scanning near-field optical/ IR microscopy using a metal tip (Hartschuh, 2008).

The near-field approach has also been applied to Raman spectroscopy and a spatial resolution initially of ~100 – 200 nm (Smith et al., 1995; Jahncke et al., 1996; Webster et al., 1998, 1998) that improved later to ~20 nm (Hartschuh, Anderson, et al., 2003; Hartschuh, Sánchez, et al., 2003) was experimentally demonstrated by scanning a sharp metal tip in a raster over the sample surface, as done in the case of apertureless SNIM. Apart from spatial resolution, another basic limitation with Raman scattering as a vibrational spectroscopy is the extremely low cross-sections involved, of 10^{-30} cm^2 (or 10^{-14} $Å^2$); this can be amplified to give tip-enhanced or surface-enhanced Raman spectroscopy (TERS or SERS) with typical enhancement factors of 10^4 – 10^6, and a maximum reported enhancement factor of 10^{15} that allows single molecule Raman spectroscopy (Kneipp et al., 1997; Nie & Emory, 1997). In spite of these remarkable improvements in spatial resolution with near-field vibrational spectroscopies, atomic scale changes in fabricating the metal tip makes quantitative measurements challenging (Huang et al., 2015), and tips might prevent characterization by driving chemical reactions in some cases (Christopher et al., 2011).

Inelastic neutron scattering vibrational spectroscopy does not suffer from an inherent wavelength limitation like photons as usual neutron wavelengths (~1.798 Å for thermal neutrons with standard velocity 2.20 km/s) are of the order of interatomic spacings (Squires, 2012). However, focusing the neutron beam onto the sample using elliptical or parabolic mirrors and guides yields a beam spot having a full-width at half-maximum (FWHM) of the order of 0.8 mm at best (Chen et al., 1992; Mildner et al., 1993; Schanzer et al., 2018; Stahn & Glavic, 2016). Even if all problems of lenses and recording media could be solved, neutron fluxes are such that for achieving a spatial resolution of 100 nm, the exposure time might be few years (Henderson, 1995). Other disadvantages to neutron-based vibrational spectroscopy are that they are expensive and owing to the

requirement of an accelerator, they are only available at national user facilities around the world.

The ultimate goal for high spatial resolution vibrational spectroscopy would be to perform analysis at molecular resolution. Atomic vibrations control all thermally activated processes in materials, including diffusion, heat transport, phase transformations and surface chemistry. Atomic and molecular heterogeneities such as interfaces, adsorbates, and defects (including vacancies, interstitials, dislocations, and grain boundaries) often regulate kinetic pathways and are associated with vibrational modes that are substantially different from bulk modes. The jump frequency characterizing kinetic processes is of great practical importance and is determined by local phonon and molecular vibrational modes in a system. Realizing atomic/molecular resolution vibrational spectroscopy would provide a completely new tool for probing local structure and chemistry at such heterogeneities. For example, in the case of adsorbates on catalysts, it would allow individual molecules to be detected and correlated with local atomic structure. This requires the combined ability to detect localized modes while performing simultaneous atomic resolution imaging, which in other words is referred to as high-resolution chemical imaging.

Techniques for atomic resolution imaging have been limited to scanning tunneling microscopy (STM) and (scanning) transmission electron microscopy ((S)TEM). Besenbacher and co-workers have pioneered the application of STM techniques to problems in surface chemistry and catalysis. The remarkable atomic resolution images of individual adsorbate molecules interacting on metal and oxide surfaces have provided valuable insights into the molecular processes taking place (Helveg et al., 2000; Lauritsen & Besenbacher, 2006; Tao & Crozier, 2016; Vang et al., 2007; Wendt et al., 2008). However, present scanning probe methods like STM have been mostly limited to *planar*

surfaces, and it has not been possible to image self-standing nanoparticle systems with curved or more complex geometries at atomic resolution.

1.4 (Scanning) transmission electron microscopy as a general high spatial resolution characterization tool

Transmission electron microscopy is a powerful technique for exploring nanoparticles and their surfaces with atomic resolution. A brief description of the history, the process of image formation, and the different modes of operation for a TEM and a STEM are presented in Section 2.1.1 and 2.1.2, respectively. Aberration correction of the magnetic lenses employed in both has made atomic resolution imaging routine, and for their contribution to the development of an aberration corrector for the TEM and the STEM, Harald Rose, Maximilian Haider, Knut Urban, and Ondrej Krivanek were honored with the Kavli Prize in Nanoscience 2020. For imaging, a resolution of 0.39 Å has recently been demonstrated using ptychography with pixel array detectors (Jiang et al., 2018) and 0.8 Å is now routinely available in both aberration-corrected conventional and scanning TEMs (Findlay et al., 2009; Hojo et al., 2010; Krivanek et al., 2008; Pennycook, 2012; Smith, 2008).

In a STEM, a highly focused electron probe is raster scanned across the specimen while recording a signal of interest, and the size of the probe directly affects the spatial resolution that can be achieved. To form a probe smaller than a (hkl) Miller plane spacing, the convergence semi-angle of the probe should be at least that corresponding to the (hkl) Bragg angle. Once you have such a probe, it is possible to resolve two atoms laterally separated by the interplanar spacing, d_{hkl} (Pennycook & Nellist, 2011). Different types of atomic resolution image-contrast conditions can be leveraged by choosing to collect electrons scattered by the specimen to different angles – conventional bright field images, annular bright field images, low-, medium-, and high-angle annular dark field (ADF)

images etc. High-angle annular dark field (HAADF) images are formed from electrons scattered over angles much larger than the convergence semi-angle, typically greater than 80 mrad. This signal is sensitive to atomic number and for this reason it has also been called Z-contrast imaging and is widely used for acquiring atomic-resolution STEM images (Hillyard & Silcox, 1995; Pennycook & Jesson, 1990; Treacy et al., 1978; Voyles et al., 2003). For realization of atomic resolution chemical imaging, this signal can be used for imaging while collecting spectroscopic information about the specimen simultaneously using either energy-dispersive X-ray spectroscopy (EDXS) or electron energy-loss spectroscopy (EELS) (Muller et al., 2008; Varela et al., 2004). EDXS is associated with the X-ray emission when an electron from a higher energy-level replaces an electron from a lower energy-level that was removed during an ionization event by the fast electron. EELS is the analysis of the energy distribution of initially monoenergetic electrons that have inelastically interacted with a specimen and lost energy in the process. A detailed description of the history of EELS and the physical origin of different energy-loss signals is presented in Section 2.1.3.

1.5 High spatial resolution vibrational spectroscopy using STEM EELS

It can be seen that EDXS cannot be a vibrational spectroscopy; however, as EELS is associated with all types of electron-specimen interactions that lead to the electron losing some amount of energy, it might be possible to perform vibrational spectroscopy with EELS. In fact, it is – vibrational spectroscopy has previously been performed with EELS in the reflection mode by bringing in low-energy electron beams at grazing incidence to the specimen surface (Ibach & Mills, 2013). The penetration depth of such incident electron beams is just a few atomic layers and *high-resolution* EELS (HREELS), as the technique is commonly referred to, is mainly a surface vibrational spectroscopy. In STEM EELS, the energy-spread in the electrons ejected from the gun was mainly responsible for

preventing them from being used for vibrational spectroscopy. When the electron beam is transmitted through the specimen, most electrons are unscattered or elastically scattered with zero energy-loss. These electrons form the zero-loss peak (ZLP) in EELS, the strongest signal in the spectrum, and all energy-loss signals from inelastic scattering lie on the tail of the ZLP. Ideally, the ZLP should be a Dirac delta function centered at 0 meV. In reality, however, electrons ejected from a cold field emission gun have a finite energy distribution and an inherent energy-spread of ~250 – 300 meV at half the ZLP maximum. At 1/1000th of the ZLP maximum, the energy-spread is >1 eV. Thus, all energy-loss signals from vibrations excited by the electron beam, which are usually below 500 meV, are hidden by the more intense ZLP tail. Developments in electron source monochromation reduced the energy-spread of electrons ejected by the gun to between 9 and 26 meV (Figure 1.5), which enabled the first ever detection of vibrational modes with STEM EELS (Miyata et al., 2014; Krivanek et al., 2014). Today, this figure has further improved to 4.2 meV at 30 kV accelerating voltage (Krivanek et al., 2019). The energy-loss spectrum with an unsaturated ZLP acquired when the electron beam is not passing through a specimen and the microscope is aligned to near perfection is called the instrument response function or the experimental point-spread function (PSF) for EELS. All energy-loss signals are a convolution of this instrument response function and the inelastic scattering probability for the signal of interest. The full-width at half-maximum (FWHM) of the unsaturated ZLP in the instrument response function is referred to as the *energy-resolution* of the technique. Although this energy-resolution is much inferior to that achievable with IR absorption, Raman scattering or inelastic neutron scattering vibrational spectroscopies, it is improving at a fast rate and it might be possible to reach <1 meV energy resolution in the next decade or so. Also, the routine spatial resolution offered by vibrational STEM

EELS is equivalent to or better than the best offered by these common techniques, as will be demonstrated in this dissertation.

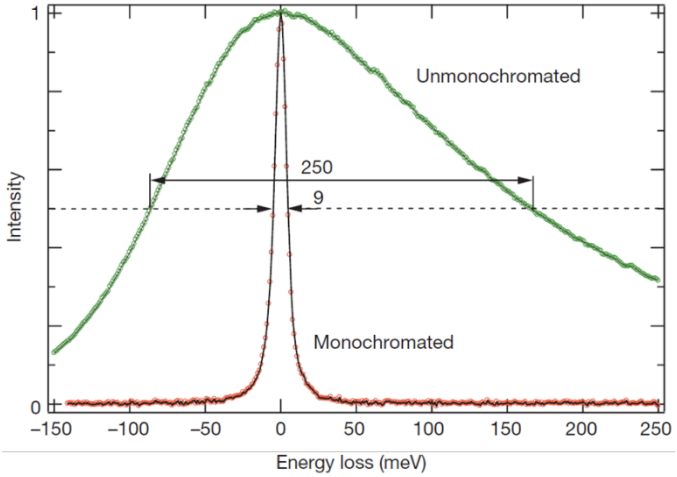

Figure 1.5. 9 meV full-width at half-maximum monochromated ZLP compared to the 250 meV energy-spread of an unmonochromated beam produced by the system's cold field emission electron gun (Krivanek et al., 2014).

The electron interactions in vibrational EELS can be discussed in terms of dipole and impact scattering as done in HREELS literature (Ibach & Mills, 2013). As an atom in the specimen vibrates, it modulates the electric dipole moment of its environment in a time-dependent fashion. An electron in the incident beam senses a long-range induced electric field of dipolar character, and this produces small-angle scattering which is typically substantially more intense than the scattering observed at large angles. This gives rise to non-negligible delocalization (see Section 2.1.3) of the vibrational signal for such ultra-low energy-losses that limits the practical spatial resolution to 5 – 20 nm (Crozier et al., 2016; Crozier, 2017; Venkatraman et al., 2018). When dipole scattering is present, one observes a cone of inelastic scattering sharply peaked about the optic axis of the incident electron beam. The characteristic scattering angle depends on the energy-loss, and it is of the orders of microradians for dipole vibrational energy-loss signals. For small scattering angles, with the dipole component dominant, it is possible to obtain a simple and useful

form for the scattering probability without having to resort to a microscopic description of the electron-substrate interaction (Ibach & Mills, 1982; Ritchie, 1957). The response of the specimen medium to the polarizing electric field of the incident electron can be approximated by a frequency-dependent optical dielectric function and the energy-loss is then determined by the work done by the induced electric field in the polarized specimen medium on the incident electron (Ritchie, 1957). The spectral features observed when dipole scattering is dominant are similar to those observed in IR absorption spectroscopy (Rez et al., 2016).

The incident electrons can also undergo impact scattering, which is associated with short range interactions, essentially collisions of the fast electron with the core of an atom – its nucleus and the core electrons, that result in high-angle scattering. In the impact scattering regime, the angular and energy variation of the energy-loss scattering probability contains detailed structural information on the entity which produces the scattering (Ibach & Mills, 2013). These spectral features appear in inelastic neutron scattering but not in IR absorption spectroscopy and through EELS studies in the impact scattering regime, one has the possibility, in principle, of obtaining structural information with atomic resolution. With high-angle scattering, it is necessary to turn to a fully microscopic description to describe the scattering probability theoretically. The classical dielectric theory with an optical dielectric function falls short in the description of these modes. A complete analysis of the scattering of electrons from a vibrating entity will incorporate both the dipolar and impact scattering contributions into a single expression for the scattering probability.

1.6 Literature on vibrational STEM EELS

Since the first experimental demonstrations of vibrational EELS in 2014, there have been many reports on different aspects of the technique, including few that are a part

of this dissertation. An attempt is made to summarize most of these reports in the context of dipole and impact scattering. Theoretical treatments have explored the scattering cross section (Rez, 2014) and spatial resolution of vibrational energy-loss signals (Rez, 1993; Dwyer, 2014; Dwyer, 2017; Egerton, 2015; Forbes & Allen, 2016) with some of these suggesting the possibility of atomic spatial resolution. In transmission-beam vibrational EELS, the energy-loss signal has contributions from both dipole and impact scattering, and its spatial resolution is hugely influenced by which contribution dominates, which is a topic of ongoing investigation. The question of dominant contribution can depend on the bonding between atoms in the material and/or the nature of the vibrational mode. For example, many optical vibrational modes in ionic materials are dipole scattering dominant, while in all materials, all acoustic vibrational modes are impact scattering dominant. To explore this complicated dependence of spatial resolution in the vibrational energy-loss signal, different groups have conducted experimental and theoretical studies on model materials like BN, MgO, SiO_2, Si, SiC etc. as there is extensive literature from other bulk and surface vibrational spectroscopies for these materials. Also, these specimens were readily available or easy to prepare.

In ionic materials like MgO, SiO_2, BN, and SiC, the vibrational energy-loss spectrum in the forward scattering direction (the optic axis of the spectrometer is the same as that of the incident beam) is complicated (Govyadinov et al., 2017b; Lagos et al., 2017; Lourenço-Martins & Kociak, 2017; Lagos et al., 2018; Venkatraman et al., 2018a; Konečná, Venkatraman, et al., 2018a; Li et al., 2019; Li et al., 2020). Energy-loss signals from optical vibrational modes are dipole scattering dominated as long as the allowed scattering angles are smaller than the associated Bragg angles of the specimen. Under such conditions, the intensity and spectral position of dipole signals is a strong function of the probe position relative to the specimen geometry. There is a significant contribution from the surface

(edge and corner too, wherever possible) modes to the spectrum for typical TEM specimen dimensions (Figure 1.6). These modes are associated with a *Restrahlen* band, where the real part of the dielectric function goes negative between the transverse and longitudinal mode energies. Signals associated with these modes manifest as phonon polaritons, which are standing waves created from the hybridization of optical vibrational modes with the broad frequency electromagnetic radiation field of the fast electron. The spatial resolution of these dipole signals is of the order of tens of nm, which is poor by electron microscopy standards. All of these points will be described in more detail with experiments and dielectric simulations in Chapters 3, 4 and 6. The existence of an energy-gain signal in the forward direction (vibrational modes transferring energy to the fast electron) was also shown by other researchers, and the ratio of the intensities of the energy-loss and gain signals was used to measure the absolute temperature in the specimen with 1 K precision (Idrobo et al., 2018; Lagos & Batson, 2018).

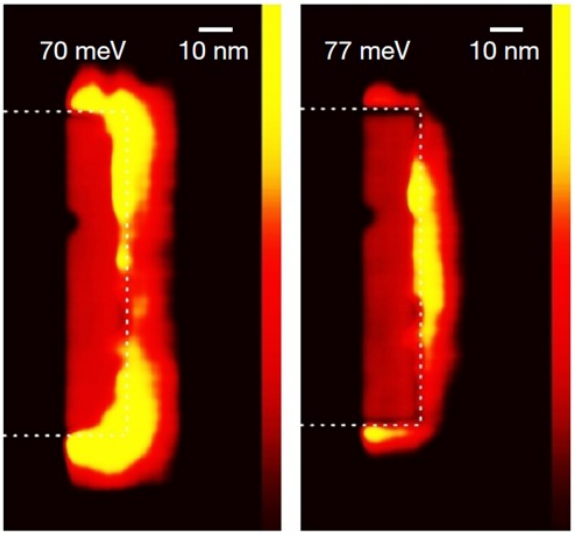

Figure 1.6. Experimental demonstration of geometry dependent corner (70 meV) and edge (77 meV) vibrational modes (phonon polaritons) in MgO (Lagos et al., 2017).

In an attempt to explore the possibility of higher spatial resolution with the impact scattering contribution to the energy-loss signal, Dwyer and colleagues shifted the electron

diffraction pattern over the spectrometer entrance aperture such that there was no overlap between the objective and the collection apertures (Dwyer et al., 2016). This ensured that the small scattering angle dipole contribution to the spectrum was greatly diminished and the recorded energy-loss signal was impact scattering dominated. A spatial resolution of 2 nm was demonstrated in the BN optical phonon, a ten-fold improvement from the configuration when the phonon energy-loss signal was dipole scattering dominated. However, the convergence semi-angle employed in these experiments was 6 mrad, which was insufficient to resolve atomic columns, hence, lattice resolution was not possible. Hage and colleagues extended this approach by using a large enough convergence angle to form a sub-Å sized probe and demonstrated atomic resolution (Figure 1.7) in energy-filtered images with contributions from acoustic and optical BN phonons (Hage et al., 2019). They recently used this approach to demonstrate a localized modification of the vibrational response due to a single substitutional Si impurity atom in graphene (Hage et al., 2020). Another novel aspect that has resulted from the off-axis spectrometer configuration is the ability to perform momentum resolved vibrational spectroscopy with nanometer spatial resolution (Hage et al., 2018). However, as a direct consequence of Heisenberg's uncertainty principle, there is a trade-off between momentum and spatial resolution (Senga et al., 2019).

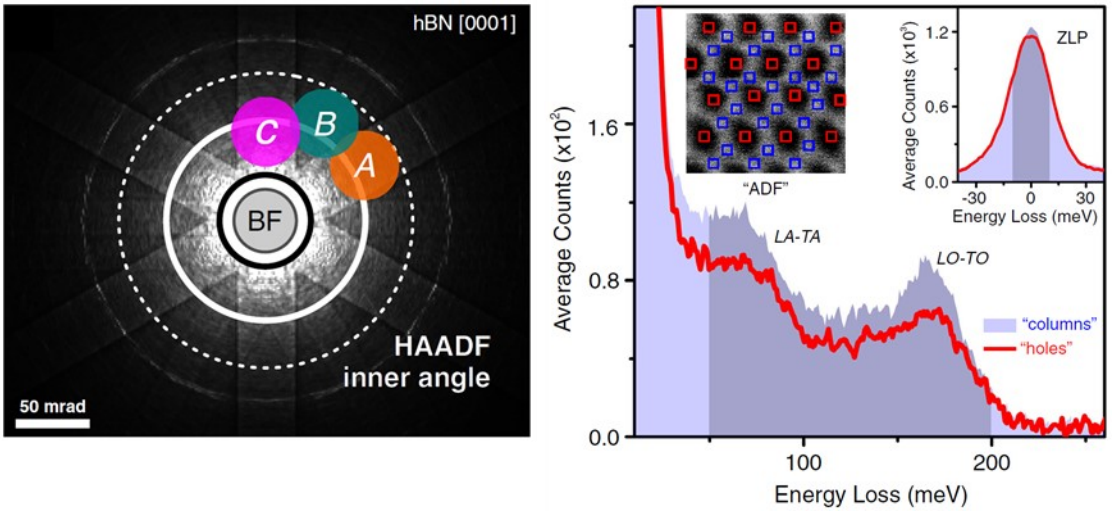

Figure 1.7. (a) Convergent beam electron diffraction pattern with 31 mrad probe convergence semi-angle (solid white circle) from hexagonal BN oriented into the [0001] zone axis. BF shows the optic axis of the incident electron beam while A, B, or C show the relative optic axis of the spectrometer during acquisition. (b) Average energy-loss spectra acquired from BN with the spectrometer in position C and the probe on atomic columns or in holes, showing a visible intensity difference in the acoustic and optical vibrational signals (Hage et al., 2019).

An approach to avoid dipole scattering in the forward direction (on-axis spectrometer) is to choose vibrational modes that are IR inactive or in other words, that do not modulate the bond dipole moment. These would be acoustic modes in all materials, optical modes in non-ionic materials, and symmetric stretching and deformation modes in ionic materials. In crystals, the list would also include short wavelength optical phonon modes at Brillouin zone boundaries (BZBs). The energy-loss signals of such excitations would be impact scattering dominated (Ibach & Mills, 2013). The impact character of such energy-loss signals will be demonstrated experimentally in Chapters 5 and 6, and it will be shown that these vibrational signals have atomic resolution. This work has been published (Venkatraman et al., 2019).

The delocalized nature of dipole vibrational signals has been leveraged to minimize radiation damage in the aloof mode, when the electron beam is positioned a few nm away from the specimen and travels through vacuum, and detect the vibrational spectrum from guanine (Rez et al., 2016), water and its derivatives on individual nanoparticle surfaces (Crozier et al., 2016) and in a graphene liquid cell (Jokisaari et al., 2018), disordered carbon nitrides (Haiber & Crozier, 2018) etc. It has also been used to identify site-specific isotopic labels in L-alanine (Hachtel et al., 2019) as shown in Figure 1.8 and determine orientation dependent symmetry of normal modes in $B_{12}P_2$ crystals (Radtke et al., 2019). Some preliminary experimental results from attempting to investigate adsorbates on the catalyst nanoparticle surfaces with aloof beam vibrational EELS are presented in Chapter 7.

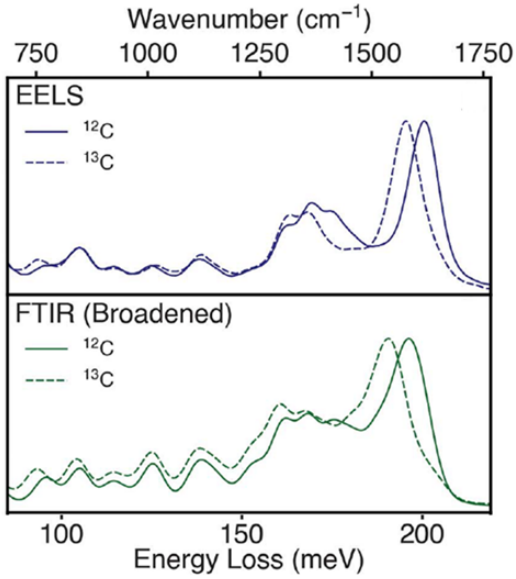

Figure 1.8. Experimental spectra acquired with monochromated aloof vibrational EELS (top) for ^{12}C L-Alanine (solid line) and ^{13}C-isotopically-labeled L-Alanine (dashed line), exhibiting an observable isotopic shift of the dominant peak. FTIR vibrational spectra (bottom) from the same powders used for EELS, broadened with a Gaussian function to match the energy resolution in EELS (~6 meV) and showing a highly similar shift of the dominant peak (Hachtel et al., 2019).

1.7 Objectives and outline

This dissertation is aimed towards developing the technique of high spatial resolution vibrational spectroscopy using monochromated aberration-corrected STEM EELS. As illustrated in the previous sections, there are multiple facets to this development, and as will be seen in subsequent chapters, interpretation of data can get complicated. This necessitates that experiments be performed on model materials for which there is extensive literature available from other vibrational spectroscopies, and that experiments be corroborated with theory. To this end, we have endeavored to choose model materials like SiO_2, Si, BN, PVP/Au, CO_2/MgO, CO/Pt etc. Also, classical dielectric theory simulations, both analytical and numerical, are performed to interpret experimental data wherever possible.

The next chapter is dedicated to a description of the methods used in different parts in the dissertation. These include the basics of image formation in a TEM and a STEM, the physics of inelastic electron scattering that gives rise to an energy-loss spectrum, and the application of classical dielectric theory to simulate low-loss and vibrational EELS. Chapter 3 focuses on investigating the character and spatial resolution of vibrational signals in SiO_2 as the electron probe is scanned across an atomically abrupt SiO_2/Si interface, and corroborating experimental results with the classical dielectric theory. The influence of surfaces and an interface on the asymmetric Si-O bond stretch vibrational signal, which is dipole dominant, is studied and it is shown that the experimental results can be accurately simulated by approximating the response of SiO_2 with its optical dielectric function. Chapter 4 is predominantly a theoretical investigation of the effect of patterning a thin-film with a 2x2 array of holes on the vibrational modes from SiO_2 studied in Chapter 3. The effect of changing the hole radius, the separation between adjacent holes and the position of the electron beam relative to the pattern is

explored. Preliminary experimental results based on the simulations mentioned have also been presented.

Chapter 5 part focuses on the first experimental demonstration of atomic spatial resolution achieved with vibrational EELS in optical and acoustic phonons in a covalently bonded material like Si, where impact scattering is dominant, and any dipole scattering is a weak second-order effect. It is also shown that high spatial resolution mapping of vibrational signals is possible in oxides like SiO_2, which has mixed ionic – covalent bonding, by selecting the symmetric Si-O bond stretch vibrational signal, which is impact scattering dominant. Chapter 6 deals with the influence of varying the probe convergence angle and the spectrometer collection angle on the vibrational spectrum from hexagonal BN, which shows both dipole and impact scattering dominated signals in the forward direction. The visibility of impact signals in the spectrum is investigated as a function of the scattering angles available to the fast electron in exciting various vibrational modes.

In Chapter 7, the long-range nature of the dipole vibrational signals is leveraged in the aloof-beam mode to perform potentially damage free detection of adsorbates on the surface of metal and oxide nanoparticles. The probe is positioned a few nanometers away from the adsorbate layer of interest and is sensitive enough to detect a monolayer of CO chemisorbed on a Pt microparticle. Preliminary experiments show that the ultimate goal of performing facet dependent investigation of adsorbates on catalyst nanoparticles is currently limited by the efficiency of detector systems employed. Future adoption of direct-electron detection will immensely broaden the scope of vibrational EELS to accommodate the study of monolayer adsorbates on catalysts with better than nanometer resolution.

CHAPTER 2

METHODS

As established in Chapter 1, development of a high spatial resolution vibrational spectroscopy technique in the scanning transmission electron microscope (STEM) using electron energy-loss spectroscopy (EELS) requires the use of model material systems to simplify the interpretation of signals associated with the excitation of vibrational modes in these materials. The experimental methods used to synthesize and prepare such model materials for advanced electron microscopy will be briefly described when the acquired data is presented in subsequent chapters. In this chapter, the basic principles of physical characterization of these materials by TEM, STEM and EELS are reviewed, with a detailed subsequent description of the developing field of monochromated EELS. Classical dielectric theory has been known to describe valence-loss EELS events semi-quantitatively, and gives analytical expressions to help interpret the different contributions to the energy-loss spectrum. Three such analytical expressions, relevant to the experimental geometries employed in later chapters, are used to describe vibrational-loss EELS events, and are described in detail. Finally, the use of finite element modelling with classical dielectric theory in COMSOL Multiphysics is described to numerically simulate vibrational energy-loss events in complicated geometries.

2.1 Electron microscopy and spectroscopy

The ability to obtain simultaneous structural, electronic, and chemical information from a variety of materials used in different kinds of physical and life science research at the micrometer to atomic length scales renders electron microscopy and spectroscopy as a widely adopted characterization technique. The major advantage presented by this technique, apart from unprecedented spatial resolution, is the opportunity to correlate atomic structure with elemental composition, bonding arrangements, electronic structure

etc. As the use of nanomaterials is becoming increasingly ubiquitous, the need to understand their fundamental structure-property relationships has made electron microscopy indispensable to materials research. The most powerful electron microscopes in the world today can feature monochromators, aberration-correctors, high-resolution spectrometers, high-sensitivity cameras, multiple X-ray detectors, CL detectors, cryogenic specimen stages, gaseous specimen chambers, and *in situ* heating and biasing holders to optimize the imaging and microanalysis of a wide range of materials and phenomena.

As this work is associated with exploring the workings of a high spatial resolution vibrational spectroscopy technique in a S/TEM with EELS, the following sections will briefly describe the fundamental concepts of TEM, STEM and EELS that are relevant to this work. The cited references provide a complete description of the theory, instrumentation, and applications of S/TEM and related techniques (Williams & Carter, 2009; De Graef, 2003; Egerton, 2009, 2011; Fultz & Howe, 2012; Hawkes, 1985; Hawkes & Spence, 2019; Ibach & Mills, 2013; Keyse, 2018; Kohl & Reimer, 2008; Nellist et al., 2000; Pennycook & Nellist, 2011; Zuo & Spence, 2017).

2.1.1 Transmission electron microscopy

Since the invention of the TEM in 1931 by Max Knoll and Ernst Ruska, it has been at the heart of characterization in the development of many modern technologies (Knoll & Ruska, 1932; Ruska, 1987). It earned Ruska the 1986 Nobel Prize in Physics. In the low magnification mode, TEM imaging gives sub-micrometer information about the structure of bulk solids, and of the morphology and size distribution of particles. At higher magnification, atomic resolution images can be formed to measure the interplanar spacing between crystallographic planes, and explore the structure at atomic scale heterogeneities.

Spectroscopy can be combined with different imaging modes to obtain electronic and chemical information from the specimen of interest.

The most obvious motivation for using transmission electron microscopy as a materials characterization technique is the high spatial resolution rendered by employing electron illumination over light illumination. This high spatial resolution is often leveraged to produce atomic resolution images and perform nanocharacterization of solids, liquids, and gases. The minimum resolvable distance, δ, in visible light microscopy is given by Rayleigh's criterion as

$$\delta = \frac{0.61\,\lambda}{\mu \sin\beta} \tag{2.1}$$

where λ is the wavelength of the incident light, μ is the refractive index of the viewing medium and β is the collection semi-angle of the magnifying lens. The above expression can be modified for the TEM ($\mu = 1, \sin\beta \approx \beta$), assuming the convergence angle of the condenser lens to be the same as the collection angle of the magnifying lens such that β is twice of what it was in Equation 2.1. The minimum resolvable distance is then given by $\sim 1.22\,\lambda/\beta$; the spatial resolution is directly proportional to the wavelength of the incident beam. Visible light has a wavelength range from 380 to 740 nm, while the electron wavelength typically employed in a TEM is <10 pm. Thus, it can be seen that spatial resolution can be significantly enhanced by employing electron radiation instead of visible light (Williams & Carter, 2009).

The construction of a conventional TEM is schematically illustrated in Figure 2.1. An electron source sits at the top of a TEM column, and electrons are tunneled from the source across a potential barrier or thermally excited over the work function of the source. The ejected electrons are transferred to the specimen by the condenser lens system, which

helps control the brightness, spot size and convergence of the beam incident on the specimen. The incident electrons are transmitted through the specimen and the scattered electrons pass through the objective lens system, forming the primary image. This makes the objective lens the most important lens in the TEM. However, aberrations in the objective lens can ultimately limit resolution in TEMs. The primary image is highly magnified by the intermediate and projector lenses and then focused onto the viewing screen or detector.

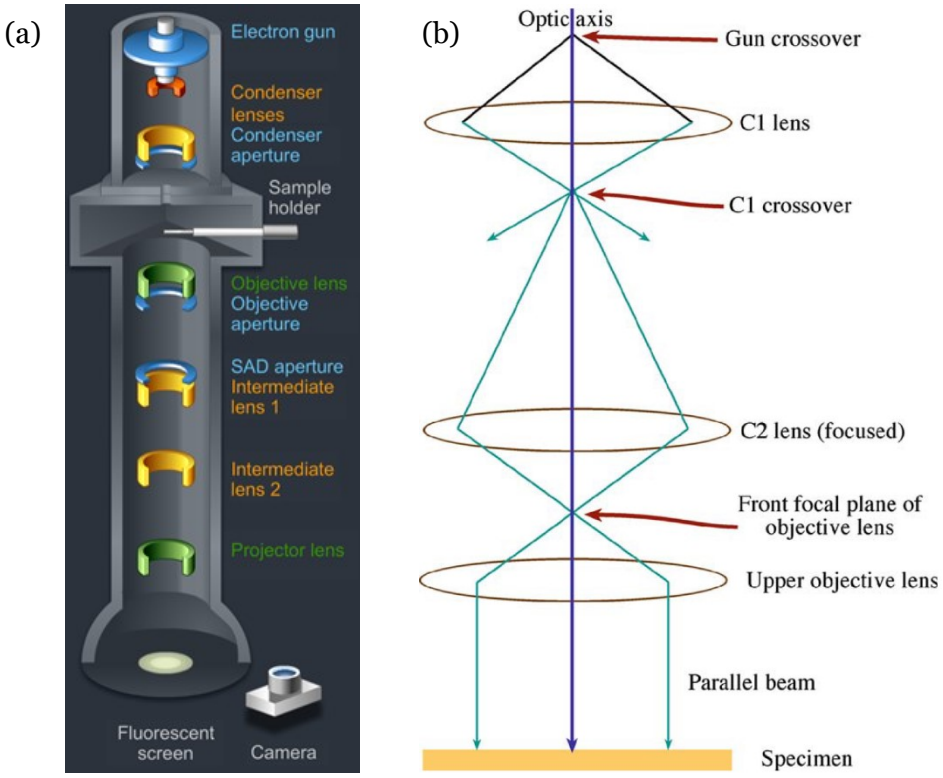

Figure 2.1. (a) Construction of a conventional TEM; figure is adapted from the virtual TEM section on MyScope, an online learning platform by the Microscopy Australia. (b) Ray diagram of a parallel electron beam incident on the TEM specimen (Williams & Carter, 2009).

Electron-specimen interactions in a TEM form the basis of diffraction, emission of characteristic X-rays or CL radiation, electron energy-loss etc. These electron-specimen

interactions are referred to as scattering of the incident electrons by the specimen, and electron scattering can be broadly classified as being either elastic, implying a negligible energy-transfer (if the scattering angles are small) or inelastic, implying a finite energy-transfer. Figure 2.2 schematically shows the elastic and inelastic scattering of incident electrons by a single C atom (Egerton, 2011). Incoherent elastic scattering results predominantly from an attractive electrostatic interaction of the incident electron with the atomic nuclei, whose intense local electric field causes the incident beam to be deflected through high angles. Coherent elastic scattering contributes to diffraction, which involves the interference of scattered electron-waves and causes the scattered intensity distribution to peak sharply at angles characteristic of the interplanar spacing. Inelastic scattering results predominantly from a repulsive interaction of the incident electron with the electron cloud surrounding the nucleus. This can include ionization as the incident electron ejects a core-shell electron from an atom, by losing the characteristic amount of energy required to remove an electron from a particular orbital. A higher energy orbital electron can then fall into a lower energy orbital to replace the knocked out electron, resulting in emission of X-rays or an Auger electron in the process. Similarly, the incident electron can also excite a bound electron into an unoccupied electronic state above the Fermi level by transferring the energy required for the transition, subsequently followed by a downward transition to fill the hole, resulting in the emission of light (near-infrared, visible, or ultraviolet). As an alternative to these single electron transitions, the incident electron can excite collective oscillations of the outer shell valence electron density across many atoms, often referred to as a plasmon. Inelastic scattering involving energy transfer of few tens to hundreds of meV is also possible and is associated with exciting vibrational modes in materials. These electron-specimen interactions form the basis of all TEM imaging and spectroscopy techniques.

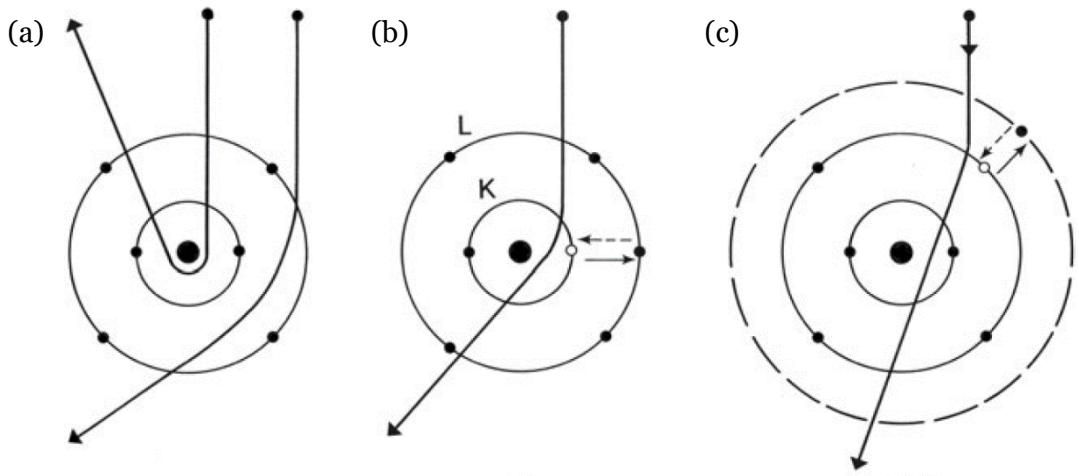

Figure 2.2. Schematic of classical electron scattering from a single C atom. (a) Elastic scattering due to Coulomb attraction from the nucleus. Inelastic scattering due to Coulomb repulsion from inner-shell (b) or outer-shell (c) electrons. Excitation and de-excitation are depicted by short solid and broken arrows, respectively (Egerton, 2011).

Contrast in conventional TEM images arises from changes in the amplitude and/or phase of the electron wave as it passes through the specimen. In a typical TEM image, contrast due to both amplitude and phase changes are present, but it is usually possible to choose imaging conditions such that one image contrast mechanism dominates. Amplitude contrast can originate from two sources, viz. mass-thickness contrast, and diffraction contrast. Mass-thickness contrast arises primarily from incoherent elastic scattering of the electron wave, and is strongly dependent on the atomic number of the specimen and the spatial variation in its thickness. This is a prominent image contrast mechanism in the low magnification mode. Diffraction contrast arises primarily from coherent elastic scattering of the electron wave, also called Bragg scattering, and is strongly dependent on the crystal structure and orientation of the specimen. This can also be prominent at low magnification. By tilting the specimen to an orientation such that only one Bragg beam is strongly excited along with the directly transmitted beam, referred to as the two-beam imaging condition, a strong diffraction contrast image can be formed.

Strong diffraction contrast is immensely helpful to locate crystallographic defects as the diffracting planes close to the defect are altered by its strain field.

On the other hand, phase contrast in images arises from the interference of scattered waves that are out of phase with each other. Thus, for strong phase contrast, multiple beams are required to interfere, and this contrast mechanism is extremely sensitive to instrument and specimen parameters like objective lens defocus, aberrations, specimen thickness, orientation, and scattering factor. This makes image interpretation notoriously complex, and researchers often have to resort to image simulations to verify the atomic-level origin of contrast in the experimental data.

2.1.2 Scanning transmission electron microscopy

The first STEM was constructed in 1938, a few years after the development of the TEM by Knoll and Ruska in 1931, by Baron Manfred von Ardenne in Berlin (von Ardenne, 1938). The motivations for the development of the TEM and the STEM were quite different. The TEM was developed along the principles of the optical microscope with the objective of exceeding its resolution, although it was realized later that the contrast mechanisms were quite different for optical and electron microscopy (Ruska, 1987). The STEM was developed with the objective of developing a SEM and with the motivation to develop camera tubes for television (von Ardenne, 1996). It was von Ardenne's hypothesis that electrons transmitting the specimen merely have to be detected and would not need to be refocused to form a high-resolution image. This would avoid degradation of the image due to chromatic aberrations in the imaging lenses (von Ardenne, 1985). von Ardenne published the first STEM image of ZnO crystals in his 1938 paper, showing a resolution of 40 nm, followed by demonstration of a four-fold increase in resolution to 10 nm less than an year later (von Ardenne, 1938). The major limitation of von Ardenne's

STEM was noise, and he turned his attention to the development of the SEM and the TEM following Ruska's design (von Ardenne, 1996). Further development of the STEM was not done till 1966 when Albert Crewe proposed the incorporation of a field-emission electron source to overcome the existing limits on resolution (Crewe, 1966). This yielded an instrument with 5 nm resolution, with subsequent improvements pushing the resolution first to 5 Å (Crewe et al., 1970; Crewe & Wall, 1970) and then to 2.5 Å (Wall et al., 1974), thereby realizing the imaging of single atoms in the electron microscope. Further improvements in imaging and detection instrumentation have pushed the current resolution achievable with the STEM to 0.39 Å at 80 kV (Jiang et al., 2018), with the formation of sub-1 Å sized probes now routinely possible with aberration correction (Krivanek et al., 2003, 1999; Krivanek et al., 2008; Krivanek et al., 2008).

The fundamental difference between the TEM and STEM is the (non-) convergence of the electron beam when it is incident on the specimen. Figure 2.3a represents the electron optics employed in a STEM. The incident electrons are focused into a small convergent probe that can be scanned in a raster across the specimen using scan coils, like in a SEM. Unlike TEM, wherein intermediate lenses located after the specimen plane are needed to adjust magnification, scan coils located ahead of the specimen plane are adjusted to progressively scan over smaller regions in a STEM. Instead of inserting post-specimen apertures to isolate the bright field or dark field signals as in a TEM, detectors are placed post specimen in a STEM to capture electrons scattered at specific angles. Thus, the image is built point by point as the electron beam scans across the field of view. As the focused electron probe is incident on the specimen, a convergent beam electron diffraction (CBED) pattern is formed post specimen and the electrons are scattered into overlapping Bragg disks, which is different from the spot diffraction pattern formed due to parallel illumination in the TEM. This is shown schematically in Figure

2.3b. The degree of overlap in the Bragg disks depends on the incident beam convergence angle. A direct consequence of the overlapping Bragg disks is that the central disk in a STEM can contain phase contrast information, unlike the direct beam in a TEM, which mostly uses parallel illumination (the exception would be holographic techniques in a TEM).

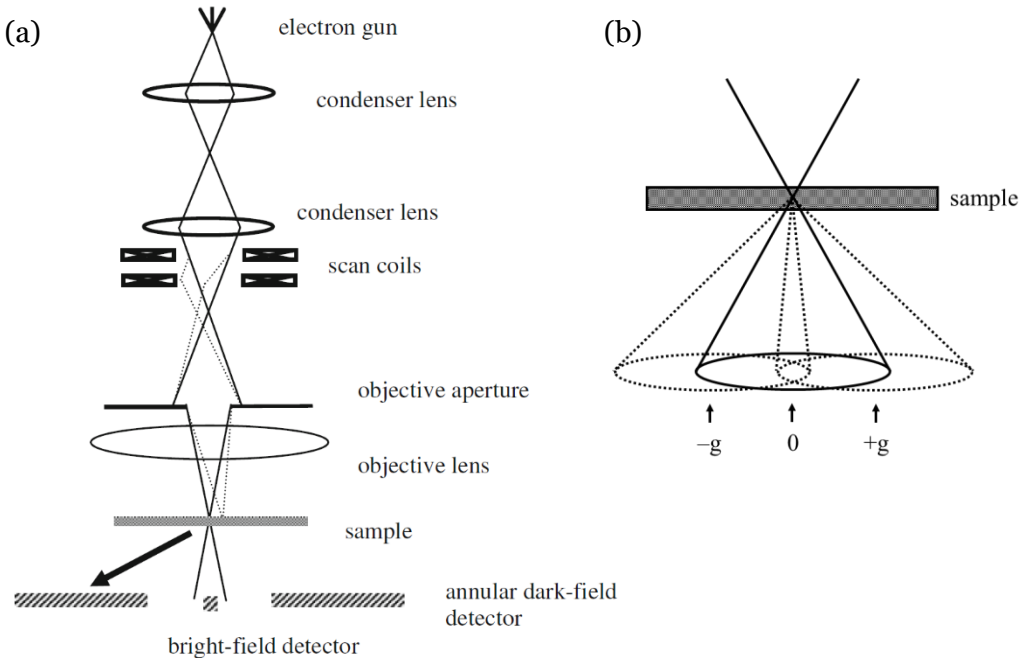

Figure 2.3. (a) Schematic of the basic operating principles and the electron optics employed in a STEM (Pennycook & Nellist, 2011). (b) Overlapping Bragg disks as the CBED pattern, as opposed to the spot diffraction pattern due to parallel incidence in a conventional TEM.

By inserting various post-specimen detectors and varying the camera length, the angular distribution of scattered electrons used to form a STEM image can be finely controlled. This, in turn, controls the contrast in the image. Transmitted electrons in a STEM are typically detected by employing an on-axis bright field (BF) detector and/or an annular dark field (ADF) detector. The detection angles for these modes relative to the probe convergence angle, α, are represented in Figure 2.4. The BF detector makes use of

the interference in the region of multiple overlap between the direct beam disk and the diffracted (Bragg) beam disks, resulting in the formation of a coherent phase contrast image. Optimum acceptance angles for the BF detector would typically be α. An alternative to BF STEM imaging is to employ an annular BF (ABF) detector aperture, or a beam stopper to project an annulus of the direct beam disk on the BF detector, to perform ABF imaging. Rose proposed that this would improve the efficiency of a STEM phase contrast image and demonstrated that the highest signal to noise ratio was obtained for an image formed by the difference between the ABF signal and the remainder of the BF disk (Rose, 1974). ABF STEM imaging has been shown to be particularly robust for imaging light elements like hydrogen and oxygen (Findlay et al., 2009; Findlay et al., 2014; Ishikawa et al., 2011; Okunishi et al., 2012).

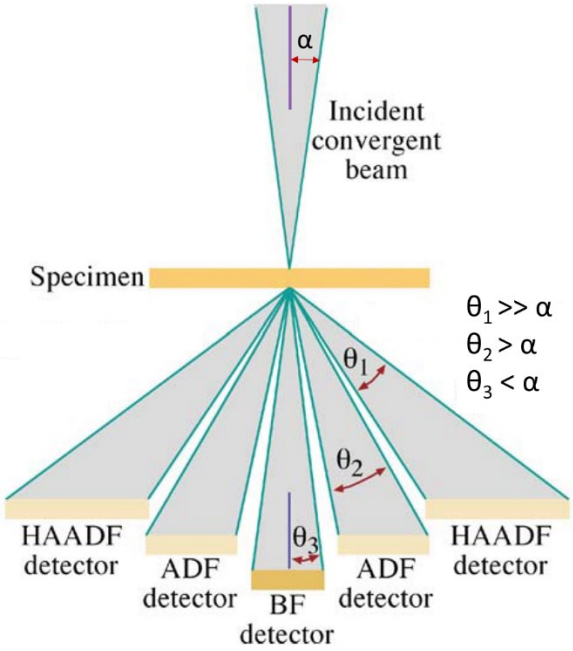

Figure 2.4. Schematic representation of detection angles for different STEM imaging modes (Williams & Carter, 2009).

The ADF detector collects electrons scattered over an annular region outside the BF disk, with an inner radius typically ranging from a few tens to 100 mrad and an outer radius of a couple hundred milliradians. Lattice contrast in ADF STEM images arises due to interference between the overlapping diffraction disks (Spence & Cowley, 1978). As all Bragg beams may be collected with an annular detector, ADF STEM images may have better contrast as compared to DF TEM images wherein the objective aperture just collects a fraction of the diffracted beams. At high scattering angles (~100 mrad), the scattering is almost entirely thermal diffuse (Howie, 1979) and the imaging is completely incoherent. This is referred to as the high-angle ADF (HAADF) imaging mode. HAADF images have enhanced compositional contrast (Treacy et al., 1978) and are referred to as Z-contrast images due to the contrast being very sensitive to atomic number in these images. The ease of interpretation of HAADF images has made it the most popular STEM imaging mode. An example of a BF and HAADF STEM image of a Si crystal oriented along the [110] zone axis is shown in Figure 2.5.

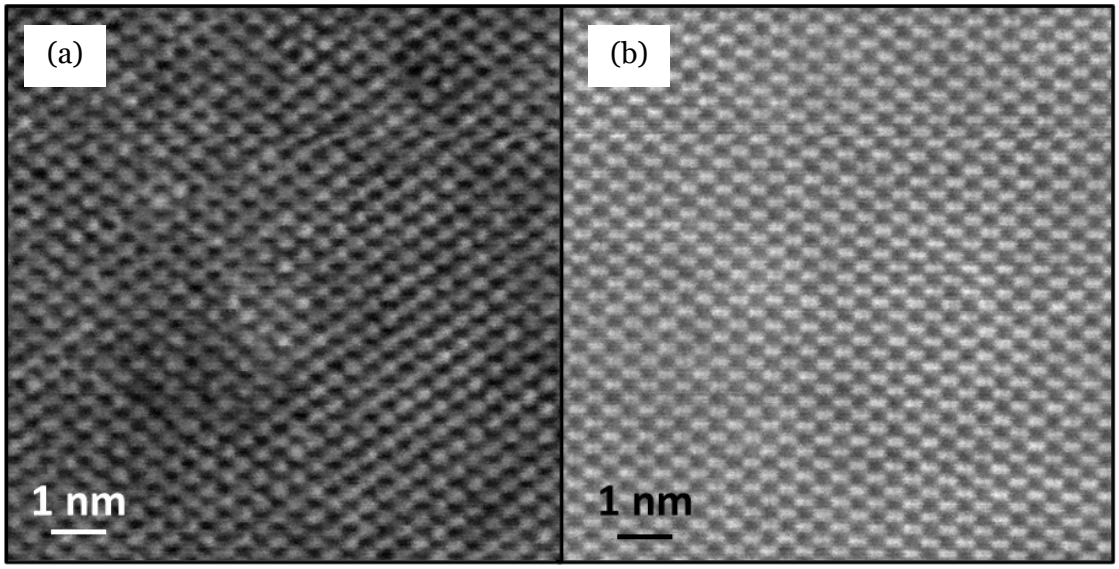

Figure 2.5. (a) BF and (b) HAADF STEM image of Si oriented along [110] zone axis.

Aberration correction

Although the spatial resolution of electron microscopes is ultimately limited by diffraction effects, imperfections in the electron lenses like spherical and chromatic aberrations limit the practically achievable resolution. Spherical aberration occurs when the lens field behaves differently for off-axis rays as compared to on-axis ones. For electromagnetic lenses, the more off-axis the electron is, the more strongly it is deflected towards the optic axis. This leads to a point object being imaged as a finite disk, and the resolving power of the microscope is worsened as specimen details are degraded by the imaging process. A ray diagram demonstrating spherical aberration is shown in Figure 2.6a. The coefficient of spherical aberration, C_s, is an important parameter for a lens, and the size of the finite disk image of a point object at the image plane due to spherical aberration is defined as $2C_s\beta^3$, where β is the maximum collection angle of the lens aperture. Typical values of C_s range from 0.5 to 3 mm. Relatively recently, C_s correctors developed by Rose and colleagues for the TEM (Urban et al., 1999) and by Krivanek and colleagues for the STEM (Krivanek et al., 1999) have been commercialized. Chromatic aberration occurs when electrons of different energies passing through an electromagnetic lens are focused differently. In a TEM, when the electron beam is incident on the specimen, electrons having a range of energies are created due to inelastic scattering in the specimen, and the objective lens focuses the electrons of lower energy more strongly such that a point in the object is blurred into a disk in the image plane. A ray diagram demonstrating chromatic aberration is shown in Figure 2.6b. As there are no lenses after the specimen in a STEM, chromatic aberration occurs mainly due to the energy spread in the electron beam, which can be minimized by employing an in-column monochromator after the electron source (Boersch et al., 1962; Krivanek et al., 2009; Mook & Kruit, 1997; Terauchi et al., 1991).

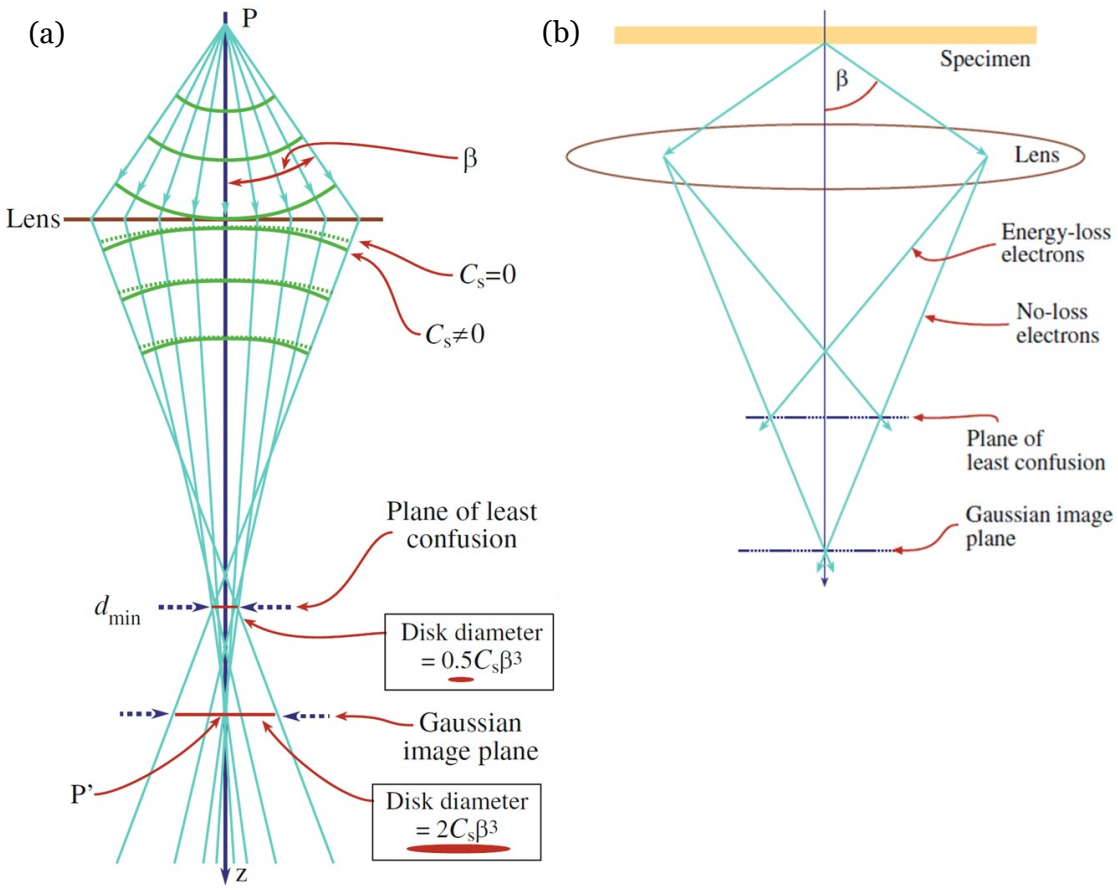

Figure 2.6. Ray diagrams for spherical (a) and chromatic (b) aberrations (Williams & Carter, 2009). A plane of least confusion and a Gaussian image plane can be identified in both diagrams; they represent a blurred version of the original object.

The correction of spherical aberrations has greatly improved the spatial resolution achievable with the STEM. A review of the history of aberration correction in electron optics can be found in these references (Rose, 2008; Krivanek et al., 2008; Hawkes, 2009). Aberration correction in the STEM was first successfully achieved by using a quadrupole/octupole corrector installed on an old VG microscopes HB5 (Krivanek et al., 1999; Krivanek, 1997), although the resolution was limited to between 2.3 and 3.4 Å due to microscope instabilities. Shortly after, an improved corrector was installed on a VG HB 501 STEM operated at an accelerating voltage of 100 kV, which was able to resolve the dumbbells in Si [110] demonstrating a resolution of 1.36 Å (Dellby et al., 2001). This was

better than the theoretical resolution limit of 2.2 Å for an uncorrected lens, and was a new record for resolution at 100 kV. Pushing the accelerating voltage to 120 kV improved the resolution to 0.8 Å (Batson et al., 2002). The improved visibility of single atoms was one of the most striking prospects of aberration correction. Figure 2.7 shows images of single La atoms on γ-Al_2O_3 with and without aberration correction from a VG HB603U STEM operated at 300 kV (Pennycook et al., 2003). It can be seen how aberration correction significantly improves contrast, resolution, and signal to noise ratio. Another advantage of aberration correction was that an order of magnitude more current could now be contained in a probe of the same size as before aberration correction (Krivanek et al., 2003). This is particularly useful for low-intensity signals and can benefit spectroscopic applications such as elemental mapping with X-rays or energy-loss electrons due to enhanced signal generation.

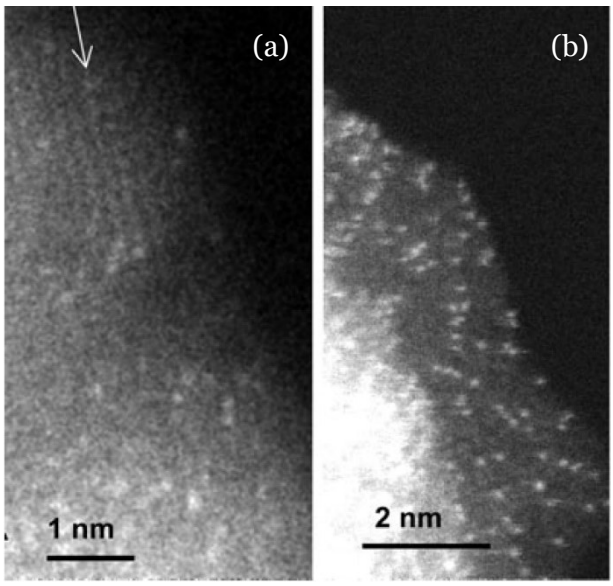

Figure 2.7. ADF images of single La atoms on γ-Al_2O_3 obtained before (a) and after (b) aberration-correction, showing an improvement in contrast, resolution, and signal-to-noise ratio (Pennycook et al., 2003). Arrow in (a) shows fringes from the γ-Al_2O_3.

2.1.3 Electron energy-loss spectroscopy (EELS)

EELS is a robust technique to probe the physical, chemical, and optical properties of matter. It involves analyzing the energy distribution of electrons that initially have the same energy after they have interacted with the specimen. This interaction can be limited to a few atomic layers when the primary energy of the incident electrons is low (100 – 1000 eV) and they are reflected from a solid surface as in high-resolution EELS (HREELS), exchanging energy with the vibrational modes and valence electron excitations of surface atoms (Ibach & Mills, 2013). If the primary electron energy is high, surface-sensitive "reflection" EELS can only be performed if the electrons are incident on the surface at glancing angles (incidence angle > 80°) (Atwater et al., 1993; Creuzburg & Raether, 1963; Krivanek et al., 1983; Lohff, 1963; Powell, 1968). If the primary electrons are incident perpendicular to the surface of a thin specimen (< 100 nm) with a sufficiently high kinetic energy (≥ 30 keV), the electrons are completely transmitted through the specimen without any reflection or absorption. Thus, all interaction takes place inside the specimen and important structural and chemical information about the specimen can be obtained by passing the transmitted electrons through a spectrometer that disperses the electrons according to their energy. This can be conveniently performed in TEM or STEM as electromagnetic lenses are already present to focus the electrons and guide them into a spectrometer. This allows the diffraction and imaging capabilities of the microscope to be leveraged, and gives EELS the added advantage of high spatial resolution, enabling analysis down to single atom length scales. In the TEM, EELS can be performed either as energy-filtered TEM (EFTEM) imaging (Crozier, 1995) wherein electrons that have a lost a specified amount of energy are used to form a real space image, or by spectral acquisition using a slightly convergent or area-selected parallel beam, allowing the freedom to select the specimen region which will give rise to the spectrum. In STEM EELS, a spectrum can

be acquired at each probe position in a region of interest (ROI), enabling pixel by pixel spectral acquisition with sub-nanometer spatial resolution, while simultaneously recording a HAADF image of the ROI. In this dissertation, transmission EELS in a STEM was the primary method of spectroscopic analysis and discussion in the text below will focus on this electron optical geometry.

Before moving on to physical processes that are responsible for the features observed in an energy-loss spectrum, the history of transmission mode EELS is briefly reviewed. The energy distribution of transmitted electrons was reported for the first time from a thin-film of Al (Ruthemann, 1941), by employing an incident energy of 2 – 10 keV, using a magnetic spectrometer and a photographic plate but no focusing lens. The spectrum consisted of a series of peaks associated with plasma oscillations in Al (Bohm & Pines, 1951). By employing two condenser lenses to focus 25 – 75 keV electrons to a spot size of 20 nm, the first microprobe/shadow microscope was made to perform microanalysis by using inner shell losses (Hillier & Baker, 1944). However, due to a poor vacuum system, hydrocarbon contamination caused specimens to become opaque in the few seconds that the electron beam was incident on them. This prompted increasing the beam spot size to 200 nm, and K-shell ionization edges were recorded from several elements while L- and M-shell edges were recorded from iron. An alternative design for a spectrometer that used electrostatics to disperse electrons according to their energy was published few years later (Mollenstedt, 1949). Electrons were passed between two cylindrical electrodes that slowed them down, resulting in high off-axis chromatic aberrations which yielded a large dispersion and high energy resolution. This spectrometer was fitted at the bottom of conventional TEMs in many laboratories which enabled recording of energy-loss spectra as a function of position in the specimen or scattering angle using the diffraction pattern (Egerton, 2011). A spectrometer with another

alternative design that used both electric and magnetic fields to disperse electrons, referred to as a Wien filter, was employed to analyze transmission energy-loss measurements (Boersch et al., 1962). They used a second Wien filter as a monochromator for incident electrons of 25 keV energy that enabled an energy resolution of 4 – 6 meV, allowing vibrational and intraband electronic excitations to be detected. However, due to the absence of a strong focusing lens, the beam size on the specimen was 10 μm, implying a poor spatial resolution.

Since the 1970s, EELS started attracting the attention of electron microscopists, either for using inelastically scattered electrons to form an EFTEM image, or for performing microanalysis of light elements in specimens by measuring the intensities of inner shell ionization edges in the energy-loss spectrum. That the magnetic field produced between two prism shaped pole pieces can be used for imaging was demonstrated by an in-column energy filter (Castaing & Henry, 1962), and plasmon-loss EFTEM images were recorded that showed diffraction contrast due to elastic scattering and "chemical contrast" associated with different crystallographic phases (Castaing, 1975). In other laboratories, the Castaing-Henry energy-filter was also used for recording images and spectra from inner shell ionization energy losses (Colliex & Jouffrey, 1972; Egerton & Whelan, 1974; Henkelman & Ottensmeyer, 1974). For high-voltage microscopes, the purely magnetic "omega filter" design was adopted (Rose & Plies, 1974), and improved by the Zeitler group in Berlin, resulting in a commercial energy-filtering TEM (Bihr, 1991). The design for a post-column energy filter that employed an energy-selecting slit with three post-slit quadrupoles to either record EFTEM images or energy-loss spectra was also proposed (Krivanek & Ahn, 1986). It was commercialized by Gatan as the currently popular Gatan Imaging Filter (GIF) due the high-quality EELS output, ease of operation and ease of installation on any microscope column. On the other hand, energy-filtering was first

performed with the STEM to improve the images of heavy single atoms on thin substrates (Crewe, 1966). Researchers installed different types of energy-filters on the STEM – electrostatic, magnetic and the electromagnetic Wien filter (Batson, 1995; Browne, 1971; Isaacson & Scheinfein, 1983) to explore the possibilities offered by high spatial resolution EELS.

Elemental microanalysis with EELS required that a single-prism magnetic spectrometer be installed at the bottom of the microscope column. The electron optical arrangement that is now widely used consists of a prism that considers the final crossover in the microscope column as its object and a spectrometer entrance aperture can be used to either select the region of interest on the specimen in the case of EFTEM or to control the collection angle in the case of STEM EELS. This arrangement was first employed at the Cavendish laboratory in Cambridge (Wittry, 1969). Serial recording of the spectrum was achieved by scanning it at the energy selecting slit that is located before a single channel electron detector. An important technological advance was the realization of a parallel detection spectrometer, with which an energy-loss spectrum could be recorded simultaneously using a position-sensitive detector like a photodiode or a charge-coupled diode (CCD). In this instrument, the prism was aberration corrected up to the second order, a three post-prism quadrupole lens based magnification system was used to project the spectrum, with independent adjustment of dispersion and spectrum width, onto a scintillating yttrium-aluminum garnet screen that was coupled to a photodiode array which in later designs was replaced by a CCD (Krivanek et al., 1987). Adding a second prism and three flexible dodecapole elements, allowed the cancellation of aberrations in the spectrometer up to the third order (Haider, 1989). Next generation spectrometers incorporated multiple multipole (12 to 16 poles) elements before and after the prism, and detectors having low noise and a high dynamic range, resulting in faster acquisition, lesser

aberrations, high stability and ultrahigh energy resolution (Gubbens et al., 2010), as demonstrated by the current generation Nion Iris spectrometers (Krivanek et al., 2019).

The physical origin of energy-loss by incident electrons can be attributed to a variety of processes including inner shell excitations, outer shell excitations, inter- and intra-band transitions, and vibrational mode excitations within the specimen. Each of these processes has an associated range of energy-losses, and edges or peaks in the energy-loss spectrum can be interpreted to provide a wealth of information on composition, bonding arrangements, and optical properties from the specimen. A typical energy-loss spectrum from a thin specimen of the superconducting oxide $YBa_2Cu_3O_7$, over a range of 1000 eV, is shown in Figure 2.8. The y-axis of the spectrum is displayed in a logarithmic scale due to the rapid decrease in electron intensity with energy-loss. The dominant feature in the spectrum is the zero-loss peak (ZLP) which represents transmitted electrons that either scatter elastically or excite ultra-low energy acoustic vibrational modes for which the energy transfer is less than the experimental energy-resolution. The full-width at half-maximum (FWHM) of the ZLP is a generally accepted figure of merit to gauge the instrumental energy-resolution. The ZLP also contains unscattered electrons that are spatially undeflected but undergo a phase change as they pass through the specimen. Inelastic scattering from outer shell excitations shows up in the low energy-loss (0.5 to 50 eV) region of the spectrum as a peak (series of peaks) in thin (thick) specimens. These outer shell excitations are associated with collective oscillations of the unbound valence electrons, also referred to as plasmons, and are brought about by electronic polarization created in the specimen by the electron beam. This region of the energy-loss spectrum is called the low-loss or valence-loss regime.

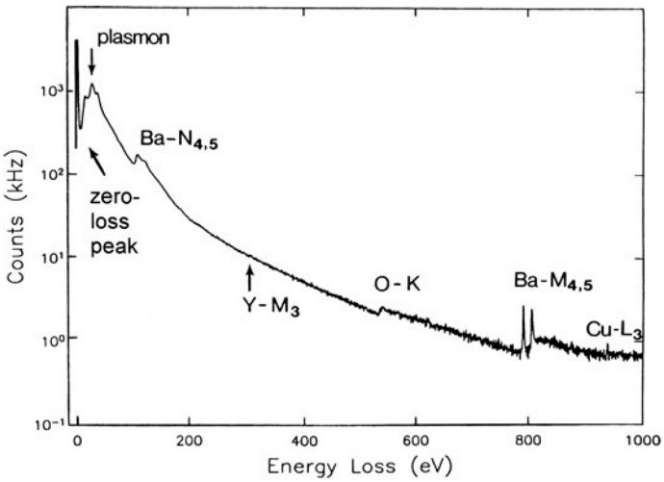

Figure 2.8. Typical energy-loss spectrum from $YBa_2Cu_3O_7$ with the electron intensity on a logarithmic scale (Egerton, 2011). The spectrum shows the ZLP, plasmon peaks, and element ionization edges.

Features in the spectrum due to inner-shell excitations are typically visible at higher energy-losses (> 50 eV); this is referred to as the core-loss regime of the spectrum. These features appear as edges rather than peaks, with signal intensity rising rapidly at approximately the binding energy of the corresponding atomic shell, and falling slowly with increasing energy-loss. The binding energy of inner shell electrons is a function of the scattering atom's number and therefore, the core-loss region of the energy-loss spectrum reveals which elements are present in the specimen. Measuring the background subtracted area under the appropriate ionization edge can yield a quantitative elemental analysis of the specimen composition. When combined with a STEM, quantitative elemental analysis can be performed using core-loss spectra read out at each pixel, to yield an elemental map showing the location from which the signal originates in the specimen, possibly with atomic resolution. The core-loss spectrum from a solid specimen often shows a pronounced fine structure referred to as the energy-loss near edge structure (ELNES), within 50 eV of the ionization edge, that is heavily influenced by atoms surrounding the excited atom. The interpretation of this fine structure requires solid state physics

arguments, and these are described in many review articles (Brydson et al., 1991; Himpsel et al., 1991; Mizoguchi et al., 2010; Rez et al., 1995; Rez et al., 1991). The interpretation approaches include: 1) the ELNES is proportional to a convolution of the initial and final density of states at the site of the excited atom, 2) it arises because of multiple elastic scattering of the ejected electron by the local (1 nm) environment of the excited atom, 3) in covalent materials, it can be interpreted by approximating the band structure by a linear combination of atomic orbitals of the excited atom and its nearest neighbors, or 4) originating due to coupling of the angular momentum of the hole created by the ionization process to the net angular momentum of partially filled orbitals in the excited atom. The core-loss spectrum also shows intensity oscillations that are detectable over several hundred electron volts after the ionization edge if no ionization edges follow within this region. This is called the extended energy-loss fine structure (EXELFS), and it originates due to interference between the wavefront of the ejected electron and the reflected wavefront from its elastic backscattering from neighboring atoms. Recent developments in monochromators for electron microscopes has unveiled a new regime for EELS – the vibrational-loss regime – associated with inelastically scattered electrons that excite vibrational modes in the specimen, with typical energy-losses in the range of 30 – 500 *meV* (Krivanek et al., 2014; Miyata et al., 2014).

Energy-loss spectra recorded from thin specimens have features that originate from single inelastic scattering events. Plural inelastic scattering, associated with features originating from multiple inelastic scattering events, can occur in thick specimens. The energy-loss of such features is the sum of the energy-losses of the corresponding individual inelastic scattering events. Plural scattering can manifest in the low-loss regime as a series of plasmon peaks at multiples of the plasmon energy. In the core-loss regime, an electron that has undergone an inner-shell excitation may also cause an outer-shell excitation,

resulting in a broad peak above the ionization threshold, with the separation approximately equaling the plasmon energy. Plural inelastic scattering will be an appreciable process in specimens whose thickness exceeds the inelastic mean free path (IMFP), which is the average distance between two scattering events. The IMFP is inversely proportional to the scattering cross-section; for outer shell inelastic scattering it is of the order of ~100 nm for an incident electron energy of 100 keV, while it is larger for inner shell scattering events. Typical thicknesses of TEM specimens ≤ 100 nm; thus, the probability of outer shell plural scattering is significant for TEM specimens, but that of inner shell plural scattering is negligible. Plural scattering effects are generally unwanted and can be removed from the spectrum by various deconvolution procedures.

The low-loss spectrum provides a convenient method to determine local specimen thickness using EELS (Egerton, 2011). Poisson statistics determines the probability, P_n, that an electron undergoes n collisions while passing through the specimen as,

$$P_n = \left(\frac{1}{n!}\right) m^n e^{-m} \tag{2.2}$$

where m is the mean number of collisions experienced by the transmitting electron and is given by the ratio of the specimen thickness to the IMFP, yielding,

$$P_n = \left(\frac{1}{n!}\right)\left(\frac{t}{\lambda}\right)^n e^{-\frac{t}{\lambda}} \tag{2.3}$$

The probability of the transmitted electron not being scattered can be obtained by setting $n = 0$ in equation 2.2. This probability is also equal to the ratio of the intensity in the ZLP, I_0, to the total intensity in the spectrum, I_t, thus giving,

$$P_0 = \frac{I_0}{I_t} = e^{-\frac{t}{\lambda}} \tag{2.4}$$

This gives us the useful expression, often referred to as the 't/λ ratio':

$$\frac{t}{\lambda} = \ln\left(\frac{I_t}{I_0}\right) \tag{2.5}$$

For Poisson statistics to be valid, the following assumptions should hold: 1) The scattering angles should be small so that the distance travelled by electrons inside the specimen experiencing different orders of scattering is identical. 2) The electrons should transmit the specimen at normal incidence, so that second and higher order surface scattering is negligible. 3) The specimen should be of uniform thickness within the area from which the spectrum is recorded, so that there is not over- or under-estimation of the intensity under the ZLP. In this dissertation, the t/λ ratio determined from the valence energy-loss spectrum was used for local thickness measurement for the specimens used in Chapters 4, 5 and 6.

The angular distribution of inelastic scattering is expressed as a differential cross section $d\sigma_i/d\Omega$, which represents the probability of an incident electron being inelastically scattered per unit solid angle, Ω, by a given atom. For an element with atomic number Z, the differential cross section for scattering angle θ can be explicitly written as (Colliex et al., 1984),

$$\frac{d\sigma_i}{d\Omega} = \frac{4\gamma^2 Z}{a_0^2 k_0^4} \frac{1}{(\theta^2 + \bar{\theta}_E^2)^2} \left\{1 - \left[\frac{\theta_0^4}{(\theta^2 + \bar{\theta}_E^2 + \theta_0^2)^2}\right]\right\} \tag{2.6}$$

where $\gamma = 1/\sqrt{1-(v/c)^2}$ is the relativistic factor for an incident electron with velocity v and c is the velocity of light in vacuum, 3 x 10^8 m/s, a_0 is Bohr's atomic radius, 5.29 x10^{-11} m, $k_0 = 2\pi/\lambda$ is the incident electron wavevector, $\bar{\theta}_E = \bar{E}/2\gamma E_0$ is the characteristic angle for mean energy loss $\bar{E}$ and $\theta_0 = (k_0 r_0)^{-1}$ is a characteristic angle of elastic scattering, where r_0 is the screening radius given either by the Wentzel potential or by the Thomas-

Fermi screening length. The first two terms in Equation 2.6 represent the Rutherford cross section for scattering by Z atomic electrons that are considered to be stationary free particles, and the term in braces is an inelastic form factor (Schnatterly, 1979). In the angular range $\bar{\theta}_E < \theta < \theta_0$, the differential cross section falls as $1/\theta^2$ whereas above θ_0 it falls as $1/\theta^4$. It can then be said that the angular distribution of inelastic scattering is approximately a Lorentzian function with angular width $\bar{\theta}_E$ and a gradual cutoff at θ_0. For a carbon specimen, taking $E_0 = 100\ keV$ and $\bar{E} = 37\ eV$, $\bar{\theta}_E = 0.2\ mrad$ and $\theta_0 = 20\ mrad$ (Isaacson, 1977) and the mean and median angles for inelastic scattering are estimated as $\bar{\theta} = 20\bar{\theta}_E = 4\ mrad$ and $\tilde{\theta} = 10\bar{\theta}_E = 2\ mrad$ respectively. Inelastic scattering is thus concentrated into much smaller scattering angles than elastic scattering.

A more detailed description of inelastic scattering of electrons by an atom, including the dependence of scattering intensity on energy-loss, given by Bethe theory, requires that each atomic electron be described in terms of a transition from an initial state of wavefunction ψ_0 to a final state of wavefunction ψ_n. The differential cross section can then be written as,

$$\frac{d\sigma_n}{d\Omega} = \frac{4\gamma^2}{a_0^2 k_0^4} \frac{1}{(\theta^2 + \theta_E^2)^2} \frac{k_1}{k_0} |\varepsilon_n(q)|^2 \qquad (2.7)$$

where k_0 and k_1 are the electron wavevectors before and after scattering, respectively. The first two terms represent the Rutherford cross section for scattering by a single free electron. The ratio k_1/k_0 is close to unity when energy-loss is much smaller than the incident electron energy. The final term in Equation 2.7, referred to as an inelastic form factor or a dynamical structure factor, is the square of the modulus of the transition matrix element defined as,

$$\varepsilon_n(q) = \int \psi_n^* \sum_j \exp\left(i\boldsymbol{q}.\boldsymbol{r}_j\right) \psi_0 d\tau = \langle \psi_n \left| \sum_j \exp\left(i\boldsymbol{q}.\boldsymbol{r}_j\right) \right| \psi_0 \rangle \qquad (2.8)$$

where $\hbar\boldsymbol{q} = \hbar(\boldsymbol{k}_0 - \boldsymbol{k}_1)$ is the momentum transferred to the atom and $\boldsymbol{r}_j$ represents the coordinates of the atomic electrons. The inelastic form factor is a property of the target atom and is independent of the incident electron energy. Bethe introduced a closely related quantity called the generalized oscillator strength (GOS), defined as (Bethe, 1930; Inokuti, 1971),

$$f_n(q) = \frac{E_n}{R} \frac{|\varepsilon_n(q)|^2}{k_0^2 a_0^2} \frac{1}{(\theta^2 + \theta_E^2)} \qquad (2.9)$$

where $R = 13.6\ eV$ is Rydberg's constant and E_n is the energy required for the transition. Substituting into Equation 2.7,

$$\frac{d\sigma_n}{d\Omega} = \frac{4\gamma^2 R}{E_n k_0^2} \frac{1}{(\theta^2 + \theta_E^2)} \frac{k_1}{k_0} f_n(q) \qquad (2.10)$$

The energy-loss spectrum is a continuous function of energy-loss E, so it is more convenient to define a GOS per unit energy-loss, $df(E,q)/dE$. The angular and energy dependence of inelastic scattering can then be expressed as a double differential cross section,

$$\frac{d^2\sigma}{dEd\Omega} = \frac{4\gamma^2 R}{E k_0^2} \frac{1}{(\theta^2 + \theta_E^2)} \frac{k_1}{k_0} \frac{df(E,q)}{dE} \approx \frac{4\gamma^2 R}{E k_0^2} \frac{1}{(\theta^2 + \theta_E^2)} \frac{df(E,q)}{dE} \qquad (2.11)$$

It can be seen that the main term contributing to the angular distribution of inelastic scattering is the Lorentzian function $(\theta^2 + \theta_E^2)^{-1}$, with θ_E being the half-width at half-maximum of this distribution. For low scattering angles and energy-loss, the angular distribution of the GOS is constant and independent of θ. This is called the dipole region; the GOS is then called the dipole oscillator strength and it characterizes the response of an

atom to incident photons. As the GOS per unit loss is a function of both the momentum transfer and energy-loss, it is convenient to visualize it in a two-dimensional plot, referred to as the Bethe surface. An example of the Bethe surface for the carbon K-shell ionization edge is shown in Figure 2.9 (Egerton, 1979). At energy-losses close to the binding energy of the ejected electron, the GOS is strongly forward peaked corresponding to the dipole region and can be associated with a relatively large impact parameter. At larger energy-loss, the angular distribution is concentrated into a Bethe ridge, centered around a value of θ that satisfies,

$$k_0^2 a_0^2(\theta^2 + \theta_E^2) \approx E/R \qquad (2.12)$$

This θ is called the Bethe ridge angle, $\theta_r \approx \sqrt{2\theta_E}$ for small angle scattering and non-relativistic incident electrons. Such an interaction is associated with small impact parameter scattering by a single inner shell electron and Equation 2.12 is that for Rutherford scattering by a free stationary electron. The broadening of the ridge is the effect of electron binding in the atom, which implies that the ejected electron is not stationary and has a finite kinetic energy.

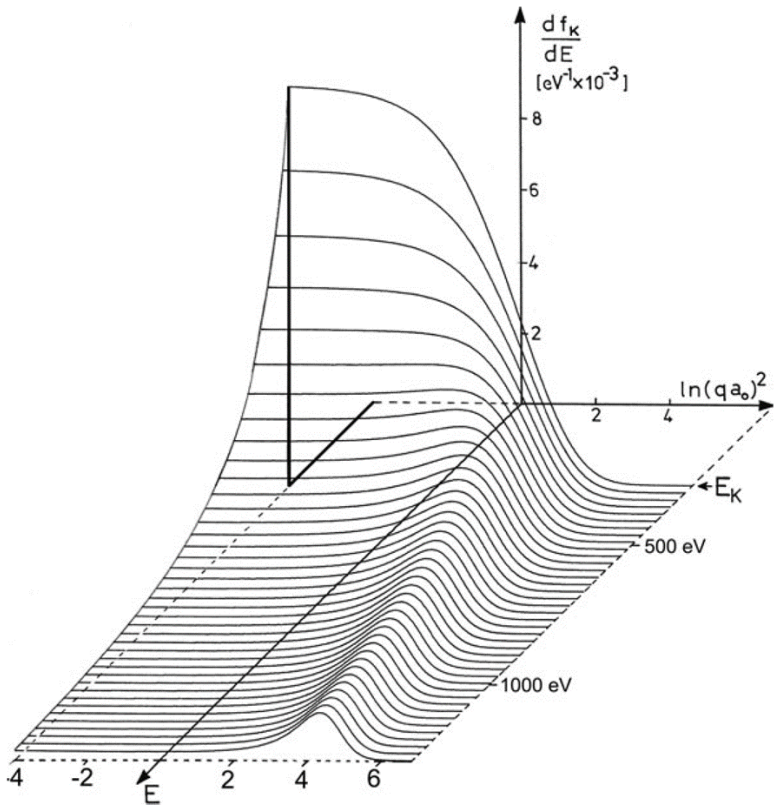

Figure 2.9. Bethe surface for K-shell ionization of carbon (R. Egerton, 1979). The GOS is zero for energy-loss E below the threshold of ionization E_K. q on the horizontal axis is related to the scattering angle as described earlier.

Equations derived from the atomic models above can be used to describe the inelastic scattering process in single atoms and can be straight forwardly applied to gaseous specimens. However, for a solid specimen, the GOS differs from that for a single atom as it is influenced by chemical bonding around the excited atom that modifies the valence electron wavefunctions, thereby complicating outer shell scattering (Pines, 2018). There are also collective excitations launched by the fast electron in a solid specimen, involving many atoms as opposed to one. An alternative could be to approximate the interaction of the transmitted electron with the specimen by a dielectric response function $\varepsilon(\omega, q)$. The expression for the stopping power of an infinite medium experienced by fast electrons, dE/dz, is equal to the backward force acting on the transmitted electron in the

direction of motion and also to the product of the electrostatic potential gradient in the z direction and the electronic charge (Ritchie, 1957). It was shown that,

$$\frac{dE}{dz} = \frac{2\hbar^2}{\pi a_0 m_0 v^2} \iint \frac{q_y \omega \, Im[-1/\varepsilon(\omega, q)]}{q_y^2 + (\omega/v)^2} d\omega \, dq_y \tag{2.13}$$

where $m_0 = 9.1 \times 10^{-31}\, kg$, $\boldsymbol{v}$ is the electron velocity in the z-direction, q_y is the component of momentum transfer perpendicular to $\boldsymbol{v}$ and $\omega = E/\hbar$. The stopping power can also be expressed in terms of the double differential cross section as,

$$\frac{dE}{dz} = \iint n_a E \frac{d^2\sigma}{dE d\Omega} dE d\Omega \tag{2.14}$$

where n_a is the number of atoms per unit volume of the medium. Equating the above expressions and simplifying,

$$\frac{d^2\sigma}{dE d\Omega} \approx \frac{1}{\pi^2 a_0 m_0 v^2 n_a} \frac{1}{(\theta^2 + \theta_E^2)} Im\left[\frac{-1}{\varepsilon(\omega, q)}\right] \tag{2.15}$$

where $Im(-1/\varepsilon(\omega, q))$ is called the energy-loss function. It provides a complete description of the medium's response to the transmitting fast electron. It can be seen that Equation 2.15 has the same Lorentzian angular dependence as the corresponding Bethe Equation 2.11. In the region of small angle scattering (dipole scattering region), the dielectric function $\varepsilon(\omega, q)$ doesn't vary with q and can be replaced by $\varepsilon(\omega, 0)$, which is the permittivity of the medium at the angular frequency $\omega = E/\hbar$. This permittivity can be readily obtained by optical ellipsometry measurements and the optical dielectric function $\varepsilon(\omega, 0)$ for many materials have been reported in literature (Palik & Ghosh, 1998). The dielectric response theory has been extensively used with an optical dielectric function to aid the interpretation of low energy-loss spectra (Browning et al., 2011; de Abajo, 2010; de Abajo & Howie, 1998; de Abajo & Aizpurua, 1997; de Abajo & Sáenz, 2005; Erni &

Browning, 2008; Mkhoyan et al., 2007; Reed et al., 1999; Stöger-Pollach, 2008; Stöger-Pollach & Schattschneider, 2007; Ugarte et al., 1992) and relatively recently, it has also been used to interpret features in the vibrational energy-loss spectra that originate from dipole scattering of incident electrons (Crozier, 2017; Govyadinov et al., 2017; Konečná, Venkatraman, et al., 2018; Lagos et al., 2017, 2018; Venkatraman et al., 2018). In this dissertation, it has been used to compare experiments with theory in Chapters 3 and 4. Inner-shell inelastic scattering involves high energy-losses and high momentum transfer that can be correlated with large scattering angles, hence, the optical dielectric function cannot be used and the Bethe theory has to be implemented, accounting for multiple scattering while calculating the final state wavefunction ψ_n to interpret experimental data. In Chapters 5 and 6, it will be demonstrated that certain features in the vibrational energy-loss spectrum associated with large angle scattering cannot be described using the dielectric theory with an optical dielectric function while other features associated with small angle scattering can.

The long-range nature of the electrostatic interaction between the fast electron and atomic electrons in the specimen is responsible for inelastic scattering and this imposes a basic limit on the spatial resolution of the EELS signal. This limitation is called delocalization, and is defined as the width of the real-space distribution of intensity of the inelastically scattered electrons after accounting for elastic effects and all instrumental aberrations (Muller & Silcox, 1995; Pennycook et al., 1995). This intensity distribution is known as the point spread function (PSF) of inelastic scattering, and the PSF at a distance r from the optic axis is proportional to the square of the two-dimensional Fourier transform ($FT2$) of the scattering amplitude per unit solid angle, $d\psi/d\Omega$,

$$PSF(r) \propto \{FT2[d\psi/d\Omega]\}^2 \propto \left\{FT2[dI/d\Omega]^{1/2}\right\}^2 \qquad (2.16)$$

where $dI/d\Omega$ is the intensity of inelastic scattering per unit solid angle which is proportional to $(\theta^2 + \theta_E^2)^{-1}$ over most of the angular range; the PSF comes out to be (Egerton, 2017),

$$PSF(r) \propto (k_0 r)^{-2} \exp(-2k_0\theta_E r) = (k_0 r)^{-2} \exp(-2r/b_{max}) \qquad (2.17)$$

where $b_{max} = (k_0\theta_E)^{-1} = v/\omega$ is the Bohr adiabatic limit (Bohr, 1913). At large scattering angles, the inelastic scattering intensity per unit solid angle falls off more rapidly than the Lorentzian function and is proportional to $(\theta^2 + \theta_E^2)^{-1}(\theta^2 + \theta_r^2)^{-1}$. The PSF then comes out to be,

$$PSF(r) \propto (1 + r^2/r_0^2)^{-1} \exp(-2k_0\theta_E r) \qquad (2.18)$$

This PSF has a sharp central peak and tails that extend over atomic dimensions for typical core-loss scattering, or stretch beyond 1 nm for valence-electron losses (Egerton, 2011). For low energy losses, $\theta_r >> \theta_E$ and radial dependence of the PSF is approximately r^{-2}, a large fraction of the intensity is present in the PSF tails. At high energy losses, θ_r/θ_E is smaller and more of the intensity lies within the central peak. This leads to a more localized signal which can be measured only by placing the focused electron beam directly on the atom or molecule of interest (Egerton, 2009; Muller & Silcox, 1995; Prange et al., 2012). Thus, delocalization is small for high energy-losses where the angular distribution of inelastic scattering is broad and the PSF correspondingly narrow – implying a signal with high spatial resolution, while it is large for low energy-losses where the angular distribution is narrow and the PSF correspondingly broad – implying a relatively low spatial resolution signal.

2.1.4 Monochromated STEM EELS

It was mentioned in the previous section that current generation spectrometers like the Nion Iris have aberrations corrected up to fifth order (Lovejoy et al., 2018), and such spectrometers can be tuned so that the energy resolution is only limited by the energy spread in the electron source. It was also mentioned that the EELS energy resolution is defined to be the FWHM of the ZLP in an energy-loss spectrum recorded in vacuum. The energy resolution for a cold field emission gun (FEG) electron source is around 0.3 eV (Batson, 1986; Crewe, 1971; Isaacson & Scheinfein, 1983) while that for a thermionic or Schottky emission sources is around 0.5 – 0.8 eV (Fransen, 1998; Kim et al., 1997; Swanson & Schwind, 2009). While such energy resolution is reasonable for elemental mapping with core-loss EELS, it might limit the ability to resolve detail in the ELNES and the EXELFS. The tail of such a ZLP will extend to high energies and might bury certain low-loss features under its background, or might result in the inaccurate measurement of bandgap for a low bandgap semiconductor. This energy resolution will also limit the detection of peaks separated by 100 meV or less (typical peak separations observed in vibrational spectroscopy). Using a monochromator, the energy spread of electrons incident on the specimen can be reduced, typically to several hundred or tens of meV, with the most advanced monochromated instrument giving an energy resolution of 4.2 meV for 30 keV incident electron energy (Krivanek et al., 2019). This enables reliable observation of spectral features in the range of 30 – 500 meV, like those associated with bandgap states and vibrational excitations.

A monochromator typically produces an energy spectrum by energy-dispersing electrons emitted by the source with a magnetic prism. The spectrum is then projected onto an energy-selecting slit which defines the range of energies admitted into the microscope column. A second prism returns the beam to the optic axis. The energy-loss

spectrometer also energy-disperses the transmitted electrons and projects the spectrum onto a detector, as mentioned previously. Thus, the two instruments are closely related and obey the same electron-optical concepts. The history of development of transmission EELS reviewed earlier involved the description of a Wien filter being used by Boersch and colleagues at Berlin as both a spectrometer and a monochromator to eventually achieve an energy resolution of 3 meV for 25 – 30 keV incident electron energy, although with a spatial resolution of 10 μm (Boersch et al., 1962, 1964). Development of subsequent monochromators proceeded for both reflection based HREELS, wherein meV-scale energy resolution was achieved (Ibach & Mills, 2013), and transmission based EELS in electron microscopes aimed at high spatial resolution.

Terauchi and colleagues at JEOL fitted two modified Wien filters to a JEM-1200EX as a monochromator and an analyzer, equipped with retardation lenses to achieve 81 meV energy resolution at 60 kV accelerating voltage with a simultaneous spatial resolution of 190 nm (Terauchi et al., 1991). Both the Wien filters were operated at the microscope accelerating voltage with the potential in the retardation lenses set to a shared arbitrary value between 20 and 2000 V. This made the energy-resolution independent of the instabilities in the microscope accelerating voltage and power supplies to the energy-dispersing elements. Improvements in the Wien filter designs led to achieving an energy-resolution of 12 meV at 60 kV accelerating voltage, with a small beam current insufficient for spectroscopic applications. Increasing to a beam current sufficient for spectroscopy increased the energy resolution to 25 meV.

Another strategy was to put the monochromator within the gun at high voltage, wherein limited acceleration leads to a high dispersion which yields higher energy resolution. A short-field Wien filter with a single dispersive system and an energy-selecting slit on high voltage was proposed to be placed directly after the source (Mook &

Kruit, 1999). This reduced the stability- and precision-demands on the electrical supplies, but because the focusing action of such a filter was weak, a gun lens was used to focus the beam on the slit. The filter reduced the precision required on pre-alignment too, and could also be used as a deflector to align the beam on the 150 nm wide Nanoslits. The design predicted an energy-resolution of 50 meV with after-monochromation beam currents of 1 nA using a Schottky FEG source (Mook & Kruit, 1999). However, the low energies at which the electrons were dispersed meant more sensitivity to stochastic Coulomb beam broadening, also called the Boersch effect (Boersch, 1954). Philips Research Laboratories (later FEI microscopes) developed a longer, single Wien filter gun monochromator in which the dispersed electrons were accelerated before reaching the slit (Tiemeijer, 1999). This reduced the electrostatic charging at the slit and demonstrated an energy-resolution of 100 meV with low (<30 nA) total beam current.

The practical incorporation of the monochromator in a (S)TEM by FEI and JEOL to yield sub-100 meV energy resolution with negligible degradation in spatial resolution and sufficient current in the monochromated beam for spectroscopy resulted in accurate measurements of band gap threshold and inter-band excitations for low band-gap semiconductors (Park et al., 2009), Cerenkov radiation (Stöger-Pollach et al., 2006), surface-plasmons in spherical nanoparticles (Link & El-Sayed, 1999) and longitudinal, transverse, and cluster plasmon modes in nano-rods and -prisms (Bosman et al., 2007; Nelayah et al., 2007). Monochromation also helped resolve more detail in the inner shell energy-loss spectra due to, for example, spin orbit splitting in the Al $L_{2,3}$ edge of α-Al_2O_3 or splitting of the Co L_3 white line into four peaks due to atomic multiplet effects (Grogger et al., 2008).

An electrostatic version of the omega filter as a monochromator which consists of an energy-selecting slit in its mid-plane was proposed in 1990, in which the second half of

the filter cancels any energy-dispersion caused by the slit (Rose, 1990). This design has the advantages of avoiding a high-stability current supply and no magnetic hysteresis means low drift. However, it has complex electron optics and lacks flexible energy-dispersion – the width of the slit has to be changed to change the energy resolution.

A purely magnetic monochromator and spectrometer placed on ground potential with all magnetic prisms connected in series and having the same power supply was proposed by scientists at Gatan (Krivanek et al., 1991). This eliminated the dependence of energy selected by the monochromator on the microscope high tension (HT) and of energy resolution on instabilities in the prism current. To keep the dispersed beam centered on the variable slit aperture, the difference between the beam current falling on the two halves of the slit was fed back to the HT in a fast feedback loop. There were two issues in this design, of beam brightness as the dispersed beam was not undispersed after energy selection, and of energy resolution due to no provision for extra magnification of the dispersed beam. These were resolved in an improved design that used a dispersing-undispersing "alpha" prism arrangement and consisted of quadrupoles before the slit to magnify the spectrum by 100x at the slit (Krivanek et al., 2009). In combination with a Gatan Quantum spectrometer (Gubbens et al., 2010) and an aberration-corrected Nion STEM, the system achieved an energy-resolution of 12 meV at 60 keV primary energy (Krivanek et al., 2014). When combined with a Nion Iris spectrometer (Lovejoy et al., 2018) an energy-resolution of 4.2 meV was achieved at 30 keV primary energy which degraded to 5.7 meV at 60 keV, 8 meV at 100 keV, and 14.7 meV at 200 keV (Krivanek et al., 2019).

The improvement in energy-resolution achieved with better instrumentation – 26 meV by JEOL in the JEM-2400FCS operated at 80 keV and 10 meV by Nion in the UltraSTEM 100 at 60 keV, opened up the regime of performing vibrational spectroscopy

with EELS, by showing the vibrational energy-loss spectrum from an ionic liquid and various inorganic and organic solids (Krivanek et al., 2014; Miyata et al., 2014). Rapid developments in the field have allowed spatially resolved, damage free detection for a variety of organic and inorganic material-systems including vibrational fingerprints in biological specimens (Rez et al., 2016), detection of water and its derivatives on individual nanoparticle surfaces (Crozier et al., 2016), probing variations in the amine content of graphitic carbon nitride photocatalysts (Haiber & Crozier, 2018), orientation-dependent determination of normal vibrational modes in anisotropic $B_{12}P_2$ crystals (Radtke et al., 2019) and identifying site-specific isotopic labels in L-alanine (Hachtel et al., 2019). Correlating vibrational modes with nanoscale structures is already impacting a wide range of important scientific problems such as measurement of surface and bulk vibrational excitations in MgO nanocubes (Lagos et al., 2017), probing hyperbolic phonon polaritons in anisotropic hBN nanoflakes (Govyadinov et al., 2017a), measuring temperature in nanometer-sized areas with 1 K precision (Idrobo et al., 2018; Lagos & Batson, 2018), and determining phonon dispersion in nanoparticles (Hage et al., 2018; Senga et al., 2019). Theoretical treatments have explored the issue of spatial resolution (Dwyer, 2014; Dwyer, 2017; Egerton, 2015; Forbes & Allen, 2016; Rez, 1993, 2014) and sensitivity (Konečná, Neuman, et al., 2018; Kordahl & Dwyer, 2019; Rez, 2014) of vibrational EELS, with there being considerable interest to demonstrate atomic resolution and/or single particle sensitivity. As stated in Chapter 1, pushing the limits of spatial resolution and sensitivity with vibrational EELS is the objective of this dissertation, and experimental demonstrations of the same will be provided in Chapters 5 and 7.

2.2 Simulating vibrational energy-loss spectra using the classical dielectric theory

It was mentioned earlier that inelastic scattering involving collective low energy-loss excitations with small scattering angles can be treated by approximating the response of the specimen to the incident electron beam with its complex, frequency-dependent optical dielectric function. The optical dielectric function of an ionic material characterizes the polarization response of a medium to an external electric field and thus, is closely related to the vibrational properties of the material. Therefore, features in the energy-loss spectrum associated with vibrational excitations caused by ionic polarization can be interpreted with the classical dielectric theory, as done extensively for plasmon loss features caused by electronic polarization. The theory assumes the trajectory of the fast electron to be unaffected by interactions with the specimen, and it assumes the specimen to be a homogenous, forming surfaces and interfaces by having abrupt boundaries with other media. It is also assumed that only one electron interacts with the specimen at a time and there is no interaction or correlation between successive incident electrons. Employing dielectric theory to interpret energy-loss spectra yields simple terms called energy-loss functions, which approximate the spectrum when all other contributing effects are neglected. The following text reviews analytical expressions for the inelastic scattering probability derived using the classical dielectric theory for simple specimen geometries. For complicated geometries, it is not possible to obtain analytical expressions, and the electric field induced by the fast electron in the specimen has to be calculated numerically.

The inelastic scattering probability per unit path length and energy-loss, $d^2P/dzdE$, of fast electrons transmitting an infinite slab with dielectric function $\varepsilon(\omega)$ is given by (Ritchie, 1957),

$$\frac{d^2P}{dzdE} = \frac{e^2}{\pi^2\hbar v^2}\frac{1}{q_\perp^2 + (\omega/v)^2} Im\left(\frac{-1}{\varepsilon(\omega)}\right) \tag{2.19}$$

where e is the electronic charge, $q_\perp$ is the momentum transfer perpendicular to v, and $\varepsilon(\omega) = \varepsilon_r(\omega) + i\varepsilon_i(\omega)$ with ε_r and ε_i as the real and imaginary part respectively. The first term is a constant with a $1/v^2$ dependence on the electron velocity, the second term represents the angular distribution of inelastic scattering with $q_\perp = k_0\theta$ and $\omega/v = k_0\theta_E$, while the third term, $Im(-1/\varepsilon) = \varepsilon_i/(\varepsilon_r^2 + \varepsilon_i^2)$, is known as the bulk energy-loss function because the energy-loss for bulk or volume excitations corresponds to the energy-loss associated with a maximum in this function and that occurs wherever the denominator $\varepsilon_r^2 + \varepsilon_i^2$ is minimum. Equation 2.19 was derived by assuming no retardation and neglecting the influence of surfaces on energy-loss, which is called the infinite slab approximation. Extending this model to an infinite slab with an interface between two media with dielectric response functions ε_1 and ε_2, and the electron beam passing through ε_1, the differential inelastic scattering probability is (A. Howie & Milne, 1985),

$$\begin{aligned}\frac{d^2P}{dzdE} = \frac{e^2}{2\pi^2\varepsilon_0\hbar^2v^2}\Bigg\{&Im\left(-\frac{1}{\varepsilon_1}\right)\times\ln\left(\frac{q_{\perp,c}v}{\omega}\right)\\ &+\left[-Im\left(-\frac{1}{\varepsilon_1}\right)+Im\left(-\frac{2}{\varepsilon_1+\varepsilon_2}\right)\right]\times K_0\left(\frac{2\omega b}{v}\right)\Bigg\}\end{aligned} \tag{2.20}$$

where ε_0 is the permittivity of free space, $q_{\perp,c}$ is the cut-off momentum transfer perpendicular to the electron velocity and is determined by the collection angle allowed by the spectrometer entrance aperture. $Im(-1/\varepsilon_1)$ is the bulk energy-loss function, and $Im(-2/\varepsilon_1+\varepsilon_2)$ is called the interface energy-loss function; it represents the influence of an abrupt interface on the energy-loss spectrum. It is seen that both the square bracket terms are multiplied by $K_0(2\omega b/v)$, where $K_0(z) = 1/2\int_{-\infty}^{\infty}\left(e^{izt}/\sqrt{t^2+1}\right)dt$ is the modified Bessel function of zero order and b is the distance of the electron beam from the

$\varepsilon_1/\varepsilon_2$ interface while it is passing through medium ε_1. It can be seen that this K_0 Bessel function dictates the spatial variation of the bulk and interface energy-loss functions. It causes an attenuation of the bulk term as b decreases i.e. as the beam moves towards the interface; this is called the *begrenzungs* (meaning 'limiting' in German) effect. The attenuation coincides with an increase in the interface term. For large values of $z = 2\omega b/v$, $K_0(z)$ behaves like $e^{-z}/\sqrt{z}$ while for small values, it has a more rapid logarithmic variation. Considering retardation effects, the differential scattering probability for a beam passing through medium ε_1 becomes (Garcia-Molina et al., 1985; Moreau et al., 1997; Wang, 1996),

$$\frac{d^2P}{dEdz} = \frac{e^2}{2\pi^2\varepsilon_0\hbar^2v^2}\int_0^{q_{y,c}} \mathrm{d}q_y \,\mathrm{Im}\left\{\left(-\frac{1-\varepsilon_1\beta^2}{\varepsilon_1\alpha_1}\right) + e^{-2\alpha_1|b|}\left(\frac{1-\varepsilon_1\beta^2}{\varepsilon_1\alpha_1}\right) + e^{-2\alpha_1|b|}\left(-\frac{2}{\varepsilon_1\alpha_2+\varepsilon_2\alpha_1}+\frac{2\beta^2}{\alpha_1+\alpha_2}\right)\right\}, \tag{2.21}$$

where $\beta = \frac{v}{c}$, $\alpha_1 = \sqrt{Q^2 - \frac{\varepsilon_1\omega^2}{c^2}}$, $\alpha_2 = \sqrt{Q^2 - \frac{\varepsilon_2\omega^2}{c^2}}$ and $Q^2 = q_y^2 + \left(\frac{\omega}{v}\right)^2$. The integration above is performed up to the cutoff $q_{y,c}$ to prevent divergence of the integral for the wavevector component $q_y \to \infty$. The first term in the curly brackets is the retarded bulk energy-loss function, while the second term is the begrenzungs term – negative of the first term and multiplied by an inverse exponential dependence on the distance of the beam from the interface – that causes the bulk term to attenuate towards the interface. The third term is the retarded interface energy-loss function and it is multiplied by the same spatial dependence as the begrenzungs term, although here that implies an increase in the interface term as the beam moves towards the interface.

Kröger derived the inelastic scattering probability, considering both bulk and surface effects, as well as transition radiation and retardation effects, when the electron beam transmits a thin-film of thickness t, with dielectric function $\varepsilon(\omega)$ (Kröger, 1968). It can be used to predict the angular and thickness dependence of different features in the energy-loss spectrum. These analytical expressions have been used to simulate vibrational energy-loss spectra from SiO_2 in Chapter 3. Analytical expressions cannot be obtained for the case of a thin-film consisting of an interface between two media with dielectric functions ε_1 and ε_2, considering volume, surface, and interface effects. In such and more complicated cases, it is convenient to solve Maxwell's equations numerically to obtain the induced electric field due to the interaction of a fast electron with an arbitrary shaped specimen. Various numerical methods have been employed to simulate the energy-loss spectrum, viz., boundary element method (BEM), discrete dipole approximation (DDA) method, finite-difference time-domain (FDTD) method, and finite element method (FEM) in frequency domain (Cao et al., 2015; Das et al., 2012; de Abajo & Howie, 2002; Geuquet & Henrard, 2010; Henrard & Lambin, 1996; Hohenester & Trügler, 2012; Raza et al., 2014; Wiener et al., 2013). In this dissertation, we use FEM in the frequency domain in COMSOL Multiphysics to numerically simulate the vibrational energy-loss spectra for various sample geometries. The Radio Frequency toolbox is used to solve the wave equation for the total electric field in the frequency domain. The fast electron beam is approximated as a charge localized at position $\boldsymbol{r}_e = (x_0, y_0, \boldsymbol{v}t)$ at time t, traveling with velocity $\boldsymbol{v}$ along the z direction. The current density produced by the electron can then be expressed as,

$$\boldsymbol{j}_e(\boldsymbol{r}, t) = -e\boldsymbol{v}\delta\big(\boldsymbol{r} - \boldsymbol{r}_e(t)\big) \tag{2.22}$$

$$\boldsymbol{j}_e(\boldsymbol{r}, t) = -e\boldsymbol{v}\delta(x - x_0)\delta(y - y_0)\delta(z - vt) \tag{2.23}$$

where $\delta(x)$ is the Dirac delta function. Taking the Fourier transform with respect to time yields,

$$j_e(\boldsymbol{r},\omega) = -ev\delta(x-x_0)\delta(y-y_0)e^{i\omega z/v} \tag{2.24}$$

The field of the electron beam induces an electromagnetic field in the material which acts back on the electron. Considering the induced electric field to be $\boldsymbol{E}^{ind}(\boldsymbol{r},t)$ and neglecting the perpendicular force on the electron due to its high velocity (Ritchie, 1957), the electron energy-loss can be expressed as,

$$\begin{aligned}\Delta E = e\int \boldsymbol{v}.\boldsymbol{E}^{ind}dt &= e\int v\,E_z^{ind}(\boldsymbol{r}_e(t),t)dt \\ &= e\int dt\int v\,E_z^{ind}(\boldsymbol{r},t)\delta\big(\boldsymbol{r}-\boldsymbol{r}_e(t)\big)d\boldsymbol{r}\end{aligned} \tag{2.25}$$

Combining Equations 2.22 and 2.25, the energy-loss can be expressed as,

$$\begin{aligned}\Delta E = -\int dt\int d\boldsymbol{r}\,E_z^{ind}(\boldsymbol{r},t)j_e(\boldsymbol{r},t) \\ = -\int d\boldsymbol{r}\int_{-\infty}^{\infty}dt\,E_z^{ind}(\boldsymbol{r},t)j_e(\boldsymbol{r},t)\end{aligned} \tag{2.26}$$

Using Parseval's theorem,

$$\int_{-\infty}^{\infty}dt f_1(t)f_2(t) = \frac{1}{\pi}\int_0^{\infty}d\omega\,Re[F_1(\omega)F_2^*(\omega)] \tag{2.27}$$

where $F(\omega)$ is the Fourier transform of $f(t)$, and applying it to Equation 2.26,

$$\Delta E = -\frac{1}{\pi}\int d\boldsymbol{r}\int_0^{\infty}d\omega\,Re\big[E_z^{ind}(\boldsymbol{r},\omega)j_e^*(\boldsymbol{r},\omega)\big] \tag{2.28}$$

Taking the conjugate of Equation 2.24 and substituting into Equation 2.28 yields,

$$\Delta E = \frac{ev}{\pi}\int_0^\infty d\omega \int dxdydz\, Re\left[E_z^{ind}(x,y,z,\omega)\delta(x-x_0)\delta(y - y_0)e^{-i\omega z/v}\right] \tag{2.29}$$

$$= \frac{ev}{\pi}\int_0^\infty d\omega \int dz\, Re\left[E_z^{ind}(x_0,y_0,z,\omega)e^{-i\omega z/v}\right]$$

The total energy-loss can be expressed in terms of a probability of inelastic scattering per unit energy-loss, $dP_{inelastic}/dE$, where $E = \hbar\omega$ is the energy-loss as,

$$\Delta E = \int_0^\infty E\frac{dP_{inelastic}}{dE}dE = \int_0^\infty \hbar^2\omega\frac{dP_{inelastic}}{dE}d\omega \tag{2.30}$$

Combining Equations 2.29 and 2.30 gives the probability of inelastic scattering per unit energy-loss as,

$$\frac{dP_{inelastic}}{dE} = \frac{ev}{\pi\hbar^2\omega}\int dz\, Re\left[E_z^{ind}(x_0,y_0,z,\omega)e^{-i\omega z/v}\right] \tag{2.31}$$

The right hand side expression in Equation 2.31 is evaluated numerically in COMSOL Multiphysics for any arbitrary material geometry. The material is defined by its frequency dependent optical dielectric function. All simulations are performed twice, once with the material defined by its corresponding dielectric function $\varepsilon(\omega)$ and once with the material defined as vacuum, preserving all other aspects of the model. The energy-loss probabilities obtained from the two cases are then subtracted to get the energy-loss from the interaction of the beam with the material. This also accounts for any artefacts due to the finite length of the electron beam in the model.

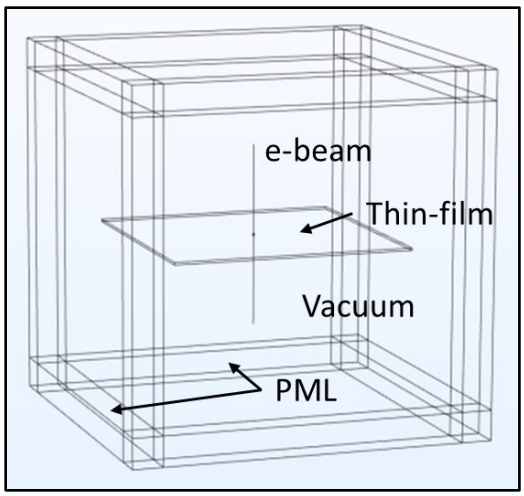

Figure 2.10. Geometrical arrangement for the numerical simulation of an energy-loss spectrum from a thin-film. The electron beam is considered to be a line of current that transmits the thin-film at normal incidence. The geometry is enveloped by Perfectly Matched Layers to attenuate any electric field at the boundaries.

An example of the geometrical arrangement in a typical EELS simulation is shown in Figure 2.10. The electron beam characterized by a straight line carrying an Edge Current $I = I_0 e^{i\omega z/v}$ passes through a rectangular slab specimen characterized by the dielectric function ε_{slab}. This is surrounded by a cube representing a vacuum environment with $\varepsilon = 1$, referred to as the simulation domain. Enveloping the cube are Perfectly Matched Layers (PML) which help attenuate the electric field at the simulation domain boundaries so that there are no unphysical field reflections. The simulation domain is divided into discrete elements using the Free Tetrahedral mesh, with a high density close to the electron beam, inside the slab and in areas of high field concentration and gradients, that is allowed to relax towards the simulation domain boundaries. The PML is divided with a Swept mesh having 5-10 layers. The dimensions of the mesh elements is dictated by the typical wavelengths involved in the simulation. The inelastic scattering probability per unit energy-loss can then be evaluated using Equation 2.31 directly with this software as an

Edge Probe, Integral along the electron's trajectory. Such numerical calculations were performed to simulate vibrational energy-loss spectra from SiO_2 in Chapter 4.

CHAPTER 3

THE INFLUENCE OF SURFACES AND INTERFACES ON HIGH SPATIAL RESOLUTION VIBRATIONAL EELS FROM SIO2

3.1 Motivation

As discussed in Chapters 1 and 2, this dissertation was motivated by the then-recent advances in monochromator design which allowed the detection of vibrational excitations with EELS in a STEM (Krivanek et al., 2014; Miyata et al., 2014). This opened up questions about the character of electron interactions that lead to the excitation of vibrational modes and the spatial resolution of the energy-loss signal generated by such an excitation. As also mentioned in Chapter 1, previous studies of vibrational excitations at different relevant material-surfaces with reflection-based HREELS gave insights about the character of electron interactions to excite vibrational modes. Importantly, these studies recognized two mechanisms of exciting vibrational modes with electrons – long-range Coulomb interactions of the incident electrons with the electron cloud in a chemical bond that polarizes the medium, called dipole scattering, and short-range interactions with the core electrons and nucleus of an atom in the bond, called impact scattering. These insights percolated into the STEM-based vibrational EELS community and early investigations set out with the objective to explore the dipole or impact character of the vibrational EELS signal. It was found in these studies that dipole scattering dominated the vibrational energy-loss spectrum in the forward scattering geometry, where the optic axis of the spectrometer is the same as the incident beam, and it was believed that the impact scattering signal was too weak to be detected in this configuration (Krivanek et al., 2014). The long-range interaction and small scattering angles associated with dipole scattering implied that the energy-loss signal was highly delocalized, and it was demonstrated

experimentally that this delocalization could be leveraged to detect the BN phonon in the aloof mode, where the beam is positioned outside the sample, yielding significant intensity even when the beam is 100 nm away from the sample (Govyadinov et al., 2017). It was proposed that collecting large-angle scattered electrons could be a way to enhance the strength of the impact scattered signal and it was experimentally demonstrated that high spatial resolution (~2 nm) BN phonon signals could be collected by shifting the detector to an off-axis configuration (Dwyer et al., 2016).

The question of spatial resolution for vibrational EELS was still not well understood at the beginning of this dissertation research and hence, required more experimental and theoretical exploration. An approach to determine the spatial resolution of a vibrational energy-loss signal was to study its variation across a specimen/vacuum surface or across an interface between two specimens. The comparison between spatial variation of the energy-loss signal and the HAADF signal could tell how delocalized the vibrational signal is; localized vibrational signals will trace the HAADF signal profile while delocalized signals would not. Many of the previous spatially-resolved vibrational EELS experiments were focused on material-surfaces where the long-range electric field associated with the fast electron is unscreened when the electron is in the vacuum (Govyadinov et al., 2017a; Lagos et al., 2017). It is also important to investigate the spatial dependence of the vibrational signal at materials interfaces where screening and relativistic effects may be important. In this chapter, the character and spatial variation of the SiO_2 vibrational signal at an abrupt SiO_2/Si interface is investigated in the forward scattering geometry. Dielectric theory is employed to understand how the vibrational excitation varies both in energy-loss and intensity at different locations on the sample. For the SiO_2 vibrational peak, the non-relativistic dielectric formulations give a reasonable description of the spatial variation of the signal with distance from the interface. The

predicted exponential dependence of the signal with distance from the interface shows that, in practice, nanometer resolution is achievable even though the scattering has a predominant long-range Coulomb character. We then explore the influence of retardation effects and interface excitations on the form of the vibrational spectrum with emphasis on the energy of the Si-O bond-stretch mode. Coupling of entrance and exit surfaces as well as interface effects lower the energy of the resonance by up to 20 meV and the interfacial peak shows nanometer localization.

3.2 Methods

3.2.1 Sample preparation

A clean room Si wafer was subjected to thermal oxidation at 900°C to obtain a 3 μm film of SiO_2 on the Si substrate. The oxidized wafer was then prepared for STEM EELS analysis by performing a lift-out procedure using a Ga-ion beam and an Omniprobe on the Nova 200 NanoLab (FEI) focused ion beam (FIB) combined with a scanning electron microscope (SEM). First, a 0.5 – 1 μm thick Pt line was deposited on the oxidized Si wafer using ion beam assisted chemical vapor deposition (CVD) to mark the region of interest and to protect the underlying region from being sputtered away during subsequent milling steps. Next, high beam currents of ~20 nA were used to mill away large amounts of material from the front of the region of interest, roughly ~2 μm away from the Pt line, using the "stair-step" cut. A rectangular cut was used to mill away material from the back of the region of interest. Finer probe sizes were subsequently used to thin the specimen to ~1 μm in thickness. As the target thickness was reached, the stage was tilted by 45° and ~1 nA beam current was used to undercut the bottom of the specimen along with ¾ of the left and right edges such that there was very little material holding the specimen. Next, the Omniprobe was positioned to touch the FIB milled specimen and the probe was welded to

the specimen using FIB CVD capabilities. Final FIB cuts were then performed with ~0.1 nA beam current and the milled specimen was cut free such that it was lifted out of the bulk material and was only attached to the Omniprobe. The probe/specimen assembly was then positioned next to a 3mm slotted Cu TEM half-grid with "posts" for attaching the specimen and FIB CVD was used to attach the specimen to the grid. The probe was then milled free from the specimen and conventional low-kV FIB milling practices were used to thin the specimen to electron transparency. Figure 3.1a shows a BF TEM image of the lift-out specimen. Its thickness measured using SEM approached ~100 nm near the edges and ~80 nm near the SiO_2/Si interface. The interface plane normal is parallel to the (001) crystallographic plane in Si while the electron projection zone axis is along the [110] crystallographic direction in Si.

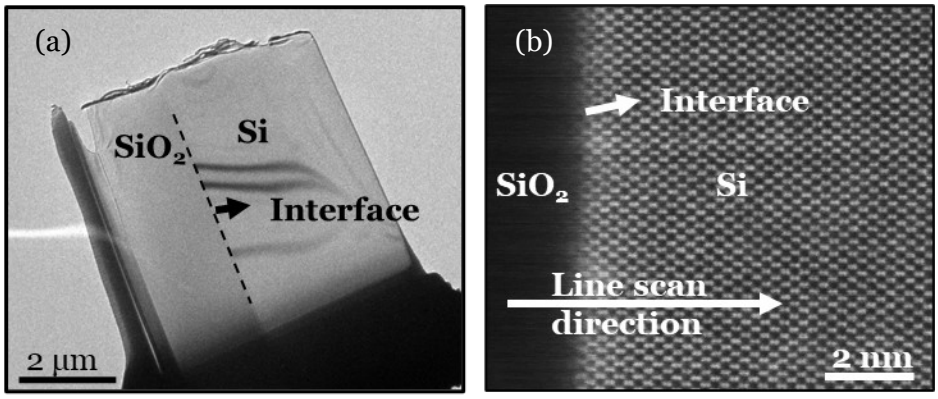

Figure 3.1. Bright field (BF) TEM image of the lift-out specimen is shown in (a). Atomic-resolution annular dark field (ADF) scanning TEM (STEM) image of the SiO_2/Si interface is shown in (b) – SiO_2 is amorphous whereas Si is crystalline.

3.2.2 Experimental EELS Acquisition

STEM EELS analysis on the specimen was performed using a NION UltraSTEM 100 aberration-corrected microscope equipped with a monochromator, operated at 60 kV (Krivanek et al., 2009; Krivanek et al., 2008). The probe convergence angle was either 15

or 30 mrad (15 mrad for a larger scan range, 30 mrad for the shorter one), and a 1mm spectrometer entrance aperture was used corresponding to a collection semi-angle of 15 mrad. Aberration correction of the magnetic lenses up to the fifth order helped in making probes of ~0.12 nm diameter with beam currents of ~100 pA (Krivanek et al., 2003). During the monochromated experiment, the probe size was ~1.6 nm, the beam current was ~10 pA, and energy resolution was 16 meV. An atomic-resolution annular dark-field STEM image of the SiO_2/Si interface in Figure 3.1b shows amorphous SiO_2 in contact with crystalline Si in the [110] projection. The image shows that the interface is atomically abrupt.

To map the spatial variation and determine the delocalization of the SiO_2 vibrational signal across the interface, typical EELS linescans were performed along the Si [001] crystallographic direction as shown in Figure 3.1b. Energy-loss spectra were recorded with step sizes ranging from 0.2 nm to 20 nm depending on the desired scan range. The linescan data was processed using the Gatan Microscopy Suite. A dispersion of 1 or 2 meV per channel was used to record the spectra. The spectra were calibrated by setting the center of the saturated zero-loss peaks to 0 meV. The uncertainty in energy position was the channel width i.e. ±1 meV (or ±2 meV depending on the dispersion used). In the energy-loss range of interest, each raw spectrum in a linescan has contributions to the background from the tail of the zero-loss peak. For background subtraction, a power law model of the form AE^{-r}, where E is the energy-loss with A and r as constant parameters, was fitted to two 20 meV windows just before and after the vibrational signal.

3.3 Results and Discussion

3.3.1 Vibrational EELS in SiO_2 and Si

Typical background subtracted spectra obtained after processing, when the beam is positioned in SiO_2 and Si respectively, far away from the interface (> 300 nm), are shown in Figure 3.2. Two vibrational signals are observed at ~144 meV and ~100 meV when the beam is in SiO_2. The ~144 meV signal is associated with an asymmetric Si-O "bond-stretching" mode wherein bridging O atoms move in the opposite direction relative to their Si nearest neighbors and parallel to the Si-Si lines. The ~100 meV signal is associated with

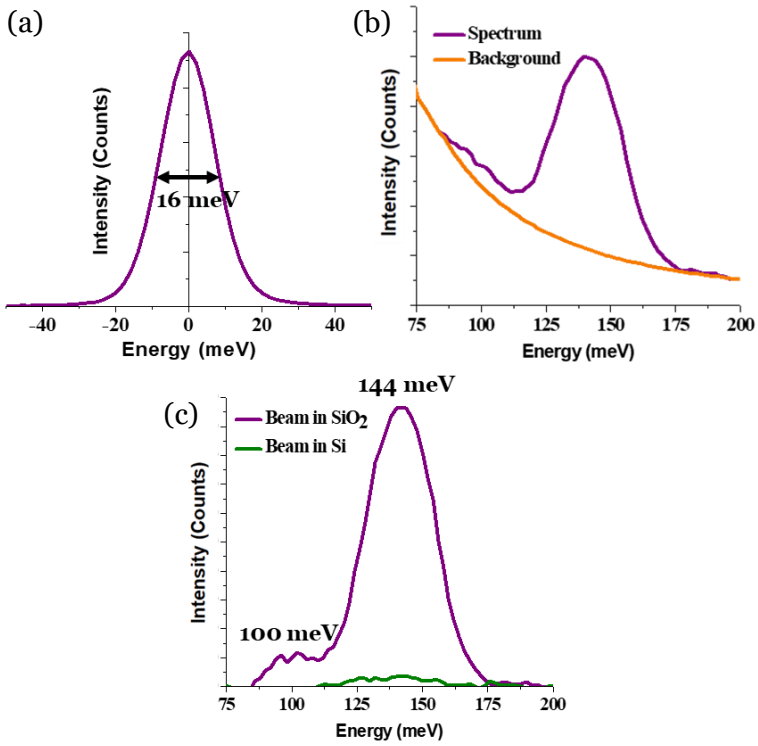

Figure 3.2. The experimental energy-resolution of 16 meV is demonstrated by the FWHM of an unsaturated ZLP, as shown in (a). (b) shows the power-law background subtraction routine used. Experimental vibrational signals obtained in the energy-loss region of interest in SiO2 and Si are shown in (c). A vibrational signal corresponding to the SiO2 "bond-bending" mode at ~100 meV and "bond-stretching" mode at ~144 meV are observed in SiO2. The signal in Si is from surface oxide layers.

a symmetric Si-O "bond stretching plus bending" mode wherein O atoms move approximately at right angles to the Si-Si lines and in the Si-O-Si planes (Hass, 1970). When the beam is in Si, a weak and broad peak is observed at ~144 meV which corresponds to the vibrational signal from surface oxide layers. No vibrational signal from Si was observed in the energy-loss range of interest.

To interpret the experimental data, classical dielectric theory was adapted using an optical dielectric function. There are many treatments of electron scattering for samples of different geometry with and without retardation effects (de Abajo, 2010). For example, the energy-loss probability for a non-relativistic electron moving with uniform velocity v crossing a single surface from vacuum into a specimen with relative frequency-dependent dielectric function $\varepsilon(\omega)$ is proportional to the bulk energy-loss function, $\mathrm{Im}\{-1/\varepsilon\}$, and a surface energy-loss function, $\mathrm{Im}\{-2/(1+\varepsilon)\}$, with an addition term that represents the begrenzungs effect which lowers the bulk energy-loss intensity (see section 3.3.2) (Raether, 1967, 1980). A non-retarded expression is given for an electron moving parallel to an interface between two infinite slab media having frequency-dependent dielectric functions $\varepsilon_1(\omega)$ and $\varepsilon_2(\omega)$ (Howie & Milne, 1985),

$$\frac{d^2P}{dzdE} = \frac{e^2}{2\pi^2\varepsilon_0\hbar^2v^2}\left\{Im\left(-\frac{1}{\varepsilon_1}\right)\times\ln\left(\frac{q_{\perp,c}v}{\omega}\right) + \left[-Im\left(-\frac{1}{\varepsilon_1}\right)+Im\left(-\frac{2}{\varepsilon_1+\varepsilon_2}\right)\right]\times K_0\left(\frac{2\omega b}{v}\right)\right\} \tag{3.1}$$

where ε_0 is the permittivity of free space, $q_{\perp,c}$ is the cut-off momentum transfer perpendicular to the electron velocity and is determined by the collection angle allowed by the spectrometer entrance aperture. This expression is proportional to the sum of the bulk energy-loss function of the medium the electron is passing through and a second term that

has a K_0 Bessel function dependence on the distance of the probe from the interface, often called the impact parameter, b. This second term consists of an interface energy-loss function, $\mathrm{Im}\{-2/(\varepsilon_1+\varepsilon_2)\}$, again in addition to a begrenzungs effect term.

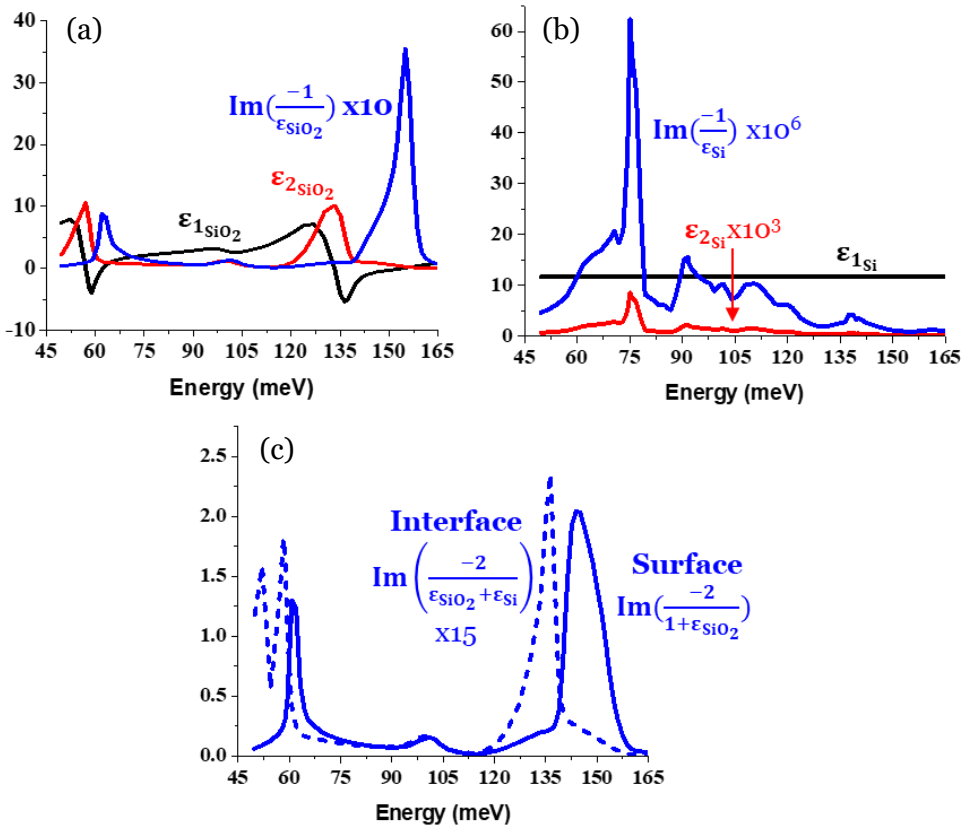

Figure 3.3. Real (ε_1) and imaginary (ε_2) parts of the dielectric functions and the bulk energy-loss functions (Im(-1/ε)) of SiO_2 and Si are plotted as a function of energy-loss in (a) and (b) respectively. The imaginary part of the dielectric function of Si is scaled by a factor of 10^3 while the energy-loss functions of SiO_2 and Si are scaled by a factor of 10 and 10^6, respectively. The vacuum/SiO_2 surface (solid line) and SiO_2/Si interface (dashed line) energy-loss functions are plotted in (c). The interface energy-loss function is scaled by a factor of 15.

These bulk, surface, and interface loss functions are important because they often approximate the form of the energy-loss spectrum when relativistic or polaritonic effects are small. The real and imaginary parts of the frequency-dependent optical dielectric function and the bulk energy-loss function for SiO_2 and Si are plotted in Figure 3.3a and

3.3b respectively (Palik & Ghosh, 1998). The bulk energy-loss function for SiO_2 has a maximum at 155 meV where $\varepsilon_{SiO_2}(\omega) = 0$, whereas that for Si is 10^5 times weaker in intensity as compared to SiO_2 due to a large real part and a small imaginary part of the optical dielectric function of Si. The vacuum/SiO_2 surface and SiO_2/Si interface energy-loss functions for this infinite slab geometry, plotted in Figure 3.3c, have their maxima at 144 meV and 136 meV, respectively. Note that the interface energy-loss function is scaled by a factor of 15.

The energy-loss spectrum can be calculated using the non-retarded (Equation 3.1) and retarded (Equation 3.2) infinite slab models. Specifically, if an electron (charge e) is moving along the z-direction (along the thickness) with a velocity v in an infinite medium characterized by the frequency-dependent optical dielectric function $\varepsilon_1(\omega)$ parallel to an interface with another infinite medium having optical dielectric function $\varepsilon_2(\omega)$, the differential energy-loss probability P per unit path length z for an energy-loss E including retardation effects is given by (Moreau et al., 1997; Wang, 1996),

$$\frac{d^2P}{dEdz} = \frac{e^2}{2\pi^2\varepsilon_0\hbar^2v^2}\int_0^{q_{y,c}} \mathrm{d}q_y \,\mathrm{Im}\left\{-\frac{1-\varepsilon_1\left(\frac{v}{c}\right)^2}{\varepsilon_1\alpha_1} + e^{-2\alpha_1|b|}\left(\frac{1-\varepsilon_1\left(\frac{v}{c}\right)^2}{\varepsilon_1\alpha_1}\right) - e^{-2\alpha_1|b|}\left(\frac{2}{\varepsilon_1\alpha_2+\varepsilon_2\alpha_1} - \frac{2\left(\frac{v}{c}\right)^2}{\alpha_1+\alpha_2}\right)\right\}, \tag{3.2}$$

where c is the speed of light in vacuum, ε_0 is the permittivity of vacuum, $\alpha_1 = \sqrt{Q^2 - \varepsilon_1\omega^2/c^2}$, $\alpha_2 = \sqrt{Q^2 - \varepsilon_2\omega^2/c^2}$ and $Q^2 = q_y^2 + (\omega/v)^2$. The electron is travelling in

the z-direction through medium ε_1, b is the impact parameter i.e. distance from the interface, q_y is momentum in the y (parallel to the interface) direction, and $q_{y,c}$ is the y momentum cutoff. The non-retarded approximation can be easily derived by letting $c \to \infty$. Simulated vibrational energy-loss spectra in SiO_2 and Si, at beam positions far away from the interface (> 300 nm), based on Equations (3.1) and (3.2), excluding and including retardation effects, are shown in Figure 3.4. The loss probability was integrated over the experimental collection angle of 15 mrad, and the simulated spectra were broadened with the instrumental response function to compare them with the experimental spectra of Figure 3.2. The simulations show the symmetric Si-O stretching plus bending mode at 100 meV in SiO_2, but the bond stretching mode is predicted to peak at 153 meV in both, the non-retarded and retarded simulations. The shift to 144 meV observed in the experimental energy-loss spectrum is the effect of the surface of the foil, which is discussed in Section 3.3. We observe that the non-retarded and retarded simulations of vibrational EELS in SiO_2 look almost the same.

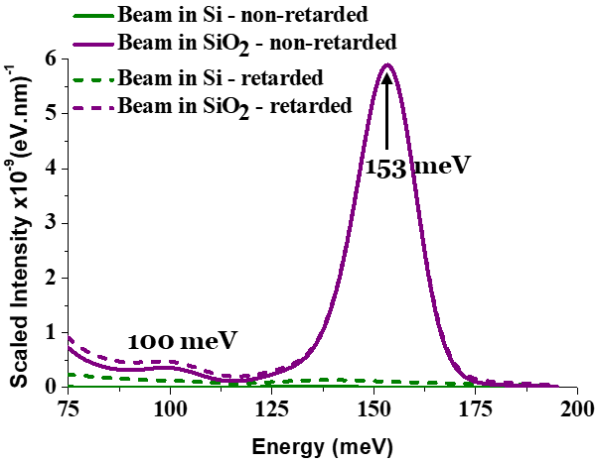

Figure 3.4. Simulations based on analytical solutions to the non-retarded (solid curves) and retarded (dashed curves) dielectric theories are shown in the figure. The Si-O "bond-bending" and "bond-stretching" vibrational signals are observed at 100 meV and 153 meV, respectively. All spectra are convoluted with the experimental energy resolution of ~16 meV.

As mentioned above, the loss function from Si is almost 10^5 times weaker than that from SiO_2, resulting in a simulated Si vibrational peak at 74 meV with very low intensity. However, a comparison between the retarded and non-retarded calculations (Figure 3.5) shows that retardation effects obscure the visibility of the dipole phonon signal in Si for an accelerating voltage of 60 kV. The reason for these large retardation effects is the high real part of the dielectric function for Si (~11.7) and in contrast, a very small imaginary part (of the orders of 10^{-3} and lower), which results in the relativistic velocity limit of the electron for no emission of Ćerenkov radiation to be 8.77×10^7 m/s (Jackson, 1999). This gives the limiting accelerating voltage for electrons to be ~23.4 kV, which is far lower than our accelerating voltage of 60 kV. Although this does not directly affect its intensity, a large Ćerenkov background statistically swamps the dipole phonon signal. Thus, under typical TEM experimental conditions, the dipole vibrational spectrum from Si will always be dominated by relativistic effects.

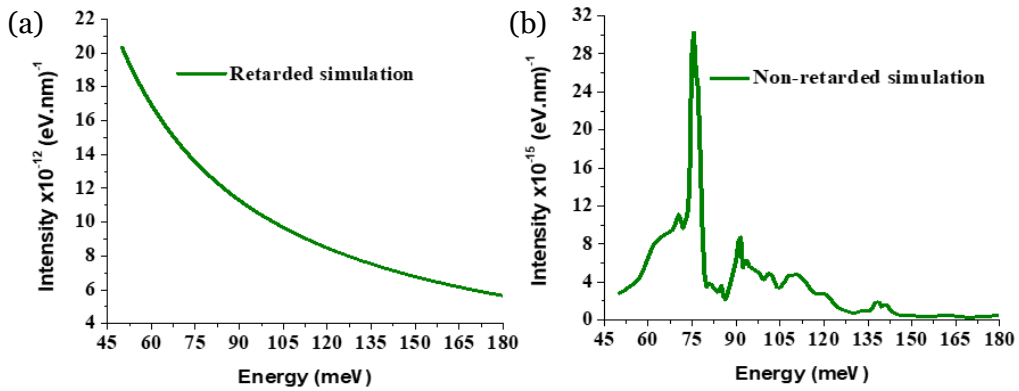

Figure 3.5. Simulated transmission EELS spectra when the beam is in Si with and without retardation effects are shown in (a) and (b) respectively. It is observed that (a) has three orders of magnitude more intensity than (b) and thus, retardation effects mask any inherent simulated dipole vibrational signal in Si.

3.3.2 Spatial variation of the 144 meV vibrational signal across the SiO_2/Si interface

To map the spatial variation of the 144 meV vibrational signal across the SiO_2/Si interface, the signal was integrated over a 15 meV window centered on the peak position and plotted against the distance of the probe from the interface in Figure 3.6. The background subtracted vibrational signal should be divided by the zero-loss peak intensity to account for differences in elastic scattering and thickness across the specimen. However, this could not be done since the center of the zero-loss peak is saturated. Therefore, the signal profile was normalized with respect to the negative tail of the zero-loss peak. Ignoring any weak energy-gain signal on the negative side of the peak, this tail is mainly proportional to the elastic scattering intensity. The integrated signal profile is constant and at a maximum far (> 300 nm) from the interface on the SiO_2 side, after which it starts to decrease and drops rapidly within 20 nm of the interface. The SiO_2 signal in the Si side comes predominantly from the presence of surface oxide layers. Close to the interface, there might also be contribution from the SiO_2/Si interface signal (section 3.3.4).

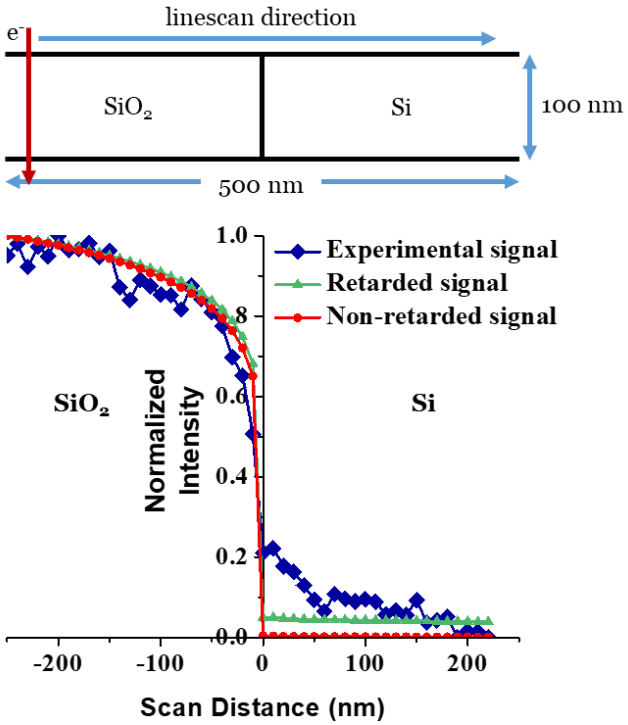

Figure 3.6. Spatial variation of the integrated 144 meV vibrational signal in SiO_2 and Si as a function of the distance of the electron probe from the interface is shown in the figure. The interface is at 0 nm and negative distance denotes that the electron probe is in SiO_2 while positive distance denotes that the electron probe is in Si. The signal in Si is due to surface oxide layers.

The infinite slab model was used to predict the spatial variation of the SiO_2 signal according to Equations (3.1) and (3.2). The non-retarded and retarded forms were integrated over a 15 meV energy-loss window centered at 153 meV and over the experimental collection angle of 15 mrad and are plotted over the experimental data in Figure 3.6. An agreement between the experimental and theoretical spatial variation profiles, based on both non-retarded and retarded dielectric theories, is also shown in the figure. This agreement demonstrates the dipole dominant nature of the experimental vibrational signal from SiO_2.

Note that the first term in Equations (3.1) and (3.2) corresponds to the retarded bulk energy-loss function in the medium where the electron is moving, which would peak

approximately at LO vibrational mode energy. The second begrenzungs term, has the same functional dependence but opposite sign as the bulk energy-loss function and is rapidly attenuated with increasing distance from the interface. Hence, as b tends to zero, the begrenzungs term increases and causes the Si-O bond-stretch vibrational signal to drop to zero at the interface. Note that the integrated signal initially falls slowly more than 200 nm from the interface and reaches 80% of its maximum value at 40nm from the interface. The final 50% drop occurs much more rapidly over only 5 nm. Thus, while delocalization causes a change in the SiO_2 signal more than 200 nm from the interface, the exponential dependence on impact parameter causes a rapid decay within only 5 nm of the interface. In effect, the width at half-maximum of the spatial variation profile of the integrated bond-stretch signal is only 5 nm while the width at $1/10^{th}$ maximum is ~100 nm. Again, it is observed that the non-retarded and retarded dielectric theories show almost similar spatial variations in SiO_2, suggesting that retardation effects in the energy-loss spectra are negligible for this material.

3.3.3 Entrance and exit surface coupling in thin-film SiO_2

The analytical expressions given in Equations (3.1) and (3.2) assume that the lateral dimensions of the specimen are infinite relative to the electron beam and that there are no losses associated with the entrance and exit surface of the TEM sample, both of which are not true for our specimen. If the thickness of the specimen is within an order of v/ω, where v is the incident electron velocity and ω is the energy-loss frequency, the infinite slab approximation breaks down and the transmitted electron loses energy to surface vibrational signals at a comparable probability to bulk vibrational signals (Egerton, 2011; Kröger, 1968; Ritchie, 1957). For an accelerating voltage of 60 kV and an energy-loss of 153 meV, $v/\omega \approx 600$ nm; thus, the transmitted electron in this experiment

(~100 nm sample thickness) should excite surface vibrational signals at a comparable probability to bulk vibrational signals.

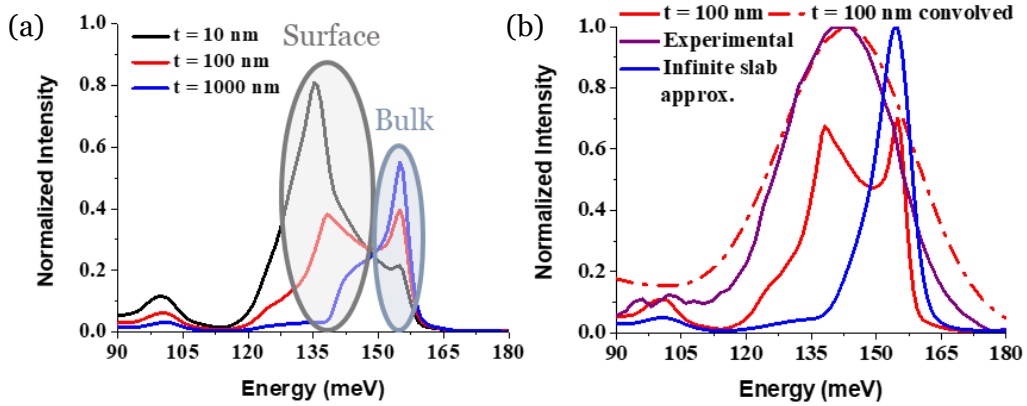

Figure 3.7. Simulated energy-loss spectra for SiO_2 thin-films of varying thicknesses (t = 10 nm, 100 nm, 1000 nm) shown in (a) demonstrate the domination of surface contribution over bulk for t ≤ 100 nm. The energy-loss spectrum for a 100 nm SiO_2 thin-film before (solid red) and after (dashed red) convolution with the experimental energy resolution of 16 meV is shown in (b). An agreement on signal energy position of the convolved spectrum and the experimental thin-film energy-loss spectrum (purple) is also shown. The blue curve refers to the simulated spectrum for an infinite slab geometry. All spectra were calculated for an electron beam accelerated at 60 kV and an experimental collection angle of 15 mrad.

At distances of 200 nm or greater from the SiO_2/Si interface, the experimental energy-loss spectrum will approximate the spectrum from a simple thin-film of SiO_2. For a thin-film geometry, the energy-loss probability contains three loss channels: a bulk energy-loss probability which would correspond to the beam in an infinite medium, a begrenzungs contribution and the surface energy-loss probability, both of which increase with decreasing film thickness. For slabs of thickness of the order of v/ω or less, the upper and lower surfaces are coupled which gives rise to symmetric and asymmetric guided slab modes (Heinz Raether, 1980). The Kröger formula (Kröger, 1968) predicts the inelastic scattering probability for a fast electron travelling through a thin-film having a frequency-dependent dielectric function $\varepsilon(\omega)$ in vacuum considering bulk, surface, and retardation

effects. Calculations based on the Kröger formula for the inelastic scattering probability of a fast electron transmitting a thin-film of SiO_2 in vacuum for varying film thicknesses (t = 10 nm, 100 nm and 1000 nm) as shown in Figure 3.7a reveal that as the thin-film thickness decreases the surface contribution increases at the expense of the bulk contribution. It is observed that for typical (S)TEM sample thicknesses of ≤ 100 nm, the contribution to the energy-loss spectrum from the surface dominates that from the bulk. Convolving the energy-loss probability for a 100 nm thick SiO_2 film with the experimental energy resolution of 16 meV gives, as shown in Figure 3.7b, an excellent agreement on the energy position of the experimental thin-film SiO_2 signal. This agreement between experiment and theory based on the optical dielectric function for SiO_2 demonstrates the dipole dominant character of the 144 meV vibrational signal.

3.3.4 SiO_2/Si interface vibrational signal

Within 5 nm of the SiO_2/Si interface, there is a shift in the thin-film peak position associated with the presence of the interface signal. Higher spatial resolution EELS linescans were performed with a pixel step size of 0.2 nm within a distance $|b| \leq 5$ nm of the SiO_2/Si interface to explore the spatial variation of the interface signal. As shown in Figure 3.8a, a shift is observed in the energy position of thin-film SiO_2 signal from 144 meV at 5 nm from the interface in SiO_2 to 136 meV at the interface. The energy position of the vibrational signal at the interface corresponds to the SiO_2/Si interface energy-loss function (Figure 3.3c). The linescan was decomposed into a linear combination of two reference experimental spectra using linear least squares regression. One reference spectrum was recorded far away (~300 nm) from the SiO_2/Si interface that contains the thin-film vibrational signal at 144 meV and the other recorded at the interface is dominated by the SiO_2/Si interface vibrational signal at 136 meV (the bulk signal should

be very small when the probe is positioned at the interface). Figure 3.8b and 3.8c show the decomposed thin-film SiO_2 and SiO_2/Si interface vibrational spectra in SiO_2 at an interval of every 1 nm within 5 nm from the interface. The spatial variation of the decomposed thin-film SiO_2 and SiO_2/Si interface signals in SiO_2 within 5 nm of the interface is shown in Figure 3.8d.

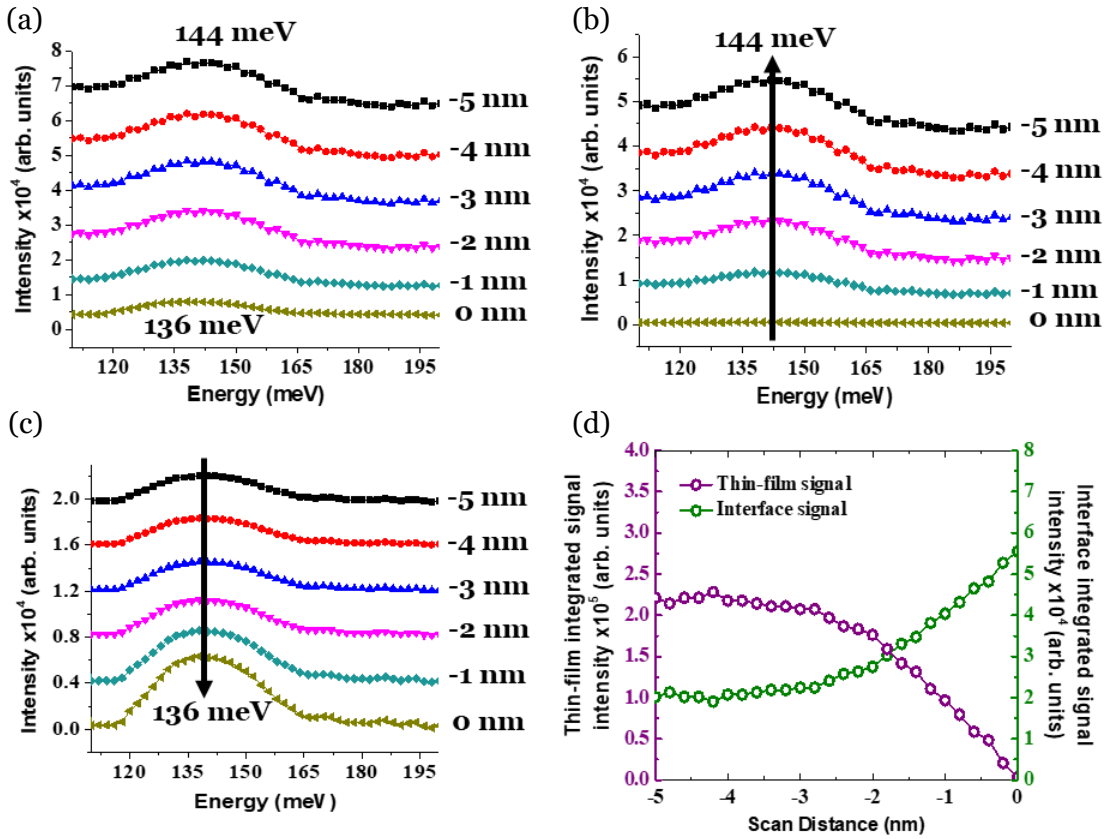

Figure 3.8. Variation in the energy position of the experimental vibrational signal in SiO_2 at 5 nm, 4 nm, 3 nm, 2 nm, 1 nm, and 0 nm from the SiO_2/Si interface is shown in (a). The signal is decomposed into thin-film SiO_2 and SiO_2/Si interface vibrational signals using linear least squares regression. The decomposed thin-film SiO_2 and SiO_2/Si interface vibrational signals are shown in (b) and (c) respectively. The spatial variation of the decomposed signals is shown in (d). The thin-film SiO_2 vibrational signal at 144 meV follows the begrenzungs effect while the interface SiO_2/Si vibrational signal at 136 meV increases in intensity up to the interface.

In agreement with the lower resolution linescan, the thin-film SiO_2 signal drops steeply to zero within 5 nm of the SiO_2/Si interface. A comparison of strength in Figure 3.3c shows that the SiO_2/Si interface energy-loss function is 15 times weaker than the bulk energy-loss function. Experimentally, Figure 3.8d shows that the maximum value of the interface signal is a factor of 4 weaker that the bulk signal strength at 5 nm. Far from the interface, the bulk signal would be a factor of two larger than the signal at 5 nm to give an experimentally measured bulk to interface signal ratio of a factor of 8. The factor of two discrepancy between theory and experiment (i.e. 15 versus 8) may be in part caused by the presence of thin oxide layers on the adjacent Si which are not considered in the analysis.

Even though the interface signal is weak, in practice Fig 3.8d shows that, it is localized to within a few nanometers of the interface because of the exponential dependence on impact parameter. Experimentally, the signal will only be easy to detect when the electron probe is within a few nanometers of the interface. This means that nanometer resolution probing of interfacial vibrational modes is possible even using long-range Coulomb scattering. This is a major finding of the current work and suggests that probing more complex interface modes with nanometer resolution should be feasible.

3.4 Conclusions

We have investigated the characteristics of the vibrational stretch signals in transmission STEM EELS from a thin film sample containing an abrupt SiO_2/Si interface. Specifically, the variation in energy and intensity of the signals with electron probe position is explored experimentally and theoretically. In the SiO_2 side, the main vibrational stretch signal is observed to lie in the range 136 – 144 meV depending on the position of the probe relative to the interface. The integrated intensity of the thin film SiO_2 signal shows an exponential drop as the probe approaches the interface. The spatial

variation can be accurately modelled using non-relativistic dielectric theory which predicts that the SiO_2 bulk signal intensity will be exactly zero when the probe is positioned on the interface. It is important to emphasize that the predicted intensity of zero at the interface for the bulk characteristic vibrational signal is fundamentally different from the typical nanoscale behavior of characteristic core-loss signals in EELS, which typically fall by 50 % when the probe is on the interface. This difference is caused by the begrenzungs effect which is characteristic of the dielectric theory. In this case, the bulk vibrational signal intensity shows a detectable decrease starting at 200 nm and it reaches 50% of its full value when the probe is within 5 nm of the interface. The intensity then falls sharply to zero over the remaining 5 nm.

The drop in the bulk vibrational signal is correlated with the rise of a much weaker interface vibrational response at 136 meV. The interface signal shows a maximum intensity at the interface and drops exponentially as the probe moves into the SiO_2. For the experimental conditions employed here, the interface signal is effectively localized to within 2 nm of the interface. In addition to shifts in the peak energy associated with the SiO_2/Si interface, surface effects can lead to changes in peak energy. The vibrational spectra for thin films typical of TEM samples are dominated by coupling of the entrance and exit surface excitations which, for the 100 nm thick sample employed here, give a peak energy that is 9 meV lower than the bulk peak.

In summary, this experimental and theoretical investigation of the bulk, interface and surface vibrational signals demonstrates that, in practice, monochromated STEM EELS allows nanometer resolution vibrational information to be obtained from materials interfaces even when the signal is dominated by long-range Coulomb interactions characteristic of dipole scattering. In the next chapter, we will theoretically investigate the

spatial variation of the coupled surface excitations by performing numerical calculations for the energy-loss probability as the electron beam is moved towards the SiO_2/vacuum edge surface of the thin-film. Then, we will explore the influence of patterning a SiO_2 thin-film with a 2x2 array of holes on the simulated vibrational energy-loss spectrum as the hole dimensions and separation are varied and as the electron beam is moved to different positions across to the array. Finally, we also present preliminary experimental results from performing vibrational EELS linescans from the center of the hole array to the center of one of the holes in an amorphous-carbon-coated patterned SiO_2 thin-film.

CHAPTER 4

CHARACTERIZING PHONON POLARITONS IN PATTERNED SiO_2 THIN-FILMS

4.1 Motivation

In the previous chapter, it was inferred that the energy-loss spectrum from a thin-film TEM specimen will have a significant contribution from the coupled entrance-and-exit-surface vibrational modes. This was simulated using analytical expressions derived by Kröger (Kröger, 1968) for the inelastic scattering probability for an electron beam transmitting a laterally-infinite thin-film of finite thickness at normal incidence, considering contributions from entrance and exit surface vibrations to the energy-loss probability. Analytical expressions used in the previous chapter are insufficient to theoretically determine the spatial variation of the bulk *and* the coupled entrance-and-exit-surface vibrational modes across an abrupt interface. In this chapter, we employ numerical, fully relativistic, classical electrodynamics simulations in a finite element method based software, COMSOL Multiphysics, to evaluate the induced electric field in the specimen by solving Maxwell's equations. This induced field is then used to determine the inelastic scattering probability per unit energy-loss ($dP_{inelastic}/dE$) as outlined in Section 2.2.

It is found that in addition to the phonon-phonon coupling between the beam-entrance and exit surface vibrational modes, there is a phonon-photon coupling between the surface vibrations and a narrow part of the broad frequency radiation electromagnetic field due to the fast electron (Jackson, 2012). These coupled phonon-photon modes are called surface phonon polaritons (SPhPs). The criterion responsible for this coupling is the opposite sign of the real part of the complex dielectric function of SiO_2 (negative) and

vacuum (positive) between 133 meV and 155 meV (referred to as a Restrahlen band in solid state physics). The coupled entrance-exit SPhPs are surface standing waves at the two vacuum/SiO_2 surfaces, whose electromagnetic fields decrease exponentially into both media. The spectral position of these SPhPs is strongly geometry dependent and can be determined by a thorough analysis of the momentum space (Konečná et al., 2018). It is seen that as the electron beam moves from the bulk towards a truncated surface in a SiO_2 slab, there is a coupling between the beam-entrance or the beam-exit and the truncated surface vibrations, resulting in the excitation of a different SPhP from the entrance-exit SPhP.

The wavelengths of SPhPs can be ten times smaller than the free-space photon wavelength for the same energy of excitation, and can thus be leveraged to control light beyond the diffraction limit (Dai et al., 2014). SPhPs are also attractive due to their potential in non-radiative heat transfer (Jones et al., 2013). An effective approach to control the excitation of the two aforementioned SPhPs would be to pattern a thin-film and characterize the excitation of these SPhPs at different positions of the electron beam relative to the pattern. This could be followed by subsequent optimization of the pattern such that specific regions support one SPhP while other regions support the other SPhP. In this chapter, the excitation of geometry-dependent SPhPs in a SiO_2 thin film patterned with a 2x2 array of holes will be investigated using numerical simulations performed in COMSOL Multiphysics based on the classical dielectric theory and the finite element method. The influence of changing hole dimensions and hole separation on the excitation of SPhPs at different electron beam positions will be explored. Preliminary experimental data will then be presented to qualitatively support the simulation results.

4.2 Methods

4.2.1 Numerical vibrational EELS simulations with COMSOL Multiphysics

As described in Section 2.2, the classical dielectric theory can be employed in the frequency domain with the Radio Frequency toolbox in COMSOL Multiphysics to determine the inelastic scattering probability per unit energy-loss for vibrational energy-loss events. The electric field induced by the fast electron in the material is evaluated numerically by breaking the entire simulation geometry into a large number of discreet elements using Free Tetrahedral meshing and solving Maxwell's partial differential equations for each element. The electron beam is characterized by a straight line carrying current $I = I_0 e^{i\omega z/v}$, where $I_0 = 100\, pA$ is roughly equivalent to the current in a typical monochromated EELS experiment, and the material is defined by its frequency-dependent complex dielectric function $\varepsilon(\omega)$.

Figure 4.1a shows the simulation set up for the electron beam transmitting a SiO_2 thin-film having lateral dimensions of 4 μm and thickness of 40 nm. The electron beam and thin-film are enclosed in a cube having a side of 5 μm which is known as the simulation box. This is enveloped by perfectly matched layers (PML) which help attenuate the electric field at the simulation domain boundaries so that there are no unphysical field reflections. The thin-film selection is assigned the optical dielectric function of amorphous SiO_2 which was obtained from the Handbook of Optical Constants (Palik & Ghosh, 1998) while the rest of the simulation domain is assigned a dielectric function $\varepsilon(\omega) = 1$, representing vacuum.

4.2.2 Sample preparation for electron microscopy

PELCO Silicon Dioxide support films for TEM with 40 nm membrane thickness were purchased from Ted Pella Inc. The support films consist of pure and amorphous SiO_2. They are manufactured using the PELCO 200 nm Silicon Nitride support films as a platform, which are 0.5 mm x 0.5 mm windows on a 3 mm Si frame. A 40 nm thick layer of amorphous SiO_2 is deposited on the Si_3N_4 membrane and the membrane is patterned into 24 apertures using advanced MEMS manufacturing technologies. Each aperture is etched back to the SiO_2 thereby leaving a 40 nm free-standing amorphous SiO_2 thin-film suspended by a 200 nm optically transparent Si_3N_4 support mesh, which is supported on a 3 mm Si frame. Such a grid with 24 apertures of 40 nm thick amorphous SiO_2 films was introduced into the Nova 200 NanoLab (FEI) FIB for making different patterns of holes in the thin-films using the Ga-ion beam. The thin-films were amorphous carbon coated before introduction into the FIB to avoid charging associated artefacts in SiO_2 during patterning.

4.2.3 STEM EELS acquisition

Electron microscopy measurements were performed using the Nion UltraSTEM 100, a dedicated aberration-corrected STEM equipped with a monochromator which reduces the energy spread of electrons ejected from the cold FEG source. Although the microscope can routinely form 1 Å sized probes with large convergence angles (~30 to 40 mrad), a smaller convergence angle of 19 mrad was employed along with a 1 mm spectrometer collection aperture corresponding to a collection semi-angle of 20 mrad to majorly excite dipole vibrational modes in SiO_2, and this degrades spatial resolution. Vibrational EELS linescans were performed in which energy-loss spectra were acquired at every pixel along the linescan and the pixel size was varied freely. The energy dispersion

during EELS acquisition was 0.68 meV per channel and exposure times were optimized for high signal-to-noise ratio in the vibrational energy-loss signals causing saturation of the ZLP maxima in all EELS acquisitions. The carbon-coated and patterned SiO_2 thin-film TEM sample was baked at 140°C for 12 hours prior to being loaded into the microscope to burn off all volatile hydrocarbons located on sample surfaces and prevent contamination. To explore the contribution of amorphous carbon to the vibrational spectrum from the patterned SiO_2 thin-film, EELS acquisitions were planned to be performed twice, once with the carbon coated sample and again after removing the carbon coating by subjecting the sample to 2 – 4 seconds of oxygen plasma and repeating this process ten times. However, EELS acquisitions after the removal of carbon-coating were not performed at the time of writing this dissertation and will be a part of future work. The energy-loss spectra were calibrated as described previously. Custom MATLAB codes were used to fit a Gaussian-Lorentzian function to the background preceding the signal of interest in a procedure similar to that used in the previous chapter. Other data processing was performed using the Gatan Microscopy Suite. Background subtracted energy-loss signals along a linescan were normalized with the negative edge of the ZLP to account for elastic scattering and thickness effects as done previously.

4.3 Results and discussion

4.3.1 SPhPs in truncated SiO_2 thin-films

Figure 4.1b shows two simulated energy-loss spectra between 120 and 170 meV, one obtained by performing numerical simulations in COMSOL Multiphysics as described in Section 4.2.1 and the other obtained using Kröger's analytical expression for a laterally infinite (4 μm) SiO_2 thin-film with 40 nm thickness. Both spectra are almost identical and show two peaks at 137 meV and 155 meV, which from the previous chapter can be

respectively assigned to the parallel SPhP and bulk modes (refer to Table 4.1 for label and mode description). The excellent agreement between the two spectra validates the COMSOL Multiphysics simulation, as it was demonstrated in the previous chapter that Kröger's analytical expression could be used to recreate the experimental dipole energy-loss spectrum for a 100 nm thick SiO_2 film, when the simulated spectrum was broadened with the instrumental response function.

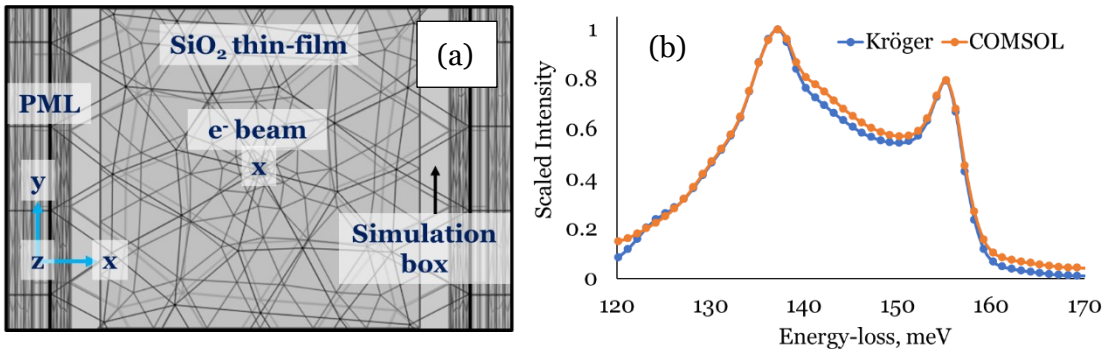

Figure 4.1. (a) Simulation set up for the electron beam transmitting a SiO_2 thin-film with 4 μm lateral dimensions and 40 nm thickness. The free-tetrahedral meshing employed to divide the simulation geometry into discreet elements is also shown. (b) Vibrational energy-loss spectrum from a 40 nm SiO_2 thin-film calculated analytically using Kröger's expression and numerically with COMSOL Multiphysics.

It is of interest to investigate how the excitation of different vibrational modes depends on the electron beam position as it is moved towards a truncated SiO_2/vacuum surface. Figure 4.2a shows a schematic representation of the simulation geometry employed to perform this investigation, while Figures 4.2b and 4.2c show simulated spectra obtained at the beam positions shown in 4.2a. Four beam positions are chosen with different impact parameter b, which is the distance of the beam from the truncated surface. In three of these, the electron beam is transmitted through the specimen while in the aloof spectrum, the beam is transmitted through vacuum, positioned 1 nm away from the truncated surface.

At b = 500 nm, the simulated spectrum looks quite similar to that obtained with the beam positioned at the center of the thin-film. The parallel SPhP and bulk modes are observed at 137 and 155 meV. This suggests that the electron beam is unable to sense the truncated surface when the distance between the two is 500 nm or more. As the beam moves to b = 100 nm, there is no change in the bulk intensity. However, the 137 meV peak splits into two, at 136 and 140 meV, accompanied by a decrease in peak intensity. This peak splitting can be interpreted as a change in coupling due to the ability of the beam to sense a third surface. The introduction of the truncated surface causes a decoupling of the parallel SPhP, and favors the weak coupling between SPhPs at the beam-entrance or exit surface and the truncated surface, referred to as the orthogonal SPhP at 136 meV (Table 4.1). Simultaneously, it also causes the excitation of the uncoupled SPhP at 140 meV. At b = 1 nm, the bulk peak intensity decreases by ~30% from the previous spectrum due to the begrenzungs effect, while the orthogonal SPhP increases in intensity and shifts to 137 meV – its limiting energy, confirming the above interpretation. There is no excitation of the uncoupled or the parallel SPhP. When the beam moves into aloof mode with b = 1 nm, there is negligible excitation of the bulk vibration. However, the excitation of the orthogonal SPhP is almost as strong it was in the previous spectrum (in transmission mode with b = 1 nm).

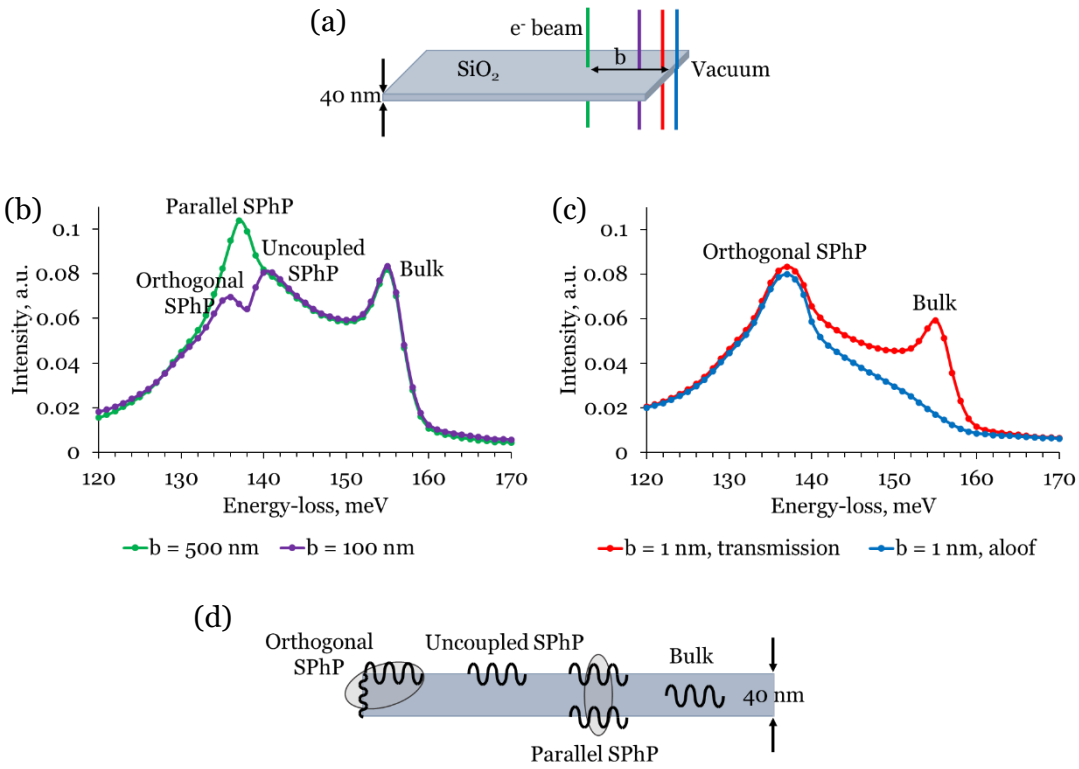

Figure 4.2. (a) Schematic of the simulation geometry showing the beam positions for subsequent calculations. (b), (c) Simulated vibrational energy-loss spectra at the beam positions shown in (a). (d) Schematic representation of the different modes observed as the beam moves towards the truncated surface.

Label	**Mode description**	**Energy, meV**
Bulk	Bulk Si-O vibrational stretch	155
Uncoupled SPhP	SPhP from a single uncoupled surface	142
Parallel SPhP	Coupling between SPhPs at the beam-entrance and beam-exit surfaces	137
Orthogonal SPhP	Coupling between SPhPs at the beam-entrance or beam-exit surface and the truncated surface	137

Table 4.1. Different vibrational modes excited in the truncated SiO_2 thin-film.

4.3.2 Simulating vibrational EELS in a patterned SiO_2 thin-film

4.3.2.1 Changing hole radius

In order to investigate the influence of patterning a 40nm thick SiO_2 film on the excitation of the different SPhPs, a 2x2 array of holes was constructed at the center of the thin-film geometry, as shown schematically in Figure 4.3a. The electron beam was placed at two positions, the center of the 2x2 array (depicted as C) and the midpoint of the line segment joining the centers of two adjacent holes (depicted as M). Hole radius was varied to be 60 nm, 75 nm, and 90 nm, while the center-to-center separation between two adjacent holes was kept constant at 200 nm. Simulated spectra obtained as the hole radius was varied with the electron beam placed at the two mentioned positions are shown in Figure 4.3b and 4.3c. All simulated spectra show peaks corresponding to the four vibrational modes shown in Table 4.1 for the truncated thin film. However, the details of relative intensities and spectral positions of the peaks is strongly influenced by the pattern geometry.

When the beam is at C (Figure 4.3a), the bulk peak (155 meV) is not affected by a change in hole dimensions because even for the largest hole radius of 90 nm, the nearest hole surface is >50 nm away from the electron beam. Thus, the begrenzungs effect does not attenuate the signal enough to see a significant intensity difference. Unlike the bulk peak, there is a monotonic increase in intensity in both the polariton peaks with a decreasing hole radius. Decreasing the hole radius while keeping the hole separation constant implies that the hole surfaces are gradually shifting away from the electron beam. Thus, for the uncoupled SPhP (142 meV), an increase in intensity with decreasing hole radius is expected due to an increase in the available surface area for the polariton to exist. The 136 meV peak also increases as the hole surfaces move away from the beam,

suggesting that it is associated more with the parallel SPhP and less with the orthogonal SPhP. If it were associated more with the orthogonal SPhP, the peak intensity would decrease as the surfaces move away. The peak intensity increases due to more efficient coupling in the parallel SPhP.

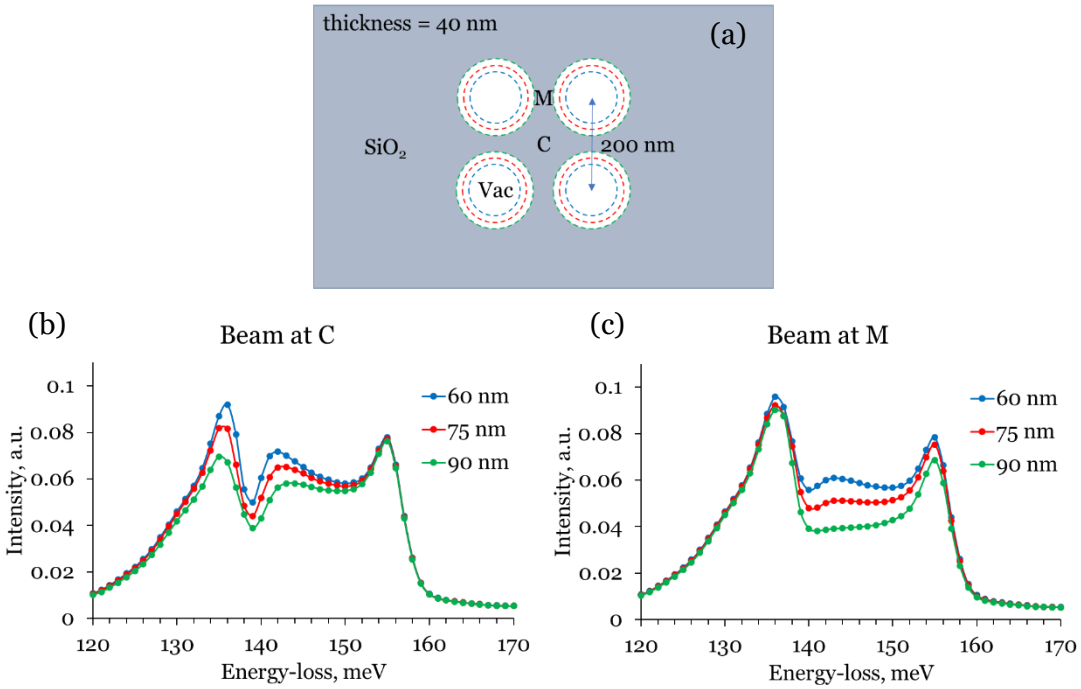

Figure 4.3. (a) Schematic of the simulation geometry showing the two electron beam positions (marked by 'C' and 'M') relative to the array. (b), (c) Simulated vibrational energy-loss spectra at the two beam positions as the hole radius was varied to be 60, 75 and 90 nm. Hole separation was kept constant at 200 nm.

The contribution from the orthogonal SPhP to the 136 meV peak can be deduced by comparing Figures 4.3b and 4.3c. The peak intensity increases when the beam is moved from position C to M. This effect is largest for the largest hole radius due to a more drastic decrease in the distance of the beam from the hole surface when it is moved from position C to M (from 51 to 10 nm for 90 nm hole radius, 66 to 25 nm for 75 nm hole radius, and 81 to 40 nm for 60 nm hole radius).

When the beam is at position M, there is an appreciable drop in the bulk peak as the hole radius is increased from 60 to 90 nm due to the begrenzungs effect. The uncoupled SPhP peak intensity increases with decreasing hole radius due to an increase in surface area. The increase in the 136 meV peak with decreasing hole radius is due to the increase in the parallel SPhP contribution to the signal.

4.3.2.2 Changing hole separation

Simulations were also performed by increasing hole separation while keeping the hole radius constant at 75 nm, as shown schematically in Figure 4.4a. Simulated spectra obtained as the hole separation is increased from 200 to 400 nm are shown in Figures 4.4b and 4.4c. When the beam is at position C, there is no effect on the bulk peak intensity as the hole separation increases, which is expected, as the hole surfaces are 66, 137 and 208 nm away from the electron beam for separations of 200, 300 and 400 nm respectively, which implies that the begrenzungs effect is not at play. The 136 meV peak intensity has a much stronger contribution from the parallel SPhP than the orthogonal SPhP due to which its intensity remains unchanged as the separation is increased. The uncoupled SPhP demonstrates increased coupling as the hole separation increases, as it increases in intensity and shifts from 142 to 139 meV.

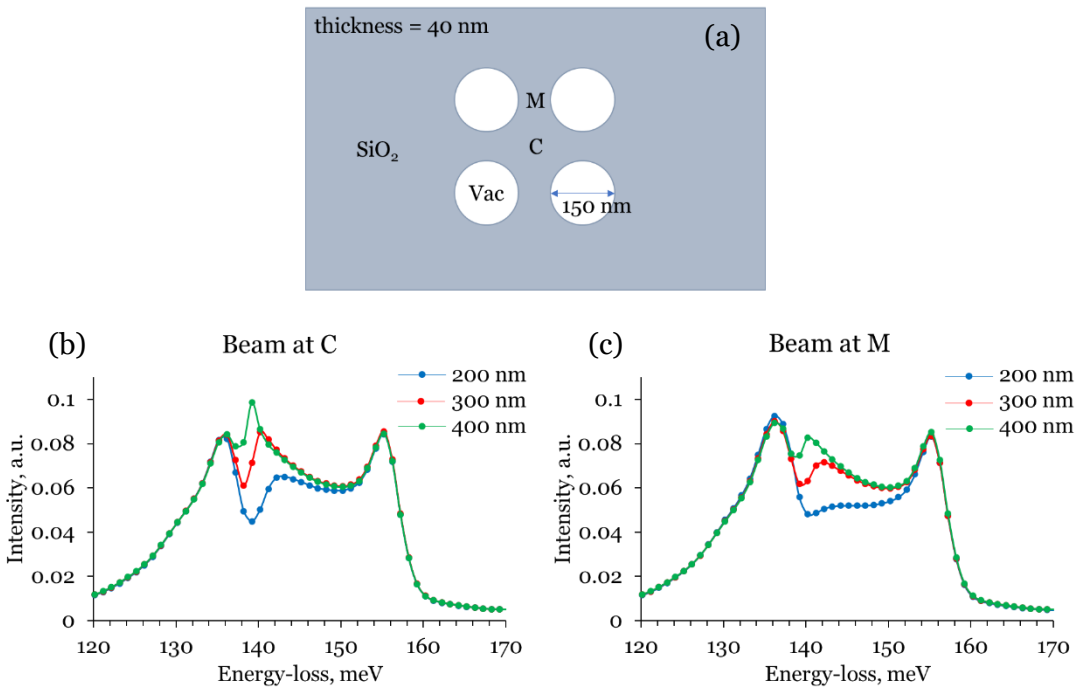

Figure 4.4. (a) Schematic of the simulation geometry showing the two electron beam positions (marked by 'C' and 'M') relative to the array. (b), (c) Simulated vibrational energy-loss spectra at the two beam positions as the hole separation was varied to be 200, 300 and 400 nm. Hole radius was kept constant at 75 nm.

When the electron beam is at position M, the bulk peak intensity remains unchanged due to its negligible attenuation by the begrenzungs effect as the hole surfaces are quite far from the beam for all three hole separations. The 136 meV peak intensity increases slightly as the hole separation decreases from 400 to 200 nm which might be due to an increased orthogonal SPhP contribution. As the hole separation increases from 200 to 400 nm, the uncoupled SPhP demonstrates increased coupling as it increases in intensity and shifts from 142 to 140 meV.

Thus, patterning the thin-film with an array of holes creates an interesting interplay in the excitation of the uncoupled, parallel, and orthogonal SPhPs. When the electron beam is at position C, it facilitates excitation of the parallel *and* uncoupled SPhPs

strongly while exciting the orthogonal SPhP very weakly. As the hole surfaces move away from the electron beam either due to decreasing radius or increasing separation, there is an increased excitation of the parallel SPhP, evident in the increasing 136 meV peak intensity as the hole radius decreases and in the shift in spectral position of the uncoupled SPhP peak as the hole separation increases. The orthogonal SPhP contribution to the 136 meV peak is evident from the increase in peak intensity when the electron beam is moved from position C to M for all simulations. When the beam is at position M, the uncoupled SPhP peak increases in intensity with increasing hole separation and shifts towards 139 meV, demonstrating increased coupling. The bulk peak intensity is strongly attenuated by the begrenzungs effect only when the electron beam is positioned less than 10 nm from the hole surface.

4.3.3 Position dependent vibrational EELS simulations in a patterned SiO_2 thin-film

Now that the influence of hole radii and separation has been investigated, vibrational spectra are simulated as the electron beam is moved around different positions relative to the 2x2 hole array pattern. The hole radius and separation are kept constant at 75 and 200 nm, respectively. The electron beam is moved in three principal directions – from position C to the center of a hole (*diagonal* linescan), from position C to M (*vertical* linescan), and from position M to an adjacent hole center (*horizontal* linescan). A schematic of the simulation geometry for the diagonal linescan is shown in Figure 4.5a and the simulated spectra obtained at the depicted beam positions (impact parameter in legend) are shown in Figure 4.5b. Positive impact parameters denote transmission mode and negative ones denote aloof mode.

The bulk peak behaves as expected from the analysis in the previous sections; there is an appreciable drop in its intensity in the transmission mode only when the beam is at position 3, while it is negligible in intensity in the aloof mode. The 136 meV peak also behaves as expected; its intensity increases as the beam steps towards the hole surface in both transmission and aloof mode due to an increase in the contribution from the orthogonal SPhP.

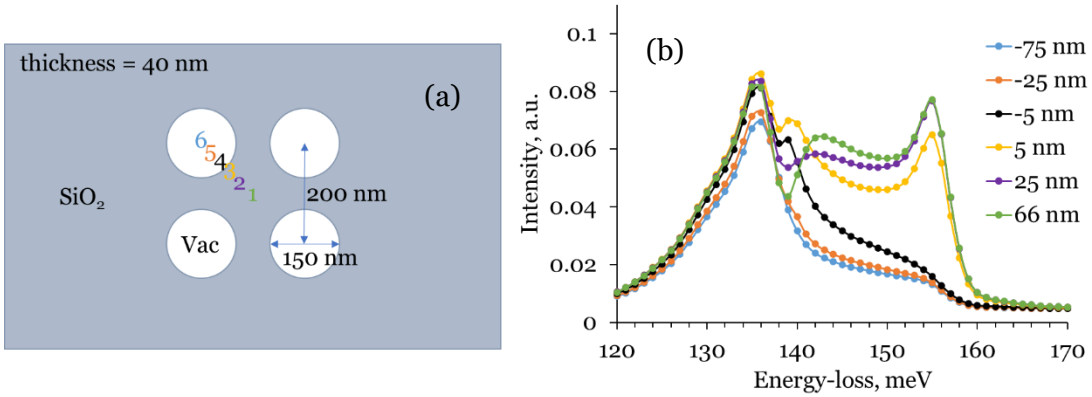

Figure 4.5. (a) Schematic of the simulation geometry showing electron beam positions along a diagonal linescan at which spectra were simulated when the hole radius and separation were 75 nm and 200 nm, respectively. (b) Simulated vibrational energy-loss spectra at the positions shown along the linescan. Impact parameters are shown in legend; positive ones denote transmission while negative ones denote aloof.

The peak flanked by the 136 and 155 meV peaks shows unexpected behavior as the beam position changes. When at position 1, a strong uncoupled SPhP peak is seen at 142 meV. When at position 2, this peak intensity decreases due to inefficient excitation of the uncoupled SPhP caused by the beam stepping closer to the hole surface. This is expected from the truncated thin-film analysis. However, when the beam shifts to position 3, the 142 meV peak vanishes and is replaced by a more intense and sharper peak at ~139 meV. This new peak is also present when the beam shifts to position 4, although its intensity is weaker. As beam moves to positions 5 and then 6, the 139 meV peak ceases to exist. The

origin of this new peak is under investigation. One hypothesis is that the peak arises due to constructive interference between SPhPs propagating towards the hole surface and those reflected by this surface when the beam is very close to it (Konečná et al., 2018). A similar constructive interference argument can also be made for the aloof beam case. More simulations will be performed in the future to test this hypothesis.

A schematic of the simulation geometry for the vertical linescan is shown in Figure 4.6a and the simulated spectra obtained at the depicted beam positions are shown in Figure 4.6b. All spectral features can be interpreted from the truncated thin-film analysis. As the beam moves from position 1 to 5, the bulk peak remains largely unaffected as the hole surfaces are 25 to 66 nm away from the beam and the begrenzungs effect is not at play. The uncoupled SPhP peak decreases in intensity due to a decrease in the surface area for the polariton to exist. Finally, the 136 meV peak increases in intensity due an increased contribution from the orthogonal SPhP.

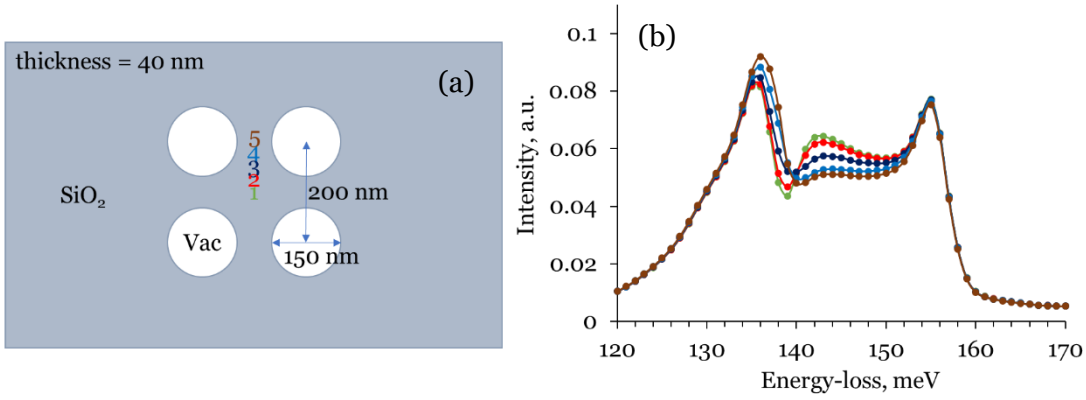

Figure 4.6. (a) Schematic of the simulation geometry showing electron beam positions along a vertical linescan at which spectra were simulated when the hole radius and separation were 75 nm and 200 nm, respectively. (b) Simulated vibrational energy-loss spectra at the positions shown along the linescan.

A schematic of the simulation geometry for the horizontal linescan is shown in Figure 4.7a and the simulated spectra obtained at the depicted beam positions are shown in Figure 4.7b. The bulk peak intensity drops due to the begrenzungs effect as the beam moves from position 1 to 2, after which it is negligibly excited as the beam moves into aloof mode. The 136 meV peak intensity remains unchanged when the beam moves from position 1 to 2, implying that most of the contribution to the peak is from the parallel SPhP. The peak intensity decreases with increasing impact parameter in the aloof mode, which is expected. The uncoupled SPhP peak is weakly excited only at position 1. At position 2, there is a small bump at 141 meV which is hypothesized to be due to the aforementioned constructive interference between the excited SPhPs and their reflected counterparts. More simulations will be performed in the future to investigate the origins of this peak.

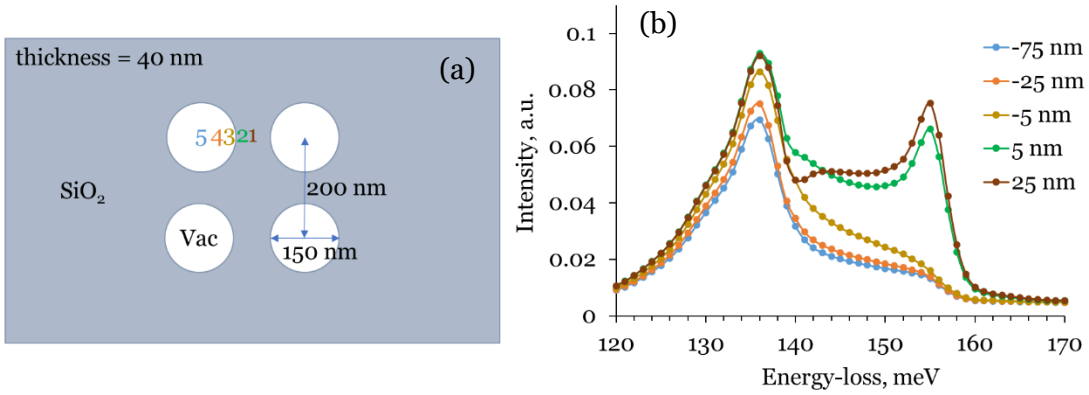

Figure 4.7. (a) Schematic of the simulation geometry showing electron beam positions along a horizontal linescan at which spectra were simulated when the hole radius and separation were 75 nm and 200 nm, respectively. (b) Simulated vibrational energy-loss spectra at the positions shown along the linescan. Impact parameters are shown in legend; positive ones denote transmission while negative ones denote aloof.

4.3.4 Experimental EELS from a patterned SiO_2 thin-film

Preliminary EELS acquisitions were performed as described in Section 4.2.3 on a pristine SiO_2 thin-film of 40 nm thickness and an amorphous-carbon (aC) coated SiO_2 thin-film before and after patterning with a 2x2 array of slightly elliptical holes. The short and long axis length of the holes are 150 and 200 nm, respectively, and the hole separation is ~250 nm. Figure 4.8 shows the background-subtracted vibrational spectra from the pristine and aC-SiO_2 thin-film (before patterning) between 20 and 200 meV. The pristine thin-film spectrum shows two strong signal peaks at ~58 and 139 meV which correspond to SPhPs in the thin-film associated with the Si-O-Si rocking mode and the asymmetric Si-O stretching mode respectively, and a weak peak at ~100 meV which corresponds to the symmetric Si-O stretching and deformation bulk mode (Lagos et al., 2018; Venkatraman et al., 2018b; Konečná et al., 2018; Li et al., 2019). The parallel SPhP and bulk peaks at 137 and 155 meV are broadened with the instrumental response function, which results in a single peak at 139 meV with a strong shoulder at 148 meV. The spectrum from the aC-SiO_2 thin-film looks similar to that from the pristine thin-film near the ~58 and 100 meV peak, but has a different shape near the ~139 meV peak. The peak for the higher energy-loss signal is now at ~146 meV with a strong shoulder at ~135 meV. The reversal in intensities of the bulk and surface peaks from the two specimens could be due to the increase in the film thickness due to the carbon coating. The shift in their spectral positions will be explored as a part of future work on this dissertation.

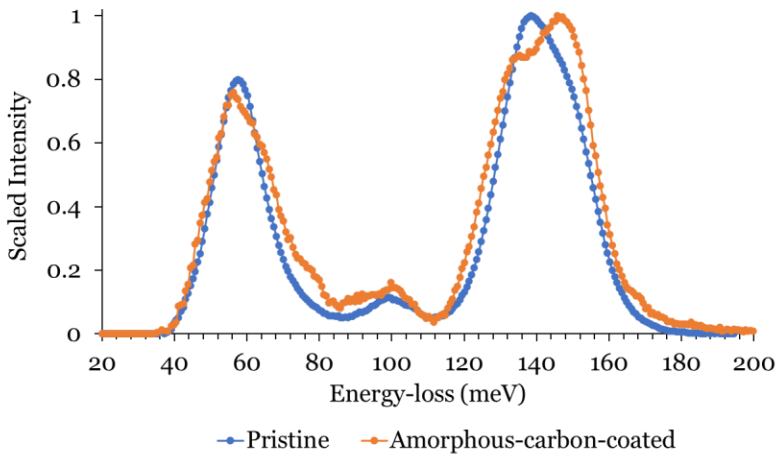

Figure 4.8. Experimental background-subtracted vibrational energy-loss spectra from a pristine and aC-SiO_2 thin-film. Probe convergence and spectrometer collection semi-angles were 19 and 20 mrad, respectively.

Diagonal EELS linescans were performed across the 2x2 array of holes in the aC-SiO_2 thin-film. As the simulations discussed earlier were focused on 120 to 170 meV as the region of interest, parametric background subtraction for experimental spectra was performed after the ~100 meV bulk peak. Figure 4.9a shows a monochromated ADF STEM image of the patterned thin-film with the dark contrast depicting the holes and the bright contrast depicting aC-SiO_2. A linescan was performed along the solid red line and vibrational spectra from beam positions depicted on the linescan are shown in Figure 4.9b. The spectrum from position 1 shows a peak at ~147 meV with a strong shoulder at ~130 meV, which could be a convolution of the bulk, parallel, and uncoupled SPhP modes. At position 2, the spectrum intensity decreases, however the shape and spectral positions of the observed peaks remains unchanged. At position 3, the spectrum intensity decreases drastically and there is a reversal in the intensity of the two peaks. The spectral positions of the two peaks changes to ~138 and ~150 meV. In addition to the begrenzungs effect for the bulk peak, this could be due to an increased excitation of the orthogonal SPhPs and a decreased excitation of the parallel and uncoupled SPhPs. As the beam goes into the

vacuum (positions 4 and 5), the lower energy-loss peak first shifts to ~136 meV and then to ~134 meV. The reason for this shift has not been explored yet.

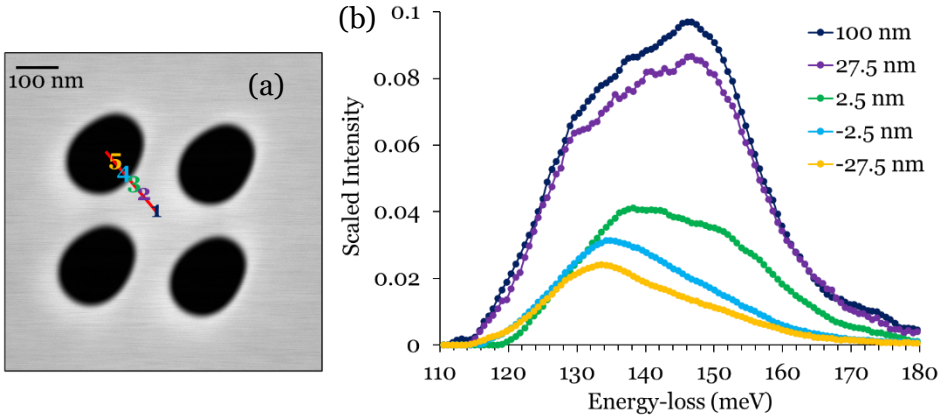

Figure 4.9. (a) Monochromated ADF STEM image of the 2x2 hole-array pattern showing the experimental diagonal linescan direction (red line). (b) Background-subtracted vibrational energy-loss spectra from the depicted positions along the diagonal linescan. Impact parameters are shown in legend; positive ones denote transmission while negative ones denote aloof.

Thus, preliminary experiments show that patterning of the thin-film influences vibrational EELS from SiO_2 in a complicated manner, as also seen in the simulations presented earlier. Although some observations can be qualitatively explained from the understanding developed through simulations, the experimental results need to be analyzed in further detail for accurate interpretation. It is desirable to perform experiments on SiO_2 after removing the aC-coating since it will be more directly comparable with the simulations. The influence of the aC-coating on the excitation of SPhPs also remains to be explored theoretically.

4.4 Conclusion

In this chapter, we have investigated the influence of patterning a SiO_2 thin-film with a simple array of holes primarily using numerical simulations based on the classical dielectric theory and the finite element method. It is seen that SiO_2 supports SPhPs whose excitation is strongly geometry dependent and whose intensity and spectral positions are a strong function of the beam position relative to various specimen features. Simulations demonstrate that the truncated SiO_2 film surface affects spectral features relative to the laterally infinite film by causing a decoupling in the parallel SPhP and introducing the orthogonal SPhP when the beam can sense the truncated surface. It is also observed that a simple array of holes has a strong influence on spectral features and complicates interpretation further. The influence of varying three different parameters was considered – hole radius, hole separation, and beam position relative to the holes, the findings of which can be summarized as follows:

1. The electron beam can excite the parallel *and* uncoupled SPhPs simultaneously as two separate signals in the patterned thin-film. The uncoupled SPhP is pretty straight-forward to interpret; its intensity increases with increasing surface area. Evidence of increased coupling can be seen when the hole surfaces move more than 100 nm away from the beam, and at such and larger impact parameters, the spectrum starts to evolve towards that from a laterally infinite thin-film.

2. The parallel SPhP is the major contributor to the 136 meV peak as long as the beam is >10 nm away from a hole edge.

3. The orthogonal SPhP contributes very weakly to the spectrum and is effective only when the beam is moved very close to the hole surface (<10 nm impact parameter).

4. When the beam is within 5 nm from the hole surface, interference between excited SPhPs and those reflected from hole surfaces might result in a new spectral peak at a completely different spectral position. The intensity and spectral position of this interference peak might be greatly influenced by the distance of another hole surface from the beam.

Preliminary EELS acquisitions from the pristine and aC-coated SiO_2 films show that carbon coating might affect the spectral position of the polariton signal in addition to the thickness effect resulting in a reversal of the polariton and bulk peak intensities. Thus, it is desirable to perform experiments after removing the carbon-coating to validate simulations. Also, in order to accurately interpret experimental spectra from the aC-SiO_2 patterned film, simulations need to be performed by accounting for the response from aC and its effect on the SPhPs. Both of these investigations will be carried out as future work on this project.

Till this chapter, dipole energy-loss signals in the transmission mode which are excited due to long-range Coulomb interactions with the electron cloud were the point of focus. In the next two chapters, short-range interactions between the electron beam and core of an atom which yield impact energy-loss signals will be explored.

CHAPTER 5

ATOMIC RESOLUTION VIBRATIONAL SPECTROSCOPY WITH ELECTRON IMPACT SCATTERING

5.1 Motivation

Atomic vibrations control all thermally activated processes in materials including ionic, atomic and electron diffusion, heat transport, phase transformations, and surface chemical reactions. Atomic and molecular heterogeneities such as interfaces and adsorbates, and defects such as vacancies, interstitials, dislocations, and grain boundaries often regulate kinetic pathways and are associated with vibrational modes that are substantially different from bulk modes. The jump frequency characterizing thermally activated processes is of great practical importance and is determined by the local phonon and molecular vibrational modes of the system. High spatial resolution vibrational spectroscopy is required to probe these local modes.

As seen in Chapter 1, high spatial resolution vibrational spectroscopy can be performed in a monochromated STEM using EELS. There are several experiments demonstrating that a vibrational energy-loss signal is spatially resolved to tens of nm, with a few showing resolution of tens of Å. However, prior to this work, there has been only one experimental demonstration of atomic resolution in energy-filtered images that include contributions from phonons (Hage et al., 2019). To perform atomic resolution vibrational EELS, the experiment must allow scattered electrons spanning a range of angles up to at least a Bragg angle to interfere (Spence, 2009). For a STEM, this challenge can be addressed by appealing to the reciprocity principle first described by Cowley (Cowley, 1969). In STEM, an electron probe smaller than a (hkl) Miller plane spacing can only be formed if the incident electron beam has a convergence semi-angle of at least the Bragg

angle. In the sample, momentum transfers will take place across such a convergent probe spanning at least one Bragg angle (or Brillouin zone boundary) ensuring that a high spatial resolution signal will be collected by a spectrometer located on the optic axis of the microscope (see Figure 5.1a). The convergent illumination condition required to create the small probe and achieve high spatial resolution necessarily means the vibrational EELS signal entering the spectrometer will consist of an integral over regions of momentum space spanning more than one Brillouin zone boundary. This is also true for atomic resolution core-loss EELS and is a consequence of the uncertainty principle.

An experimental challenge for achieving atomic resolution with vibrational EELS is to suppress or avoid the strong, delocalized dipole signal. For ionic materials, dipole signals, which often arise due to asymmetric stretching or deformation modes involving adjacent cations and anions, are many times stronger than impact signals (Rez, 2014). The dipole signal is strongly forward peaked; to avoid it, Dwyer et al. displaced the spectrometer entrance aperture outside the cone of convergence of the electron beam achieving a spatial resolution of better than 20 Å of a BN specimen edge (Dwyer et al., 2016). However, their convergence angle was not sufficient to resolve atomic columns. Hage et al. have recently extended this approach and showed that energy filtered images, which include contributions from acoustic and optical phonons recorded at high scattering angles (>60 mrad), show atomic resolution (Hage et al., 2019). The intensity of the high angle EELS signal is weak, and no attempt was made to isolate specific phonon peaks from the non-characteristic background signal. Moreover, the intensity of the EELS signal is modulated by the collected elastic scattering signal, which also shows atomic resolution contrast and may dominate the contrast in an energy-filtered image.

In this chapter, a completely different approach to avoid the dipole signal is demonstrated that does not require off-axis high scattering angle detection, but instead relies on the presence of specific vibrational modes that can only be excited via highly localized impact scattering. This approach differs from prior work in several important respects. Here a conventional, on-axis EELS geometry is employed, where the signal strength is strong. Spectral processing approaches are used to isolate the impact signal associated with specific vibrational modes from the non-characteristic background and dipole contributions. Corrections are made for the collected elastic signal to minimize ambiguities in the interpretation of the spatial variation of the vibrational signal. Finally, spatial variations in both the spectral intensity and shape further are shown, thereby demonstrating that the sensitivity of the impact peak to the probe position within the unit cell.

The approach is initially developed and demonstrated on Si, a non-ionic elemental semiconductor where impact scattering predominates since any dipole signal will be a second order effect due to bond polarization by the passing fast electron as seen with relativistic and non-relativistic dielectric theory simulations from Chapter 3. For ionic materials SiO_2 was selected due to familiarity with the material, and because it shows an impact scattering dominated signal that lies at a different energy-loss than the stronger dipole peaks. The experiments presented here demonstrate that a localized impact signal in amorphous SiO_2 can be used to define the interface between amorphous SiO_2 and crystalline Si with 5 Å resolution.

5.2 Methods

5.2.1 Sample Preparation

A MAG*I*CAL magnification calibration reference standard for TEM was purchased from Electron Microscopy Sciences. It is an ion-milled cross-sectional TEM sample made from a silicon single crystal with a molecular beam epitaxy (MBE) grown semiconductor multilayer consisting of four sets of five ~10 nm thick $Si_{0.81}Ge_{0.19}$ alloy layers, alternating with ~13 nm thick pure silicon layers. The purchased TEM specimen was lightly ion milled at voltages of 0.1 kV using the Gatan Precision Ion Polishing System (PIPS) II to restrict the thickness of any amorphous SiO_2 layer on Si to < 1 nm. Cross-sections of Si and $Si_{0.81}Ge_{0.19}$ in the sample are in a $[\bar{1}10]$ zone axis orientation. A second sample was prepared to investigate the Si (crystalline)/SiO_2 (amorphous) interface as described in Section 3.2.1. In this case, the Si was in the [110] zone axis orientation and the interface plane normal was parallel to the [002] direction in Si.

5.2.2 Monochromated STEM EELS measurements

STEM EELS analysis on both samples was performed using an aberration-corrected and monochromated NION UltraSTEM 100, operated at 60 kV. The probe convergence semi-angle was 28 mrad, and the corresponding collection semi-angles employed were either 12 or 24 mrad. To record spectra, a dispersion of 1 or 2 meV per channel was used with the 12 mrad collection angle and 0.37 meV per channel was used with the 24 mrad collection angle. During acquisition, the axis of the incident beam and that of the spectrometer coincide. Aberration correction of the magnetic lenses up to the fifth order produced probes of ~0.12 nm diameter with beam currents of ~100 pA. During the monochromated experiment, the beam current was ~10 pA, and energy resolution was

15 meV for the 12 mrad collection semi-angle acquisition and 10 meV for the 24 mrad collection semi-angle acquisition. The monochromated probe size was estimated to be ~0.17 nm. Figure 5.1a shows a schematic of the employed STEM EELS configuration with 28 mrad probe convergence and either 12 or 24 mrad spectrometer collection semi-angles while Figure 5.1b shows a schematic diagram depicting the scattering geometry relative to the reciprocal lattice of Si.

EELS linescans were performed across multiple Si unit cells with a step size of 0.6 or 0.2 Å to investigate the variation in the vibrational energy-loss signal within a single unit cell. All linescan data was processed with combination of custom MATLAB code, the FIJI-Cornell Spectrum Imager (Cueva et al., 2012) and the Gatan Microscopy Suite. Linescan spectra were calibrated by using cross-correlation to set the center of the ZLP to 0 meV. The spectra were normalized to the total intensity going into the spectrometer to account for the elastic scattering variation along the linescan. Custom MATLAB code was used to fit a pseudo-Voigt function (sum of a Gaussian and a Lorentzian function) to the background which arises from the tail of the ZLP and other non-characteristic vibrational losses. A two-window model was employed; the function was fit in and interpolated between the two windows. It was observed that in the energy-loss region of interest, the background varies rapidly, and traditional functions such as the power law are unable to fit it accurately, which necessitated the search for a better background model, finding the pseudo-Voigt function to be particularly well-suited. The variation in the intensity of the background-subtracted vibrational spectra from Si was modelled with a simple two-Gaussian peak fitting model.

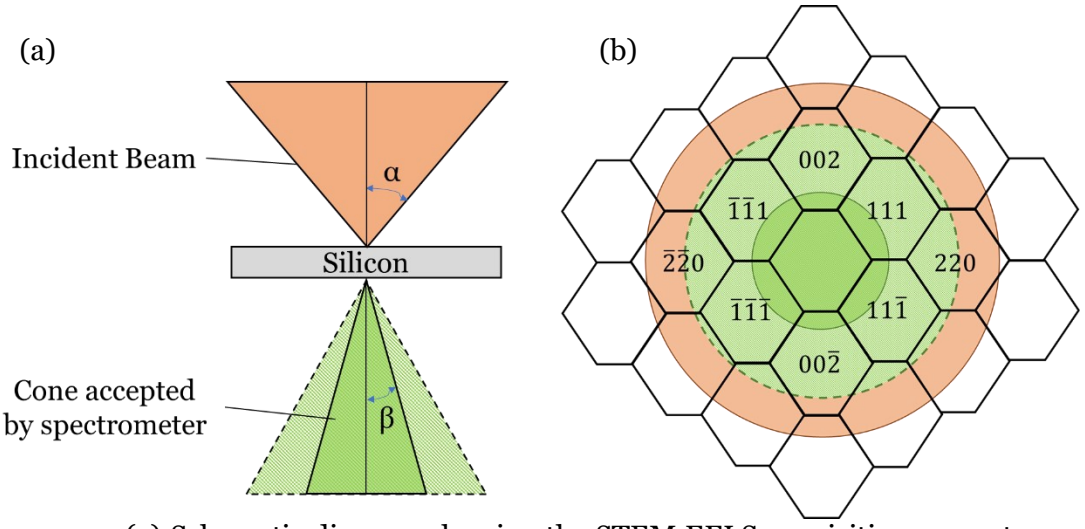

Figure 5.1. (a) Schematic diagram showing the STEM EELS acquisition geometry used in experiment with α = 28 mrad and β = 12 or 24 mrad. (b) Schematic diagram in reciprocal space showing incident beam convergence (orange circle) of 28 mrad and spectrometer acceptance ranges of 24 and 12 mrad (dashed and solid green circles respectively) relative to the Brillouin zones in Si covered by the incident beam.

5.3 Results and discussion

5.3.1 Typical vibrational EELS from Si

Figure 5.2a shows a typical raw energy-loss spectrum from Si and Figure 5.2b shows the same spectrum after background subtraction, with a strong vibrational peak at ~60 meV and a secondary peak at ~45 meV. In vibrational EELS, the intensity and shape of the phonon spectra entering the spectrometer can be expressed as a product of a projected density of states and a position dependent transition probability. Qualitative insights on the origin of spectral features can be ascertained from the phonon dispersion curves for Si, which have been determined using density functional theory (Jain et al., 2013; Ong et al., 2013) (reproduced in Figure 5.2c), and experimentally (Dolling & Cowley, 1966). Flat parts of the dispersion curves give rise to maxima in the phonon density of states contributing to stronger spectral intensity (Ashcroft & Mermin, 2011).

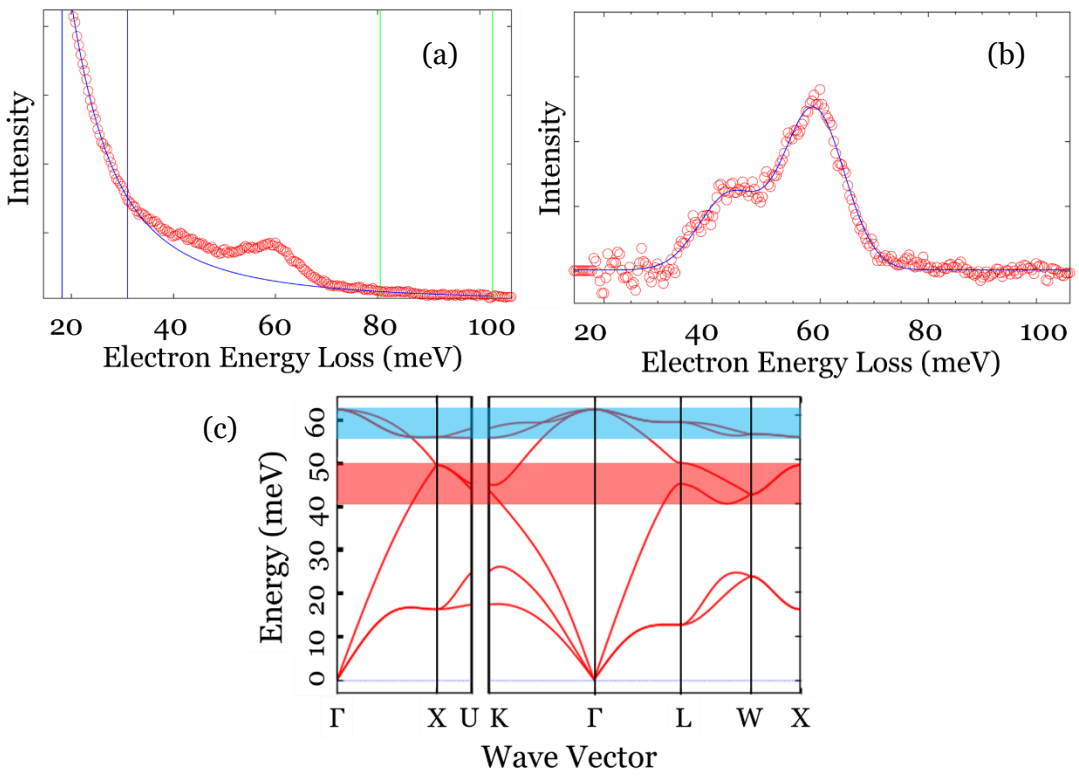

Figure 5.2. (a) A typical raw vibrational energy-loss spectrum from Si acquired with β = 24 mrad (red circles). Blue curve shows the background subtraction model employed. The vertical lines (blue and green) show the windows used to fit the background. (b) The same spectrum after background subtraction. Here, the blue curve shows the two Gaussian peak fitting model employed, which shows good agreement with the data. (c) Dispersion surfaces in for Si (Jain et al., 2013; Ong et al., 2013) – blue and red shaded areas corresponds to peaks in the density of states on the upper branches from 55 – 62 meV (optical) and on a lower branch from 41 – 48 meV (optical and acoustic).

The higher energy peak in the spectrum (~60 meV) is associated with the upper transverse optical branches of the dispersion curves, which are shaded blue in Figure 5.1c, while the lower energy shoulder is associated with longitudinal acoustic and optical modes which are shaded red. The contributions from the high and low energy branches to the spectral intensity can be quantified with a simple peak fitting model. Two Gaussians, constrained to have widths between 10 and 30 meV, were fitted to background subtracted spectra, with peak positions constrained to lie in the ranges 40 – 50 meV and 55 – 63 meV, corresponding to the lower and higher energy bands described above. The two Gaussian

model fits the experimental data points excellently (Figure 5.2b). Inelastic neutron scattering (Figure 5.3) shows similar features between 40 and 60 meV (Kulda et al., 1994), and these are not observed with IR spectroscopy, confirming that the signals observed in EELS are associated with impact scattering and not with dipole scattering and in principle, should be highly localized.

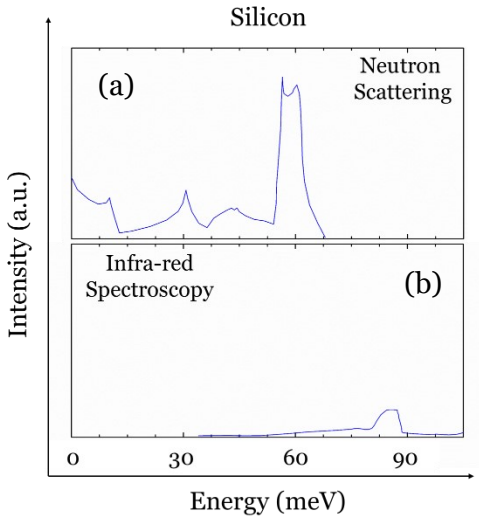

Figure 5.3. Inelastic neutron scattering data (a) and IR absorption spectrum (b) from Si (Dolling & Cowley, 1966). For Si, the relevant peaks are at approximately 40, 50 and 60 meV and are consistent with the dispersion curves shown in Figure 5.2c. The IR peak at 75 meV is extremely weak and is not observed in the EELS spectra (indeed, dielectric theory simulations suggest that the 75 meV peak would be obscured by Cerenkov radiation (Section 3.3.1 , Figure 3.5)).

5.3.2 EELS linescans within the Si unit cell

To explore the localized nature of the vibrational EELS signals, the spectral intensity was investigated as a function of electron probe position by performing linescans across a Si unit cell. The images in Figure 5.4a and 5.4b were recorded from Si in the [$\bar{1}$10] projection with the monochromator slit inserted to give an energy resolution of 10 meV with a spectrometer entrance aperture corresponding to a collection angle of 24 mrad.

EELS linescans were performed along the [110] direction with a typical step size of about 0.2 Å. The total intensity entering the spectrometer passes through minima and maxima as the probe moves on and off the atomic columns primarily due to interference effects associated with the phase contrast elastic bright-field signal. To correct for the spatial variation in the total number of electrons entering the spectrometer due to elastic scattering, each spectrum in the linescan was normalized to the total intensity before determining the vibrational peak intensities. Figure 5.4c shows the resulting vibrational spectra when the probe is positioned on and off the Si dumbbell columns and Figure 5.4d shows the integrated intensity of the low energy and high energy peaks as the probe is moved across the unit cell. The spectral intensity of the 60 meV peak increases by almost 40%, when the probe is positioned on the column. Figure 5.4d demonstrates a spatial resolution of < 2 Å and clearly shows that atomic resolution vibrational spectroscopy can be accomplished in the forward scattering geometry using a signal associated with impact scattering. The signal from the lower energy peak is noisier but also shows atomic resolution.

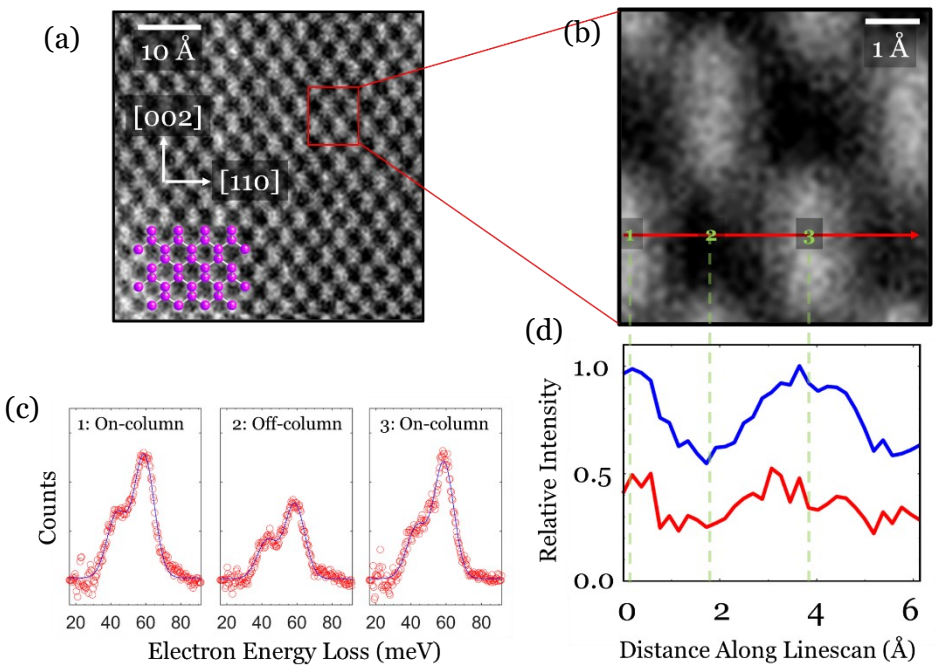

Figure 5.4. (a) Atomic resolution annular dark field (ADF) image with electron beam monochromation of ~10 meV from Si in [$\bar{1}$10] projection with light contrast corresponding to Si dumbbell column pairs. A model of Si in the [$\bar{1}$10] projection overlaid on the ADF image shows the position of atomic columns that form dumbbells. (b) Magnified image of area indicated by red box in (a). The arrow indicates position and direction of EELS linescan acquisition. (c) Individual spectra from different positions along linescan shown by the green x-symbols in (b). As in Figure 5.1, the red circles are experimental data points, and the blue line is the result of the Gaussian fit. (d) The variation in intensity for higher (blue) and lower (red) energy phonons over the linescan indicated in (b). The profiles are spatially aligned with the ADF image in (b), as indicated by dashed green guidelines. An increase in phonon intensity can be observed around the dumbbell columns.

When the collection semi-angle was reduced to 12 mrad, the intensity difference for the on and off column probe positions increased to 60% for the 60 meV line scan. Figure 5.5 shows the spectra and integrated peak intensities as a function of position (linescan step size 0.6 Å) for this smaller collection angle. Interestingly, whilst the intensity of the higher energy signal still tracks with the HAADF signal peaking on the column, the maximum of the lower energy signal is offset from the column position. Furthermore, in contrast with the large collection angle data, the energies of both peaks change significantly as the probe moves between the columns. The lower energy peak

increases in intensity to a maximum as the probe approaches the column, and its energy position shifts from ~40 to 50 meV. The higher energy peak shifts from 60 to 58 meV as the probe moves onto the column. One of the possibilities for this change in signal shape and intensity could be the variation in elastic scattering within the unit cell. However, coherent elastic scattering may cause changes in the absolute intensities of all the vibrational signals simultaneously. If the inelastic scattering processes causing these vibrational excitations were delocalized, this would give no change in the relative intensities of the observed peaks. However, Figure 5.5c shows a significant change in relative peak intensities, further demonstrating that the high spatial resolution is substantially associated with a highly localized vibrational excitation process.

For the small collection angle data, the lower energy peak shows an asymmetry in the intensity with respect to the atomic column position which also correlates with an asymmetry in the bright-field signal entering the spectrometer. Simulations of convergent beam patterns show that small (~1 mrad) misalignments between the incident cone and the cone defined by the spectrometer entrance aperture, as well as small (~1 mrad) tilts of the specimen can introduce an asymmetry to the intensity distribution in the bright-field signal recorded on either side of the atomic columns (Venkatraman et al., 2019). Contributions to vibrational spectra from near the Brillouin zone boundaries may also be sensitive to small detector shifts or specimen tilts, which may explain the asymmetry we observe. This is an interesting effect although it is out of the scope of the current dissertation, and future studies will explore the origin of the observed asymmetry with theory and experiments.

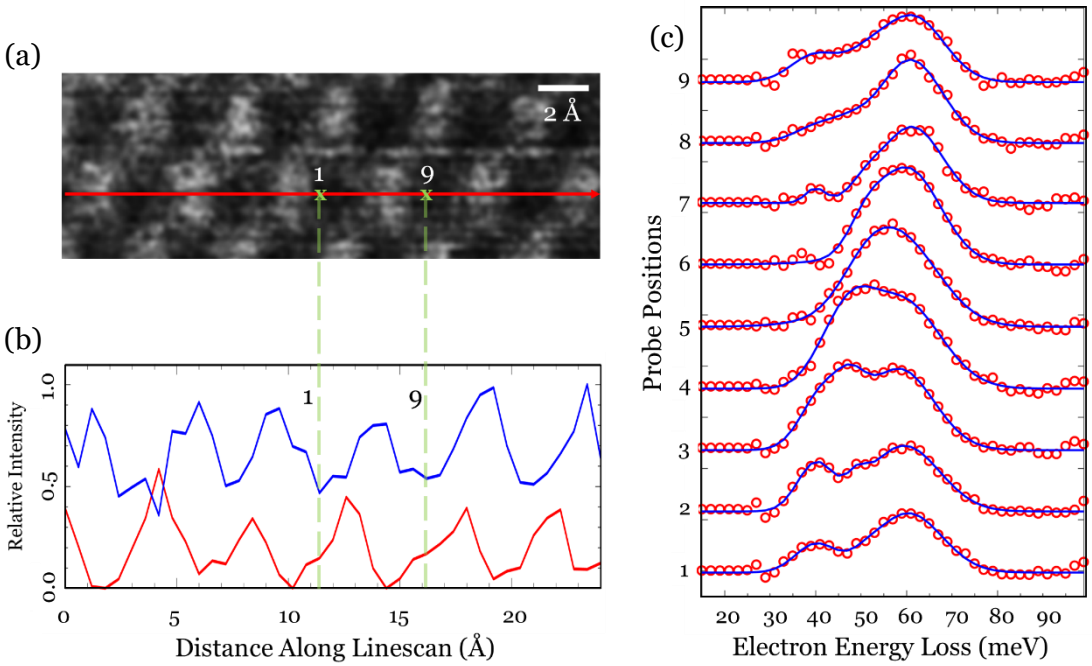

Figure 5.5. (a) ADF image of Si dumbbells with arrow indicating position and direction of EELS linescan acquisition. (b) The variation in intensity for higher (blue) and lower (red) energy phonons over the linescan indicated in (a). A strong increase in higher energy phonon intensity can be observed around the dumbbell columns. The maxima of the lower energy phonon intensity are offset relative to the dumbbell columns. (c) Raw spectra at 9 individual probe positions all separated by 0.6 Å along the linescan between the labels 1 and 9 shown in (a) and (b). It also shows the two Gaussian fits to the spectra at all probe positions. This highlights the variation in intensity and shape of the spectra with less than 1Å shifts in probe position.

The low energy peak lies at ~ 50 meV when the electron probe is located close to the atomic column and is associated with the upper branches between the X and L points of the Brillouin zone (Figure 5.1c). When the probe is located between the columns the energy shifts down to ~ 40 meV, which is associated with other points in the 2D $(\bar{1}10)$ section of the Brillouin zone. The change in energy suggests that the transition probability for launching phonons along different directions is strongly influenced by the probe position.

A form of momentum filtering also occurs for the higher energy optical peak and can be interpreted in terms of a simple classical picture where small impact parameter collisions are associated with high momentum transfer. When the probe is on the atomic column (small impact parameter), the peaks shift down to 56 – 58 meV corresponding to the higher momentum transfers associated with excitations at the Brillouin zone boundaries. When the probe is positioned between the columns (large impact parameter), the spectral peak appears at around 60 meV which is associated with relatively low momentum transfers in the first Brillouin zone (i.e. perhaps a third of the way between the Γ point and the boundary). Atomic resolution can arise from these low momentum transfer modes with pure elastic scattering followed by a normal phonon scattering process in the first Brillouin zone. Alternatively, it could arise via Umklapp scattering from neighboring Brillouin zones without the need for elastic scattering. Given that the sample thickness is on the order of the extinction distances (~ 50 nm) for Bragg beams, it is likely that the resulting signal with atomic resolution is a combination of both possibilities but a quantitative interpretation of the contributions from normal and Umklapp scattering would require detailed calculations.

5.3.3 Impact scattering dominated vibrational modes in ionic materials

High spatial resolution in vibrational EELS is also possible from ionic materials provided suitable impact peaks can be identified where the dipole contribution is very weak. SiO_2 is an oxide with mixed ionic-covalent bonding and the background-subtracted vibrational energy-loss spectrum (Figure 5.6a) shows peaks at 58, 100 and 144 meV which correspond to vibrational excitations associated with the Si-O-Si rocking mode, the symmetric Si-O stretching and deformation bulk mode and the asymmetric Si-O

stretching mode as seen in Chapters 3 and 4. Also shown in Figure 5.6a is a dielectric theory simulation based on Kröger's analytical expression for the dipole vibrational spectrum from a SiO_2 film of 100 nm thickness, broadened with the 16 meV experimental PSF. It can be seen that features at 58 and 144 meV in the experimental and simulated spectra agree excellently, but the signal at 100 meV is much stronger in the experiment. This suggests that the signal has a weak dipole component (Figure 5.6a) and a significant impact component which is confirmed by comparing IR and neutron measurements of SiO_2 vibrational modes as shown in Figure 5.6b (Lehmann et al., 1983; Arai et al., 1992; Haworth et al., 2010). Both spectra show strong peaks around ~55 meV and between ~130 and 160 meV, but only the inelastic neutron scattering data shows a strong 100 meV peak.

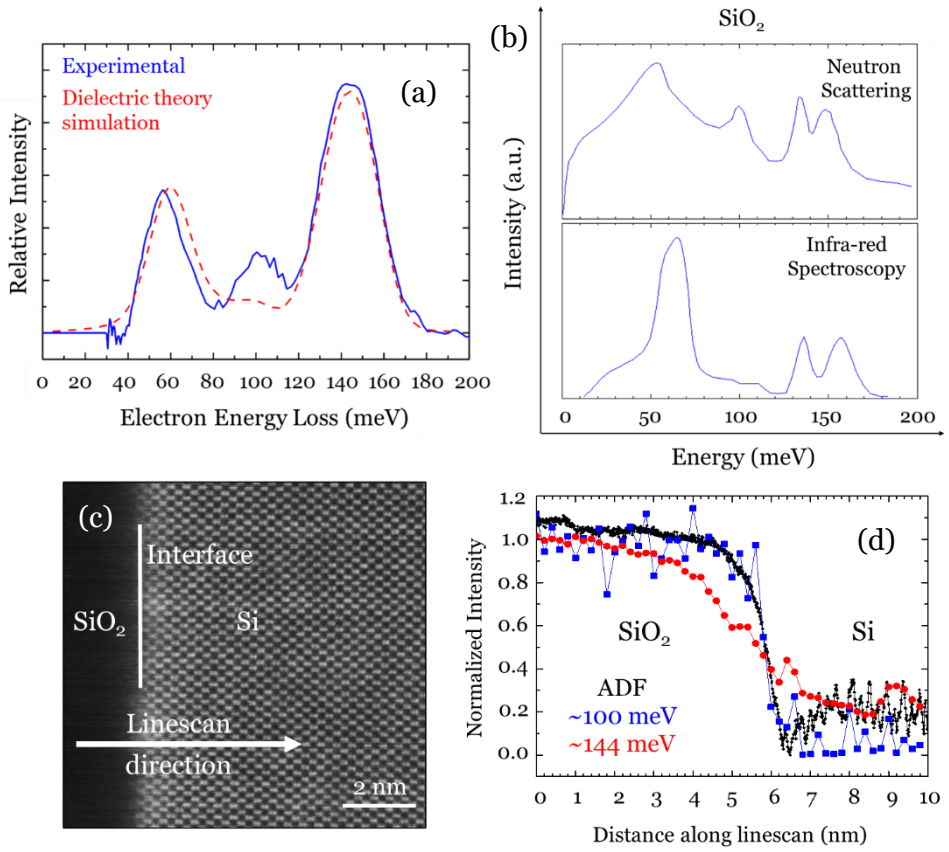

Figure 5.6. (a) Experimental energy-loss spectrum in SiO_2 far from interface (solid blue) and dielectric theory simulation of the spectrum (dashed red). The peak at ~100 meV does not appear strongly in the dielectric simulation, indicating that it is predominantly excited by impact scattering. (b) Inelastic neutron scattering data and IR absorption spectrum from SiO_2 (Lehmann et al., 1983; Arai et al., 1992). For SiO_2, the neutron scattering shows peaks at 55, 100, 138 and 150 meV. The IR shows three peaks at similar energies but the peak at 100 meV is absent since it is primarily associated with impact scattering. The EELS shows peaks like those in the neutron scattering although we do not resolve the separate peaks at 138 and 150 meV. (c) Atomic resolution ADF image of the SiO_2/Si interface showing linescan direction across the interface. (d) Normalized signal profiles across the interface – 100 meV (blue) and 144 meV (red) – overlaid on the ADF signal profile.

The spatial resolution of the SiO_2 peaks was explored by performing EELS linescans across a SiO_2/Si interface. The impact component of the 100 meV signal was isolated by subtracting the contribution arising from the tails of the preceding and succeeding dipole signals. All the signals were normalized to the total spectral intensity to correct for elastic scattering. The sharpness of the profile from the impact signal is

controlled by SiO_2/Si interface abruptness. As seen in Chapter 3, according to dielectric theory, the long-range Coulomb nature of dipole scattering and associated begrenzungs effect should cause a dipole signal to significantly drop at 20 – 30 Å from the interface (Venkatraman et al., 2018). An atomic-resolution ADF image of the interface along with direction of the performed linescan is shown in Figure 5.6c. The spatial variation profiles of the 144 meV dipole and the 100 meV impact signals along the linescan overlaid on the ADF profile are shown in Figure 5.6d. The ADF signal variation benchmarks the abruptness and mass thickness changes in the sample near the interface. The 144 meV dipole signal starts dropping more than 30 Å before the ADF signal and drops to a finite intensity associated with the aloof beam counterpart of the dipole signal right after the interface. This can be attributed to the begrenzungs effect. However, the 100 meV impact signal shows a much sharper profile by following the ADF signal and dropping over a distance of ~5 Å across the interface. It is also seen that unlike the 144 meV signal, the 100 meV signal profile drops to zero right after the interface, further demonstrating its impact dominant character due to which it does not have an aloof counterpart. This shows that high spatial resolution is not limited to elemental semiconductors but is possible in all materials (including amorphous materials) which possess peaks where impact scattering dominates over dipole scattering. Figure 5.7 shows the importance of background subtraction and normalization to the total spectrometer signal intensity on the sharpness of the 100 meV signal profile. Without these processing steps, the 100 meV profile starts to drop ~10 – 20 Å before the impact component of the signal and drops to a finite value (and not zero) as the beam moves across the interface into Si.

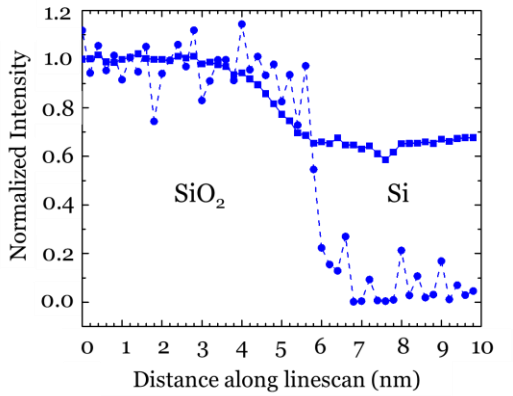

Figure 5.7. Signal profiles for the 100 meV SiO_2 vibrational mode across the abrupt SiO_2/Si interface shown in Figure 4b. The solid profile (square marker) is obtained by integrating the vibrational signal over 20 meV with no background subtraction. The dashed profile (round marker) is obtained after background subtraction, removal of dipole contribution, and normalizing to the total spectral intensity to correct for elastic scattering. This impact component can be used to estimate the interface width to 5Å. This highlights the importance of background subtraction and normalization to elastic scattering in determining the accurate spatial variation of any vibrational energy-loss signal. Both profiles were scaled to unity in SiO_2.

5.4 Conclusion

In conclusion, we have demonstrated atomic resolution vibrational spectroscopy by using a monochromated, aberration corrected STEM with a large convergence angle and a conventional on-axis spectrometer geometry. Our approach selects modes associated with impact scattering, which yield high spatial resolution for both ionic and covalent materials. In crystalline Si, with only covalent bonding, vibrational peaks corresponding to both optical and acoustic phonons were observed, and we achieved a spatial resolution of better than 2 Å. The signal intensity is strongest with the probe positioned over atomic columns. We observed significant changes in spectral shape with sub-angstrom shifts in probe position for smaller collection angles, which is qualitatively explained by a momentum filtering effect. In amorphous SiO_2, with mixed ionic-covalent

bonding, the 100 meV vibrational mode, with a significant impact scattering component, yielded a spatial resolution of 5 Å.

The method presented in this chapter is an important advance that allows the influence of local atomic structure on vibrational modes to be explored directly in the on-axis STEM EELS geometry. In future work on this dissertation, we will apply this method to investigate changes in the character of vibrational modes around atomic-scale structural heterogeneities such as point defects, dislocations, grain boundaries and surfaces. These changes in vibrational modes should yield fundamental new insights into important thermally activated processes in materials. In the next chapter, we explore the influence of varying probe convergence and spectrometer collection semi-angles on the intensity and spectral positions of both dipole and impact scattering dominated vibrational energy-loss signals from hexagonal boron nitride (h-BN). h-BN is a layered anisotropic material with mixed ionic-covalent bonding in the plane of the B – N chemical bond and van der Waal's bonding perpendicular to it. It is hypothesized that a change in the convergence or collection semi-angles would not affect dipole signals, but would hugely influence the visibility of impact signals in the energy-loss spectrum.

CHAPTER 6

THE EFFECT OF CONVERGENCE AND COLLECTION ANGLES ON ELECTRON IMPACT SCATTERING

6.1 Motivation

As seen in the previous chapters, in polar materials with mixed ionic-covalent bonding, the vibrational energy-loss spectrum from dipole scattering is complicated. In amorphous SiO_2, the dipole contribution is associated with bulk modes and SPhPs whose excitation is strongly geometry dependent as seen in Chapter 4 and as shown by the presence of edge and corner SPhPs in MgO nanocubes at different energy positions (Lagos et al., 2017). In anisotropic van der Waals materials like h-BN, opposing signs of the in-plane (containing ionic B-N bonds) and out-of-plane dielectric functions results in the excitation of volume or edge-surface hyperbolic phonon polaritons (HPhPs) in the upper Restrahlen band (Govyadinov et al., 2017). Energy-loss signals associated with phonon polaritons are spatially delocalized to tens of nanometers (Konečná et al., 2018), although in practice it might be possible to achieve nanometer spatial resolution using corner or edge SPhP modes (Lagos et al., 2017).

It was seen in the previous chapter that impact scattered vibrational energy-loss signals have atomic resolution. From a classical picture, short-range interaction implies that impact scattering is associated with a large momentum transfer which means that its characteristic scattering angles are large. Thus, in general, dipole scattering dominates in the forward direction (the optic axis of the spectrometer is the same as that of the incident beam) while impact scattering dominates outside the convergent cone of the STEM probe. However, even in the forward direction, the electron beam can excite vibrational modes that do not modulate the bond dipole moment and cannot be strongly excited by dipole scattering, such as acoustic modes in all materials, optical modes in non-ionic materials,

and symmetric stretching and deformation modes in ionic materials. In crystals, the list would also include short wavelength optical phonon modes at Brillouin zone boundaries (BZBs). The energy-loss signals associated with these excitations would be impact scattering dominated (Ibach & Mills, 2013). As was seen in the previous chapter, the SiO_2/Si interface width was estimated with sub-nanometer precision with such a signal associated with the symmetric Si-O stretching and deformation mode in amorphous SiO_2.

In this chapter, we want to explore the effect of varying probe convergence (α) and spectrometer collection (β) semi-angles on the vibrational energy-loss spectrum from a crystalline h-BN nanoflake oriented along the [0001] zone axis. Since it is associated with small scattering angles, the dipole scattering dominated contribution to the spectrum would be unaffected by a large change in probe convergence. This would be unlikely for the impact scattering dominated contribution. We hypothesize that as the convergence semi-angle becomes large enough to include BZBs from the boron nitride crystal, impact scattering dominated energy-loss signals from vibrational modes at BZBs will become more significant. To test this hypothesis, we have employed α = 10 and 33 mrad, as the Bragg angle for completely encompassing the first Brillouin zone (BZ) in h-BN is 19.5 mrad. We also want to explore the excitation of impact scattering dominated vibrational modes as a function of β. Therefore, we employ β = 7 and 28 mrad for EELS acquisition.

6.2 Methods

6.2.1 Specimen preparation

High purity h-BN powder (99.8% pure) with average lateral dimensions of 5 μm and thicknesses of 300 nm was purchased from US Research Nanomaterials Inc. The powder was ultrasonicated in electronic grade (99.999% pure) isopropyl alcohol (IPA), purchased from Sigma Aldrich, for 1 hour. Ultrasonication helps exfoliate the layered h-BN powder into thinner flakes. A drop from the ultrasonicated solution was casted onto a

3 mm, lacey carbon-film coated, 200 mesh Cu TEM grid purchased from Pacific Grid-Tech and the grid was dried under a heat lamp for 1 hour. The specimen was baked at 140°C for 12 hours prior to introduction into the microscope to burn off all volatile hydrocarbons and prevent any contamination.

6.2.2 Monochromated STEM EELS measurements

STEM EELS analysis on the specimen was performed using the aberration-corrected and monochromated Nion UltraSTEM 100, operated at 60 kV. α was either 10 or 33 mrad, and β was either 7 or 28 mrad. Figure 6.1a shows the STEM EELS geometry employed during experimentation, the shaded triangles representing smaller convergence and collection cones. It was routinely possible to make 1Å sized probes with highly convergent probes due to aberration correction up to the fifth order (Krivanek et al., 2003), and monochromation enabled a routine energy-resolution of 10 meV (Krivanek et al., 2009). Each h-BN nanoflake was oriented into the [0001] zone axis before EELS acquisition. Figure 6.1b overlays circles representing the different convergence and collection angles employed on the hexagonal BZs of [0001] h-BN. Energy-loss information was either acquired in the form of 'point-and-shoot' spectra from different positions on the h-BN nanoflake or as linescans across the edge of the flake wherein energy-loss spectra were recorded at every pixel along the linescan, with the pixel size being 2Å. An energy-dispersion of 0.66 meV per channel was used to record vibrational energy-loss spectra. Parametric two-window background subtraction was performed to isolate the energy-loss features from the background of the tail of the zero-loss peak (ZLP) and uncharacteristic energy-losses preceding the feature of interest using custom MATLAB code. Other data processing was performed with the Gatan Microscopy Suite. The spectra were calibrated by setting the center of the ZLP to 0 meV, and the error in measuring energy-loss was the channel width i.e. ± 0.66 meV. The flake thickness was estimated by performing low-loss

EELS with 10 mrad probe convergence, 40 mrad spectrometer collection and a dispersion of 50 meV per channel to determine the ratio of flake thickness to the inelastic mean free path for valence-shell inelastic scattering from h-BN, which comes to 76 nm at 60 kV (Iakoubovskii et al., 2008).

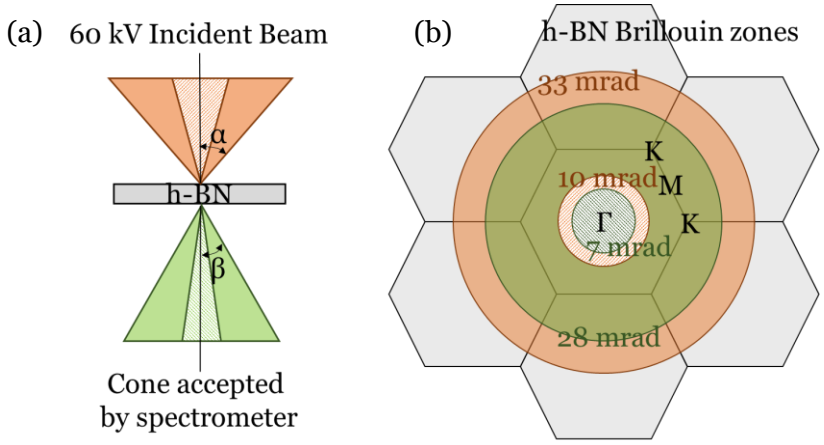

Figure 6.1. (a) STEM EELS geometry employed during data acquisition. The solid orange cone above the sample denotes α = 33 mrad, while the shaded orange cone denotes α = 10 mrad. The solid green cone below the sample represents β = 28 mrad, while the shaded green cone represents β = 7 mrad. (b) Circles representing the different convergence and collection semi-angles employed are overlaid on the hexagonal Brillouin zones of h-BN in the [0001] zone axis orientation.

6.3 Results and discussion

6.3.1 EELS acquisitions in the dipole limit

A typical background subtracted vibrational energy-loss spectrum from a h-BN nanoflake recorded with α = 10 and β = 7 mrad, is shown in Figure 6.2a. The inset shows an annular dark field (ADF) image of the flake and the position of the probe relative to its edge. Flake thickness was estimated to be 52 nm from low-loss EELS measurements. The spectrum shows a strong peak at 194 meV having an intense shoulder at 176 meV, and a very weak peak at 100 meV. Phonon dispersion curves from bulk h-BN obtained using inelastic X-ray scattering spectroscopy have been reproduced in Figure 6.2b to aid in the interpretation of spectral features (Serrano et al., 2007).

In the current electron-optical geometry, only long-wavelength optical phonon modes from the central region of the hexagonal BZ in h-BN i.e. the Γ point can be excited by the probe, as depicted schematically in Figure 6.1b. Due to the typically small scattering angles involved in their excitation, these modes are dipole scattering dominated. None of the phonon modes from BZBs contribute to the energy-loss spectrum, and the spectral features can be identified by looking at flat parts in the dispersion curves close to the Γ point. Thus, the 194 meV peak is associated with the bulk h-BN longitudinal optical (LO) phonon mode, while the 176 meV shoulder is associated with the bulk h-BN transverse optical (TO) phonon mode. The weak peak at 100 meV seems to be the out-of-plane optical (ZO) phonon mode in h-BN.

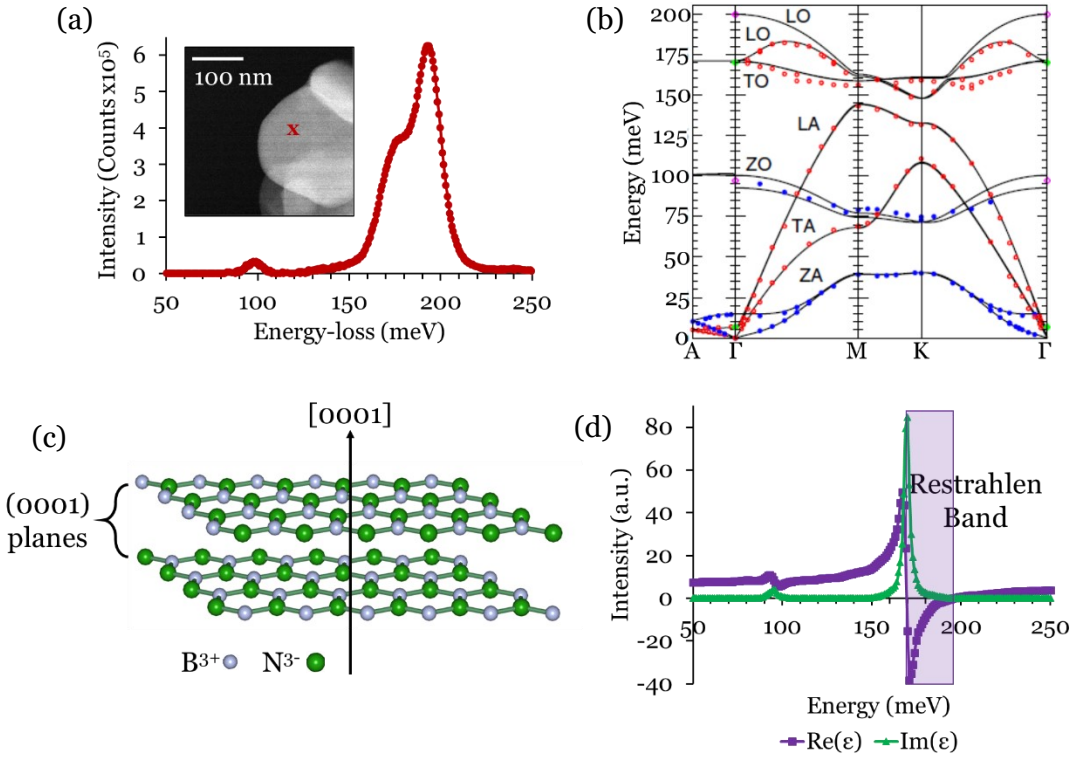

Figure 6.2. (a) Background subtracted vibrational spectrum with 10 mrad convergence and 7 mrad collection. (Inset) ADF image of the h-BN nanoflake showing probe position on the flake. (b) Phonon dispersion curves from bulk h-BN (Serrano et al., 2007). (c) Schematic representation of layered h-BN depicting its crystallography in the [0001] zone axis orientation. (d) In-plane dielectric function of h-BN showing the Restrahlen band between 170 and 196 meV (Geick et al., 1966).

In an electron optical geometry where only dipole scattering dominated vibrational modes close to the Γ point are excited, features in the energy-loss spectrum can be described by approximating the collective response of h-BN to the electric field of the electron with its optical dielectric function (Ritchie, 1957; Venkatraman et al., 2018). h-BN is an anisotropic layered material, schematically represented in Figure 6.2c, with van der Waal's forces responsible for bonding between the boron nitride planes and mixed ionic-covalent bonding in the boron nitride planes (Geick et al., 1966). Thus, it has different dielectric functions along the (0001) plane (in-plane) and perpendicular to it (out-of-plane). In the STEM EELS geometry with the specimen oriented along the [0001] zone-axis, in-plane modes contribute much more strongly to the energy-loss spectrum than out-of-plane modes due to the finite probe convergence. The in-plane dielectric function is shown in Figure 6.2d (Geick et al., 1966). It can be seen that the real part of the in-plane dielectric function is negative between 170 and 196 meV; this region is called the Restrahlen band. These are also the energy-values for the TO and LO phonon modes derived from Kramers-Kronig analysis of infrared reflection spectra, showing good agreement with the Γ point values in the dispersion curves. The real part of the out-of-plane dielectric function is positive in this region. The opposite sign of the real part of in-plane and out-of-plane dielectric functions leads to an indefinite dispersion for electromagnetic waves propagating through h-BN (Poddubny et al., 2013). [0001] h-BN nanoflakes can thereby support volume and edge-surface HPhPs due to anisotropy, and a previous vibrational energy-loss study from h-BN suggests that the peaks at 176 and 194 meV correspond to the volume HPhP and the bulk LO phonon modes respectively (Govyadinov et al., 2017).

6.3.2 Increasing the probe convergence to include Brillouin zone boundaries

Figure 6.3a shows an ADF image of the same h-BN nanoflake as described previously, while also showing the probe positions for three subsequent EELS acquisitions. The background subtracted energy-loss spectrum acquired with $\alpha = 33$ mrad and $\beta = 7$ mrad is shown in Figure 6.3b. The spectral shape is starkly different from Figure 6.2a, there are many additional peaks. The strongest spectral feature is still the peak at 194 meV, while the second strongest feature is the peak at 175 meV, which has a strong shoulder at 160 meV. Moreover, there are three weak and broad peaks at 74 meV, 100 meV and 134 meV. From the discussion above, the peaks at 100, 175 and 194 meV can be identified as the ZO phonon, the volume HPhP and the bulk LO phonon, respectively. The peaks at 74, 134 and 160 meV can be qualitatively identified by matching the peak energies the flat parts in the dispersion curves in Figure 6.2b. All three peaks seem to correspond to short wavelength phonon modes at the BZBs with the weak 74 meV peak being associated with a combination of the transverse acoustic (TA) and ZO phonon, the broad 134 meV peak being associated with the longitudinal acoustic (LA) phonon and the 160 meV shoulder being associated with a combination of the TO and LO phonon. The 100 meV peak might also have some contribution from the TA mode at the BZBs. All vibrational excitations that are observed in this chapter are labelled and described with their spectral positions in Table 6.1.

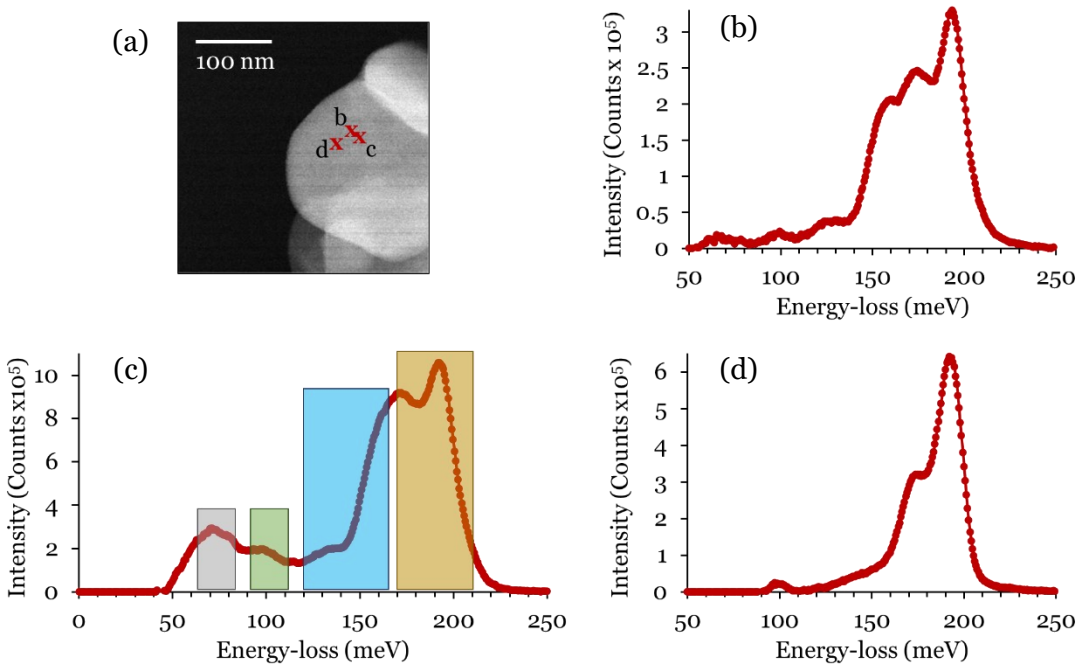

Figure 6.3. (a) ADF image of the h-BN nanoflake showing the probe positions on the flake during acquisition of spectra in (b), (c), and (d). (b) Background subtracted spectrum acquired with α = 33 mrad and β = 7 mrad. (c) Background subtracted spectrum acquired with α = 33 mrad but β = 28 mrad. The four windows chosen to estimate the integrated intensities relative to the strongest dipole signal between 170 and 210 meV are also shown. (d) Background subtracted spectrum acquired with α = 10 mrad and β = 28 mrad.

Label	**Mode description**	**Energy, meV**
Bulk	Bulk LO phonon from BZ center	194
Volume HPhP	Volume hyperbolic phonon polariton	176
Edge HPhP	Edge-surface hyperbolic phonon polariton	184
Convolved HPhP	Convolution of volume and edge-surface HPhP	179
TO/LO	TO/LO BZB phonon	160
LA	LA BZB phonon	134
ZO	ZO phonon from BZ center	100
TA/ZO	TA/ZO BZB phonon	74

Table 6.1. Different vibrational modes excited by the electron beam in [0001] h-BN.

When α = 33 mrad, the Bragg angles of 11.2 mrad and 19.5 mrad for the (1100) and (1000) Bravais-Miller planes are covered by the convergent probe, and modes at BZBs in

h-BN can be excited with this on axis STEM EELS geometry. This was less likely in the previous configuration with α = 10 mrad, as depicted in Figure 6.1b. The outermost circle shaded with solid orange represents α = 33 mrad, the second smallest circle shaded with orange lines represents α = 10 mrad. The innermost circle shaded with green lines represents β = 7 mrad. Figure 6.1b shows that multiple K-M-K BZBs are encompassed when α = 33 mrad that are left out when α = 10 mrad. Although β = 7 mrad implies that electrons scattered up to 17 mrad will also be collected by the spectrometer, the fraction of such electrons among the collected electrons is appreciably small and observably below current detection limits.

Due to the high momentum transfer and large scattering angles involved with excitation of BZB phonon modes by transmitted electrons, they are impact scattering dominated, and signals associated with them are highly localized in space – an implication of the uncertainty principle. It was shown in the previous chapter that these modes cannot be described using the optical dielectric function in classic electrodynamics. The TO/LO shoulder falls outside the Restrahlen band, while the TA/ZO and LA signals have acoustic character – hence, these excitations cannot couple with a component of the broad frequency electromagnetic field of the transmitting electron to create PhPs. It is generally accepted that due to the small characteristic scattering angles and large ionic polarization caused by the electron beam in polar materials, a dipole energy-loss signal is much stronger than an impact signal in the forward scattering configuration. However, the TO/LO impact signal is roughly half as intense as the dipole polariton and bulk modes, thereby implying that impact scattering dominated vibrational modes can be studied in polar materials with a high signal-to-noise ratio (SNR) in this electron optical configuration.

6.3.3 Effect of the spectrometer collection angle

Increasing β to 28 mrad increases the total intensity of inelastically scattered electrons going into the spectrometer, and should result in an increase in the energy-loss signal. The intensity of unscattered and elastically scattered electrons going into the spectrometer also simultaneously increases, resulting in an increase in the background to the spectrum. The background subtracted spectrum recorded with α = 33 mrad and β = 28 mrad is shown in Figure 6.3c. Qualitatively, there is roughly a three-to-four-fold increase in the overall energy-loss signal intensity in comparison to Figure 6.3b due to an increase in β. The dipole region of the spectrum above 170 meV looks very similar in shape to that in Figure 6.3b, although the volume HPhP is more intense in the present spectrum relative to the bulk mode. All impact signals from Figure 6.3b are observed.

At this point, it would be useful to compare the average integrated intensities of the impact and dipole energy-loss signals in the three cases discussed so far. To do this, the signal is integrated across a window of finite width, and the integrated signal intensity is then divided by the window width. Four windows have been chosen for the entire spectrum in line with the signals observed thus far, the first window being from 60 to 80 meV, the second from 90 to 110 meV, the third from 120 to 165 meV, and the fourth from 170 to 210 meV, as depicted in Figure 6.3b. As the volume HPhP and the bulk modes are strongly present in all spectra, the average integrated intensity in each window is finally divided by that in the fourth window. Thus, the intensities can be analyzed as a fraction of the strongest dipole signal (170 – 210 meV). These fractional intensities are shown in Table 6.2.

With α = 10 mrad, the impact signal from the LA and TO/LO modes is almost negligible (some intensity arises from the tails of the ZO and volume HPhP modes) relative to the strongest dipole signal, while it is roughly half of the dipole signal when α = 33 mrad.

An increase in β has negligible effect on this impact signal relative to the dipole signal. This is due to an increase in both, the impact signal due to an increased contribution from BZB modes resulting from higher available scattering angles, and the volume HPhP signal due to the probe position being farther from the edge relative to the case with smaller β. The ZO mode is observed to be 25 times weaker than the strongest dipole signal with α = 10 mrad. Increasing α to 33 mrad causes a two-fold increase relative to the strongest dipole signal which might be due to contribution from the TA mode. It could also be due to a larger component of the scattering wavevector being perpendicular to the out-of-plane polarization that is responsible for exciting this mode. Four-fold increase in β results in four-fold relative increase in the ZO mode primarily due to a larger tail in the preceding impact signal, and also due to more contribution from the TA mode and larger available scattering angles. The impact signal from the TA/ZO mode is not present with α = 10 mrad, but is present with α = 33 mrad due to the inclusion of BZBs. Unlike the LA and TO/LO signals, an increase in β from 7 mrad to 28 mrad results in a seven-fold increase in the average integrated intensity of the TA/ZO signal relative to the dipole signal.

Figure 6.3d shows the background subtracted spectrum obtained when α = 10 mrad and β = 28 mrad. The spectrum looks very similar to Figure 6.2a, which was obtained with the same α but with β = 7 mrad. It shows the bulk, the volume HPhP, and the ZO dipole signals. An impact signal from the TA/ZO mode is not observed, but there is weak intensity between 120 and 165 meV corresponding to the LA and TO/LO modes. The average integrated intensities of the dipole and impact signals relative to that of the strongest dipole signal for the present case are also shown in Table 6.1. The relative intensity from the ZO dipole signal is roughly the same as that with α = 10 mrad and β = 7 mrad. However, the relative intensity from the LA and TO/LO impact signals is 2.5 times

of that with α = 10 mrad and β = 7 mrad, but still about less than a third of the cases with α = 33 mrad.

α, β	60 – 80 meV	90 – 110 meV	120 – 165 meV	170 – 210 meV
10, 7	0	0.04	0.06	1
33, 7	0.05	0.07	0.44	1
33, 28	0.34	0.24	0.46	1
10, 28	0	0.03	0.15	1

Table 6.2. Integrated intensities as a fraction of the strongest dipole signal.

6.3.4 Linescans across the h-BN edge with large convergence and collection angle

The spatial variation of the impact and dipole signals described above across the edge of a nanoflake can reveal the delocalization in the signals and thus, their spatial resolution. To map the spatial intensity variation, linescans were performed across the flake edge with α = 33 mrad and β = 28 mrad. An ADF image in Figure 6.4a shows the linescan position relative to the flake; length of the linescan is 50 nm and the step size for EELS acquisition is 0.2 nm. The background subtracted vibrational spectra acquired at the two extremes of the linescan, one as the beam is transmitting through the h-BN flake and the other as the beam passes through vacuum, are shown in Figure 6.4b. It was not possible to employ an accurate parametric background model that could be subtracted from all spectra in the linescan to reveal features below 110 meV in transmission spectra without introducing artefacts in the aloof spectra and vice versa; therefore, the background model was fit to the spectra after the 100 meV ZO phonon signal.

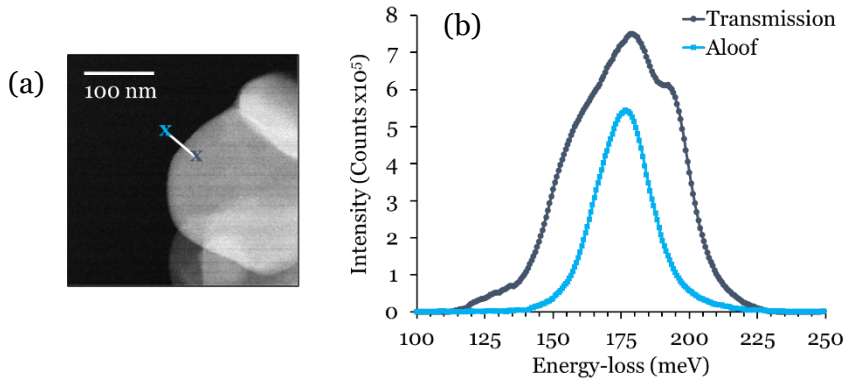

Figure 6.4. (a) ADF image of h-BN nanoflake showing the position of the linescan across the flake edge. Linescan length = 50 nm, 250 pixels along the linescan. (b) Background subtracted transmission (29 nm impact parameter) and aloof (21 nm impact parameter) beam spectra from h-BN at the two extremes of the linescan with α = 33 mrad and β = 28 mrad.

The dipole region (170-210 meV) of the transmission spectrum acquired with a 29 nm impact parameter looks different from that observed earlier (Figure 6.3c). The strongest spectral feature is a broad and asymmetric peak at 179 meV. When the electron beam is near the edge on a h-BN nanoflake, another HPhP is excited at the edge-surface of the flake peaking at 184 meV (Govyadinov et al., 2017a). The 179 meV signal corresponds to a convolution of the volume and edge-surface HPhP signals, referred to as the convolved HPhP (Table 6.1). Other spectral features include the bulk, TO/LO and LA mode signals. The aloof beam spectrum with a 21 nm impact parameter looks starkly different from the transmission spectrum, showing only one sharp volume HPhP signal.

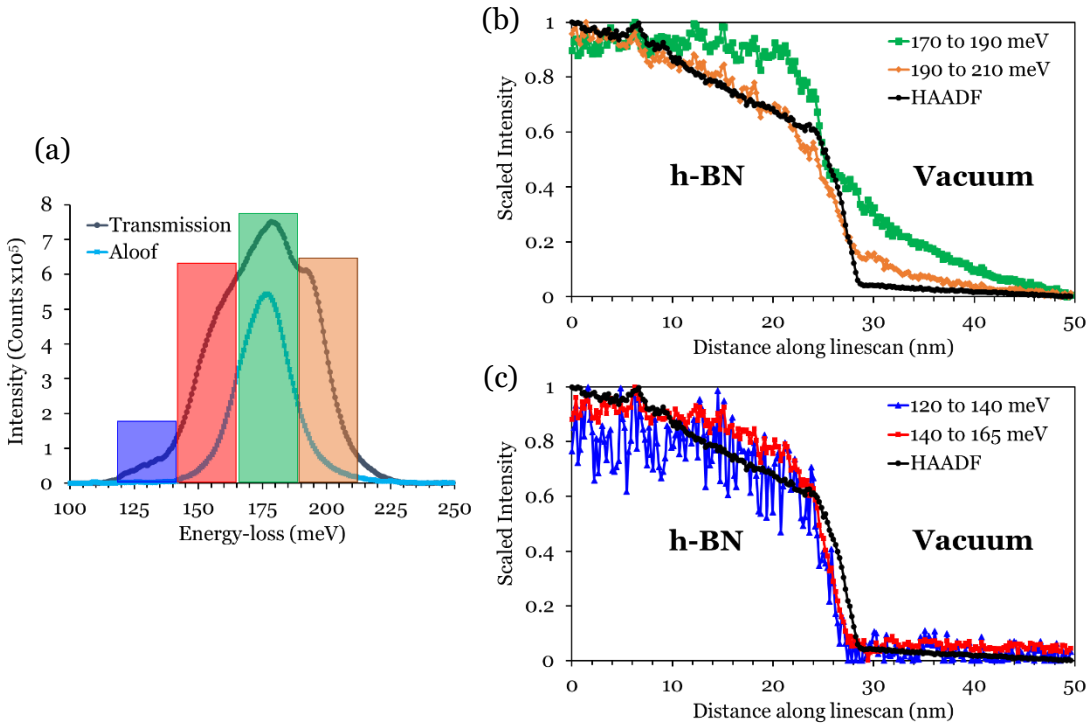

Figure 6.5. (a) Background subtracted transmission and aloof beam spectra from the two extremes of the linescan shown in Figure 6.4 depicting the integration windows chosen for determining the spatial variation of impact and dipole signals along the linescan. (b) Spatial variation of dipole signals along the linescan overlaid on the HAADF profile. (c) Spatial variation of impact signals along the linescan overlaid on the HAADF profile.

To map the spatial variation of impact and dipole signals across the h-BN/vacuum edge, the signals were integrated over 20 – 25 meV windows and the integrated intensities were plotted as a function of the distance of the probe along the linescan. Figure 6.5a shows the positions of the integration windows relative to spectral features in both transmission and aloof beam modes. The background subtracted signal must be normalized by the total signal going into the spectrometer to account for elastic scattering and thickness effects along the linescan. However, the center of the ZLP was saturated during EELS acquisition. Therefore, the signal was normalized relative to the negative tail of the ZLP, integrated between -250 and -200 meV. No energy-gain signal is observed on the negative ZLP tail; thus, this signal is mainly proportional to the number of electrons entering the spectrometer. The spatial variation profiles of dipole signals are shown in

Figure 6.5b while that of impact signals are shown in Figure 6.5c, with the simultaneously acquired HAADF signal profile overlaid on both plots for comparison.

The spatial variation profile of the bulk signal follows a decreasing HAADF profile up to ~10 nm impact parameter, which confirms that it is a bulk signal. The signal then drops more rapidly from ~60% of its maximum at ~10 nm impact parameter to ~15% of its maximum at the h-BN/vacuum edge. Meanwhile, the HAADF signal drops from ~60% of its maximum at ~5 nm impact parameter to ~4% of its maximum at the edge. Thus, the bulk signal in h-BN is more delocalized than the HAADF signal and this is attributed to the begrenzungs effect which is characteristic of a bulk dipole energy-loss signal as the probe moves towards a boundary (R. F. Egerton, 2011; Venkatraman et al., 2018a). The signal in vacuum comes from the tail of the aloof signal associated with the volume HPhP at 176 meV (see Figure 6.5a).

The convolved HPhP signal profile does not follow the HAADF signal profile; it is approximately constant up to ~10 nm impact parameter after which it drops rapidly till the probe is ~3 nm from the edge. It then decreases less steeply to ~30% of its maximum value at the edge. The constancy in the convolved HPhP profile with decreasing flake thickness (shown by the HAADF profile) implies that it is more of a surface signal. This is expected as the edge-surface HPhP is more intense than the volume HPhP in the transmission spectrum due to the probe being close to the flake edge. Thus, it dominates the spatial variation profile. It also suggests that the convolved HPhP signal is much more delocalized than the bulk which is characteristic of a polariton signal (Konečná, Venkatraman, et al., 2018b). The inflection observed in the convolved HPhP profile when the probe is ~3 nm from the interface can be attributed to increased excitation of the edge-surface HPhP accompanied by a simultaneous decrease in the volume HPhP excitation.

The aloof signal from the HPhPs is the only spectral feature observed as the probe moves into vacuum, so the spatial variation in vacuum is associated with this signal.

The spatial variation profiles of impact signals shown in Figure 6.5c are very different from those of dipole signals; the impact signal profiles are generally sharper. The TO/LO signal profile is slightly off the HAADF profile when the probe is in h-BN and farther than ~5 nm from the edge. This is due to the tail of the edge-surface HPhP signal contributing to the spatial variation of the TO/LO mode. The TO/LO and HAADF profiles start to drop at the same point, although the phonon signal profile seems to be sharper than the HAADF signal. The LA signal profile is much noisier than the other profiles due to a low SNR in the spectrum. However, due to negligible tails from dipole polariton signals, the LA signal profile traces the HAADF profile much better than the TO/LO profile. Both the HAADF and the LA signal profiles start to drop steeply at the same point too, when the probe is ~5 nm from the edge, and as with the TO/LO profile, the LA profile is observed to be sharper than the HAADF profile. All signal profiles in the figure drop to approximately zero as the probe approaches the edge and have negligible intensity as the probe moves into vacuum. The absence of an aloof signal confirms the non-dipole character of the excitation mechanism for these phonon modes.

An interesting observation is that the impact signal profiles drop to approximately zero ~1.5 nm before the HAADF profile. This might be due to an amorphous layer, ~1.5 nm thick, on the surface of the flake (see Figure 6.6). As the impact signals originate from BZB phonon modes, an absence of crystallinity implies that there are no Brillouin zones and thus, phonon modes from BZBs cannot be excited by the probe. The HAADF signal is known to have high spatial resolution and is routinely used to acquire atomic resolution STEM images. As the impact signal profiles trace the HAADF profile at the edge of the

flake, it can be inferred that these signals have high spatial resolution (Venkatraman et al., 2019).

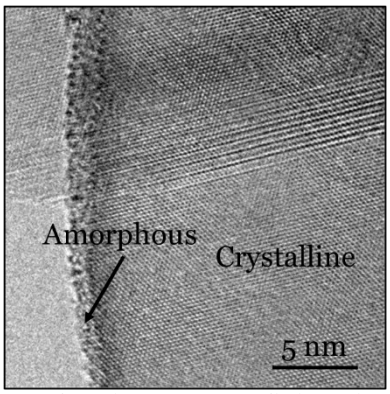

Figure 6.6. BF TEM image of a h-BN nanoflake showing ~1.5 nm thick surface amorphous layer.

6.4 Conclusion

In this chapter, the influence of probe convergence and spectrometer collection semi-angles on the vibrational spectrum from polar and crystalline h-BN obtained with monochromated STEM EELS has been explored. Specifically, optimum conditions for exciting and detecting phonon modes dominated by impact scattering of incident electrons in the forward scattering electron optical geometry were investigated. Employing a probe convergence semi-angle less than the (1000) Bragg angle of h-BN with 7 mrad collection results in only dipole scattering dominated modes associated with phonons and HPhPs from the central region of the hexagonal Brillouin zone contributing to the energy-loss spectrum. The volume and edge-surface HPhP modes are significantly affected by the probe position relative to the specimen edge; moving the probe closer to the specimen edge increases the intensity of the edge-surface HPhP.

Increasing the probe convergence to include BZBs while employing the same collection introduces many new spectral features that peak at 74, 134 and 160 meV and are associated with short-wavelength boundary phonon modes. The large momentum transfers involved in exciting these modes implies that they are impact scattering

dominated and their energy-loss signals have high spatial resolution. Opening up the spectrometer collection semi-angle to 28 mrad increases the total signal going into the spectrometer. Placing the probe relatively far away from the edge causes an increase in the HPhP signal along with the increased 134 and 160 meV impact signals due to which their intensities relative to the strongest dipole signal between 170 and 210 meV remain unchanged. However, there is a seven-fold increase in the relative intensity of the 74 meV impact signal. Reducing the probe convergence back to 10 mrad without changing the collection semi-angle significantly reduces the intensities of all impact signals, even when the total scattering angles available are equivalent to the case with 33 mrad probe convergence and 7 mrad collection.

The spatial variation profiles for impact and dipole signals are very different as the probe is moved across the edge of a h-BN nanoflake; the dipole signals show a characteristic attenuation due to the begrenzungs effect as the probe moves towards the interface. However, the bulk LO phonon signal is more localized than the HPhP signal. Also, the edge-surface HPhP dominates over the volume polariton along the linescan as the probe is always in the vicinity of an edge. In the vacuum, these signals follow the profile of a modified Bessel function which is typical for dipole energy-loss signals. The impact signal profiles are sharper and trace the HAADF profile more strictly when the probe is in h-BN, thereby confirming their high spatial resolution. These profiles drop to their minimum value roughly 1.5 nm before the HAADF signal, which is attributed to the presence of a 1.5 nm thick amorphous surface layer that cannot support BZB phonon modes.

In summary, this experimental investigation demonstrates that high spatial resolution impact vibrational modes can be excited and detected with a comparable signal-to-noise ratio to dipole modes in a polar material with monochromated STEM EELS in the

forward scattering geometry. The convergence semi-angle influences the visibility of these modes in the energy-loss spectrum much more than the collection semi-angle. For good visibility, it is imperative to employ a convergence semi-angle that encompasses multiple Brillouin zone boundaries and combine this with a collection semi-angle that maximizes the energy-loss signal. In the next chapter, we will switch gears to the aloof mode and explore the sensitivity of vibrational EELS to detect adsorbates on the surface of nanoparticles.

CHAPTER 7

PRELIMINARY INVESTIGATION OF THE DETECTION OF ADSORBATES ON NANOPARTICLES WITH ALOOF BEAM VIBRATIONAL EELS

7.1 Motivation

As seen in the previous chapters, most of the work presented in this dissertation has focused on transmission mode vibrational EELS where signals excited by two electron scattering mechanisms – dipole and impact – were investigated. It was inferred from previous chapters that while dipole signals are spatially delocalized from a few to tens of nanometers, impact signals are atomically resolved. The delocalization associated with dipole scattered signals can be leveraged to enhance surface sensitivity by positioning the electron beam outside the sample in the so-called aloof beam mode (Howie, 1983; Egerton, 2015; Crozier, 2017). As the electron beam does not transmit the sample, bulk modes are not effectively excited and thus, dipole surface signals dominate the spectrum.

One of the perceived advantages of the aloof beam mode is the minimization of radiation damage in the specimen caused by the electron beam depositing energy into the sample. Radiation damage (Egerton, 2019) in a S/TEM is broadly divided into two categories – ionization (radiolysis) and displacement damage (knock-on). Radiolysis is associated with inelastic scattering that deposits a few to hundreds of eV energy in the specimen resulting in a permanent breakage of chemical bonds. Knock-on damage occurs if the beam passes very close to an atom and the energy deposited by the beam is larger than the atom's displacement energy. It can be seen how the knock-on damage mechanism is completely shut-off in the aloof beam mode, and radiolysis is minimized due to largely reduced inelastic scattering. The minimized damage due to aloof beam vibrational EELS can be leveraged to explore surface bonding in radiation sensitive material systems like

zeolites, metal-organic frameworks (MOFs), biological materials, adsorbate species on catalysts etc.

In this chapter, sensitivity of vibrational EELS in the aloof-beam mode is explored to investigate the local bonding arrangements of adsorbate layers on substrate surfaces. This investigation would help answer fundamental questions relevant to the functionality of catalysis such as; which surfaces catalyze a reaction, which sites on the surface are active, what intermediate products are formed etc. … Placing the focused electron probe on the adsorbate layer of interest as in transmission vibrational EELS may cause substantial radiation damage which will hinder any characterization. In aloof beam vibrational EELS, the probe is placed a few nanometers away from the substrate surface, allowing us to leverage dipole scattering associated with long-range Coulomb interactions between the electron beam and adsorbate layers while minimizing radiation damage. To study adsorbate layers on nanoparticle surfaces with aloof beam vibrational EELS, we concentrate on three adsorbate/substrate systems because of their simplicity and overall scientific importance, viz. PVP on Au nanoparticles, CO_2 on MgO nanocubes and CO on Pt particles.

7.2 Methods

7.2.1 Sample preparation

7.2.1.1 PVP ligand on Au nanoparticles

Au nanoparticles, having an average diameter of 40 nm and enveloped by a PVP ligand shell of 5 – 7 nm thickness, were purchased as an aqueous solution from NanoComposix Inc. The solution was cleaned with DI water by centrifuging it and throwing away the supernatant liquid subsequently. This process was repeated five times

after which the powder collected at the bottom of the centrifuge tube was dried under a heat lamp and dry-dispersed on a TEM grid for STEM EELS analysis.

7.2.1.2 CO_2 on MgO nanocubes

MgO nanocubes were synthesized by collecting the smoke off of burning a Mg ribbon on the walls of a dry beaker and scraping it off. MgO is very hygroscopic in nature; therefore, care was taken to keep the surroundings dry. The cubes were surface-treated by heating them in flowing O_2 at 550°C for 5 hours in a RIG-150 microreactor. After allowing the cubes to cool down, CO_2 was flowed through the surface treated cubes at room temperature for 1 hour for adsorption.

7.2.1.3 CO on Pt/CeO_2 metal-support nanoparticles

CeO_2 nanocubes were synthesized hydrothermally following the method proposed by Yang et al. (Yang et al., 2007, 2009). First, high purity $Ce(NO_3)_3 \cdot 6H_2O$ (99.99% pure, Alfa Aesar) was dissolved into distilled water and mixed with a 12 M NaOH (99.99% pure, Sigma Aldrich) solution and the mixture was stirred continuously for 30 minutes. The resulting slurry was then placed into a 50 mL autoclave and it was filled with deionized water up to ~80% of the total autoclave volume. The autoclave was then heated to 200°C for 24 hours in a furnace and cooled to room temperature. CeO_2 precipitated during the synthesis and the precipitate was isolated by centrifugation, washed multiple times with deionized (DI) water, and dried at 60°C overnight in air.

An incipient wetness impregnation technique (Ertl et al., 2008) was used to deposit Pt nanoparticles onto CeO_2 nanocubes. With impregnation, metal salt precursors containing the desired cations are dissolved in water and then mixed with the support powder. The aqueous mixture will infiltrate the host powder via capillary forces or through

physical mixing. Subsequently, the mixture is dried and then calcined at a target temperature to burn off precursors. A platinum chloride solution was prepared by dissolving a known amount of $PtCl_4$ (99.99+% pure, Alfa Aesar) in DI water as a solvent. Impregnation was carried out in a mortar by dropwise addition of the $PtCl_4$ solution equivalent to the pore volume of the CeO_2 and physically mixing the system with a pestle. After continuously mixing for 30 minutes, the resulting slurry was dried at 60°C in air for two hours to yield a powder, which was calcined at 400°C for 3 hours to facilitate decomposition of $PtCl_4$ into Pt.

The resulting Pt/CeO_2 metal-support nanoparticles were surface-treated by heating in flowing H_2 at 400°C for 3 hours in a RIG-150 microreactor. They were cooled down and CO was flowed through a bed of surface treated Pt/CeO_2 nanoparticles at room temperature for half an hour for adsorption.

7.2.2 Monochromated STEM EELS measurements

Aloof beam vibrational EELS acquisitions were performed with an aberration-corrected, monochromated Nion UltraSTEM 100, operated at 60 kV. The probe convergence and spectrometer collection semi-angles were either 28 or 19 and either 12 or 20 mrad, respectively. Due to aberration-correction up to the 5^{th} order, it was routinely possible to obtain 1 Å sized probes with high convergence angles. However, achieving atomic resolution with STEM imaging was not a strict requirement while performing these experiments. The FWHM of energy spread in the monochromated probe was 16 meV for most experiments. After installation of the Nion Iris spectrometer at ASU, this achievable energy resolution improved to 10 meV. EELS measurements were made as point-and-shoot spectra from different aloof beam positions of the beam relative to the specimen. An energy-dispersion of 0.66 or 1 meV per channel was used to record spectra. The vibrational

signal from small amounts of adsorbates on catalyst surfaces is weak, hence, exposure times for EELS acquisition were of the order of tens of seconds. Processing of acquired spectra was done using the Gatan Microscopy Suite. Parametric two-window background subtraction was performed using the power law model as stated in Chapter 3. Energy-loss spectra were calibrated by setting the center of the ZLP to 0 meV; thus, the error in signal spectral position is the channel width.

7.3 Results and discussion

7.3.1 PVP ligand on Au nanoparticles

Figure 7.1a is an ADF STEM image of Au nanoparticles enveloped by a PVP ligand shell. Presence of the ligand shell leads to mono-dispersion of the particles and they appear well separated. Figure 7.1b shows the raw aloof-beam energy loss spectrum and the background model employed while Figure 7.1c shows the background-subtracted spectrum from the PVP/Au system.

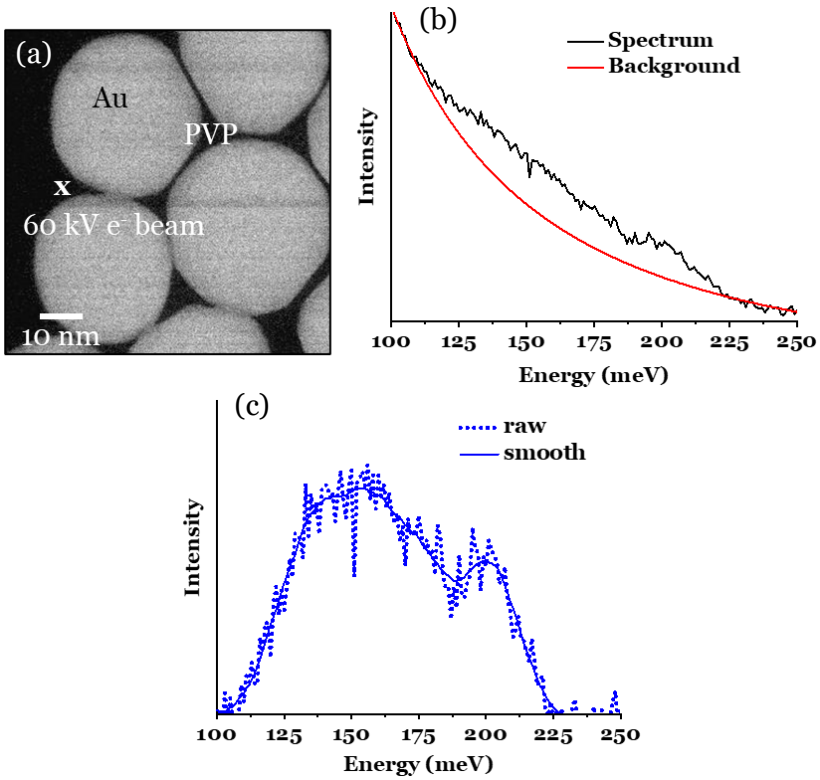

Figure 7.1. (a) Monochromated ADF STEM image of PVP/Au system. The PVP ligand shell is seen as weak contrast between adjacent 40 nm sized Au nanoparticles. (b) The raw aloof beam vibrational spectrum from PVP on Au acquired with 40s exposure and the background model employed. (c) The background-subtracted spectrum from PVP on Au showing two strong spectral features at 156 and 201 meV. Impact parameter = 8 nm.

Two strong signal peaks are observed in Figure 7.1c at 156 and 201 meV. Both are very broad and the asymmetry of the 156 meV signal suggests it to be a convolution of multiple peaks. Literature suggests that the 156 and 201 meV peaks might correspond to the C-N stretch in a tertiary amine and the C=O stretch in a cyclic ketone, respectively. The Fourier Transform InfraRed (FTIR) spectrum from pure PVP (Figure 7.2a) taken from the literature shows three major peaks at 160 meV, 177.5 meV and 210 meV associated with the C-N stretch and CH_2 wag, the C-N stretch and CH_2 scissor, and the C-N and C=O stretch, respectively (Borodko et al., 2006). Convolving the FTIR spectrum with a Gaussian broadening function to simulate the poorer energy resolution of EELS shows

discrepancies when compared with EELS spectrum, as shown in Figure 7.2b. These might be due to local structural disorder in the ligand shell, or due to radiation damage caused by the electron beam. Apart from being limited by the energy resolution, the spherical shape of the substrate and hence, the ligand shell leads to a small effective path length over which the aloof-beam signal is integrated leading to a low signal to noise ratio. In light of these limitations, to further explore the spectral difference it may be necessary to move towards cubic morphologies or larger sizes for substrates, and adsorbates which have less structural disorder.

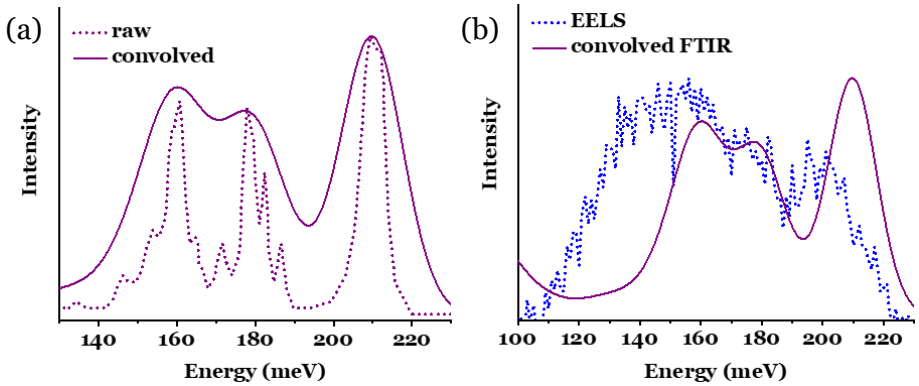

Figure 7.2. (a) The raw FTIR spectrum from pure PVP and after it is convolved with the EELS instrumental response (Borodko et al., 2006). (b) A comparison between the background-subtracted aloof beam EELS from the PVP/Au system and the convolved FTIR from pure PVP.

7.3.2 CO_2 adsorbed on MgO nanocubes

CO_2 adsorbed on MgO nanocubes fits the requirements of cubic substrate morphology and less adsorbate structural disorder. The adsorption of CO_2 on MgO results in formation of a thin layer of $MgCO_3$ on the surface. CO_2 adsorption was confirmed by performing Diffuse Reflectance Infrared Fourier Transform Spectroscopy (DRIFTS) (Mitchell, 1993), which has higher surface sensitivity compared to other FTIR variants. The DRIFT spectrum, before and after convolution with the broadening function to match

the EELS energy-resolution, shown in Figure 7.3, consists of signals associated with the vibrational modes of the carbonate and bicarbonate species at ~173 and 187 meV, and the H_2O bond-bend and bond-stretch vibrational modes at ~207 and ~405 meV, respectively (Ramis et al., 1991; Philipp & Fujimoto, 1992; Pacchioni, 1993). This leads us to hypothesize the formation of hydrated $MgCO_3$ species on the surface, as MgO is a well-known hygroscopic material.

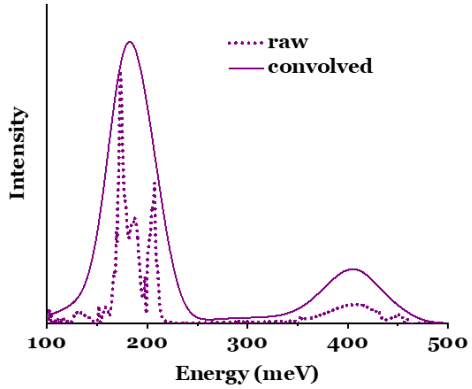

Figure 7.3. Diffuse reflectance infrared Fourier transform (DRIFT) spectrum from CO_2 adsorbed on MgO nanocubes – raw and after convolution with the EELS instrument response. Vibrational signals associated with carbonate, bicarbonate and water species can be observed in the spectrum.

Figure 7.4a is an ADF STEM image showing the probe position relative to the nanocubes for aloof-beam EELS. Figure 7.4b shows the raw aloof beam vibrational spectrum and the background model employed, while Figure 7.4c shows the background-subtracted spectrum from the hydrated $MgCO_3$/MgO system. We were unable to interpret the signals at 142 and 198 meV. However, the strongest signal in the spectrum at 344 meV is well known to correspond to the C-H vibrational stretch, which is not present in hydrated $MgCO_3$. The suggests that the electron beam triggers a reaction between CO_2 and H_2O to produce hydrocarbon species. Thus, the aloof-beam technique cannot be regarded as completely radiolysis free at the current 10 nm impact parameter and more systematic

experiments are in future required to determine the optimum conditions to control radiation damage.

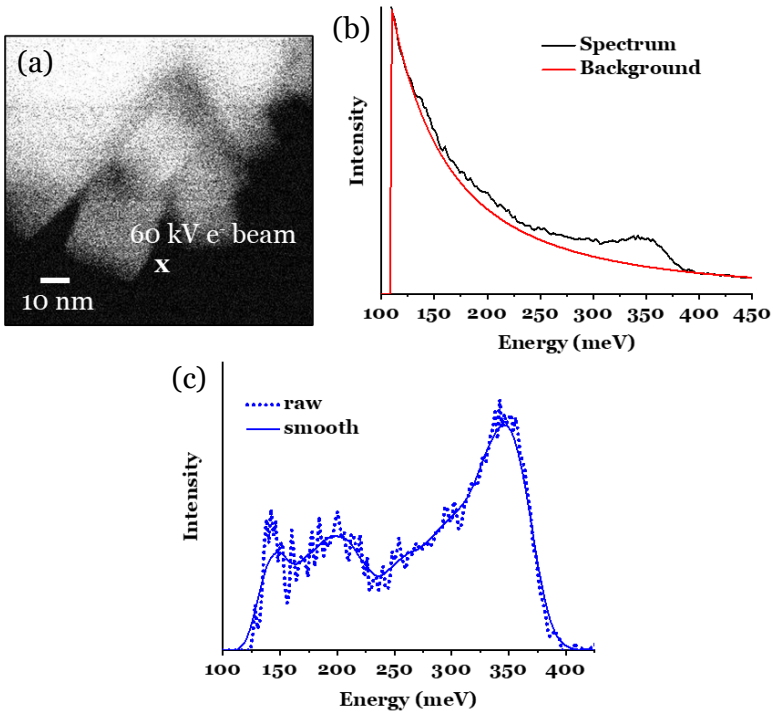

Figure 7.4. (a) Monochromated ADF STEM image of the MgO nanocubes with hydrated $MgCO_3$ adsorbed on them. (b) The raw aloof beam vibrational spectrum (40s exposure) from the specimen and the background model employed. (c) The background-subtracted spectrum from hydrated $MgCO_3$/MgO. Impact parameter = 10 nm.

7.3.3 CO adsorbed on Pt/CeO_2 metal-support nanoparticles

Aloof beam vibrational EELS measurements were also performed on the CO/Pt system. It is well known that CO adsorbs as a monolayer on Pt with a binding energy of 1.5 eV/molecule and a sticking probability of 0.8 at room temperature (Steininger et al., 1982). DRIFTS confirmed CO adsorption as the spectrum (Figure 7.5) showed a signal peak corresponding to the C-O "on-top" vibrational mode on Pt between 255 and 261 meV.

The spectrum was convolved with the EELS instrumental response to predict what we can expect from EELS.

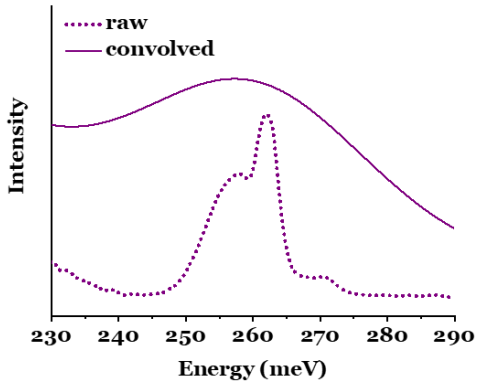

Figure 7.5. DRIFT spectrum from CO adsorbed on Pt nanoparticles supported on CeO_2 nanocubes – raw and after convolution with the instrument response function. A signal associated with the C – O 'on top' mode is observed between ~255 and 261 meV in the spectrum. The small bump at 270 meV corresponds to CO in the gas phase (Gao et al., 2008).

As CO forms a monolayer on Pt, it was decided to use large micron-sized Pt particles to have good signal-to-noise ratio (SNR) for preliminary EELS measurements. Pt micro-particles having an average diameter of 10 μm were purchased from Sigma Aldrich. The particles were surface treated, and CO was adsorbed as mentioned in Section 7.2.1.3. Figure 7.6a is an ADF STEM image of the Pt microparticle surface showing the relative probe position. Figure 7.6b shows the aloof beam energy-loss spectrum from the CO/Pt system. A signal peak at 258 meV corresponding to the C-O "on-top" vibrational mode is observed, and the signal is broad and noisy which might be due to slightly different orientations of the CO molecule relative to the Pt surface, apart from the limited energy resolution and SNR. However, we can claim to have successfully detected a monolayer of an adsorbate on the surface of a micrometer sized particle with aloof-beam EELS.

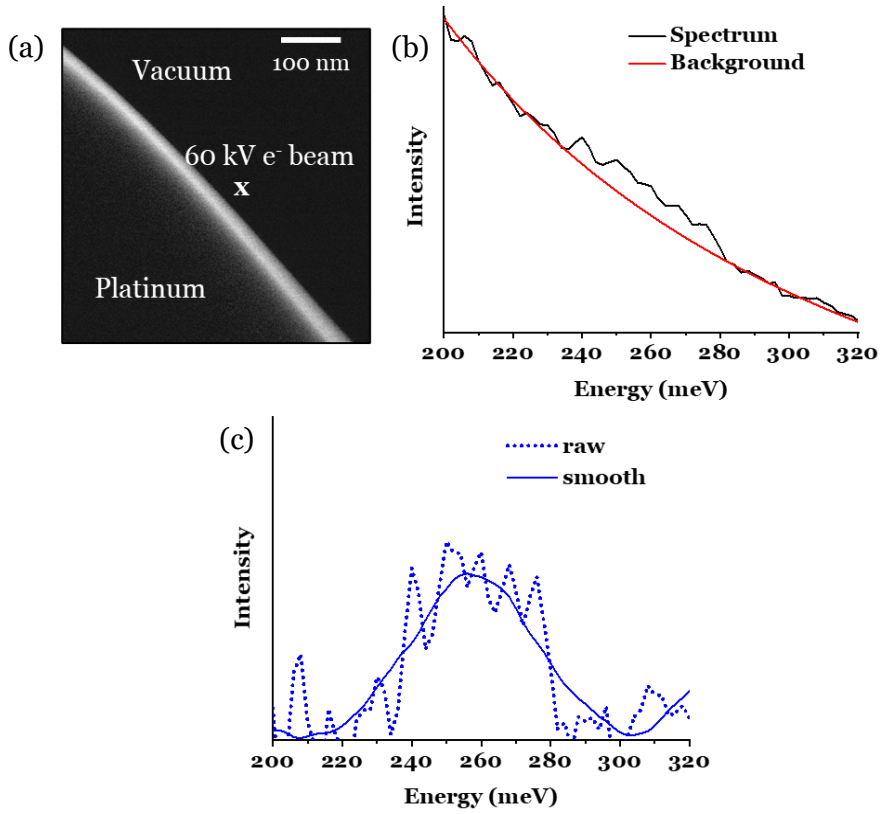

Figure 7.6. (a) Monochromated ADF STEM image of the Pt microparticle. (b) The raw aloof beam vibrational spectrum from a monolayer of CO on a Pt microparticle (20s exposure) and the background model employed. (c) Background-subtracted spectrum with 17 nm impact parameter. The C – O 'on-top' vibrational mode is observed at ~260 meV.

Sometime after these measurements the Gatan spectrometer attached to ASU's Nion microscope was replaced with the Nion Iris spectrometer which improved the energy-resolution to 8 – 10 meV in routine vibrational EELS measurements. The EELS detector was also changed to a CMOS type which had the further advantage of much faster read-outs. A second experiment was undertaken to detect a CO monolayer on a Pt nanoparticle supported on a CeO_2 nanocube. Figure 7.7a shows a monochromated ADF STEM image of the probe position relative to the Pt/CeO_2 nanoparticle ensemble while Figure 7.7b shows the background subtracted aloof beam vibrational energy-loss spectrum acquired with 6 nm impact parameter. A strong peak is observed at ~61 meV which can be

identified to be associated with aloof beam surface phonon polaritons from the CeO_2 nanocube (Crozier et al., 2017). The spectrum also shows a feature roughly around 150 meV which is much weaker than the polariton signal. Hence, the background from the polariton signal was also subtracted to get Figure 7.7c which shows a peak at ~158 meV which is probably convolved with a weak and broad peak centered roughly around 200 meV. These vibrational signals are associated with uni- and bi-dentate carbonate species on CeO_2 (Li et al., 1989; Bozon-Verduraz & Bensalem, 1994; Binet et al., 1994). The spectrum also shows a hint of a signal at ~261 meV which might be from the CO monolayer. This cannot be said with certainty as it was not possible to obtain a higher signal-to-noise-ratio (SNR) in the signal.

It can thus be concluded that the experimental study of adsorbates on catalyst surfaces at high spatial resolution with vibrational EELS still needs improvement in instrumentation, although the preliminary experiments presented here demonstrate that it should be possible. The main issue in the experiments presented has been poor SNR. This can be improved with the use of direct electron detectors as has been done for biological and other radiation sensitive materials. These detectors have a detective quantum efficiency of close to 1, which describes that the SNR in a spectrum recorded by them is almost equal to that in a spectrum recorded by an ideal detector. An improved energy resolution would also enable better detection of weak vibrational signals from adsorbates.

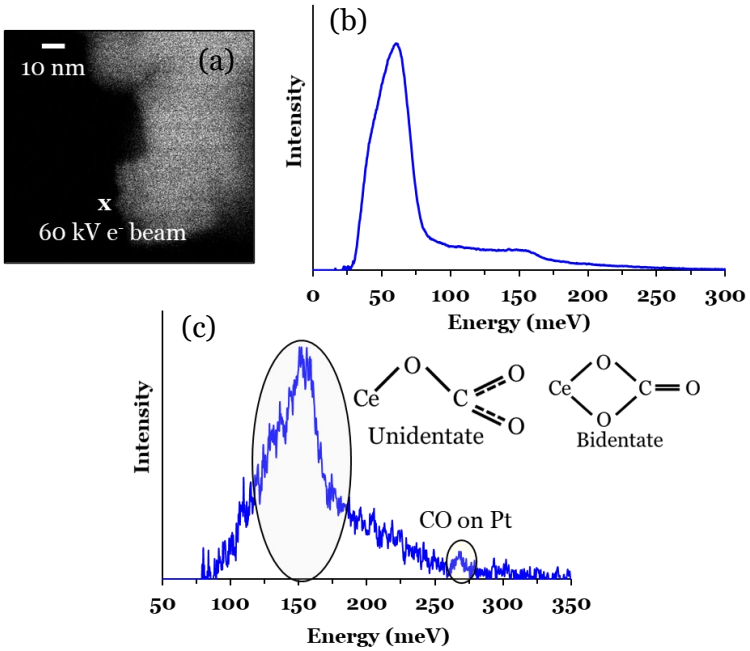

Figure 7.7. (a) Monochromated ADF STEM image of the Pt/CeO_2 nanoparticle ensemble. (b) Background-subtracted aloof beam vibrational spectrum (30s exposure) from a CO monolayer on a Pt nanoparticle supported on a CeO_2 nanocube acquired at 6 nm impact parameter showing the aloof beam polariton signal from CeO_2 at ~61 meV. (c) Removing the background from the polariton signal shows the signal from uni- and bi-dentate carbonates and a hint of signal from the "on-top" C – O mode at ~261 meV.

CHAPTER 8

CONCLUSION

The scope of this research program was to explore the dependence of intensity, spectral position, and spatial resolution of a vibrational energy-loss signal on the dominant excitation mechanism of the associated mode. It is shown that in a model material with mixed ionic-covalent bonding like amorphous SiO_2, the Si-O asymmetric bond-stretch mode is dominantly excited by electron dipole scattering. The experimental spatial variation of the signal as the probe is moved across an abrupt SiO_2/Si interface is accurately modelled using the classical dielectric theory with an optical dielectric function; spatial resolution in the signal is 5-20 nm. The begrenzungs effect, characteristic of dielectric theory, causes an exponential attenuation of signal intensity as the impact parameter decreases in SiO_2. A weak vibrational response is observed at a different spectral position when the probe is within 5 nm of the interface, with the signal intensity increasing exponentially towards the interface. It was also inferred from dielectric theory that the vibrational energy-loss spectra for thin-films typical of TEM samples have a significant contribution from the coupling between entrance and exit surface vibrational modes, yielding a signal at a different spectral position from the bulk.

The coupled surface energy-loss signal in SiO_2 is the result of a hybridization between the associated vibrational mode and the broad frequency electromagnetic radiation field of the fast electron. Such hybridized vibrational modes are referred to as surface phonon polaritons (SPhPs). The spatial variation of this SPhP in SiO_2 was explored with numerical dielectric theory simulations as the probe is moved towards a truncated SiO_2/vacuum surface in a 40 nm thick film. It is observed that as the probe moves towards the truncated surface, there is a decoupling of the parallel entrance and exit surface vibrational modes that leads to the excitation of the uncoupled single surface SPhP mode.

This is accompanied by a weak increase in the coupling between perpendicular entrance or exit and edge surfaces, referred to as the coupled edge SPhP mode. The interplay between the coupled entrance-exit, and edge, and the uncoupled single surface SPhP modes was explored theoretically in a 40 nm thick SiO_2 film patterned with a 2x2 array of holes. The most striking effect of the patterning is the simultaneous excitation of the coupled entrance-exit and the uncoupled single surface SPhPs when the beam is at the center of the array. Without the patterning, only the coupled entrance-exit SPhPs are excited. The weak effect of the coupled edge SPhP is observed only when the beam is very close to the hole edge.

It was then experimentally demonstrated that in a covalently bonded material having negligible bond dipole moment like single crystal Si, all vibrational energy-loss signals originate from electron impact scattering excitations of phonons. As observed earlier, the significant surface coupling contribution from TEM thin-films and the existence of phonon polaritons is intricately associated with a dipole scattering dominant excitation, and hence, spectral features corresponding to them are not observed in experiments on Si. A spatial resolution of better than 2 Å was achieved with both acoustic and optical Si phonons with the signal intensity being strongest with the probe positioned on atomic columns. Similar sub nm spatial resolution was also experimentally demonstrated in a material with ionic bonding character like SiO_2 by choosing the Si-O *symmetric* bond-stretch energy-loss signal to estimate the abruptness of the SiO_2/Si interface. The energy-loss signal associated with this optical vibrational mode has major impact scattering contribution which needs to be isolated from the tails of the preceding and succeeding dipole signals to achieve the sub-nm spatial resolution.

Vibrational EELS experiments were then performed on another crystalline material with mixed ionic-covalent bonding, hexagonal BN, to explore the influence of

probe convergence and spectrometer collection angles on the visibility of impact scattering dominant energy-loss signals. Unlike Si, the vibrational spectrum from h-BN is complicated by strong dipole signals from volume and surface phonon polaritons from the center of the hexagonal Brillouin zone. As the probe convergence angle is increased to include h-BN Brillouin zone boundaries (BZBs), spectral features that were not observed with a small scattering angle configuration become visible. These features originate from the impact scattering excitation of short wavelength BZB phonon modes which are associated with large scattering angles (high-momentum transfer). An interesting observation that needs further investigation is that the vibrational spectrum acquired with a large convergence and small collection is drastically different from that acquired with a small convergence and large collection. It is also observed that the spatial variation of BZB phonon impact signals traces the HAADF profile, which demonstrates high spatial resolution, unlike the profiles of dipole signals which are delocalized.

Finally, the delocalized nature of the dipole dominant energy-loss signal was leveraged in the aloof mode (thereby minimizing radiation damage) to detect the vibrational response from adsorbates on catalyst nanoparticles. The sensitivity of the technique was demonstrated by detecting a CO monolayer chemisorbed on a micrometer sized Pt particle. It was concluded from preliminary experimental results that instrumentation limitations currently hinder the ultimate goal of a facet-dependent study of bonding arrangements between adsorbates and nanoparticle catalysts. This could be improved in the future by employing direct electron detectors to improve the SNR in the acquired spectrum.

Future work

1. **Exploring the excitation and manipulation of surface phonon polaritons with experimental vibrational EELS**

As seen with numerical simulations in Chapter 4, the excitation of SPhPs can be manipulated by patterning nanoscale specimens and this manipulation can be characterized using vibrational EELS. Future experiments need to be performed to validate these simulations for the SiO_2 patterned thin-film, and the effect of carbon-coating on the excitation of SPhPs needs to be understood better, both experimentally and theoretically. Once such an understanding is developed, an investigation into the applications of precisely controlled PhPs like reducing IR losses in dielectric films, performing non-radiative heat transfer etc. would be of much interest.

2. **Characterization of defects with atomic resolution vibrational EELS**

It was experimentally demonstrated in Chapter 5 that a spatial resolution of better than 2 Å is achievable with vibrational energy-loss signals in covalently bonded Si. Such unprecedented spatial resolution can be leveraged to extract local bonding information at defects like impurities, vacancies, dislocations, stacking faults, grain boundaries etc. Thus, further experiments could first apply this technique to study defects in materials with *no ionic bonding character* like polycrystalline Si, graphene, carbon nanotubes etc., so as to avoid any complications from dipole scattering. For example, in polycrystalline Si oriented along the <110> zone axis, two perfect dislocations can be observed: a 60° dislocation which dissociates into 30° and 90° partials that have a stacking fault between them, and a screw dislocation which dissociates into two 30° partials (Kittler & Reiche, 2011). In the few tens of atomic layers close to the dislocation core, the Si lattice is going to be strained, which will alter the spectral position of a local vibrational mode, relative to that from an ideal lattice. Vibrational EELS linescans can then be performed across the dislocation line

to investigate the spatial sensitivity of the technique to tensile and compressive strains on either side of the dislocation. The spectral position of the vibrational excitation will decrease for tensile strains and increase for compressive strains relative to that from the ideal lattice. Similar investigations can be taken up to explore bonding arrangements at atomic heterogeneities in graphene or carbon nanotube, and correlate them with the electronic properties that these materials tend to offer. Once a good understanding of impact scattering from these heterogeneities is developed, bonding at defect cores can be characterized in ionic materials as well with atomic resolution vibrational EELS.

3. Realizing surface-enhanced vibrational EELS as a technique to enhance the detection sensitivity of aloof-beam EELS

In Chapter 7, it was experimentally demonstrated that aloof-beam vibrational EELS had enough sensitivity to detect a monolayer of CO on a Pt microparticle. However, poor SNR due to current instrumental limitations hindered the undisputed detection of a CO monolayer on a Pt *nanoparticle*. With improved detection capabilities, the presented experiments could be repeated to explore facet-dependent bonding arrangements at adsorption sites on catalyst surfaces and correlate them with atomic structure. One particular experimental investigation would be enhancement of the vibrational signal from adsorbates by exploiting the electromagnetic coupling between the adsorbate's vibrational mode and the substrate's local surface plasmon or phonon polariton mode, similar to surface enhanced Raman spectroscopy (SERS) (Stiles et al., 2008). This has been theoretically studied by Konečná et al. (Konečná, Neuman, et al., 2018) who found signal enhancement by an order of magnitude for the coupled system of a h-BN antenna and a 4,4'-bis(N-carbazolyl)-1,1'-biphenyl (CBP) molecular shell. Enhancement of vibrational signals due to such electromagnetic coupling can further improve the sensitivity of the technique for it to be extended to studying fractional layers or individual

adsorbate molecules (Kordahl & Dwyer, 2019). As was shown in Chapters 5 and 6, there are vibrational modes in all kinds of materials that are dominantly excited by electron impact scattering. Another interesting experiment would be to place the electron beam on an adsorbate layer of interest and get a potential atomic resolution impact signal from it. The main challenge would be radiation damage and subsequent desorption of the adsorbate. This can be circumvented by conducting an in situ experiment where the damaged and desorbed adsorbate is continuously replaced by new molecules from the gaseous environment surrounding the catalyst.

REFERENCES

Abney, W. D. W., & Festing, L. (1881). XX, On the influence of the atomic grouping in the molecules of organic bodies on their absorption in the infra-red region of the spectrum. *Philosophical Transactions of the Royal Society of London*, *172*, 887–918.

Angstrom, K. (1889). Ofversigt af K. *Vetensk. Akd. Forh*, *46*, 549.

Angstrom, K. (1890). Contributions to the knowledge of the absorption of heat rays by the various parts of the atmosphere. *Wied. Ann*, *39*, 267–295.

Arai, M., Hannon, A., Taylor, A., Wright, A., Sinclair, R., & Price, D. (1992). High resolution S (Q, E) measurement on g-SiO2. *Physica B: Condensed Matter*, *180*, 779–781.

Ashcroft, N. W., & Mermin, N. D. (2011). *Solid State Physics*. Cengage Learning. https://books.google.com/books?id=x_s_YAAACAAJ

Asmis, K. R. (2012). Structure characterization of metal oxide clusters by vibrational spectroscopy: Possibilities and prospects. *Physical Chemistry Chemical Physics*, *14*(26), 9270. https://doi.org/10.1039/c2cp40762k

Atwater, H. A., Wong, S. S., Ahn, C. C., Nikzad, S., & Frase, H. N. (1993). Analysis of monolayer films during molecular beam epitaxy by reflection electron energy loss spectroscopy. *Surface Science*, *298*(2), 273–283. https://doi.org/10.1016/0039-6028(93)90039-M

Bakker, H. J., & Skinner, J. L. (2010). Vibrational Spectroscopy as a Probe of Structure and Dynamics in Liquid Water. *Chemical Reviews*, *110*(3), 1498–1517. https://doi.org/10.1021/cr9001879

Balandin, A. A. (2011). Thermal properties of graphene and nanostructured carbon materials. *Nature Materials*, *10*(8), 569–581. https://doi.org/10.1038/nmat3064

Batson, P. E (1986). High resolution electron energy loss spectrometer for the scanning transmission electron microscope. *Rev. Sci. Inst*, *57*, 43–48.

Batson, P. E. (1995). Near-atomic-resolution EELS in silicon-germanium alloys. *Journal of Microscopy*, *180*(3), 204–210. https://doi.org/10.1111/j.1365-2818.1995.tb03679.x

Batson, P. E, Dellby, N., & Krivanek, O. L. (2002). Sub-ångstrom resolution using aberration corrected electron optics. *Nature*, *418*(6898), 617–620.

Bethe, H. (1930). Zur theorie des durchgangs schneller korpuskularstrahlen durch materie. *Annalen Der Physik*, *397*(3), 325–400.

Bihr, J. (1991). Design of an analytical TEM with integrated imaging Ω-spectrometer. *Proceedings of the 49th Annual Meeting of EMSA, 1991*, 354–355.

Binet, C., Badri, A., Boutonnet-Kizlingt, M., & Lavalley, J.-C. (1994). FTIR Study of Carbon Monoxide Adsorption on Ceria: COZ- Carbonite Dianion Adsorbed Species. *J. CHEM. SOC. FARADAY TRANS.*, *90*, 6.

Boersch, H., Geiger, J., & Hellwig, H. (1962). STEIGERUNG DER AUFLÖSUNG BEI DER ELEKTRONEN-ENERGIEANALYSE. *PHYSICS LETTERS*, *3*(2), 3.

Boersch, H., Geiger, J., & Stickel, W. (1964). Das Auflösungsvermögen des elektrostatisch-magnetischen Energieanalysators für schnelle Elektronen. *Zeitschrift Für Physik*, *180*(4), 415–424.

Boersch, H. (1954). Experimentelle Bestimmung der Energieverteilung in thermisch ausgelösten Elektronenstrahlen. *Zeitschrift Für Physik*, *139*(2), 115–146.

Bohm, D., & Pines, D. (1951). A Collective Description of Electron Interactions. I. Magnetic Interactions. *Physical Review*, *82*(5), 625–634. https://doi.org/10.1103/PhysRev.82.625

Borodko, Y., Habas, S. E., Koebel, M., Yang, P., Frei, H., & Somorjai, G. A. (2006). Probing the Interaction of Poly (vinylpyrrolidone) with Platinum Nanocrystals by UV–Raman and FTIR. *The Journal of Physical Chemistry B*, *110*(46), 23052–23059.

Bosman, M., Keast, V. J., Watanabe, M., Maaroof, A. I., & Cortie, M. B. (2007). Mapping surface plasmons at the nanometre scale with an electron beam. *Nanotechnology*, *18*(16), 165505.

Bozon-Verduraz, F., & Bensalem, A. (1994). IR studies of cerium dioxide: Influence of impurities and defects. *Journal of the Chemical Society, Faraday Transactions*, *90*(4), 653. https://doi.org/10.1039/ft9949000653

Brehm, M., Taubner, T., Hillenbrand, R., & Keilmann, F. (2006). Infrared Spectroscopic Mapping of Single Nanoparticles and Viruses at Nanoscale Resolution. *Nano Letters*, *6*(7), 1307–1310. https://doi.org/10.1021/nl0610836

Browne, M. T. (1971). Electron energy analysis in a vacuum generators HB5 STEM. *Scanning Electron Microscopy*, *1*, 827–833.

Browning, N. D., Arslan, I., Erni, R., & Reed, B. W. (2011). Low-loss EELS in the STEM. In *Scanning Transmission Electron Microscopy* (pp. 659–688). Springer.

Brydson, R., Sauer, H., Engel, W., & Zeitler, E. (1991). EELS as a fingerprint of the chemical co-ordination of light elements. *Microsc. Microanal. Microstruct.*, *2*(2–3), 159–169. https://doi.org/10.1051/mmm:0199100202-3015900

Cabannes, J. (1928). Un nouveau phénomène d'optique: Les battements qui se produisent lorsque des molécules anisotropes en rotation et vibration diffusent de la lumière visible ou ultraviolette. *CR Acad Sci*, *186*, 1201–1202.

Cao, Y., Manjavacas, A., Large, N., & Nordlander, P. (2015). Electron Energy-Loss Spectroscopy Calculation in Finite-Difference Time-Domain Package. *ACS Photonics*, *2*(3), 369–375. https://doi.org/10.1021/ph500408e

Castaing, R. (1975). Energy filtering in electron microscopy and electron diffraction. In *Physical Aspects of Electron Microscopy and Microbeam Analysis* (pp. 287–301).

Castaing, R., & Henry, L. (1962). Filtrage magnetique des vitesses en microscopie electronique. *Compt Rend Acad Sci Paris*, *255*, 76–78.

Chen, H., Downing, R., Gibson, W., Kumakhov, M., Ponomarev, I. Y., & Gubarev, M. (1992). Guiding and focusing neutron beams using capillary optics. *Nature*, *357*(6377), 391.

Christopher, P., Xin, H., & Linic, S. (2011). Visible-light-enhanced catalytic oxidation reactions on plasmonic silver nanostructures. *Nature Chemistry*, *3*(6), 467.

Coblentz, W. W. (1905). *Investigations of Infra-red Spectra...: Pt. I. Infra-red absorption spectra. Pt. II. Infra-red emission spectra* (Vol. 35). Carnegie institution of Washington.

Colliex, C., Jeanguillaume, C., & Mory, C. (1984). Unconventional modes for STEM imaging of biological structures. *Journal of Ultrastructure Research*, *88*(2), 177–206. https://doi.org/10.1016/S0022-5320(84)80007-6

Colliex, P. C., & Jouffrey, B. (1972). Diffusion inelastique des electrons dans un solide par excitation de niveaux atomiques profonds. *The Philosophical Magazine: A Journal of Theoretical Experimental and Applied Physics*, *25*(2), 491–511. https://doi.org/10.1080/14786437208226818

Cowley, J. M. (1969). IMAGE CONTRAST IN A TRANSMISSION SCANNING ELECTRON MICROSCOPE. *Applied Physics Letters*, *15*(2), 58–59. https://doi.org/10.1063/1.1652901

Creuzburg, M., & Raether, H. (1963). Über die charakteristischen Energieverluste bei Elektronenstreuung an Si-Spaltflächen. *Zeitschrift Für Physik*, *171*(2), 436–441. https://doi.org/10.1007/BF01380661

Crewe, A. V. (1966). Scanning electron microscopes: Is high resolution possible? *Science*, *154*(3750), 729–738.

Crewe, A. V. (1971). A high-resolution scanning electron microscope. *Scientific American*, *224*(4), 26–35.

Crewe, A. V., Wall, J., & Langmore, J. (1970). Visibility of single atoms. *Science*, *168*(3937), 1338–1340.

Crewe, A., & Wall, J. (1970). A scanning microscope with 5 Å resolution. *Journal of Molecular Biology*, *48*(3), 375–393.

Crozier, P. A. (1995). Quantitative elemental mapping of materials by energy-filtered imaging. *Ultramicroscopy*, *58*(2), 157–174. https://doi.org/10.1016/0304-3991(94)00201-W

Crozier, P. A. (2017). Vibrational and valence aloof beam EELS: A potential tool for nondestructive characterization of nanoparticle surfaces. *Ultramicroscopy*, *180*, 104–114. https://doi.org/10.1016/j.ultramic.2017.03.011

Crozier, P. A., Aoki, T., & Liu, Q. (2016). Detection of water and its derivatives on individual nanoparticles using vibrational electron energy-loss spectroscopy. *Ultramicroscopy*, *169*, 30–36. https://doi.org/10.1016/j.ultramic.2016.06.008

Crozier, P. A., Liu, Q., Venkatraman, K., Haiber, D. M., Bowman, W. J., March, K., & Rez, P. (2017). Exploring Vibrational and Valence Loss Spectra from Oxide Nanoparticles. *Microscopy and Microanalysis*, *23*(S1), 1544–1545.

Cueva, P., Hovden, R., Mundy, J. A., Xin, H. L., & Muller, D. A. (2012). Data processing for atomic resolution electron energy loss spectroscopy. *Microscopy and Microanalysis*, *18*(4), 667–675.

Dai, S., Fei, Z., Ma, Q., Rodin, A. S., Wagner, M., McLeod, A. S., Liu, M. K., Gannett, W., Regan, W., Watanabe, K., Taniguchi, T., Thiemens, M., Dominguez, G., Neto, A. H. C., Zettl, A., Keilmann, F., Jarillo-Herrero, P., Fogler, M. M., & Basov, D. N. (2014). Tunable Phonon Polaritons in Atomically Thin van der Waals Crystals of Boron Nitride. *Science*, *343*(6175), 1125–1129. https://doi.org/10.1126/science.1246833

Das, P., Chini, T. K., & Pond, J. (2012). Probing Higher Order Surface Plasmon Modes on Individual Truncated Tetrahedral Gold Nanoparticle Using Cathodoluminescence Imaging and Spectroscopy Combined with FDTD Simulations. *The Journal of Physical Chemistry C*, *116*(29), 15610–15619. https://doi.org/10.1021/jp3047533

de Abajo, F. G. (2010). Optical excitations in electron microscopy. *Reviews of Modern Physics*, *82*(1), 209.

de Abajo, F. G., & Howie, A. (1998). Relativistic electron energy loss and electron-induced photon emission in inhomogeneous dielectrics. *Physical Review Letters*, *80*(23), 5180.

de Abajo, F. G., & Aizpurua, J. (1997). Numerical simulation of electron energy loss near inhomogeneous dielectrics. *Physical Review B*, *56*(24), 15873.

de Abajo, F. J., & Howie, A. (2002). Retarded field calculation of electron energy loss in inhomogeneous dielectrics. *Physical Review B*, *65*(11), 115418. https://doi.org/10.1103/PhysRevB.65.115418

de Abajo, F. G., & Sáenz, J. (2005). Electromagnetic surface modes in structured perfect-conductor surfaces. *Physical Review Letters*, *95*(23), 233901.

de Graef, M. (2003). *Introduction to conventional transmission electron microscopy*. Cambridge university press.

Delaire, O., Al-Qasir, I. I., Ma, J., dos Santos, A. M., Sales, B. C., Mauger, L., Stone, M. B., Abernathy, D. L., Xiao, Y., & Somayazulu, M. (2013). Effects of temperature and pressure on phonons in FeSi 1 − x Al x. *Physical Review B*, *87*(18). https://doi.org/10.1103/PhysRevB.87.184304

Dellby, N., Krivanek, L., Nellist, D., Batson, E., & Lupini, R. (2001). Progress in aberration-corrected scanning transmission electron microscopy. *Microscopy*, *50*(3), 177–185.

Dirac, P. A. M. (1927). The quantum theory of the emission and absorption of radiation. *Proceedings of the Royal Society of London. Series A, Containing Papers of a Mathematical and Physical Character*, *114*(767), 243–265.

Dolling, G., & Cowley, R. (1966). The thermodynamic and optical properties of germanium, silicon, diamond, and gallium arsenide. *Proceedings of the Physical Society*, *88*(2), 463.

Dorner, B. (1982). *Coherent inelastic neutron scattering in lattice dynamics*. Springer.

Dwyer, C. (2014). Localization of high-energy electron scattering from atomic vibrations. *Physical Review B*, *89*(5), 054103. https://doi.org/10.1103/PhysRevB.89.054103

Dwyer, C., Aoki, T., Rez, P., Chang, S. L. Y., Lovejoy, T. C., & Krivanek, O. L. (2016). Electron-Beam Mapping of Vibrational Modes with Nanometer Spatial Resolution. *Physical Review Letters*, *117*(25), 256101. https://doi.org/10.1103/PhysRevLett.117.256101

Dwyer, C. (2017). Prospects of spatial resolution in vibrational electron energy loss spectroscopy: Implications of dipolar scattering. *Physical Review B*, *96*(22), 224102. https://doi.org/10.1103/PhysRevB.96.224102

Egerton, R. F. (1979). K-shell ionization cross-sections for use in microanalysis. *Ultramicroscopy*, *4*(2), 169–179.

Egerton, R. F. (2009). Electron energy-loss spectroscopy in the TEM. *Reports on Progress in Physics*, *72*(1), 016502. https://doi.org/10.1088/0034-4885/72/1/016502

Egerton, R. F. (2011). *Electron Energy-Loss Spectroscopy in the Electron Microscope*. Springer US. http://link.springer.com/10.1007/978-1-4419-9583-4

Egerton, R. F. (2015). Vibrational-loss EELS and the avoidance of radiation damage. *Ultramicroscopy*, *159*, 95–100. https://doi.org/10.1016/j.ultramic.2015.08.003

Egerton, R. F. (2017). Scattering delocalization and radiation damage in STEM-EELS. *Ultramicroscopy*, *180*, 115–124. https://doi.org/10.1016/j.ultramic.2017.02.007

Egerton, R. F. (2019). Radiation damage to organic and inorganic specimens in the TEM. *Micron*, *119*, 72–87. https://doi.org/10.1016/j.micron.2019.01.005

Egerton, R. F., & Whelan, M. J. (1974). Electron energy loss spectra of diamond, graphite and amorphous carbon. *Journal of Electron Spectroscopy and Related Phenomena*, *3*(3), 232–236. https://doi.org/10.1016/0368-2048(74)80015-0

Erni, R., & Browning, N. D. (2008). The impact of surface and retardation losses on valence electron energy-loss spectroscopy. *Ultramicroscopy*, *108*(2), 84–99. https://doi.org/10.1016/j.ultramic.2007.03.005

Ertl, G. (2008). Reactions at surfaces: From atoms to complexity (Nobel Lecture). *Angewandte Chemie International Edition*, *47*(19), 3524–3535.

Ertl, G., Knözinger, H., & Weitkamp, J. (2008). *Preparation of solid catalysts*. John Wiley & Sons.

Findlay, S. D., Kohno, Y., Cardamone, L. A., Ikuhara, Y., & Shibata, N. (2014). Enhanced light element imaging in atomic resolution scanning transmission electron microscopy. *Ultramicroscopy*, *136*, 31–41. https://doi.org/10.1016/j.ultramic.2013.07.019

Findlay, S., Shibata, N., Sawada, H., Okunishi, E., Kondo, Y., Yamamoto, T., & Ikuhara, Y. (2009). Robust atomic resolution imaging of light elements using scanning transmission electron microscopy. *Applied Physics Letters*, *95*(19), 191913.

Forbes, B. D., & Allen, L. J. (2016). Modeling energy-loss spectra due to phonon excitation. *Physical Review B*, *94*(1). https://doi.org/10.1103/PhysRevB.94.014110

Fransen, M. J. (1998). Experimental evaluation of the extended Schottky model for ZrO/W electron emission. *Journal of Vacuum Science & Technology B: Microelectronics and Nanometer Structures*, *16*(4), 2063. https://doi.org/10.1116/1.590128

Fultz, B., & Howe, J. M. (2012). *Transmission electron microscopy and diffractometry of materials*. Springer Science & Business Media.

Gao, H., Xu, W., He, H., Shi, X., Zhang, X., & Tanaka, K. (2008). DRIFTS investigation and DFT calculation of the adsorption of CO on Pt/TiO2, Pt/CeO2 and FeOx/Pt/CeO2. *Spectrochimica Acta Part A: Molecular and Biomolecular Spectroscopy*, *71*(4), 1193–1198. https://doi.org/10.1016/j.saa.2008.03.036

Garcia-Molina, R., Gras-Marti, A., Howie, A., & Ritchie, R. H. (1985). Retardation effects in the interaction of charged particle beams with bounded condensed media. *Journal of Physics C: Solid State Physics*, *18*(27), 5335.

Geick, R., Perry, C. H., & Rupprecht, G. (1966). Normal Modes in Hexagonal Boron Nitride. *Physical Review*, *146*(2), 543–547. https://doi.org/10.1103/PhysRev.146.543

Geuquet, N., & Henrard, L. (2010). EELS and optical response of a noble metal nanoparticle in the frame of a discrete dipole approximation. *PROCEEDINGS OF THE INTERNATIONAL WORKSHOP ON ENHANCED DATA GENERATED BY ELECTRONS*, *110*(8), 1075–1080. https://doi.org/10.1016/j.ultramic.2010.01.013

Govyadinov, A. A., Konečná, A., Chuvilin, A., Vélez, S., Dolado, I., Nikitin, A. Y., Lopatin, S., Casanova, F., Hueso, L. E., Aizpurua, J., & Hillenbrand, R. (2017a). Probing low-energy hyperbolic polaritons in van der Waals crystals with an electron microscope. *Nature Communications*, *8*(1), 95. https://doi.org/10.1038/s41467-017-00056-y

Griffiths, P. R., & De Haseth, J. A. (2007). *Fourier transform infrared spectrometry* (Vol. 171). John Wiley & Sons.

Grogger, W., Hofer, F., Kothleitner, G., & Schaffer, B. (2008). An Introduction to High-resolution EELS in Transmission Electron Microscopy. *Topics in Catalysis*, *50*(1–4), 200–207. https://doi.org/10.1007/s11244-008-9101-4

Gubbens, A., Barfels, M., Trevor, C., Twesten, R., Mooney, P., Thomas, P., Menon, N., Kraus, B., Mao, C., & McGinn, B. (2010). The GIF Quantum, a next generation post-column imaging energy filter. *Ultramicroscopy*, *110*(8), 962–970. https://doi.org/10.1016/j.ultramic.2010.01.009

Gupta, V. (2015). *Principles and applications of quantum chemistry*. Academic Press.

Hachtel, J. A., Huang, J., Popovs, I., Jansone-Popova, S., Keum, J. K., Jakowski, J., Lovejoy, T. C., Dellby, N., Krivanek, O. L., & Idrobo, J. C. (2019). Identification of site-specific isotopic labels by vibrational spectroscopy in the electron microscope. *Science*, *363*(6426), 525–528. https://doi.org/10.1126/science.aav5845

Hage, F. S., Radtke, G., Kepaptsoglou, D. M., Lazzeri, M., & Ramasse, Q. M. (2020). Single-atom vibrational spectroscopy in the scanning transmission electron microscope. *Science*, *367*(6482), 1124–1127. https://doi.org/10.1126/science.aba1136

Hage, F. S, Nicholls, R. J., Yates, J. R., McCulloch, D. G., Lovejoy, T. C., Dellby, N., Krivanek, O. L., Refson, K., & Ramasse, Q. M. (2018). Nanoscale momentum-resolved vibrational spectroscopy. *Science Advances*, *4*(6), eaar7495.

Hage, F. S., Kepaptsoglou, D. M., Ramasse, Q. M., & Allen, L. J. (2019). Phonon Spectroscopy at Atomic Resolution. *Physical Review Letters*, *122*(1), 016103. https://doi.org/10.1103/PhysRevLett.122.016103

Haiber, D. M., & Crozier, P. A. (2018). Nanoscale Probing of Local Hydrogen Heterogeneity in Disordered Carbon Nitrides with Vibrational Electron Energy-Loss Spectroscopy. *ACS Nano*, *12*(6), 5463–5472. https://doi.org/10.1021/acsnano.8b00884

Haider, M. (1989). Filtered dark-field and pure z-contrast: Two novel imaging modes in a Scanning Transmission Electron Microscope. *Ultramicroscopy*, *28*(1), 240–247. https://doi.org/10.1016/0304-3991(89)90302-1

Hartschuh, A. (2008). Tip-Enhanced Near-Field Optical Microscopy. *Angewandte Chemie International Edition*, *47*(43), 8178–8191. https://doi.org/10.1002/anie.200801605

Hartschuh, A., Anderson, N., & Novotny, L. (2003). Near-field Raman spectroscopy using a sharp metal tip. *Journal of Microscopy*, *210*(3), 234–240.

Hartschuh, A., Sánchez, E. J., Xie, X. S., & Novotny, L. (2003). High-resolution near-field Raman microscopy of single-walled carbon nanotubes. *Physical Review Letters*, *90*(9), 095503.

Hass, M. (1970). Raman spectra of vitreous silica, germania and sodium silicate glasses. *Journal of Physics and Chemistry of Solids*, *31*(3), 415–422.

Hawkes, P. W. (2009). Aberration correction past and present. *Philosophical Transactions of the Royal Society A: Mathematical, Physical and Engineering Sciences*, *367*(1903), 3637–3664.

Hawkes, P. W. (Ed.). (1985). *The Beginnings of electron microscopy*. Academic Press.

Hawkes, P. W., & Spence, J. C. (2019). *Springer Handbook of Microscopy*. Springer Nature.

Haworth, R., Mountjoy, G., Corno, M., Ugliengo, P., & Newport, R. J. (2010). Probing vibrational modes in silica glass using inelastic neutron scattering with mass contrast. *Physical Review B*, *81*(6), 060301.

Helveg, S., Lauritsen, J. V., Lægsgaard, E., Stensgaard, I., Nørskov, J. K., Clausen, B., Topsøe, H., & Besenbacher, F. (2000). Atomic-scale structure of single-layer MoS 2 nanoclusters. *Physical Review Letters*, *84*(5), 951.

Henderson, R. (1995). The potential and limitations of neutrons, electrons and X-rays for atomic resolution microscopy of unstained biological molecules. *Quarterly Reviews of Biophysics*, *28*(02), 171. https://doi.org/10.1017/S003358350000305X

Henkelman, R. M., & Ottensmeyer, F. P. (1974). An energy filter for biological electron microscopy. *Journal of Microscopy*, *102*(1), 79–94. https://doi.org/10.1111/j.1365-2818.1974.tb03968.x

Henrard, L., & Lambin, P. (1996). Calculation of the energy loss for an electron passing near giant fullerenes. *Journal of Physics B: Atomic, Molecular and Optical Physics*, *29*(21), 5127–5141. https://doi.org/10.1088/0953-4075/29/21/024

Herschel, W. (1800). XIV. Experiments on the refrangibility of the invisible rays of the sun. *Philosophical Transactions of the Royal Society of London*, *90*, 284–292.

Hillier, J., & Baker, R. F. (1944). Microanalysis by Means of Electrons. *Journal of Applied Physics*, *15*(9), 663–675. https://doi.org/10.1063/1.1707491

Hillyard, S., & Silcox, J. (1995). Detector geometry, thermal diffuse scattering and strain effects in ADF STEM imaging. *Ultramicroscopy*, *58*(1), 6–17.

Himpsel, F. J., Karlsson, U. O., McLean, A. B., Terminello, L. J., de Groot, F. M. F., Abbate, M., Fuggle, J. C., Yarmoff, J. A., Thole, B. T., & Sawatzky, G. A. (1991). Fine structure of the Ca 2p x-ray-absorption edge for bulk compounds, surfaces, and interfaces. *Physical Review B*, *43*(9), 6899–6907. https://doi.org/10.1103/PhysRevB.43.6899

Hohenester, U., & Trügler, A. (2012). MNPBEM – A Matlab toolbox for the simulation of plasmonic nanoparticles. *Computer Physics Communications*, *183*(2), 370–381. https://doi.org/10.1016/j.cpc.2011.09.009

Hojo, H., Mizoguchi, T., Ohta, H., Findlay, S. D., Shibata, N., Yamamoto, T., & Ikuhara, Y. (2010). Atomic structure of a CeO2 grain boundary: The role of oxygen vacancies. *Nano Letters*, *10*(11), 4668–4672.

Howie, A. (1979). Image contrast and localized signal selection techniques. *Journal of Microscopy*, *117*(1), 11–23.

Howie, A. (1983). Surface reactions and excitations. *Ultramicroscopy*, *11*(2–3), 141–148.

Howie, A., & Milne, R. H. (1985). Excitations at interfaces and small particles. *Ultramicroscopy*, *18*(1–4), 427–433.

Huang, T.-X., Huang, S.-C., Li, M.-H., Zeng, Z.-C., Wang, X., & Ren, B. (2015). Tip-enhanced Raman spectroscopy: Tip-related issues. *Analytical and Bioanalytical Chemistry*, *407*(27), 8177–8195.

Huth, F., Govyadinov, A., Amarie, S., Nuansing, W., Keilmann, F., & Hillenbrand, R. (2012). Nano-FTIR absorption spectroscopy of molecular fingerprints at 20 nm spatial resolution. *Nano Letters*, *12*(8), 3973–3978.

Iakoubovskii, K., Mitsuishi, K., Nakayama, Y., & Furuya, K. (2008). Thickness measurements with electron energy loss spectroscopy. *Microscopy Research and Technique*, *71*(8), 626–631. https://doi.org/10.1002/jemt.20597

Ibach, Harald, & Mills, D. L. (2013). *Electron energy loss spectroscopy and surface vibrations*. Academic press.

Idrobo, J. C., Lupini, A. R., Feng, T., Unocic, R. R., Walden, F. S., Gardiner, D. S., Lovejoy, T. C., Dellby, N., Pantelides, S. T., & Krivanek, O. L. (2018). Temperature Measurement by a Nanoscale Electron Probe Using Energy Gain and Loss Spectroscopy. *Physical Review Letters*, *120*(9), 095901. https://doi.org/10.1103/PhysRevLett.120.095901

Imelik, B., & Vedrine, J. C. (2013). *Catalyst characterization: Physical techniques for solid materials*. Springer Science & Business Media.

Inokuti, M. (1971). Inelastic collisions of fast charged particles with atoms and molecules—The Bethe theory revisited. *Reviews of Modern Physics*, *43*(3), 297.

Isaacson, M., & Scheinfein, M. (1983). A high performance electron energy loss spectrometer for use with a dedicated STEM. *Journal of Vacuum Science & Technology B: Microelectronics Processing and Phenomena*, *1*(4), 1338–1343. https://doi.org/10.1116/1.582742

Isaacson, MS. (1977). Principles and techniques of electron microscopy. In *Biological Applications* (Vol. 7, pp. 1–78). Van Nostrand-Reinhold New York.

Ishikawa, R., Okunishi, E., Sawada, H., Kondo, Y., Hosokawa, F., & Abe, E. (2011). Direct imaging of hydrogen-atom columns in a crystal by annular bright-field electron microscopy. *Nature Materials*, *10*(4), 278–281. https://doi.org/10.1038/nmat2957

Jackson, J. D. (2012). *Classical electrodynamics*. John Wiley & Sons.

Jahncke, C., Hallen, H., & Paesler, M. (1996). Nano-Raman Spectroscopy and Imaging with a Near-Field Scanning Optical Microscope. *Journal of Raman Spectroscopy*, *27*(8), 579–586.

Jain, A., Ong, S. P., Hautier, G., Chen, W., Richards, W. D., Dacek, S., Cholia, S., Gunter, D., Skinner, D., & Ceder, G. (2013). Commentary: The Materials Project: A materials genome approach to accelerating materials innovation. *Apl Materials*, *1*(1), 011002.

Jiang, Y., Chen, Z., Han, Y., Deb, P., Gao, H., Xie, S., Purohit, P., Tate, M. W., Park, J., Gruner, S. M., Elser, V., & Muller, D. A. (2018). Electron ptychography of 2D materials to deep sub-ångström resolution. *Nature*, *559*(7714), 343–349. https://doi.org/10.1038/s41586-018-0298-5

Jokisaari, J. R., Hachtel, J. A., Hu, X., Mukherjee, A., Wang, C., Konecna, A., Lovejoy, T. C., Dellby, N., Aizpurua, J., Krivanek, O. L., Idrobo, J.-C., & Klie, R. F. (2018). Vibrational Spectroscopy of Water with High Spatial Resolution. *Advanced Materials*, *30*(36), 1802702. https://doi.org/10.1002/adma.201802702

Jones, A. C., O'Callahan, B. T., Yang, H. U., & Raschke, M. B. (2013). The thermal near-field: Coherence, spectroscopy, heat-transfer, and optical forces. *Progress in Surface Science*, *88*(4), 349–392. https://doi.org/10.1016/j.progsurf.2013.07.001

Keilmann, F. (2002). Vibrational-infrared near-field microscopy. *Vibrational Spectroscopy*, *29*(1–2), 109–114.

Keyse, R. (2018). *Introduction to scanning transmission electron microscopy*. Routledge.

Kim, H. S., Yu, M. L., Thomson, M. G. R., Kratschmer, E., & Chang, T. H. P. (1997). Energy distributions of Zr/O/W Schottky electron emission. *J. Appl. Phys.*, *81*(1), 6.

Kittler, M., & Reiche, M. (2011). Structure and Properties of Dislocations in Silicon. In S. Basu (Ed.), *Crystalline Silicon—Properties and Uses*. InTech. https://doi.org/10.5772/22902

Kneipp, K., Wang, Y., Kneipp, H., Perelman, L. T., Itzkan, I., Dasari, R. R., & Feld, M. S. (1997). Single molecule detection using surface-enhanced Raman scattering (SERS). *Physical Review Letters*, *78*(9), 1667.

Knoll, B., & Keilmann, F. (1999). Near-field probing of vibrational absorption for chemical microscopy. *Nature*, *399*(6732), 134.

Knoll, M., & Ruska, E. (1932). Das elektronenmikroskop. *Zeitschrift Für Physik*, *78*(5–6), 318–339.

Kohl, H., & Reimer, L. (2008). *Transmission electron microscopy: Physics of image formation*. Springer.

Konečná, A., Neuman, T., Aizpurua, J., & Hillenbrand, R. (2018). Surface-Enhanced Molecular Electron Energy Loss Spectroscopy. *ACS Nano*, *12*(5), 4775–4786. https://doi.org/10.1021/acsnano.8b01481

Konečná, A., Venkatraman, K., March, K., Crozier, P. A., Hillenbrand, R., Rez, P., & Aizpurua, J. (2018). Vibrational electron energy loss spectroscopy in truncated dielectric slabs. *Physical Review B*, *98*(20). https://doi.org/10.1103/PhysRevB.98.205409

Kordahl, D., & Dwyer, C. (2019). Enhanced vibrational electron energy-loss spectroscopy of adsorbate molecules. *Physical Review B*, *99*(10), 104110. https://doi.org/10.1103/PhysRevB.99.104110

Kramers, H. A., & Heisenberg, W. (1925). Über die streuung von strahlung durch atome. *Zeitschrift Für Physik*, *31*(1), 681–708.

Krivanek, O., Corbin, G., Dellby, N., Elston, B., Keyse, R., Murfitt, M., Own, C., Szilagyi, Z., & Woodruff, J. (2008). An electron microscope for the aberration-corrected era. *Ultramicroscopy*, *108*(3), 179–195.

Krivanek, O. L., Dellby, N., & Lupini, A. R. (1999). Towards sub-Å electron beams. *Ultramicroscopy*, *78*(1), 1–11.

Krivanek, O. L., Ursin, J. P., Bacon, N. J., Corbin, G. J., Dellby, N., Hrncirik, P., Murfitt, M. F., Own, C. S., & Szilagyi, Z. S. (2009). High-energy-resolution monochromator for aberration-corrected scanning transmission electron microscopy/electron energy-loss spectroscopy. *Philosophical Transactions of the Royal Society A: Mathematical, Physical and Engineering Sciences*, *367*(1903), 3683–3697. https://doi.org/10.1098/rsta.2009.0087

Krivanek, O.L. (1997). *Aberration correction in the STEM*. *153*, 35–39.

Krivanek, O.L., & Ahn, C. (1986). Energy-filtered imaging with quadrupole lenses. *Electron Microscopy*, *1*, 529.

Krivanek, O.L., Ahn, C. C., & Keeney, R. B. (1987). Parallel detection electron spectrometer using quadrupole lenses. *Ultramicroscopy*, *22*(1), 103–115. https://doi.org/10.1016/0304-3991(87)90054-4

Krivanek, O.L., Corbin, G. J., Dellby, N., Elston, B. F., Keyse, R. J., Murfitt, M. F., Own, C. S., Szilagyi, Z. S., & Woodruff, J. W. (2008). An electron microscope for the aberration-corrected era. *Ultramicroscopy*, *108*(3), 179–195. https://doi.org/10.1016/j.ultramic.2007.07.010

Krivanek, O.L., Dellby, N., Hachtel, J. A., Idrobo, J.-C., Hotz, M. T., Plotkin-Swing, B., Bacon, N. J., Bleloch, A. L., Corbin, G. J., Hoffman, M. V., Meyer, C. E., & Lovejoy, T. C. (2019). Progress in ultrahigh energy resolution EELS. *Ultramicroscopy*, *203*, 60–67. https://doi.org/10.1016/j.ultramic.2018.12.006

Krivanek, O.L., Gubbens, A. J., & Dellby, N. (1991). Developments in EELS instrumentation for spectroscopy and imaging. *Microscopy Microanalysis*

Microstructures, *2*(2–3), 315–332. https://doi.org/10.1051/mmm:0199100202-3031500

Krivanek, O.L., Lovejoy, T. C., Murfitt, M. F., Skone, G., Batson, P. E., & Dellby, N. (2014). Towards sub-10 meV energy resolution STEM-EELS. *Journal of Physics: Conference Series*, *522*, 012023. https://doi.org/10.1088/1742-6596/522/1/012023

Krivanek, O.L., Nellist, P. D., Dellby, N., Murfitt, M. F., & Szilagyi, Z. (2003). Towards sub-0.5Å electron beams. *Ultramicroscopy*, *96*(3–4), 229–237. https://doi.org/10.1016/S0304-3991(03)00090-1

Krivanek, O.L., Tanishiro, Y., Takayanagi, K., & Yagi, K. (1983). Electron energy loss spectriscopy in glancing reflection from bulk crystals. *Ultramicroscopy*, *11*(2), 215–222. https://doi.org/10.1016/0304-3991(83)90239-5

Krivanek, O. L., Dellby, N., Keyse, R. J., Murfitt, M. F., Own, C. S., & Szilagyi, Z. S. (2008). Chapter 3 Advances in Aberration-Corrected Scanning Transmission Electron Microscopy and Electron Energy-Loss Spectroscopy. In *Advances in Imaging and Electron Physics* (Vol. 153, pp. 121–160). Elsevier. https://doi.org/10.1016/S1076-5670(08)01003-3

Krivanek, O. L., Lovejoy, T. C., Dellby, N., Aoki, T., Carpenter, R. W., Rez, P., Soignard, E., Zhu, J., Batson, P. E., Lagos, M. J., Egerton, R. F., & Crozier, P. A. (2014). Vibrational spectroscopy in the electron microscope. *Nature*, *514*(7521), 209–212. https://doi.org/10.1038/nature13870

Kröger, E. (1968). Berechnung der Energieverluste schneller Elektronen in dünnen Schichten mit Retardierung. *Zeitschrift Für Physik A Hadrons and Nuclei*, *216*(2), 115–135.

Kulda, J., Strauch, D., Pavone, P., & Ishii, Y. (1994). Inelastic-neutron-scattering study of phonon eigenvectors and frequencies in Si. *Physical Review B*, *50*(18), 13347.

Kurouski, D., Mattei, M., & Van Duyne, R. P. (2015). Probing Redox Reactions at the Nanoscale with Electrochemical Tip-Enhanced Raman Spectroscopy. *Nano Letters*, *15*(12), 7956–7962. https://doi.org/10.1021/acs.nanolett.5b04177

Lagos, M. J., & Batson, P. E. (2018). Thermometry with Subnanometer Resolution in the Electron Microscope Using the Principle of Detailed Balancing. *Nano Letters*, *18*(7), 4556–4563. https://doi.org/10.1021/acs.nanolett.8b01791

Lagos, M. J., Trügler, A., Amarasinghe, V., Feldman, L. C., Hohenester, U., & Batson, P. E. (2018). Excitation of long-wavelength surface optical vibrational modes in films, cubes and film/cube composite system using an atom-sized electron beam. *Microscopy*, *67*(suppl_1), i3–i13. https://doi.org/10.1093/jmicro/dfx130

Lagos, M. J., Trügler, A., Hohenester, U., & Batson, P. E. (2017). Mapping vibrational surface and bulk modes in a single nanocube. *Nature*, *543*(7646), 529–532. https://doi.org/10.1038/nature21699

Landsberg, G., & Mandelstam, L. (1928). Über die lichtzerstreuung in kristallen. *Zeitschrift Für Physik*, *50*(11–12), 769–780.

Larkin, P. (2017). *Infrared and Raman spectroscopy: Principles and spectral interpretation*. Elsevier.

Lauritsen, J. V., & Besenbacher, F. (2006). Model catalyst surfaces investigated by scanning tunneling microscopy. *Advances in Catalysis*, *50*, 97–147.

Lehmann, A., Schumann, L., & Hübner, K. (1983). Optical Phonons in Amorphous Silicon Oxides. I. Calculation of the Density of States and Interpretation of Lo□ To Splittings of Amorphous Sio2. *Physica Status Solidi (b)*, *117*(2), 689–698.

Lewis, A., Isaacson, M., Harootunian, A., & Muray, A. (1984). Development of a 500 Å spatial resolution light microscope: I. light is efficiently transmitted through λ/16 diameter apertures. *Ultramicroscopy*, *13*(3), 227–231.

Li, C., Sakata, Y., Arai, T., Domen, K., Maruya, K., & Onishi, T. (1989). Carbon monoxide and carbon dioxide adsorption on cerium oxide studied by Fourier-transform infrared spectroscopy. Part 1.—Formation of carbonate species on dehydroxylated CeO2, at room temperature. *Journal of the Chemical Society, Faraday Transactions 1: Physical Chemistry in Condensed Phases*, *85*(4), 929. https://doi.org/10.1039/f19898500929

Li, Y.-H, Qi, R., Shi, R., Li, N., & Gao, P. (2020). Manipulation of surface phonon polaritons in SiC nanorods. *Science Bulletin*, *65*(10), 820–826. https://doi.org/10.1016/j.scib.2020.02.026

Li, Y.-H., Wu, M., Qi, R.-S., Li, N., Sun, Y.-W., Shi, C.-L., Zhu, X.-T., Guo, J.-D., Yu, D.-P., & Gao, P. (2019). Probing Lattice Vibrations at SiO_2 /Si Surface and Interface with Nanometer Resolution. *Chinese Physics Letters*, *36*(2), 026801. https://doi.org/10.1088/0256-307X/36/2/026801

Link, S., & El-Sayed, M. A. (1999). *Spectral properties and relaxation dynamics of surface plasmon electronic oscillations in gold and silver nanodots and nanorods*.

Lohff, J. (1963). Charakteristische Energieverluste bei der Streuung mittelschneller Elektronen an Aluminium-Oberflächen. *Zeitschrift Für Physik*, *171*(2), 442–448. https://doi.org/10.1007/BF01380662

Lourenço-Martins, H., & Kociak, M. (2017). Vibrational Surface Electron-Energy-Loss Spectroscopy Probes Confined Surface-Phonon Modes. *Physical Review X*, *7*(4), 041059. https://doi.org/10.1103/PhysRevX.7.041059

Lovejoy, T., Corbin, G., Dellby, N., Hoffman, M., & Krivanek, O. (2018). Advances in ultra-high energy resolution STEM-EELS. *Microscopy and Microanalysis*, *24*(S1), 446–447.

Lu, F., Jin, M., & Belkin, M. A. (2014). Tip-enhanced infrared nanospectroscopy via molecular expansion force detection. *Nature Photonics*, *8*(4), 307.

Maiman, T. H. (1960). Stimulated optical radiation in ruby. *Nature*, *187*(4736), 493–494.

McCreery, R. L. (2005). *Raman spectroscopy for chemical analysis* (Vol. 225). John Wiley & Sons.

Mildner, D., Chen, H., Downing, G., & Sharov, V. (1993). Focused neutrons: A point to be made. *Journal of Neutron Research*, *1*(1), 1–11. https://doi.org/10.1080/10238169308200057

Mitchell, M. B. (1993). *Fundamentals and applications of diffuse reflectance infrared fourier transform (DRIFT) spectroscopy*. ACS Publications.

Mitchell, P. C. H. (2005). *Vibrational spectroscopy with neutrons: With applications in chemistry, biology, materials science and catalysis* (Vol. 3). World Scientific.

Miyata, T., Fukuyama, M., Hibara, A., Okunishi, E., Mukai, M., & Mizoguchi, T. (2014). Measurement of vibrational spectrum of liquid using monochromated scanning transmission electron microscopy—Electron energy loss spectroscopy. *Microscopy*, *63*(5), 377–382. https://doi.org/10.1093/jmicro/dfu023

Mizoguchi, T., Olovsson, W., Ikeno, H., & Tanaka, I. (2010). Theoretical ELNES using one-particle and multi-particle calculations. *Micron*, *41*(7), 695–709. https://doi.org/10.1016/j.micron.2010.05.011

Mkhoyan, K., Babinec, T., Maccagnano, S., Kirkland, E., & Silcox, J. (2007). Separation of bulk and surface-losses in low-loss EELS measurements in STEM. *Ultramicroscopy*, *107*(4–5), 345–355.

Mollenstedt, G. (1949). Die elektrostatische Linse als hochauflosender Geschwindigkeitsanalysator. *Optik*, *5*, 499–517.

Mook, H. W., & Kruit, P. (1997). *Electrostatic in-line monochromator for Schottky Field Emission*. *153*, 81.

Mook, H. W., & Kruit, P. (1999). On the monochromatisation of high brightness electron sources for electron microscopy. *Ultramicroscopy*, *78*(1–4), 43–51. https://doi.org/10.1016/S0304-3991(99)00034-0

Moreau, P., Brun, N., Walsh, C. A., Colliex, C., & Howie, A. (1997). Relativistic effects in electron-energy-loss-spectroscopy observations of the S i/S i O 2 interface plasmon peak. *Physical Review B*, *56*(11), 6774.

Muller, D., Kourkoutis, L. F., Murfitt, M., Song, J., Hwang, H., Silcox, J., Dellby, N., & Krivanek, O. (2008). Atomic-scale chemical imaging of composition and bonding by aberration-corrected microscopy. *Science*, *319*(5866), 1073–1076.

Muller, D., & Silcox, J. (1995). Delocalization in inelastic scattering. *Ultramicroscopy*, *59*(1–4), 195–213.

Nelayah, J., Kociak, M., Stéphan, O., de Abajo, F. J. G., Tencé, M., Henrard, L., Taverna, D., Pastoriza-Santos, I., Liz-Marzán, L. M., & Colliex, C. (2007). Mapping surface plasmons on a single metallic nanoparticle. *Nature Physics*, *3*(5), 348–353.

Nellist, P., Pennycook, S., & Hawkes, P. (2000). *Advances in Imaging and Electron Physics*.

Nie, S., & Emory, S. R. (1997). Probing single molecules and single nanoparticles by surface-enhanced Raman scattering. *Science*, *275*(5303), 1102–1106.

Okunishi, E., Sawada, H., & Kondo, Y. (2012). Experimental study of annular bright field (ABF) imaging using aberration-corrected scanning transmission electron microscopy (STEM). *Micron*, *43*(4), 538–544. https://doi.org/10.1016/j.micron.2011.10.007

Ong, S. P., Richards, W. D., Jain, A., Hautier, G., Kocher, M., Cholia, S., Gunter, D., Chevrier, V. L., Persson, K. A., & Ceder, G. (2013). Python Materials Genomics (pymatgen): A robust, open-source python library for materials analysis. *Computational Materials Science*, *68*, 314–319. https://doi.org/10.1016/j.commatsci.2012.10.028

Pacchioni, G. (1993). Physisorbed and chemisorbed CO2 at surface and step sites of the MgO (100) surface. *Surface Science*, *281*(1–2), 207–219.

Palik, E. D., & Ghosh, G. (Eds.). (1998). *Handbook of optical constants of solids*. Academic Press.

Park, J., Heo, S., Chung, J.-G., Kim, H., Lee, H., Kim, K., & Park, G.-S. (2009). Bandgap measurement of thin dielectric films using monochromated STEM-EELS. *Ultramicroscopy*, *109*(9), 1183–1188. https://doi.org/10.1016/j.ultramic.2009.04.005

Pennycook, S. J., Lupini, A. R., Varela, M., Borisevich, A., Peng, Y., Chisholm, M. F., Dellby, N., Krivanek, O. L., Nellist, P. D., Szilagyi, S. Z., & Duscher, G. (2003). Sub-Ångstrom Resolution through Aberration-Corrected STEM. *Microscopy and Microanalysis*, *9*(S02), 926–927. Cambridge Core. https://doi.org/10.1017/S1431927603444632

Pennycook, S. J., Jesson, D., & Browning, N. (1995). Atomic-resolution electron energy loss spectroscopy in crystalline solids. *Nuclear Instruments and Methods in Physics Research Section B: Beam Interactions with Materials and Atoms*, *96*(3–4), 575–582.

Pennycook, S. J., & Jesson, De. (1990). High-resolution incoherent imaging of crystals. *Physical Review Letters*, *64*(8), 938.

Pennycook, S. J. (2012). Seeing the atoms more clearly: STEM imaging from the Crewe era to today. *Ultramicroscopy*, *123*, 28–37.

Pennycook, S. J., & Nellist, P. D. (Eds.). (2011). *Scanning Transmission Electron Microscopy*. Springer New York. http://link.springer.com/10.1007/978-1-4419-7200-2

Philipp, R., & Fujimoto, K. (1992). FTIR spectroscopic study of carbon dioxide adsorption/desorption on magnesia/calcium oxide catalysts. *The Journal of Physical Chemistry*, *96*(22), 9035–9038. https://doi.org/10.1021/j100201a063

Piednoir, A., Licoppe, C., & Creuzet, F. (1996). Imaging and local infrared spectroscopy with a near field optical microscope. *Optics Communications*, *129*(5–6), 414–422.

Pines, D. (2018). *Theory of Quantum Liquids: Normal Fermi Liquids*. CRC Press.

Placzek, G. (1934). *Rayleigh-streuung und Raman-effekt* (Vol. 2). Akad. Verlag-Ges.

Poddubny, A., Iorsh, I., Belov, P., & Kivshar, Y. (2013). Hyperbolic metamaterials. *Nature Photonics*, *7*(12), 948–957. https://doi.org/10.1038/nphoton.2013.243

Pohl, D. W., Denk, W., & Lanz, M. (1984). Optical stethoscopy: Image recording with resolution λ/20. *Applied Physics Letters*, *44*(7), 651–653.

Powell, C. J. (1968). Characteristic Energy Losses of 8-keV Electrons in Liquid Al, Bi, In, Ga, Hg, and Au. *Physical Review*, *175*(3), 972–982. https://doi.org/10.1103/PhysRev.175.972

Prange, M. P., Oxley, M. P., Varela, M., Pennycook, S. J., & Pantelides, S. T. (2012). Simulation of spatially resolved electron energy loss near-edge structure for scanning transmission electron microscopy. *Physical Review Letters*, *109*(24), 246101.

Radtke, G., Taverna, D., Menguy, N., Pandolfi, S., Courac, A., Le Godec, Y., Krivanek, O. L., & Lovejoy, T. C. (2019). Polarization Selectivity in Vibrational Electron-Energy-Loss Spectroscopy. *Physical Review Letters*, *123*(25), 256001. https://doi.org/10.1103/PhysRevLett.123.256001

Raether, H. (1967). Surface plasma oscillations as a tool for surface examinations. *Surface Science*, *8*(1–2), 233–246.

Raether, H. (1980). *Excitation of plasmons and interband transitions by electrons*. Springer.

Raman, C. V. (1928). A new radiation. *Indian J. Phys.*, *2*, 387–398.

Raman, C. V. & Krishnan, K. (1928). Polarisation of scattered light-quanta. *Nature*, *122*(3066), 169–169.

Raman, C. V., & Krishnan, K. S. (1928a). The optical analogue of the Compton effect. *Nature*, *121*(3053), 711–711.

Raman, C. V., & Krishnan, K. S. (1928b). Molecular Spectra in the Extreme Infra-Red. *Nature*, *122*(3069), 278–278. https://doi.org/10.1038/122278a0

Raman, C. V. (1928). A change of wave-length in light scattering. *Nature*, *121*(3051), 619–619.

Raman, C. V., & Krishnan, K. S. (1928). A new type of secondary radiation. *Nature*, *121*(3048), 501–502.

Ramis, G., Busca, G., & Lorenzelli, V. (1991). Low-temperature CO2 adsorption on metal oxides: Spectroscopic characterization of some weakly adsorbed species. *Materials Chemistry and Physics*, *29*(1–4), 425–435. https://doi.org/10.1016/0254-0584(91)90037-U

Raza, S., Stenger, N., Pors, A., Holmgaard, T., Kadkhodazadeh, S., Wagner, J. B., Pedersen, K., Wubs, M., Bozhevolnyi, S. I., & Mortensen, N. A. (2014). Extremely confined gap surface-plasmon modes excited by electrons. *Nature Communications*, *5*. https://doi.org/10.1038/ncomms5125

Reed, B., Chen, J., MacDonald, N., Silcox, J., & Bertsch, G. (1999). Fabrication and STEM/EELS measurements of nanometer-scale silicon tips and filaments. *Physical Review B*, *60*(8), 5641.

Reichenbächer, M., & Popp, J. (2012). Vibrational spectroscopy. In *Challenges in Molecular Structure Determination* (pp. 63–143). Springer.

Rez, P., Bruley, J., Brohan, P., Payne, M., & Garvie, L. A. J. (1995). Review of methods for calculating near edge structure. *Proceedings of the 2nd International Workshop on Electron Energy Loss Spectroscopy and Imaging*, *59*(1), 159–167. https://doi.org/10.1016/0304-3991(95)00025-V

Rez, P. (1993). Does phonon scattering give high-resolution images? *Ultramicroscopy*, *52*(3–4), 260–266.

Rez, P. (2014). Is Localized Infrared Spectroscopy Now Possible in the Electron Microscope? *Microscopy and Microanalysis*, *20*(03), 671–677. https://doi.org/10.1017/S1431927614000129

Rez, P., Aoki, T., March, K., Gur, D., Krivanek, O. L., Dellby, N., Lovejoy, T. C., Wolf, S. G., & Cohen, H. (2016). Damage-free vibrational spectroscopy of biological materials in the electron microscope. *Nature Communications*, *7*, 10945. https://doi.org/10.1038/ncomms10945

Rez, P., Xudong Weng, & Hong Ma. (1991). The interpretation of near edge structure. *Microsc. Microanal. Microstruct.*, *2*(2–3), 143–151. https://doi.org/10.1051/mmm:0199100202-3014300

Ritchie, R. H. (1957). Plasma losses by fast electrons in thin films. *Physical Review*, *106*(5), 874.

Rocard, Y. (1928). *Théorie moléculaire de la diffusion de la lumière par les fluides. II.—Champ intermoléculaire et résultats d'ensemble*. *10*(10), 181–231.

Rocard, Yves. (1928). *Théorie moléculaire de la diffusion de la lumière par les fluides. I.—On néglige le champ intermoléculaire*. *10*, 116–179.

Rose, H. (1974). Electron Microscopy. *Optik*, *39*(4), 416–436.

Rose, H. (1990). Electrostatic energy filter as monochromator of a highly coherent electron source. *Optik (Stuttgart)*, *86*(3), 95–98.

Rose, H. (2008). Optics of high-performance electron microscopes. *Science and Technology of Advanced Materials*, *9*(1), 014107.

Rose, H., & Plies, E. (1974). Design of a magnetic energy analyzer with small aberrations. *Optik*, *40*(3), 336–341.

Rubens, H., & Aschkinass, E. (1898). Observations on the absorption and emission of aqueous vapor and carbon dioxide in the infra-red spectrum. *The Astrophysical Journal*, *8*, 176.

Ruska, E. (1987). The development of the electron microscope and of electron microscopy. *Reviews of Modern Physics*, *59*(3), 627.

Ruthemann, G. (1941). Diskrete Energieverluste schneller Elektronen in Festkörpern. *Naturwissenschaften*, *29*(42), 648–648. https://doi.org/10.1007/BF01485870

Schanzer, C., Schneider, M., Filges, U., & Böni, P. (2018). Variable focusing system for neutrons. *Journal of Physics: Conference Series*, *1021*, 012023. https://doi.org/10.1088/1742-6596/1021/1/012023

Schmid, T., Opilik, L., Blum, C., & Zenobi, R. (2013). Nanoscale Chemical Imaging Using Tip-Enhanced Raman Spectroscopy: A Critical Review. *Angewandte Chemie International Edition*, *52*(23), 5940–5954. https://doi.org/10.1002/anie.201203849

Schrader, B. (2008). *Infrared and Raman spectroscopy: Methods and applications*. John Wiley & Sons.

Schrödinger, E. (1926). An undulatory theory of the mechanics of atoms and molecules. *Physical Review*, *28*(6), 1049.

Senga, R., Suenaga, K., Barone, P., Morishita, S., Mauri, F., & Pichler, T. (2019). Position and momentum mapping of vibrations in graphene nanostructures. *Nature*, *573*(7773), 247–250. https://doi.org/10.1038/s41586-019-1477-8

Serrano, J., Bosak, A., Arenal, R., Krisch, M., Watanabe, K., Taniguchi, T., Kanda, H., Rubio, A., & Wirtz, L. (2007). Vibrational Properties of Hexagonal Boron Nitride: Inelastic X-Ray Scattering and *Ab Initio* Calculations. *Physical Review Letters*, *98*(9), 095503. https://doi.org/10.1103/PhysRevLett.98.095503

Shakouri, A. (2011). Recent Developments in Semiconductor Thermoelectric Physics and Materials. *Annual Review of Materials Research*, *41*(1), 399–431. https://doi.org/10.1146/annurev-matsci-062910-100445

Smekal, A. (1923). Zur quantentheorie der dispersion. *Naturwissenschaften*, *11*(43), 873–875.

Smith, D. A., Webster, S., Ayad, M., Evans, S. D., Fogherty, D., & Batchelder, D. (1995). Development of a scanning near-field optical probe for localised Raman spectroscopy. *Ultramicroscopy*, *61*(1–4), 247–252.

Smith, D. J. (2008). Development of aberration-corrected electron microscopy. *Microscopy and Microanalysis*, *14*(1), 2–15.

Somorjai, G. A., & Li, Y. (2010). *Introduction to surface chemistry and catalysis*. John Wiley & Sons.

Spence, J. C. H. (2009). *High-resolution electron microscopy*. Oxford University Press.

Squires, G. L. (2012). *Introduction to the theory of thermal neutron scattering*. Cambridge university press.

Stahn, J., & Glavic, A. (2016). Focusing neutron reflectometry: Implementation and experience on the TOF-reflectometer Amor. *Nuclear Instruments and Methods in Physics Research Section A: Accelerators, Spectrometers, Detectors and Associated Equipment*, *821*, 44–54. https://doi.org/10.1016/j.nima.2016.03.007

Steininger, H., Lehwald, S., & Ibach, H. (1982). On the adsorption of CO on Pt (111). *Surface Science*, *123*(2–3), 264–282.

Stiles, P. L., Dieringer, J. A., Shah, N. C., & Van Duyne, R. P. (2008). Surface-Enhanced Raman Spectroscopy. *Annual Review of Analytical Chemistry*, *1*(1), 601–626. https://doi.org/10.1146/annurev.anchem.1.031207.112814

Stipe, B., Rezaei, M., & Ho, W. (1998). Single-molecule vibrational spectroscopy and microscopy. *Science*, *280*(5370), 1732–1735.

Stöger-Pollach, M. (2008). Optical properties and bandgaps from low loss EELS: Pitfalls and solutions. *Micron*, *39*(8), 1092–1110. https://doi.org/10.1016/j.micron.2008.01.023

Stöger-Pollach, M., Franco, H., Schattschneider, P., Lazar, S., Schaffer, B., Grogger, W., & Zandbergen, H. W. (2006). Čerenkov losses: A limit for bandgap determination and Kramers–Kronig analysis. *Micron*, *37*(5), 396–402. https://doi.org/10.1016/j.micron.2006.01.001

Stöger-Pollach, M., & Schattschneider, P. (2007). The influence of relativistic energy losses on bandgap determination using valence EELS. *Ultramicroscopy*, *107*(12), 1178–1185. https://doi.org/10.1016/j.ultramic.2007.01.015

Stuart, B. (2004). *IR Spectroscopy: Fundamentals and Applications–Analytical Techniques in the Sciences*.

Swanson, L. W., & Schwind, G. A. (2009). Chapter 2 A Review of the Cold-Field Electron Cathode. In *Advances in Imaging and Electron Physics* (Vol. 159, pp. 63–100). Elsevier. https://doi.org/10.1016/S1076-5670(09)59002-7

Tao, F. (Feng), & Crozier, P. A. (2016). Atomic-Scale Observations of Catalyst Structures under Reaction Conditions and during Catalysis. *Chemical Reviews*, *116*(6), 3487–3539. https://doi.org/10.1021/cr5002657

Terauchi, M., Kuzuo, R., Satoh, F., Thnaka, M., Tsuno, K., & Ohyama, J. (1991). Performance of a new high-resolution electron energy-loss spectroscopy microscope. *Microscopy Microanalysis Microstructures*, *2*(2–3), 351–358. https://doi.org/10.1051/mmm:0199100202-3035100

Tiemeijer, P. (1999). *Operation modes of a TEM monochromator*. *161*, 191–194.

Treacy, M., Howie, A., & Wilson, C. (1978). Z contrast of platinum and palladium catalysts. *Philosophical Magazine A*, *38*(5), 569–585.

Ugarte, D., Colliex, C., & Trebbia, P. (1992). Surface-and interface-plasmon modes on small semiconducting spheres. *Physical Review B*, *45*(8), 4332.

Urban, K., Kabius, B., Haider, M., & Rose, H. (1999). A way to higher resolution: Spherical-aberration correction in a 200 kV transmission electron microscope. *Microscopy*, *48*(6), 821–826.

van Santen, R. A., Averill, B., Moulijn, J. A., & van Leeuwen, P. (2000). *Catalysis: An integrated approach* (Vol. 123). Elsevier.

Vang, R. T., Lægsgaard, E., & Besenbacher, F. (2007). Bridging the pressure gap in model systems for heterogeneous catalysis with high-pressure scanning tunneling microscopy. *Physical Chemistry Chemical Physics*, *9*(27), 3460–3469.

Varela, M., Findlay, S., Lupini, A., Christen, H., Borisevich, A., Dellby, N., Krivanek, O., Nellist, P., Oxley, M., & Allen, L. (2004). Spectroscopic imaging of single atoms within a bulk solid. *Physical Review Letters*, *92*(9), 095502.

Venkatraman, K., Levin, B. D. A., March, K., Rez, P., & Crozier, P. A. (2019). Vibrational spectroscopy at atomic resolution with electron impact scattering. *Nature Physics*, *15*(12), 1237–1241. https://doi.org/10.1038/s41567-019-0675-5

Venkatraman, K., Rez, P., March, K., & Crozier, P. A. (2018). The influence of surfaces and interfaces on high spatial resolution vibrational EELS from SiO2. *Microscopy*, *67*(suppl_1), i14–i23. https://doi.org/10.1093/jmicro/dfy003

von Ardenne, M. (1938). Das elektronen-rastermikroskop. *Zeitschrift Für Physik*, *109*(9–10), 553–572.

von Ardenne, M. (1985). On the history of scanning electron microscopy, of the electron microprobe, and of early contributions to transmission electron microscopy. In *"The Beginnings of Electron Microscopy"* (pp. 1–21). Academic Press Orlando.

von Ardenne, M. (1996). 4.4 reminiscences on the origins of the scanning electron microscope and the electron microprobe. In *Advances in Imaging and Electron Physics* (Vol. 96, pp. 635–652). Elsevier.

Voyles, P., Grazul, J., & Muller, D. (2003). Imaging individual atoms inside crystals with ADF-STEM. *Ultramicroscopy*, *96*(3–4), 251–273.

Wall, J., Langmore, J., Isaacson, M., & Crewe, A. (1974). Scanning transmission electron microscopy at high resolution. *Proceedings of the National Academy of Sciences*, *71*(1), 1–5.

Wang, Z. L. (1996). Valence electron excitations and plasmon oscillations in thin films, surfaces, interfaces and small particles. *Micron*, *27*(3), 265–299. https://doi.org/10.1016/0968-4328(96)00011-X

Webster, S., Batchelder, D., & Smith, D. (1998). Submicron resolution measurement of stress in silicon by near-field Raman spectroscopy. *Applied Physics Letters*, *72*(12), 1478–1480.

Webster, S., Smith, D., & Batchelder, D. (1998). Raman microscopy using a scanning near-field optical probe. *Vibrational Spectroscopy*, *18*(1), 51–59.

Weissenrieder, J., Kaya, S., Lu, J.-L., Gao, H.-J., Shaikhutdinov, S., Freund, H.-J., Sierka, M., Todorova, T. K., & Sauer, J. (2005). Atomic Structure of a Thin Silica Film on a Mo(112) Substrate: A Two-Dimensional Network of SiO 4 Tetrahedra. *Physical Review Letters*, *95*(7). https://doi.org/10.1103/PhysRevLett.95.076103

Wendt, S., Sprunger, P. T., Lira, E., Madsen, G. K., Li, Z., Hansen, J. Ø., Matthiesen, J., Blekinge-Rasmussen, A., Lægsgaard, E., & Hammer, B. (2008). The role of interstitial sites in the Ti3d defect state in the band gap of titania. *Science*, *320*(5884), 1755–1759.

Wessel, J. (1985). Surface-enhanced optical microscopy. *JOSA B*, *2*(9), 1538–1541.

Wiener, A., Duan, H., Bosman, M., Horsfield, A. P., Pendry, J. B., Yang, J. K. W., Maier, S. A., & Fernández-Domínguez, A. I. (2013). Electron-Energy Loss Study of Nonlocal Effects in Connected Plasmonic Nanoprisms. *ACS Nano*, *7*(7), 6287–6296. https://doi.org/10.1021/nn402323t

Wittry, D. B. (1969). An electron spectrometer for use with the transmission electron microscope. *Journal of Physics D: Applied Physics*, *2*(12), 1757–1766. https://doi.org/10.1088/0022-3727/2/12/317

Williams, D. B. & Carter, C. B. (2009). *Transmission electron microscopy*. Springer. doi:10.1007/978-0-387-76501-3

Zuo, J. M., & Spence, J. C. (2017). Advanced transmission electron microscopy. *Advanced Transmission Electron Microscopy, ISBN 978-1-4939-6605-9. Springer Science+ Business Media New York, 2017.*

APPENDIX A

MATLAB CODE FOR VIBRATIONAL EELS SIMULATIONS

1. Non-relativistic EELS probability for a specimen with an interface under the infinite slab approximation

The MATLAB code printed below can be used to calculate the non-relativistic inelastic scattering probability for an electron passing through an infinite slab of SiO_2 which forms an interface with an infinite slab of Si based on the analytical expression derived in (Howie & Milne, 1985). The optical dielectric functions for SiO_2 and Si were obtained from the Handbook of Optical Constants (Palik & Ghosh, 1998). The inelastic scattering probability is convolved with the instrumental response function for comparison with experiments.

```
%%
clear all;
clc;

for k = 1:191
   E = linspace(0.005,0.195,191)'; %in eV

   data = xlsread('Si_SiO2_dielectric_v1','Palik');

   % Get epR,epI for SiO2
   SiO2_epR = spline(data(:,13),data(:,14),E);
   SiO2_epI = spline(data(:,13),data(:,15),E);

   figure; plot(E,SiO2_epR,E,SiO2_epI);

   SiO2_ep = complex(SiO2_epR,SiO2_epI);

   estSiO2_bulk = imag(-1./SiO2_ep);  %bulk eels
   figure; plot(E,estSiO2_bulk);

   % Get epR,epI for Si
   Si_epR = spline(data(:,9),data(:,10),E);
   Si_epI = spline(data(:,9),data(:,11),E);

   figure; plot(E,Si_epR,E,Si_epI);

   Si_ep = complex(Si_epR,Si_epI);

   estSi_bulk = imag(-1./Si_ep);  %bulk eels
   figure; plot(E,estSi_bulk);
```

```
%% Half film thickness a; Impact parameter c=(b-a)

ep2 = SiO2_ep; %beam passing through this side of the interface
ep1 = Si_ep; %other side of the interface

  for j = 1:15001
     theta = (0:0.001:15)'*10^-3; %collection angle, rad
     q(j) = sqrt(1.6646*10^24 *((theta(j)).^2));

     v = 1.337704918032787e+08; %for 60kV voltage, m/s
     hbar = 1.05*10^-34; e = 1.6*10^-19;
     K(k,j) = sqrt((q(j)).^2 + (e*E(k)/hbar/v).^2);

     %F function
     F(k) = imag((ep1(k)-ep2(k))./(ep2(k).*(ep1(k)+ep2(k))));

     %Probability
     ep0 = 8.85*10^-12;
     n = (e^2)/(2*pi^2*hbar^2*v^2*ep0);
     X = 1.6*10^-28*n; %1/J.m = 1.6*10^-28 1/eV.nm
     Y(k) = imag(-1./ep2(k));

     for i = 1:5
        b = [1,10,50,100,500]*10^-9; %impact parameter
        A(k,i,j) = X*(Y(k)+exp(-2*b(i)*K(k,j)).*F(k))./K(k,j);
     end
  end
end

%%
Prob = sum(A,3);
figure; plot(E,Prob);
title('Transmission EELS - Beam in SiO2 - Raw');
legend('1nm','10nm','50nm','100nm','500nm');
xlabel('Energy, eV');
ylabel('Intensity, 1/(eV.nm)');

x = (-0.0495:0.0005:0.050); %x-axis for Gaussian
G = normpdf(x,0,0.004); %2nd number is mean, 3rd number is std dev
normG = (G - min(G))/(max(G) - min(G)); %normalizing the Gaussian
figure; plot(x,normG);

H = conv2(Prob,normG','same');
figure; plot(E,H);
title('Transmission EELS - Beam in SiO2 - Convolved');
legend('1nm','10nm','50nm','100nm','500nm');
xlabel('Energy, eV');
ylabel('Intensity, 1/(eV.nm)');
```

2. Relativistic EELS probability for a specimen with an interface under the infinite slab approximation

The MATLAB code printed below can be used to calculate the relativistic inelastic scattering probability for an electron passing through an infinite slab of SiO_2 which forms an interface with an infinite slab of Si based on the analytical expression derived in (Wang, 1996). The optical dielectric functions for SiO_2 and Si were obtained from the Handbook of Optical Constants (Palik & Ghosh, 1998). The inelastic scattering probability is convolved with the instrumental response function for comparison with experiments.

```
%%
clear all;
clc;

for i = 1:191
E = linspace(0.005,0.195,191)'; %in eV

data = xlsread('Si_SiO2_dielectric_v1','Palik');

%Get epR,epI for SiO2
SiO2_epR = spline(data(:,13),data(:,14),E);
SiO2_epI = spline(data(:,13),data(:,15),E);

figure; plot(E,SiO2_epR,E,SiO2_epI);

SiO2_ep = complex(SiO2_epR,SiO2_epI);

estSiO2_bulk = imag(-1./SiO2_ep);  %bulk eels
figure; plot(E,estSiO2_bulk);

%Get epR,epI for Si
Si_epR = spline(data(:,9),data(:,10),E);
Si_epI = spline(data(:,9),data(:,11),E);

figure; plot(E,Si_epR,E,Si_epI);

Si_ep = complex(Si_epR,Si_epI);

estSi_bulk = imag(-1./Si_ep);  %bulk eels
figure; plot(E,estSi_bulk);

%%
```

```
ep1 = SiO2_ep; %beam passes through this side of the interface
ep2 = Si_ep; %other side of the interface
epr = ep2./ep1;

v = 1.3377*10^8; %for 60 kV voltage
hbar = 1.055*10^-34; c = 3*10^8; e = 1.6*10^-19; %constants
beta = v/c; %relativistic factor
omega = e*E/hbar;
kz1 = ((omega/v).^2).*(1-(beta^2)*ep1);
kz2 = ((omega/v).^2).*(1-(beta^2)*ep2);

  for j = 1:15001
    theta = (0:0.001:15)'*10^-3; %collection angle
    ky = sqrt(1.6646*10^24 *(theta).^2);
    kai1(i,j) = sqrt((ky(j)^2) + kz1(i));
    kai2(i,j) = sqrt((ky(j)^2) + kz2(i));

    P(i,j) = (1-(beta^2)*ep1(i))/(kai1(i,j)*ep1(i));
    q(i,j) = kai1(i,j) + kai2(i,j);
    r(i,j) = kai1(i,j) - kai2(i,j);
    s(i,j) = kai2(i,j) + kai1(i,j)*epr(i);
    Q(i,j) = (2*(ep2(i)-ep1(i))*kai1(i,j))/((ep1(i)^2)*q(i,j)*s(i,j));
    R(i,j) = P(i,j)*r(i,j)/q(i,j);
    S(i,j) = Q(i,j) + R(i,j);

    for k = 1:5
      x0 = [1,10,50,100,500]*10^-9; %impact parameter
      T(i,k,j) = (Q(i,j)-R(i,j))*exp(-2*kai1(i,j)*x0(k))-P(i,j);
      fun(i,k,j) = imag(T(i,k,j));
    end
  end
end

%%
A = sum(fun,3);

ep0 = 8.85*10^-12;
n = (e^2)/(2*pi^2*hbar^2*v^2*ep0);

Prob = 1.6*10^-28*n*A; %1/J.m = 1.6*10^-28 1/eV.nm
figure; plot(E,Prob);
title('Transmission EELS - Beam in SiO2 - raw');
legend('1nm','10nm','50nm','100nm','500nm');
xlabel('Energy, eV');
ylabel('Intensity, 1/(eV.nm)');

x = (-49.5:0.5:50); %x-axis for Gaussian
G = normpdf(x,0,0.004); %2nd number is mean, 3rd number is std dev
normG = (G - min(G))/(max(G) - min(G)); %normalizing the Gaussian
figure; plot(x,normG);
```

```
H = conv2(Prob,normG','same');
figure; plot(E,H);
title('Transmission EELS - Beam in SiO2 - Convolved');
legend('1nm','10nm','50nm','100nm','500nm');
xlabel('Energy, eV');
ylabel('Intensity, 1/(eV.nm)');
```

3. Relativistic EELS probability for a laterally infinite thin-film

The MATLAB code printed below can be used to calculate the relativistic inelastic scattering probability for an electron passing through a laterally infinite SiO_2 thin-film of finite thickness, taking surface contributions into consideration, based on the analytical expression derived in (Kröger, 1968). The optical dielectric functions for SiO_2 was obtained from the Handbook of Optical Constants (Palik & Ghosh, 1998). The inelastic scattering probability is convolved with the instrumental response function for comparison with experiments.

```
clear all;
clc;

for i = 1:191
   E = linspace(0.005,0.195,191); % E in eV

   data = xlsread('Si_SiO2_dielectric_v1','Palik'); % data read

   % dielectric data for SiO2
   SiO2_epR = spline(data(:,13),data(:,14),E); %real part of dielectric function
   SiO2_epI = spline(data(:,13),data(:,15),E); %imaginary part of dielectric function

   figure; plot(E,SiO2_epR,E,SiO2_epI);

   SiO2_ep = complex(SiO2_epR,SiO2_epI); %complex dielectric function

   estSiO2_bulk = imag(-1./SiO2_ep);  %bulk energy-loss function
   figure; plot(E,estSiO2_bulk);

   Vac_ep = ones(1,191); %vacuum dielectric function

   %% Calculation begins here

   ep = conj(SiO2_ep); %beam passes through this medium
   et = conj(Vac_ep); %surrounding medium

   v = 1.3377*10^8; hbar = 1.055*10^-34; c = 3*10^8; %constants
   e = 1.6*10^-19; ep0 = 8.85*10^-12; me = 9.1*10^-31; %constants
   n = e^3/(4*pi^3*hbar^2*ep0*v^2); %multiplying factor for the scattering probability
   beta = v/c; %relativistic consideration
   mu = sqrt(1-ep*(beta^2)); %relativistic consideration
   gamma = 1/sqrt(1-beta^2); %set = 1 to calculate non-relativistic probability
```

```
momentum = me*v*gamma;
thetaE = E*e/momentum/v; %characteristic scattering angle

for j = 1:10001
   theta = (0:0.001:10)'*10^-3; %collection angle

   lam(i,j) = sqrt(theta(j)^2 - ep(i)*(thetaE(i)^2)*(beta^2));
   lam0(i,j) = sqrt(theta(j)^2 - et(i)*(thetaE(i)^2)*(beta^2));
   phi(i,j) = sqrt(theta(j)^2 + (thetaE(i)^2)*(1 - ep(i)*(beta^2)));
   phi0(i,j) = sqrt(theta(j)^2 + (thetaE(i)^2)*(1 - et(i)*(beta^2)));
   phi01(i,j) = sqrt(theta(j)^2 + (thetaE(i)^2)*(1 - (ep(i)-et(i))*(beta^2)));

   F211(i) = (ep(i) - et(i))^2;
   F212(j) = (2*hbar/(me*v))*((theta(j))^2);
   F21(i,j)  = F211(i)*F212(j);
   F22(i,j) = ((phi0(i,j))^4)*((phi(i,j))^4);
   F2(i,j) = F21(i,j)/F22(i,j);

   C001(i,j) = lam(i,j)/thetaE(i);

   for k = 1:4
      t = [100,250,500,1000]*10^-9; %specimen thickness
      de(i,k) = (e*t(k)*E(i))/(2*hbar*v); %multiply by e to get E in Joules which makes
de unitless

      L1(i,j) = ep(i)*lam0(i,j);
      L2(i,j) = et(i)*lam(i,j);
      C00(i,k,j) = lam(i,j)*de(i,k)/thetaE(i);
      C10(i,k,j) = tanh(C00(i,k,j));
      C20(i,k,j) = coth(C00(i,k,j));
      Lplus(i,k,j) = L1(i,j) + L2(i,j)*C10(i,k,j);
      Lminus(i,k,j) = L1(i,j) + L2(i,j)*C20(i,k,j);

      A1(i,j) = (phi01(i,j)^4)/(ep(i)*et(i));
      A21(i,k) = sin(de(i,k));
      A2(i,k,j) = ((A21(i,k))^2)/Lplus(i,k,j);
      A31(i,k) = cos(de(i,k));
      A3(i,k,j) = ((A31(i,k))^2)/Lminus(i,k,j);
      A(i,k,j) = A1(i,j)*(A2(i,k,j) + A3(i,k,j));

      B1(i) = (beta^2)*thetaE(i)/et(i);
      B2(i,j) = lam0(i,j)*((phi01(i,j))^2);
      B3(i,k,j) = (1/Lplus(i,k,j) - 1/Lminus(i,k,j));
      B4(i,k) = sin(2*de(i,k));
      B11(i,j) = B1(i)*B2(i,j);
      B12(i,k,j) = B11(i,j)*B4(i,k);
      B(i,k,j) = B12(i,k,j)*B3(i,k,j);

      C11(i,k) = (A31(i,k))^2;
      C12(i,k,j) = C10(i,k,j)/Lplus(i,k,j);
```

```
        C1(i,k,j) = C11(i,k)*C12(i,k,j);
        C21(i,k) = (A21(i,k))^2;
        C22(i,k,j) = C20(i,k,j)/Lminus(i,k,j);
        C2(i,k,j) = C21(i,k)*C22(i,k,j);
        C3(i) = -(beta^4)*((thetaE(i))^2);
        C4(i,j) = lam0(i,j)*lam(i,j);
        C5(i,j) = C3(i)*C4(i,j);
        C(i,k,j) = C5(i,j)*(C1(i,k,j) + C2(i,k,j));

        F11(i) = ((mu(i))^2)/ep(i);
        F12(i,k) = F11(i)*t(k);
        F1(i,k,j) = F12(i,k)/(phi(i,j)^2);
        fun1(i,k,j) = A(i,k,j) + B(i,k,j) + C(i,k,j);
        fun2(i,k,j) = F2(i,j)*fun1(i,k,j);
        fun(i,k,j) = n*imag(F1(i,k,j) - fun2(i,k,j));
        Prob3D(i,k,j) = 2*pi*sin(theta(j))*fun(i,k,j);
    end
  end
end

%% Plotting EEL spectra

Prob = 1.6*10^-19 * sum(Prob3D,3); %1/J = 1.6*10^-19 1/eV
Prob_by_t = Prob./t;

figure; plot(E,Prob);
title('Transmission EELS - Beam in SiO2');
legend('t=100 nm','t=250 nm','t=500 nm','t=1000 nm'); %,'t=5 nm','t=500 nm','t=50
nm''t=200 nm','t=20 nm',,'t=2 nm'
xlabel('Energy, eV');
ylabel('dP/dE, 1/(eV)');

figure; plot(E,Prob_by_t);
title('Transmission EELS - Beam in SiO2');
legend('t=100 nm','t=250 nm','t=500 nm','t=1000 nm');
xlabel('Energy, eV');
ylabel('d2P/(dE.dZ), 1/(eV.m)');

x = (-0.0495:0.0005:0.050); %x-axis for Gaussian - same number of x-axis points as x-
axis of Prob
G = normpdf(x,0,0.003); %2nd number is mean, 3rd number is std dev
normG = (G - min(G))/(max(G) - min(G)); %normalizing the Gaussian
% figure; plot(x,normG);

H = conv2(Prob,normG','same');
figure; plot(E,H);
title('Transmission EELS - Beam in SiO2 - convolved');
legend('t=100 nm','t=250 nm','t=500 nm','t=1000 nm');
xlabel('Energy, eV');
ylabel('Intensity, 1/eV');
```

APPENDIX B

COPYRIGHT AGREEMENTS

Copyright agreement for Figure 1.1

JOHN WILEY AND SONS LICENSE
TERMS AND CONDITIONS

Jul 08, 2020

This Agreement between Dr. Kartik Venkatraman ("You") and John Wiley and Sons ("John Wiley and Sons") consists of your license details and the terms and conditions provided by John Wiley and Sons and Copyright Clearance Center.

License Number	4864401192972
License date	Jul 08, 2020
Licensed Content Publisher	John Wiley and Sons
Licensed Content Publication	Wiley Books
Licensed Content Title	General survey of vibrational spectroscopy
Licensed Content Date	Dec 13, 2007
Licensed Content Pages	10
Type of use	Dissertation/Thesis
Requestor type	University/Academic
Format	Electronic
Portion	Figure/table

Number of figures/tables	1
Will you be translating?	No
Title	Towards high spatial resolution vibrational spectroscopy in a scanning transmission electron microscope
Institution name	Arizona State University
Expected presentation date	Jul 2020
Portions	Figure 2.1-3
Requestor Location	Dr. Kartik Venkatraman 850 S River Drive Unit 1110 TEMPE, AZ 85281 United States Attn: Arizona State University
Publisher Tax ID	EU826007151
Total	0.00 USD

Copyright agreement for Figures 1.2 and 1.3

Jul 08, 2020

This Agreement between Dr. Kartik Venkatraman ("You") and Elsevier ("Elsevier") consists of your license details and the terms and conditions provided by Elsevier and Copyright Clearance Center.

License Number	4864430334295
License date	Jul 08, 2020
Licensed Content Publisher	Elsevier
Licensed Content Publication	Elsevier Books
Licensed Content Title	Infrared and Raman Spectroscopy
Licensed Content Author	Peter Larkin
Licensed Content Date	Jan 1, 2011
Licensed Content Pages	19
Start Page	7
End Page	25
Type of Use	reuse in a thesis/dissertation
Portion	figures/tables/illustrations

Number of figures/tables/illustrations	2
Format	electronic
Are you the author of this Elsevier chapter?	No
Will you be translating?	No
Title	Towards high spatial resolution vibrational spectroscopy in a scanning transmission electron microscope
Institution name	Arizona State University
Expected presentation date	Jul 2020
Portions	Figures 2.8, 2.11
Requestor Location	Dr. Kartik Venkatraman 850 S River Drive Unit 1110 TEMPE, AZ 85281 United States Attn: Arizona State University
Publisher Tax ID	98-0397604
Total	0.00 USD

Copyright agreement for Figure 1.4

JOHN WILEY AND SONS LICENSE
TERMS AND CONDITIONS

Jul 08, 2020

This Agreement between Dr. Kartik Venkatraman ("You") and John Wiley and Sons ("John Wiley and Sons") consists of your license details and the terms and conditions provided by John Wiley and Sons and Copyright Clearance Center.

License Number	4864431146624
License date	Jul 08, 2020
Licensed Content Publisher	John Wiley and Sons
Licensed Content Publication	Angewandte Chemie International Edition
Licensed Content Title	Tip-Enhanced Near-Field Optical Microscopy
Licensed Content Author	Achim Hartschuh
Licensed Content Date	Oct 9, 2008
Licensed Content Volume	47
Licensed Content Issue	43
Licensed Content Pages	14

Type of use	Dissertation/Thesis
Requestor type	University/Academic
Format	Electronic
Portion	Figure/table
Number of figures/tables	1
Will you be translating?	No
Title	Towards high spatial resolution vibrational spectroscopy in a scanning transmission electron microscope
Institution name	Arizona State University
Expected presentation date	Jul 2020
Portions	Figure 2
Requestor Location	Dr. Kartik Venkatraman 850 S River Drive Unit 1110 TEMPE, AZ 85281 United States Attn: Arizona State University
Publisher Tax ID	EU826007151
Total	0.00 USD

Copyright agreement for Figure 1.5

SPRINGER NATURE LICENSE
TERMS AND CONDITIONS

Jul 08, 2020

This Agreement between Dr. Kartik Venkatraman ("You") and Springer Nature ("Springer Nature") consists of your license details and the terms and conditions provided by Springer Nature and Copyright Clearance Center.

License Number	4864440470828
License date	Jul 08, 2020
Licensed Content Publisher	Springer Nature
Licensed Content Publication	Nature
Licensed Content Title	Vibrational spectroscopy in the electron microscope
Licensed Content Author	Ondrej L. Krivanek et al
Licensed Content Date	Oct 8, 2014
Type of Use	Thesis/Dissertation
Requestor type	academic/university or research institute
Format	electronic
Portion	figures/tables/illustrations
Number of figures/tables/illustrations	1

High-res required	no
Will you be translating?	no
Circulation/distribution	1 - 29
Author of this Springer Nature content	no
Title	Towards high spatial resolution vibrational spectroscopy in a scanning transmission electron microscope
Institution name	Arizona State University
Expected presentation date	Jul 2020
Portions	Figure 1a
Requestor Location	Dr. Kartik Venkatraman 850 S River Drive Unit 1110 TEMPE, AZ 85281 United States Attn: Arizona State University
Total	0.00 USD

Copyright agreement for Figure 1.6

SPRINGER NATURE LICENSE
TERMS AND CONDITIONS

Jul 08, 2020

This Agreement between Dr. Kartik Venkatraman ("You") and Springer Nature ("Springer Nature") consists of your license details and the terms and conditions provided by Springer Nature and Copyright Clearance Center.

License Number	4864440961153
License date	Jul 08, 2020
Licensed Content Publisher	Springer Nature
Licensed Content Publication	Nature
Licensed Content Title	Mapping vibrational surface and bulk modes in a single nanocube
Licensed Content Author	Maureen J. Lagos et al
Licensed Content Date	Mar 23, 2017
Type of Use	Thesis/Dissertation
Requestor type	academic/university or research institute
Format	electronic
Portion	figures/tables/illustrations
Number of	1

figures/tables/illustrations	
High-res required	no
Will you be translating?	no
Circulation/distribution	1 - 29
Author of this Springer Nature content	no
Title	Towards high spatial resolution vibrational spectroscopy in a scanning transmission electron microscope
Institution name	Arizona State University
Expected presentation date	Jul 2020
Portions	Figure 3a
Requestor Location	Dr. Kartik Venkatraman 850 S River Drive Unit 1110 TEMPE, AZ 85281 United States Attn: Arizona State University
Total	0.00 USD

Copyright agreement for Figure 1.7

American Physical Society Reuse and Permissions License

08-Jul-2020

This license agreement between the American Physical Society ("APS") and Kartik Venkatraman ("You") consists of your license details and the terms and conditions provided by the American Physical Society and SciPris.

Licensed Content Information

License Number:	**RNP/20/JUL/027993**
License date:	08-Jul-2020
DOI:	10.1103/PhysRevLett.122.016103
Title:	Phonon Spectroscopy at Atomic Resolution
Author:	F. S. Hage et al.
Publication:	Physical Review Letters
Publisher:	American Physical Society
Cost:	USD $ 0.00

Request Details

Does your reuse require significant modifications: No

Specify intended distribution locations:	United States
Reuse Category:	Reuse in a thesis/dissertation
Requestor Type:	Academic Institution
Items for Reuse:	Figures/Tables
Number of Figure/Tables:	2
Figure/Tables Details:	Figures 1a, 2a
Format for Reuse:	Electronic

Information about New Publication:

University/Publisher:	Arizona State University
Title of dissertation/thesis:	Towards high spatial resolution vibrational spectroscopy in a scanning transmission electron microscope
Author(s):	Kartik Venkatraman
Expected completion date:	Aug. 2020

License Requestor Information

Name:	Kartik Venkatraman
Affiliation:	Individual
Email Id:	kvenka16@asu.edu
Country:	United States

Copyright agreement for Figure 1.8

THE AMERICAN ASSOCIATION FOR THE ADVANCEMENT OF SCIENCE LICENSE TERMS AND CONDITIONS

Jul 08, 2020

This Agreement between Dr. Kartik Venkatraman ("You") and The American Association for the Advancement of Science ("The American Association for the Advancement of Science") consists of your license details and the terms and conditions provided by The American Association for the Advancement of Science and Copyright Clearance Center.

License Number	4864450486406
License date	Jul 08, 2020
Licensed Content Publisher	The American Association for the Advancement of Science
Licensed Content Publication	Science
Licensed Content Title	Identification of site-specific isotopic labels by vibrational spectroscopy in the electron microscope
Licensed Content Author	Jordan A. Hachtel,Jingsong Huang,Ilja Popovs,Santa Jansone-Popova,Jong K. Keum,Jacek Jakowski,Tracy C. Lovejoy,Niklas Dellby,Ondrej L. Krivanek,Juan Carlos Idrobo
Licensed Content Date	Feb 1, 2019
Licensed Content Volume	363

Licensed Content Issue	6426
Volume number	363
Issue number	6426
Type of Use	Thesis / Dissertation
Requestor type	Scientist/individual at a research institution
Format	Electronic
Portion	Text Excerpt
Number of pages requested	1
Title	Towards high spatial resolution vibrational spectroscopy in a scanning transmission electron microscope
Institution name	Arizona State University
Expected presentation date	Jul 2020
Portions	Figure 1
Requestor Location	Dr. Kartik Venkatraman 850 S River Drive Unit 1110 TEMPE, AZ 85281 United States Attn: Arizona State University
Total	0.00 USD

Copyright agreement for Figures 2.1b

SPRINGER NATURE LICENSE
TERMS AND CONDITIONS

Jul 08, 2020

This Agreement between Dr. Kartik Venkatraman ("You") and Springer Nature ("Springer Nature") consists of your license details and the terms and conditions provided by Springer Nature and Copyright Clearance Center.

License Number	4864530229147
License date	Jul 08, 2020
Licensed Content Publisher	Springer Nature
Licensed Content Publication	Springer eBook
Licensed Content Title	The Instrument
Licensed Content Author	David B. Williams, C. Barry Carter
Licensed Content Date	Jan 1, 2009
Type of Use	Thesis/Dissertation
Requestor type	academic/university or research institute
Format	electronic
Portion	figures/tables/illustrations
Number of figures/tables/illustrations	1

Will you be translating?	no
Circulation/distribution	1 - 29
Author of this Springer Nature content	no
Title	Towards high spatial resolution vibrational spectroscopy in a scanning transmission electron microscope
Institution name	Arizona State University
Expected presentation date	Jul 2020
Portions	Figure 9.1b
Requestor Location	Dr. Kartik Venkatraman 850 S River Drive Unit 1110 TEMPE, AZ 85281 United States Attn: Arizona State University
Total	0.00 USD

Copyright agreement for Figures 2.2 and 2.8

SPRINGER NATURE LICENSE
TERMS AND CONDITIONS

Jul 08, 2020

This Agreement between Dr. Kartik Venkatraman ("You") and Springer Nature ("Springer Nature") consists of your license details and the terms and conditions provided by Springer Nature and Copyright Clearance Center.

License Number	4864470464066
License date	Jul 08, 2020
Licensed Content Publisher	Springer Nature
Licensed Content Publication	Springer eBook
Licensed Content Title	An Introduction to EELS
Licensed Content Author	R.F. Egerton
Licensed Content Date	Jan 1, 2011
Type of Use	Thesis/Dissertation
Requestor type	academic/university or research institute
Format	electronic
Portion	figures/tables/illustrations
Number of figures/tables/illustrations	2

Will you be translating?	no
Circulation/distribution	1 - 29
Author of this Springer Nature content	no
Title	Towards high spatial resolution vibrational spectroscopy in a scanning transmission electron microscope
Institution name	Arizona State University
Expected presentation date	Jul 2020
Portions	Figures 1.1, 1.3
Requestor Location	Dr. Kartik Venkatraman 850 S River Drive Unit 1110 TEMPE, AZ 85281 United States Attn: Arizona State University
Total	0.00 USD

Copyright agreement for Figure 2.3a

SPRINGER NATURE LICENSE
TERMS AND CONDITIONS

Jul 08, 2020

This Agreement between Dr. Kartik Venkatraman ("You") and Springer Nature ("Springer Nature") consists of your license details and the terms and conditions provided by Springer Nature and Copyright Clearance Center.

License Number	4864471017798
License date	Jul 08, 2020
Licensed Content Publisher	Springer Nature
Licensed Content Publication	Springer eBook
Licensed Content Title	The Principles of STEM Imaging
Licensed Content Author	Peter D. Nellist
Licensed Content Date	Jan 1, 2011
Type of Use	Thesis/Dissertation
Requestor type	academic/university or research institute
Format	electronic
Portion	figures/tables/illustrations
Number of figures/tables/illustrations	1

Will you be translating?	no
Circulation/distribution	1 - 29
Author of this Springer Nature content	no
Title	Towards high spatial resolution vibrational spectroscopy in a scanning transmission electron microscope
Institution name	Arizona State University
Expected presentation date	Jul 2020
Portions	Figure 2-1
Requestor Location	Dr. Kartik Venkatraman 850 S River Drive Unit 1110 TEMPE, AZ 85281 United States Attn: Arizona State University
Total	0.00 USD

Copyright agreement for Figures 2.4

SPRINGER NATURE LICENSE
TERMS AND CONDITIONS

Jul 08, 2020

This Agreement between Dr. Kartik Venkatraman ("You") and Springer Nature ("Springer Nature") consists of your license details and the terms and conditions provided by Springer Nature and Copyright Clearance Center.

License Number	4864530327500
License date	Jul 08, 2020
Licensed Content Publisher	Springer Nature
Licensed Content Publication	Springer eBook
Licensed Content Title	Amplitude Contrast
Licensed Content Author	David B. Williams, C. Barry Carter
Licensed Content Date	Jan 1, 2009
Type of Use	Thesis/Dissertation
Requestor type	academic/university or research institute
Format	electronic
Portion	figures/tables/illustrations
Number of figures/tables/illustrations	1

Will you be translating?	no
Circulation/distribution	1 - 29
Author of this Springer Nature content	no
Title	Towards high spatial resolution vibrational spectroscopy in a scanning transmission electron microscope
Institution name	Arizona State University
Expected presentation date	Jul 2020
Portions	Figure 22.13
Requestor Location	Dr. Kartik Venkatraman 850 S River Drive Unit 1110 TEMPE, AZ 85281 United States Attn: Arizona State University
Total	0.00 USD

Copyright agreement for Figures 2.6

SPRINGER NATURE LICENSE
TERMS AND CONDITIONS

Jul 08, 2020

This Agreement between Dr. Kartik Venkatraman ("You") and Springer Nature ("Springer Nature") consists of your license details and the terms and conditions provided by Springer Nature and Copyright Clearance Center.

License Number	4864530091522
License date	Jul 08, 2020
Licensed Content Publisher	Springer Nature
Licensed Content Publication	Springer eBook
Licensed Content Title	Lenses, Apertures, and Resolution
Licensed Content Author	David B. Williams, C. Barry Carter
Licensed Content Date	Jan 1, 2009
Type of Use	Thesis/Dissertation
Requestor type	academic/university or research institute
Format	electronic
Portion	figures/tables/illustrations
Number of figures/tables/illustrations	2

Will you be translating?	no
Circulation/distribution	1 - 29
Author of this Springer Nature content	no
Title	Towards high spatial resolution vibrational spectroscopy in a scanning transmission electron microscope
Institution name	Arizona State University
Expected presentation date	Jul 2020
Portions	Figures 6.11 and 6.13
Requestor Location	Dr. Kartik Venkatraman 850 S River Drive Unit 1110 TEMPE, AZ 85281 United States Attn: Arizona State University
Total	0.00 USD

Copyright agreement for Figure 2.7

CAMBRIDGE UNIVERSITY PRESS LICENSE
TERMS AND CONDITIONS

Jul 08, 2020

This Agreement between Dr. Kartik Venkatraman ("You") and Cambridge University Press ("Cambridge University Press") consists of your license details and the terms and conditions provided by Cambridge University Press and Copyright Clearance Center.

License Number	4864471355726
License date	Jul 08, 2020
Licensed Content Publisher	Cambridge University Press
Licensed Content Publication	Microscopy and Microanalysis
Licensed Content Title	Sub-Ångstrom Resolution through Aberration-Corrected STEM
Licensed Content Author	S. J. Pennycook, A. R. Lupini, M. Varela, A. Borisevich, Y. Peng, M. F. Chisholm, N. Dellby, O. L. Krivanek, P. D. Nellist, S. Z. Szilagyi, G. Duscher
Licensed Content Date	Jul 24, 2003
Licensed Content Volume	9
Licensed	S02

Content Issue	
Start page	926
End page	927
Type of Use	Dissertation/Thesis
Requestor type	Not-for-profit
Portion	Text extract
Number of pages requested	1
Title	Towards high spatial resolution vibrational spectroscopy in a scanning transmission electron microscope
Institution name	Arizona State University
Expected presentation date	Jul 2020
Portions	Figures 3a, 3b
Territory for reuse	World
Requestor Location	Dr. Kartik Venkatraman 850 S River Drive Unit 1110 TEMPE, AZ 85281 United States Attn: Arizona State University

Copyright agreement for Figure 2.9

SPRINGER NATURE LICENSE
TERMS AND CONDITIONS

Jul 08, 2020

This Agreement between Dr. Kartik Venkatraman ("You") and Springer Nature ("Springer Nature") consists of your license details and the terms and conditions provided by Springer Nature and Copyright Clearance Center.

License Number	4864471103852
License date	Jul 08, 2020
Licensed Content Publisher	Springer Nature
Licensed Content Publication	Springer eBook
Licensed Content Title	Physics of Electron Scattering
Licensed Content Author	R.F. Egerton
Licensed Content Date	Jan 1, 2011
Type of Use	Thesis/Dissertation
Requestor type	academic/university or research institute
Format	electronic
Portion	figures/tables/illustrations
Number of figures/tables/illustrations	1

Will you be translating?	no
Circulation/distribution	1 - 29
Author of this Springer Nature content	no
Title	Towards high spatial resolution vibrational spectroscopy in a scanning transmission electron microscope
Institution name	Arizona State University
Expected presentation date	Jul 2020
Portions	Figure 3.36
Requestor Location	Dr. Kartik Venkatraman 850 S River Drive Unit 1110 TEMPE, AZ 85281 United States Attn: Arizona State University
Total	0.00 USD

Copyright agreement for Figure 6.2b

American Physical Society Reuse and Permissions License

08-Jul-2020

This license agreement between the American Physical Society ("APS") and Kartik Venkatraman ("You") consists of your license details and the terms and conditions provided by the American Physical Society and SciPris.

Licensed Content Information

License Number:	**RNP/20/JUL/027997**
License date:	08-Jul-2020
DOI:	10.1103/PhysRevLett.98.095503
Title:	Vibrational Properties of Hexagonal Boron Nitride: Inelastic X-Ray Scattering and Ab Initio Calculations
Author:	J. Serrano et al.
Publication:	Physical Review Letters
Publisher:	American Physical Society
Cost:	USD $ 0.00

Request Details

Does your reuse require significant modifications: No

Specify intended distribution locations:	Worldwide
Reuse Category:	Reuse in a thesis/dissertation
Requestor Type:	Student
Items for Reuse:	Figures/Tables
Number of Figure/Tables:	1
Figure/Tables Details:	Figure 2
Format for Reuse:	Electronic

Information about New Publication:

University/Publisher:	Arizona State University
Title of dissertation/thesis:	Towards high spatial resolution vibrational spectroscopy in a scanning transmission electron microscope
Author(s):	Kartik Venkatraman
Expected completion date:	Aug. 2020

License Requestor Information

Name:	Kartik Venkatraman
Affiliation:	Individual
Email Id:	kvenka16@asu.edu
Country:	United States